UNIVERSITY OF CALIFORNIA

Santa Barbara

Multiple double-couple analysis of recent large earthquakes and its application in detecting the dynamic stress triggering events

A dissertation submitted in partial satisfaction of the

requirements for the degree Doctor of Philosophy

in Earth Science

by

Xiangyu Li

Committee in charge:

Professor Chen Ji, Chair

Professor Ralph J. Archuleta

Professor Toshiro Tanimoto

December 2014

The dissertation of Xiangyu Li is approved.

_____

Professor Ralph J. Archuleta

_____

Professor Toshiro Tanimoto

_____

Professor Chen Ji, Committee Chair

August 2014

Multiple double-couple analysis of recent large earthquakes and its application in detecting the dynamic stress triggering events

by

Xiangyu Li

ACKNOWLEDGEMENTS

I have spent 5 years in this world-famous beautiful place and studied in this renowned university pursuing my PhD degree. I really enjoy the time and life here and I would never forget my professors, my friends and colleagues and all those kind people who helped me in the past 5 years. All of your assistance encourages me to overcome all the frustration, failure, and problem along my research path and contributes to my fruitful life. I really appreciate that!

At first stage, I would like to show my greatest gratitude to my advisor Chen Ji for his continuous support of my PhD study and research. In research, his professional knowledge, patience, intelligence, motivation, enthusiasm and strict guidance immensely foster my problem-solving skills and independent working ability. In life, he is an easygoing and student-caring advisor, he would always like to share his idea and experience with me and give me a hand when necessary. He provides me such an exceptional and valuable opportunity to study aboard and I have truly learned what I really want. It is my great honor to work with him, Thanks!

I would also like to thank the rest of my committee members: Prof. Archuleta, Prof Tanimoto and Prof Steidl. Prof. Archuleta really builds my first impression as a geophysics expert. His professional scope, strong logic and clear explanation in research can always enlighten my further understanding in broader geophysics pictures. His comments are also very constructive and useful in my own research. Alternatively, I have benefited a lot from Prof. Tanimoto's lectures and discussion. He teaches me a lot of complicate and cut-edge geophysical technology and concepts. His impressive analytical hand-written deduction

increasingly forms my deeper understanding of geophysical principle and inverse methodology. I am also grateful to Jamie, as a committee member in my comp exam and PhD candidate qualify exam, he provided me many positive feedbacks and suggestion. Certainly, I cannot forget to mention all the excellent graduate students in geophysics group in our department. I should specially thank Guangfu Shao and his lovely wife Nanlan Zhang, who offered me tremendous helps in my research and my PhD study; my another senior Qiming Liu and his wife Yali, who helped me solve a lot of technical problems as well as answer my trivial questions with unexhausted patience; I also greatly thank Tomoko Yano, your experience and life-enjoying attitude definitely made my better life here, I enjoy the time playing tennis with you! Appreciation also gives to Jorge crempian, thank you for your time and great help in my research projects and big congratulation on your newborn baby with your wife! Stephanie Tsang, thank you so much for introducing me in the speak club! Many other thanks go to the new graduate students Mareike Adams, Luyuan Ding, Anne Lamontagne who provide me constructive comments on my presentation and writing. Additionally, I would also thank my previous fellow colleagues Eryn Burkhart, Francesco Civilini, Daniel Lavallee, Dr. Asano and his wife, Kenji Kawai, without you guys I can not have a wonderful life in UCSB!

Of equal importance is to express my gratitude to the earth science department for all the helpful class and outstanding lectures I once. My sincere thank goes to Prof. Awramik, Prof. Burbank, Prof. Cottle, Prof Lisiecki and Prof. Wyss who once taught me. I also want give my special thanks to the staff at the department, especially Hannah Smit, for your long-term kind assistance in my study.

Last but not least, I want to express my sincere gratitude to my family, especially to my mother, who always inspire me and encourage me to take a right way and positive attitude in finishing my graduate study here.

XIANGYU LI

6930 Whittier dr, Apt. #140 Tel: 805-455-7802

Goleta, CA. 93117 xiangyuli@umail.ucsb.edu

EDUCATION

PhD candidate, Geological Science, University of California, Santa Barbara,

2009 - Present. ***GPA: 4.0. (Anticipate to graduate on Oct 2014)***

B.E, Exploration geophysics, Central South University, *P.R. China, 2005-2009*

GPA: 3.6, Major GPA: 3.8.

PUBLICATIONS

X. Li, G. Shao, C. Ji, Multiple point source modeling of the Mw>8 earthquakes since 1990. (in preparation)

X. Li, C. Ji., 2012 Ms 7.3 Honshu earthquake: an earthquake doublet with different focal mechanism. (in preparation)

X. Li, G. Shao, C. Ji, .A new evidence of nearly instantaneous dynamic triggering an Mw>7 normal fault earthquake by a strike-slip earthquake: dual ruptures of 2000 Mw 8.0 New Ireland earthquake. (Submitted to Geophysical Journal International)

G. Shao, X. Li, C. Ji, (2011). Focal mechanism and slip history of 2011 M w 9.1 off the Pacific coast of Tohoku Earthquake, constrained with teleseismic body and surface waves, *Earth Planets Space,* 63, 1-15.

Yao H C, Chen R J, Li X Y, (2010). A Remote Control and Measurement System for Multi-frequency IP Instrument Based on GPRS. *Progress in Geophys*, 25(2), 692-700. (in Chinese)

PATENT

X. Li, R. Chen., Method for extracting induced polarization model parameters prospected by electrical method. *Patent No*. 200910227009.5, P. R. China, 2009.

AWARDS

2005-2006, 2006-2007 Excellent Student Prize, Central South University.

2010 Geophysics award, UCSB.

2011 AGU annual meeting Outstanding Student Paper Award.

2013 Graduate Division Dissertation Fellowship, UCSB.

2013 AAPG-SEG West Coast Student Expo distinguished student short course Award.

SKILLS

Computer language: Fortran, C, Perl, Matlab, Openmp, MPI, Assembly language.

Language: Mandarin (native), English (fluent).

RELATED WORK EXPERIENCE

03/2010- Present, Teaching Assistant, Department of Earth Science, UCSB

Course including: Physical geology; Advanced/Introduction to geophysics; Introduction to seismology; Introduction to oceanography.

MEMBERSHIP

American Geophysics Union (AGU)

Seismology Society of America (SSA)

ABSTRACTS

X. Li, C. Ji, Rupture process of the 29 May 2013 Mw 4.8 Isla Vista, California earthquake and its tectonic implication. *AGU Fall meeting,* 2013.

X. Li, Venture of full waveform inversion in detecting the dynamic stress triggering and the regional fault complexity—A multiple point source scenario. *AAPG-SEG West Coast Student Expo*, 2013.

X. Li, C. Ji, 2012 Ms 7.3 Honshu earthquake: earthquake doublet with different focal mechanisms. *SSA annual meeting*, 2013. (**Oral presentation**)

X. Li, G. Shao, C. Ji, Foreshock sequence of the April 11, 2012, Mw 8.6 Indian Ocean earthquake, *AGU Fall Meeting*, 2012. (**Oral presentation**)

X. Li, G. Shao, C. Ji, Complex rupture process of the 2000 Mw 8.1 New Ireland earthquake, a revisit, *AGU Fall Meeting*, 2011.

X. Li, G. Shao, C. Ji, Multiple Double-couple Analysis for M6-7 Earthquakes, *SCEC Annual Meeting*, 2011. **(Outstanding Student Paper Award)**

C. Ji, X. Li, G. Shao, Rupture initiation of the large subduction earthquakes: are the durations and moments of nucleation phases correlated with the final seismic moments, *AGU Fall Meeting*, 2010. (**Invited talk**)

X. Li, C. Ji, Investigation of Long-period Characteristics of Great Earthquakes through Multiple Point Source Analysis, *AGU Fall Meeting*, 2010.

X. Li, G. Shao, C. Ji, Rupture process of 2009 Mw 8.1 Samoa earthquake constrained by joint inverting teleseismic body, surface waves and local strong motion. *AGU Fall Meeting*, 2009. (**Oral presentation**)

X. Li, G. Shao, C. Ji, What did We Learn from the Exercise of the Source Inversion Validation Blind Test I, *AGU Fall meeting*, 2009.

ABSTRACT

Multiple double-couple analysis of recent large earthquakes and its application in detecting the dynamic stress triggering events

by

Xiangyu Li

Currently, the source mechanisms of global large and moderate earthquakes are routinely constrained and reported by multiple agencies using long-period seismic signals. These conventional analyses simplify the rupture process of an earthquake as single point source. On one hand, it becomes not appropriate if this earthquake has a fault dimension comparably larger than the signal's dominant wavelength or includes multiple subevents with different focal mechanisms. On the other hand, these source complexities can yield distinct seismic waves, and therefore might be deciphered through more careful waveform modeling. Such additional information is crucial for the study of earthquake physics as well as post-earthquake hazard evaluation and emergency assistance. The first part of this dissertation introduces a nonlinear inverse algorithm, which approximate an earthquake as multiple double-couple sources (MDC) and constrain them simultaneously using seismic data. The number of double-couples is determined by statistic F-test. This method has been applied to local and global large earthquakes using long-period signals, teleseismic body waves and

local broadband strong-motion records. The results demonstrated that more source information could be extracted using this MDC algorithm than the conventional moment tensor inversion algorithms, though the spatiotemporal resolution relies on the station coverage and frequency contents of seismic signals. The implements of high-quality broadband seismograph networks globally and advances in parallel computational capability enable us to conduct the MDC analysis automatically for global large earthquakes and provide more precise priori information for the subsequent finite fault inversions. It then shall be an important contribution to the routine real-time earthquake hazard analysis.

The second part of this thesis focuses on detecting the aftershocks occurring temporally close to the corresponding mainshocks with the MDC analysis and subsequently analyzing their dynamic interactions with the mainshocks using complete Coulomb stress failure criteria. The two examples presented in Chapter 3 and 4 are the 2012 Mw 7.3 Honshu earthquake and 2000 Mw 8.1 New Ireland earthquake. Our results indicated that both events are doublets. The first subevent of the 2012 Honshu earthquake is a Mw 7.3 oblique thrust earthquake beneath the seaside of the Japan trench axis at a depth of ~50 km, and followed ~13 s later by a Mw 7.3 pure normal fault rupture ~50 km to the N260^{o}E, at a depth of 25-30 km beneath the island side of the trench axis, a classic example of the plate bending. The first subevent of the 2000 Mw 8.0 New Ireland earthquake is Mw 8.0 right lateral strike-slip earthquake, which ruptured a fault plane of 140 km and following 90 s later by a Mw 7.4 normal fault earthquake beneath the outer rise region of subducted Solomon sea plate, 263 km to the south of the first subevent. Our subsequent stress calculations indicated that the rupture of the 2011 Mw 9.1 Tohoku earthquake increases the stress levels at the hypocenters

of two 2012 Honshu subevents. While the Coulomb stress increment is significantly smaller than the co-seismic stress drop of the first subevent, which at the second subevent is compatible to co-seismic stress drop. At the hypocenter of the second subevent, the rupture of the first subevent produced negative static Coulomb stress. The dynamic Coulomb stress carried by the direct P wave is negative as well, but that associating with the direct S is positive with a peak amplitude of 3.8 MPa.. Although the inverted rupture initiation time of the second subevent is 1.7 s earlier than when the positive stress reaches the maximum, this is within the uncertainty of our kinematic modeling. For the 2000 New Ireland doublet, our calculations indicate that the rupture of first subevent produces either a negative or positive but with negligible amplitude ($6x10^{-4}$MPa) static Coulomb failure stress at the hypocenter of second subevent. In contrast, a 0.91 MPa positive dynamic Coulomb stress pulse excited by the stopping phase associating with the rupture of the dominant asperity of the first subevent reaches the hypocenter of the second subevent at 86 s and keeps positive until 90 s. November 16 2000 Mw 8.0 New Ireland earthquake is then a unique example that passing of seismic waves caused a nearly instantaneous triggering of an Mw >7 normal fault earthquake 150 km away. In Chapter 5, we have performed MDC analysis and finite fault joint inversion for 2013 Mw 7.7 Balochistan earthquake using teleseismic body waves and surface waves. Volumetric and Coulomb stress perturbation are then carefully investigated to shed light on revealing the possible dynamic interaction between mud volcano eruption and seismic process of the 2013 Pakistan earthquake. In short, for the all three cases, we find that these subsequent events are correlated with the dynamic stress perturbation, rather than static stress perturbation, excited by the earlier events.

TABLE OF CONTENTS

Chapter 1

Motivation and general methodology

1.1 Motivation

Our planet has apparently moved into a period of increased seismic activity. According to the Global Centroid Moment Tensor (GCMT) project, the number of moment magnitude (Mw) 8 earthquakes in the past 16 years were eight times of those occurring from 1978 to 1994. With the development of high-quality digital seismograph network and advances in computational capability, the focal mechanisms of recent large and intermediate earthquakes have been routinely constrained using long-period seismic signals by multiple agencies (e.g., GCMT catalog, USGS CMT projects, USGS Wphase solution) and could be obtained hours after the rupture initiations. These focal mechanism solutions have been used as the inputs to further investigate the spatial-temporal variations of fault rupture and then proceed to invert the fault slip and stress orientation quickly [*Ji et al.*, 2004].

However, these routine analyses simplify the complex rupture process of an earthquake as a point source, which might not be appropriate if the earthquake has a fault dimension comparable to or much larger than the signal wavelength, or includes multiple subevents with different focal mechanisms. These subevents can be recognized given that such source complexity in terms of irregularity in the rupture propagation and in the distribution of moment release can adequately yield distinguishable seismic waves. For instance, *Tsai et al.* [2005] reported that it required approximately five point sources to match the long period

(2-5 mHz) seismic records and tackle the directivity effect of the great 2004 Mw 9.15 Sumatra Anderman Islands earthquake. An important variable indicating the source complexity is compensated linear-vector dipole (CLVD), which is defined as $-\lambda_2/\max(|\lambda_1|,|\lambda_3|)$, $\lambda_1,\lambda_2,\lambda_3$ are eigenvalues of the moment tensor, ordered such that $\lambda_1 > \lambda_2 > \lambda_3$, *Nettles* and *Ekstrom* [1998]. It has been noticed that nearly 20% of the earthquakes reported in GCMT catalog from 1977 to 1993 have 40% or more CLVD components. Though such CLVD component in terms of deviation from single double-couple could be caused by the noise of data or lateral heterogeneity of the earth, *Kuge and Kawakatsu* [1990] showed evidence that the presence of subevents with different focal mechanisms in a rupture process would lead to CLVD in the inverted CMT solutions. *Frohlich* [1994] further suggested that approximately 70% of the non-double-couple earthquakes occurring along subduction zones and oceanic ridge transforms can be explained using multiple events hypothesis. When the solution includes large CLVD, the real fault plane might be significantly different from the nodal planes of the best double-couple inferred from the moment tensor solution [*Henry et al.*, 2002].

The research work in this thesis includes two portions. First we propose a quick multiple double-couple (MDC) inverse algorithm to study the global large earthquakes using long period or broadband seismic records. We will introduce the method in the following section 1.2 using the long period (0.011 Hz to 0.1 Hz) strong motion records of the 1999 Hector Mine earthquake as an example. Subsequently, in Chapter 2 the same idea will be applied to study Mw>8 earthquakes from 1990 to 2011 using long period (2-5 mHz) teleseismic waveforms; in Chapter 3, 2012 Mw 7.3 Honshu doublet are studied using broadband body waves. Second, the application of MDC analysis led to the discoveries that some large

earthquakes are doublets. The dynamic interactions between subevents then draw our attention. We then develop a synthetic algorithm to calculate the dynamic stress perturbation using 1D layered structure and apply this method to explain not only the interactions of earthquakes in Chapter 3 and Chapter 4 but also mud volcanoes in Chapter 5. A quick review of the finite fault inversion [*Ji et al.*, 2002a; b; *Ji et al.*, 2003a] and Coulomb failure stress can be found in section 1.3.

1.2 Multiple double-couple (MDC) inversion

We approximate an earthquake as summation of multiple subevents. *Henry et al.* [2002] show that spurious large non-double-couple components can be obtained in inversions for the full deviatoric moment tensor for shallow crustal earthquakes due to inaccurate Earth models. They also pointed out that the traditional ‘‘best double-couple’’ solution does not in general provide an optimal estimate of a double-couple mechanism, and is only reliable when the non-double-couple component of the full deviatoric solution is small. Considering the dominant double-couple mechanism of common crustal, tectonic earthquakes and the error introduced when we have to use 1D earth models to generate synthetic earth response, we choose to approximate each subevent as a double-couple rather than a full or deviatoric moment tensor.

Suppose the kinematic rupture process of a shear rupture could be approximated as a series of **N** double-couples. The excited 3-component displacement could be expressed as

$$u_Z(r,t) = \sum_{j=1}^{N} M_0^j(t-\tau_c^j) * \sum_{i=1}^{3} A_{ij}(\varphi_j,\lambda_j,\delta_j) * G_{ij}^Z(r-r_j,t)$$
$$u_R(r,t) = \sum_{j=1}^{N} M_0^j(t-\tau_c^j) \sum_{i=1}^{3} A_{ij}(\varphi_j,\lambda_j,\delta_j) * G_{ij}^R(r-r_j,t)$$
$$u_T(r,t) = \sum_{j=1}^{N} M_0^j(t-\tau_c^j) \sum_{i=1}^{2} A_{i+3\,j}(\varphi_j,\lambda_j,\delta_j) * G_{ij}^T(r-r_j,t) \quad (1)$$

Here U_z, U_R and U_T denotes the vertical, radial and transverse components, respectively, of the surface displacement at location $\boldsymbol{r}$. j=1, 2, … N denote the index of subevents. For the j-th subevent, its strike, dip, and rake are $\varphi_j, \lambda_j, \delta_j$, respectively. A centroid location of r_j indicates its location and τ_c is its centroid time. $\mathbf{M_0^j}$ is the moment rate function of the j-th double-couple. G_{ij}^Z, G_{ij}^R and G_{ij}^T are the Green's functions of these 3 components caused by the rupture of the i-th fundamental fault (i=1, 2, 3) at the location of the j-th subevent (j=1,2, …, N). Following [*Langston*, 1981], we use i=1 for vertical strike-slip fault, (i=2) vertical dip-slip fault and (i=3) 45° dip-slip fault. $A_{ij}(\varphi_j, \lambda_j, \delta_j)$ are geometric coefficients defined as

$$A_{1j}(\varphi_j,\lambda_j,\delta_j) = \sin 2\varphi_j \cos\lambda_j \sin\delta_j + \frac{1}{2}\cos 2\varphi_j \sin\lambda_j \sin 2\delta_j$$
$$A_{2j}(\varphi_j,\lambda_j,\delta_j) = \cos\varphi_j \cos\lambda_j \cos\delta_j - \sin\varphi_j \sin\lambda_j \cos 2\delta_j$$
$$A_{3j}(\varphi_j,\lambda_j,\delta_j) = \frac{1}{2}\sin\lambda_j \sin 2\delta_j$$
$$A_{4j}(\varphi_j,\lambda_j,\delta_j) = \cos 2\varphi_j \cos\lambda_j \sin\delta_j - \frac{1}{2}\sin 2\varphi_j \sin\lambda_j \sin 2\delta_j$$
$$A_{5j}(\varphi_j,\lambda_j,\delta_j) = -\sin\varphi_j \cos\lambda_j \cos\delta_j - \cos\varphi_j \sin\lambda_j \cos 2\delta_j \quad (2)$$

Here φ_j denotes the difference between station azimuth and fault strike angle. λ_j and δ_j are rake and dip angles of the j-th point source, respectively. Source time function is approximated as a triangle function.

We model every subevent with 9 parameters, which are strike, dip, rake, scalar seismic moment, centroid time, half-duration, and centroid location in terms of latitude, longitude,

and depth. When we use very long period seismic data, the half duration of this triangle function (t_h) is often not well constrained. We can simply fix it using the empirical relationship $t_h=2.26*10^{-6}M_0^{1/3}$, Mo is the inverted seismic moment in Nm [*Ekstrom et al.*, 2005a].. Then if we use N point sources to approximate the source, the total number of unknowns is 9*N or 8*N.

We constrain these parameters by matching the synthetic waveforms with observations. We use a combination of L1 and L2 norms to measure the misfit between the data and synthetics in the wavelet domain [*Ji et al.*, 2002a; b]. Subsequently, taking into account the nonlinear constraint of pure double-couple inversion, we search for the model that is associated with the minimum of the objective function using the nonlinear global optimal "heat-bath" algorithm [*Sen and Stoffa*, 1991b].

While the "heat bath" algorithm could achieve a global optimal solution within the model space and the solution is independent of the initial model, it is computationally expensive because one inversion usually requires millions forward calculations. We have significantly sped up this process by optimizing the algorithms. In particularly, we adopt the Open Multi-Processing application program interface (OpenMP API) to take advantage of the multithread capability of modern CPUs. Using a PC workstation with a 2.66 Ghz i7 4-core CPU, the inversion of single point source can be accomplished within one minute. We are then able to quickly test a large set of possible models.

1.3 Example: 1999 Mw 7.1 Hector Mine earthquake

In this section, we test the feasibility of MDC inversion using the local strong motion observations. We shall show here that the well-known complex fault geometry of the 1999 Mw 7.1 Hector Mine earthquake could be resolved using MDC analysis.

The 1999 *M*w 7.1 Hector Mine, California, earthquake is a shallow strike-slip event that occurred in a remote, sparsely populated part of the southern California. This earthquake is known for its complex fault geometry (Fig. 1, Scientists of the USGS *et al.*, 2000). It ruptured two fault zones, the Lavic Lake fault to the north and the Bullion fault to the south. The former was mapped after this event. The overall length of surface faulting is approximately 41 km, but most of the surface slip is along the central part of Lavic Lake fault, where the surface rupture changes direction from 322^o in the north segment to 346^o in the south. Further in-depth analyses indicated that Lavic Lake fault separates into two faults to the north and forms a "Y-Shape" structure [*Ji et al.*, 2002a]. Bullion fault has a strike of 322^o. The total seismic moment is about $6.0\text{-}6.3 \times 10^{19}$ Nm and included at least three dominant sub-events from north to south, releasing 37%, 41%, and 22% of the total moment, respectively.

The Hector Mine earthquake occurred in an era before the high rate GPS data became available. This study is then entirely based on the broadband strong motion records archived by the data center of the California Integrated seismic network (CISN). We select records of twenty stations with epicentral distances from 50 km to 150 km. The waveforms of close-fault records are sensitive to the small-scale spatiotemporal variations of the fault rupture and cannot be properly modeled using a few point sources. The latency time of more distant stations may be too big to be used for near real-time analysis. In total we have used the 3-component records at 20 stations (Figure 1.1). We have first band-pass filtered all the data from 10 s to 90 s, and then integrated them to velocity records. We shall point out that the limitation of the longest period is mainly used to guarantee a stable integration of the strong

motion records and could be longer if we had used high rate GPS data instead. The shortest period is affected by the quality of the velocity structure.

We approximate the complex rupture process of the 1999 Hector Mine earthquake as *N* double-couples. For each of them, we simultaneously invert for the values of its centroid location (latitude, longitude, and depth), focal mechanism (strike, dip, rake), scalar moment, centroid time and half duration, for a total of 9 free parameters (Figure 1.1). The total number of unknowns is then *9*N*. For a initial global inversion, we let scalar moment change from $5*10^{18}$Nm to $5.5*10^{19}$Nm; rake varies from 90° to 270°; dip changes from 0° to 90° and strike changes from 0° to 360°; centroid time changes from 0 to 30s; half duration changes from 1 to 11s; The latitude changes from 34.35° to 34.75°; the longitude changes from -116.5° to -116.1°, and the depth varies between 2 and 20km.

The Hector Mine earthquake occurred in Mojave Desert. Previous studies suggest that the earth response in this region could be properly modeled using 1D Mojave model [*Jones and Helmberger*, 1998]. Using the FK code [*Zhu and Rivera*, 2002] we have constructed a Green's function lookup table. In this table, the hypocenter depth changes from 2 km to 20 km with spatial interval of 0.5 km; the horizontal spatial interval is 0.2 km. Green's function of any source-station used in equation 1 then can be interpolated from this lookup table.

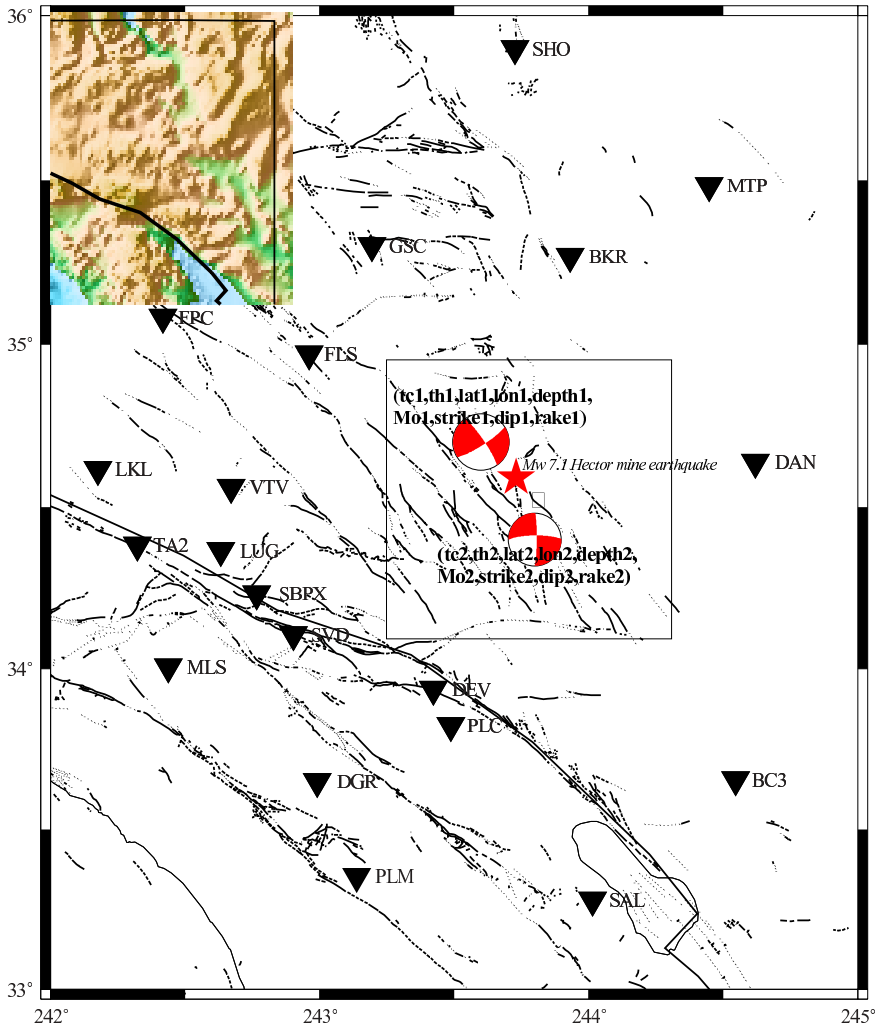

Figure 1.1: Distribution of 20 strong-motion stations (black inverted triangles). The star represents the epicenter of Hector Mine earthquake and rectangular box denotes the source region.

We gradually increase the number of double-couples from one to four, and find that the variance reduction of waveform fits, which is defined as $100\%*(1-\Sigma(o-s)^2/\Sigma o^2)$(where o and s represent observations and synthetics, respectively), stably increases from 40% to 80% . The amplitude ratio at Figure 1.3 has also been significantly improved by using more

double-couples. Figure 1.3 compares the observations (black lines) with synthetic seismograms predicted using the model with only one point sources (blue dashed lines) as well as these predicted using the model with four point sources (red lines). It is obvious that the model with single point source cannot explain the observations, while the model with four point sources produce a nearly perfect fit for the data, especially for the transverse component. It is striking that the Y-shape geometry has been clearly derived from our MDC modeling This analysis suggests that it is possible to derive the source complexity of large earthquakes in southern California from near-field seismic or high-rate GPS observations even without prior geological information, though the precision of results is affected by the station coverage, signal-noise ratio, and appropriate frequency bandwidth, etc.

For typical magnitude 7-8 earthquakes, the rupture duration is generally less than 1 minute. It will take another minutes for Rayleigh waves reaching the station 150 km away. Hence, when such an earthquake occurs, the waveforms used in this study could be available less than 2 minutes with all used stations satisfied our criterion record enough signals for such a study.

In short, we have demonstrated that the complex fault geometry of the 1999 Hector Mine earthquake could be resolved using local strong motion observations. However, we should point out that the multiple point source approximation is appropriate here because the source-station distances are larger than the dominant wavelength of seismic waves. The success of this test is to a large degree due to the good velocity structure in that the earthquake occurred within Mojave desert where 1D Jone & Helmberger (JH) model has been proven to be a good approximation.

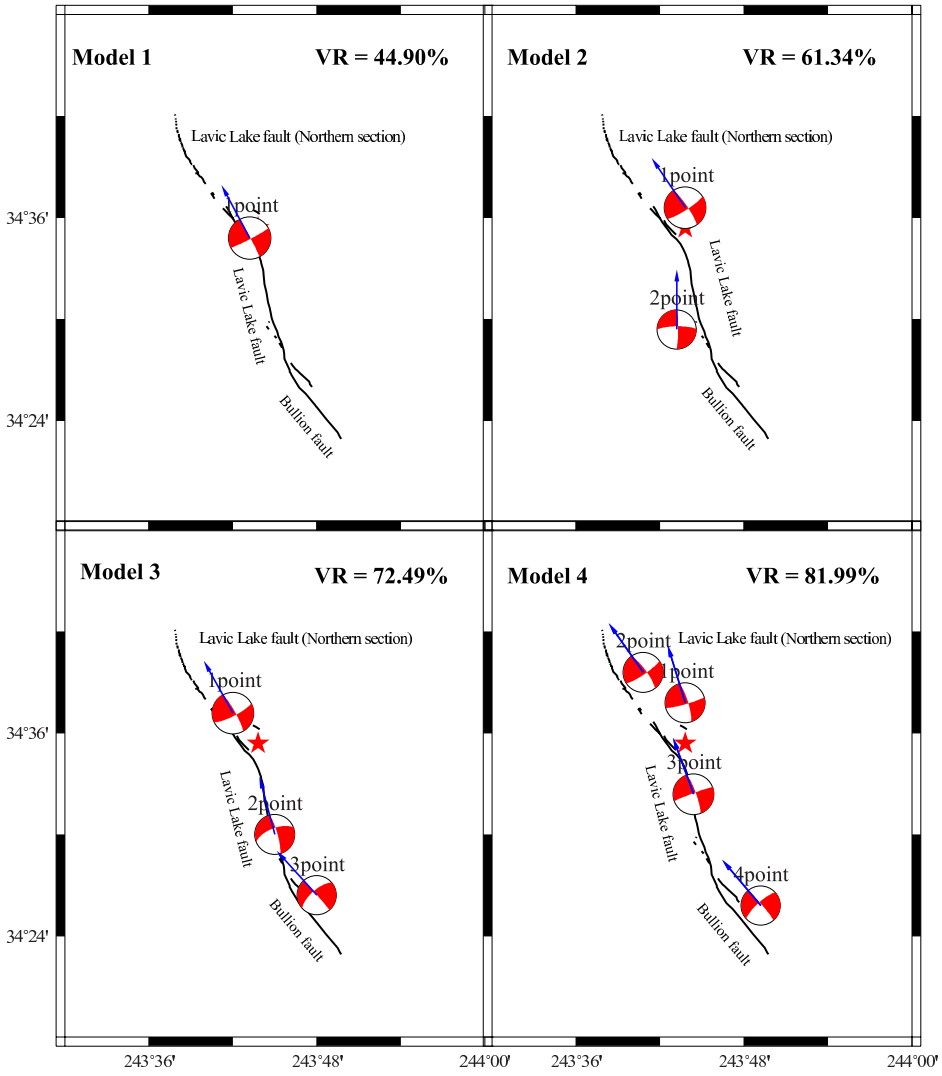

Figure 1.2: Summary of MDC models using different numbers of point sources. Model 1, 2, 3, 4 represents the MDC model using 1, 2, 3, 4 point sources, respectively. The variance reduction is shown on top right. Notice that each MDC model nicely coincides with the nearby complex fault geometry, and Model 4 exactly resolves the essential Y-shape structure of this earthquake.

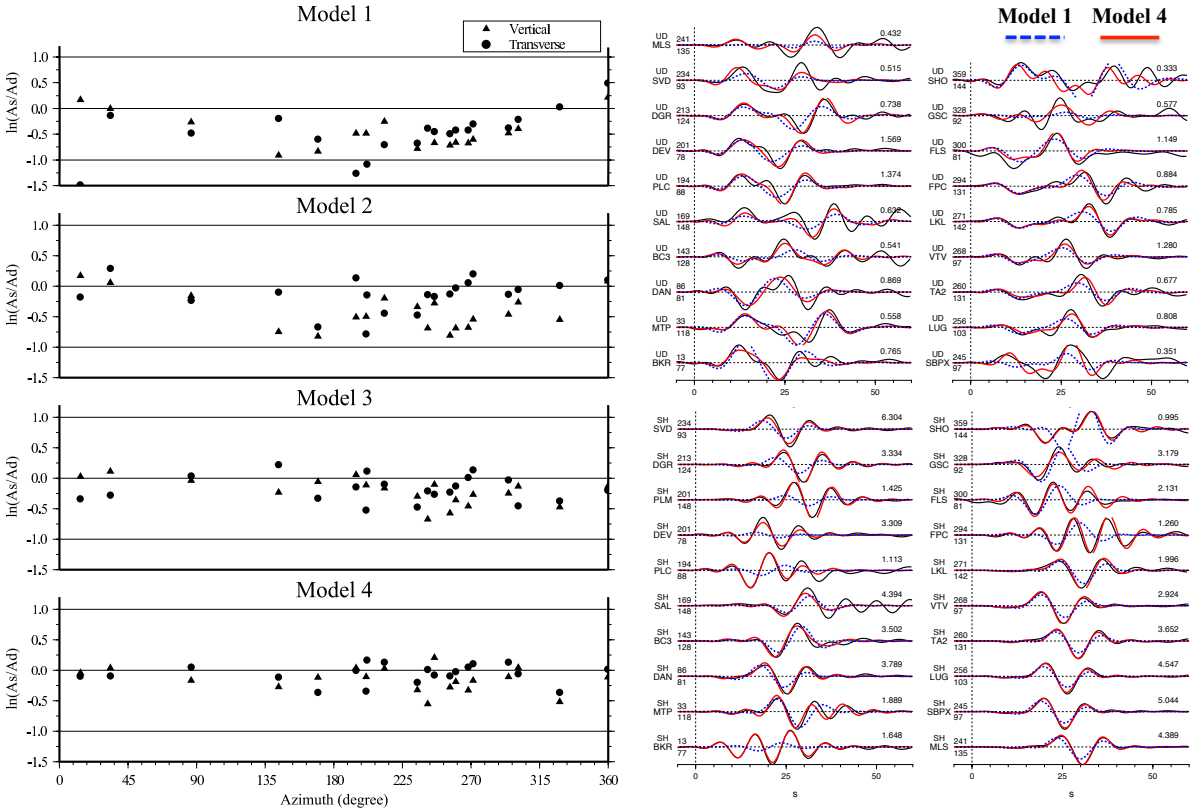

Figure 1.3: The amplitude ratio (left) is the ratio of amplitude between synthetics and data in log scale. Amplitude ratio equal to zero means they perfectly match. Vertical and transverse components are denoted by triangle and circle, respectively. Waveform fits of Model 1 (blue dotted line) and Model 4 (red line) between synthetics and data (black line) are given at right. The number at the end of each trace is the peak amplitude of the observation. The number above the beginning of each trace is the source azimuth and below is the epicentral distance.

1.4 Finite fault inversion

According to the representation theory, the response of an earthquake can be represented as the convolution of the slip rate function and Green's function integrated over the fault

area of the rupture. Numerically, we can discretize the fault into small subfaults. And for each subfault, we form its Green's function as the summation of many point sources. The displacement $u(t,\vec{x})$ at site $\vec{x}$ could be approximated as the summation of the contributions of a regular grid of subfaults [e.g., *Hartzell and Heaton*, 1983; *Ji et al.*, 2002b; *Olson and Apsel*, 1982]:

$$u(t,\vec{x}) = \sum_{j=1}^{n}\sum_{k=1}^{n} D_{jk}[\cos(\lambda_{jk})Y_{jk}^{1}(V_{jk},t) + \sin(\lambda_{jk})Y_{jk}^{2}(V_{jk},t)]\dot{s}_{jk}(t) \tag{3}$$

Here, j is the j-th subfault along strike, and k is the k-th subfault down dip. D_{jk}, λ_{jk}, and $\dot{s}_{jk}(t)$ are the dislocation amplitude, rake angle, and slip rate function, respectively. V_{jk} is the average rupture velocity between the hypocenter and subfault jk. The terms $Y_{jk}^{1}(V_{jk},t)$ and $Y_{jk}^{2}(V_{jk},t)$ are the subfault Green's functions for a unit slip in the strike direction and down-dip direction, respectively. Each function is obtained by summing the responses of point sources uniformly distributed over the subfault, where the number of point sources depends on the size of subfaults and the highest frequency studied [*Ji et al.*, 2002b].

For each subfault, we invert for the slip amplitude, rake angle, rupture time, and shape of an analytic slip rate function. The source time function ($\dot{s}(t)$) is approximated by a set of simple analytic functions defined as

$$\dot{s}(t) = \begin{cases} \dfrac{1}{t_s + t_e}[1 - \cos(\pi t / t_s)] & (0 < t \le t_s) \\ \dfrac{1}{t_s + t_e}[1 + \cos[\pi (t - t_s) / t_e]] & (t_s < t < t_s + t_e) \end{cases} \tag{4}$$

Here, t_s and t_e are the starting-phase and ending-phase times of an analytic normalized slip rate function $\dot{s}(t)$ [*Ji et al.*, 2003b].

Finite fault models represent the space-time distribution of slip on a parameterized fault plane. The slip history can be reflected by the differential times and amplitudes of seismic waves arriving at stations distributed around the source. Both seismic waveforms and static displacements can be used to constrain the source model. In our approach, the waveform inversion is carried out in the wavelet domain and wavelet coefficients are compared using both L1 and L2 norms. During inversions, a simulated annealing method [*Sen and Stoffa*, 1991b] is adopted to search for preferred kinematic parameters that can minimize our objective function.

1.5 Static and dynamic stress perturbation

It is well known that the occurrence of an earthquake could affect the seismicity rate locally and sometimes even globally. One way to explain this effect is the theory of Coulomb failure criterion [Lin and Stein, 2004]. Based on the finite fault model of the specified master fault plane, the Coulomb failure function (CFF) of a point on the target fault plane could be calculated to evaluate the effects of regional static stress field or dynamic triggering. The time-dependent Coulomb failure function at a particular point x in space outside the master fault can be defined as:

$$\Delta\mathrm{CFF}(\mathrm{x},\mathrm{t}) = \Delta\tau(\mathrm{x},\mathrm{t}) + \mu' \cdot \Delta\sigma(\mathrm{x},\mathrm{t}) \quad (5)$$

Here $\Delta\tau$ is the shear stress, μ' is the effective friction coefficient with a generic value of 0.4, and $\Delta\sigma$ is the normal stress change. While $t \rightarrow \infty$ or until all the waves have passed the point, the above equation represents the static stress change. Positive value of the ΔCFF is ordinarily interpreted to stimulate failure both for the case of static and dynamic stress change. Negative static stress change is supposed to delay or prohibit the failure on the target fault while negative dynamic stress perturbations may generate equivocal results. Dynamic interaction between different fault systems and the transient stress perturbation associate with passing seismic waves can hasten failure of seismic events. However, it is extremely difficult to deduce if large tectonic seismic events (Mw >7) have been triggered.

In this thesis, we attempt to deduce such induced seismic activity and demonstrate their spatial-temporal correlation with the rupture of a nearby earthquake by studying their dynamic stress interaction. In Chapter 3 and 4, we investigate two earthquake doublets, and in Chapter 5 we study the impending mud volcano eruption following the 2013 Pakistan earthquake. During these studies, we investigate the static and dynamic stress perturbations caused by mainshock or first subevent of the doublets. We initially assume a half-space earth model and adopt Coulomb 3.3 software package [*Lin and Stein*, 2004] to calculate static stress as a reference. To study the dynamic stress evolution, we computed the synthetic seismograms at the surrounding points of the target location using the FK discrete wavenumber code [*Zhu and Rivera*, 2002] based on our inverted slip model. In this case, 1-D layered velocity structure can be used instead of half space model. We compute the displacement field at a typical sample rate of 4 Hz and then calculate strain change in the vicinity of target region. By calculating the spatial derivation of synthetic displacement field, we can estimate both the static and dynamic strain field, and subsequently estimate the

time-dependent stress field of 6 components. Finally, we can obtain the stress perturbation in any orientation by projecting the 6 components onto a preferred fault plane. All of these events share a similar feature: the static stress perturbation caused by nearby earthquakes has negligible or even negative effect on triggering the second event. Their transient stress perturbation would be of more interest.

Note that such stress calculation strongly relies on the finite source model of mainshock. Therefore, an accurate source model derived from effective MDC analysis can play a very important role in quick determination of regional stress perturbation, and therefore is significant to real-time earthquake hazard analysis.

Chapter 2:

Multiple double-couple analysis of Mw>8 shallow earthquakes between 1990 and 2011 using long-period seismic waveforms

Abstract

The rupture complexity of 18 Mw >=8 shallow earthquakes from 1990 to 2011 are systematically studied using multiple double-couple (MDC) analysis. Each earthquake is approximated as a summation of multiple double-couples. The focal mechanisms, moment, locations, and centroid time of each double-couple are simultaneously inverted by matching the long period (2-6 mHz) seismic waveforms recorded by global seismic stations. The maximum number of double-couples is decided when further increasing the number of point sources lead to statistically negligible improvement in waveform fits. Uncertainty of inverted parameters is explored by searching the ensemble of models with acceptable fit to the data. For five of these earthquakes, to approximate their sources as more than one double-couples leads to significant improvement in fitting the observations. Three of these five earthquakes are megathrust events. We also notice that the strike changes resolved from MDC analysis among their subevents are consistent with the changes of the geometry of nearby trench axes.

2.1 Introduction

In this chapter, we apply the multiple double-couple (MDC) analysis to 18 Mw>8 earthquakes occurring from 1990 to 2011. Their centroid times, centroid locations and the best double-couple inferred from their GCMT solutions, along with their CLVD components are summarized in Table 2.1. Their focal mechanisms are plotted in Figure 2.1 on the global topography map (ETOPO2). Note that the centroid depths of these earthquakes are all shallower than 100 km, and most of them are located along the plate boundaries. Fifteen of them are mega-thrust events on the subducted interfaces; two are strike-slip events, and two are normal-fault events.

The broadband teleseismic waveforms recorded by Global Seismographic Network (GSN) and stored at the IRIS data center were downloaded for this study. We model the earth response using the non-rotation anisotropic Preliminary Reference earth model [*Dziewonski and Anderson*, 1981] and ignore the 3D heterogeneities of earth structure. We band-pass filtered the data from 2 mHz to 6 mHz using a FIR filter and re-sampled the waveforms using a sample interval of 4 sec, after removing instrument responses, Generally, the propagation of long-period surface waves with frequency larger than 0.01 Hz is highly sensitive to the lateral heterogeneities of the 3D earth structure. As the spatial and temporal resolution are limited by the shortest wavelength and period used, it will be an important future effort to increase the frequency band by using the 3D Green's functions. We generally use a record length of 1 hour and carefully select stations with a distance from 30° to 110° for our inversion. Benefiting from the dense global networks, we are able to obtain more than 50 long-period waveforms for every earthquake, which generally guarantees excellent azimuth coverage of the source region. For long-period seismic waves, we had pre-

calculated these Green's functions using a normal mode superposition algorithm to enhance the speed of the MDC analysis. The horizontal grid interval of this lookup table is 0.1°. The depth in this table changes from 4 km to 701.5 km with a constant interval of 2.5 km.

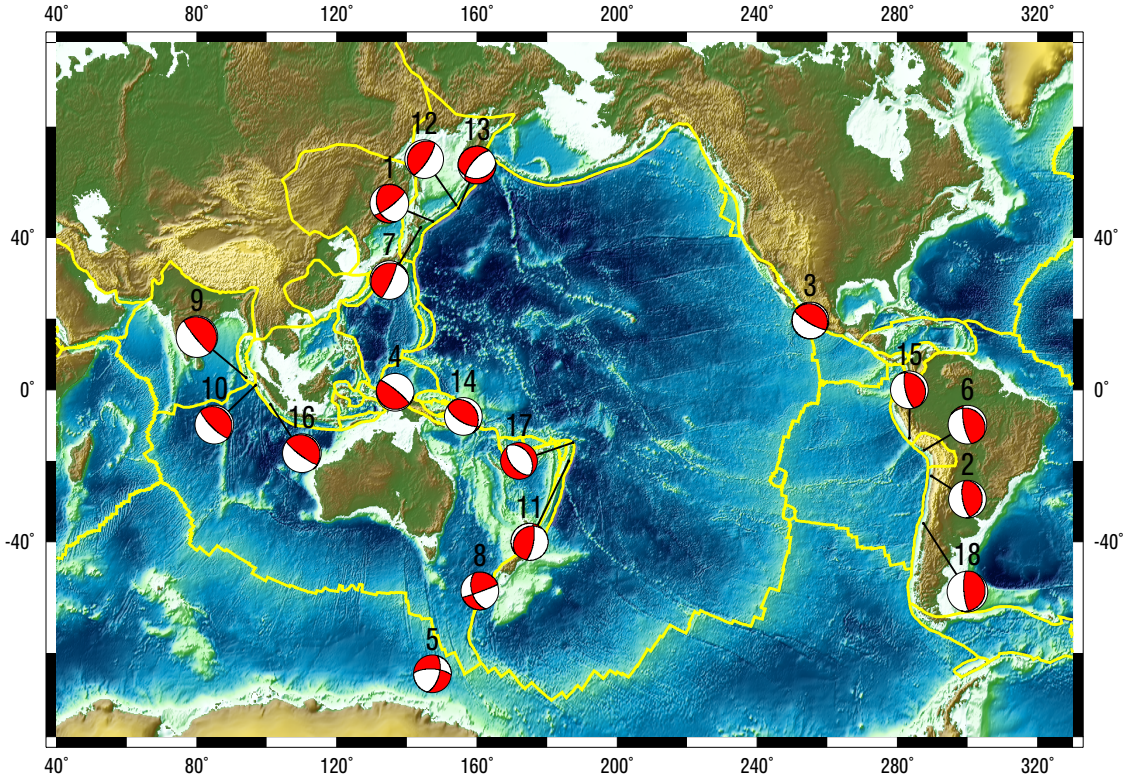

Figure 2.1: Location and focal mechanism of 18 earthquakes from our single point source models in Table 2. There are 14 thrust events, 2 strike slip events and 2 normal fault events. Solid line represents the plate boundary. Note that our focal mechanisms are consistent with the corresponding plate boundaries. We use more than 50 long-period waveforms in the inversion for each earthquake, which usually provide good azimuth coverage of the source region.

2.2 Single double-couple Analysis

Table 1: Comparison of results of double-couple inversion solutions and the corresponding best double-couples derived from GCMT solutions of 18 Mw >8.0 earthquakes from1994 to 2011. The corresponding comparison with GCMT is in bold.

No	Date (yy/mm/dd)	Centroid time (s)	Lat (°)	Long (°)	Mo ()	Strike (°)	Dip (°)	Rake (°)	Depth (km)	CLVD
1	1994/10/04	30	43.40	147.50	3.08e+28	**160**/53	**35**/78	**21**/123	58	
		30.2	43.60	147.63	3.00e+28	**158**/50	**41**/74	**24**/128	68.2	0.039
2	1995/07/30	36	-24.20	-70.30	1.55e+28	**9**/166	**21**/71	**112**/82	22	
		33.4	-24.17	-70.74	1.21e+28	**354**/177	**22**/68	**87**/91	28.7	0.037
3	1995/10/09	41	19.50	-104.80	0.85e+28	**309**/121	**13**/77	**98**/88	12	
		33.1	19.34	-104.80	1.15e+28	**302**/120	**9**/81	**92**/90	15.0	0.021
4	1996/02/17	35	-0.70	136.60	2.18e+28	**102**/309	**10**/81	**63**/95	10	
		33.1	-0.67	136.62	2.41e+28	**103**/305	**11**/80	**69**/94	15.0	0.012
5	1998/03/25	44	-62.90	147.30	1.69e+28	**273**/16	**68**/61	**-31**/205	33	
		37.4	-62.99	148.64	1.70e+28	189/**281**	73/**84**	174/**17**	28.8	0.411
6	2001/06/23	73	-17.20	-72.40	4.18e+28	**303**/168	**20**/76	**47**/104	29	
		69.2	-17.28	-72.71	4.67e+28	**310**/159	**18**/74	**63**/98	29.6	0.060
7	2003/09/25	32	42.20	144.00	2.82e+28	**252**/23	**12**/82	**138**/81	24	
		31.8	42.21	143.84	3.05e+28	**250**/28	**11**/82	**132**/83	28.2	0.048
8	2004/12/23	36	-49.90	160.90	1.87e+28	**70**/162	**87**/54	**144**/4	28	
		26.5	-49.91	161.25	1.63e+28	**69**/163	**74**/78	**167**/16	27.5	0.060
9	2004/12/26	135	3.40	94.20	2.92e+29	**317**/141	**6**/84	**86**/90	16	

		139	3.09	94.26	3.95e+29	**329**/129	**8**/83	**110**/87	28.6	0.030
10	2005/03/28	60	1.30	96.90	5.60e+28	**324**/134	**14**/76	**100**/88	40	
		55	1.67	97.07	1.05e+29	**333**/125	**8**/83	**118**/86	25.8	0.000
11	2006/05/03	30	-20.10	-173.70	1.12e+28	**228**/10	**22**/72	**126**/77	66	
		23.4	-20.39	-173.47	1.12e+28	**226**/11	**22**/72	**123**/78	67.8	0.018
12	2006/11/15	52	46.70	154.10	3.15e+28	**213**/33	**14**/76	**90**/90	14	
		50.2	46.71	154.33	3.51e+28	**215**/33	**15**/75	**92**/89	13.5	0.011
13	2007/01/13	27	46.10	154.70	1.99e+28	**83**/220	**30**/67	**-51**/250	8	
		26.9	46.17	154.80	1.78e+28	**266**/43	**39**/59	**-54**/245	12.0	0.055
14	2007/04/01	48	-7.70	156.20	1.68e+28	**331**/121	**28**/65	**117**/76	14	
		42.5	-7.79	156.34	1.57e+28	**333**/117	**37**/59	**121**/69	14.1	0.068
15	2007/08/15	67	-13.80	-76.50	1.42e+28	**327**/167	**20**/71	**71**/97	32	
		60.0	-13.73	-77.04	1.12e+28	**321**/171	**28**/65	**63**/104	33.8	0.044
16	2007/09/12	53	-4.20	101.00	5.20e+28	**324**/127	**10**/80	**107**/87	30	
		48.8	-3.78	100.99	6.71e+28	**328**/123	**9**/82	**114**/86	24.4	0.003
17	2009/09/29	32	-15.10	-172.50	1.19e+28	**141**/326	**53**/37	**-93**/274	8	
		15.8	-15.13	-171.97	1.66e+28	**119**/346	**38**/62	**-131**/-63	12.0	0.165
18	2010/02/27	67	-35.80	-72.50	1.99e+29	**18**/175	**15**/76	**112**/84	25	
		58.9	-35.98	-73.15	1.86e+29	**19**/172	**18**/74	**116**/82	23.2	0.047

We start our study by approximating each event as a single double-couple and subsequently constraining its focal mechanism, seismic moment, centroid location and time using the data mentioned above. We have initially allowed large search regions for each

parameter during preliminary studies and then carried out a more accurate search of each parameter with constrained ranges determined from the preliminary inversion. For instance, at the beginning, we set the range of centroid time from 0 s to 100 s with a step of 4 s for most of earthquakes, and we let the centroid locations (both latitude and longitude) change by as much as 2.5° from their hypocenters. The depth commonly ranges from 10 km to 50 km with an increase of 4 km except for the event 1 and event 11, which were allowed to change from 10 km to 80 km. The range of scalar seismic moment Mo is typically chosen with respect to GCMT results, e.g. from 1/5 to 5 of seismic moment from GCMT. Whereas we use a global range for strike angle (from 0° to 360° increased by 3°), dip angle (from 0° to 90° increased by 2°) and rake angle (from 0° to 360° increased by 4°). Subsequently, using the parameters determined with the coarse estimates, a follow-up inversion with a detailed search of each variable is implemented to obtain our ultimate models.

The inverted results are summarized in Table 1, accompanied by the GCMT best double-couple solutions. The simulated annealing searches for the global optimal source model by looking for the global minimum value of the given objective function within the model space defined above. Let's assume that this global minimum value is ε. It is often safe to argue if the objective function value of one model is less than 5% larger than ε, i.e., $<1.05\ \varepsilon$, this model is still feasible in terms of fitting the data. During the simulated annealing inversions, we have stored all of these models and subsequently approximate the marginal probability distribution of each parameter using a histogram constructed from them. Figure 2.3 shows the histograms associated with event No. 2, the 1995 Mw 8.0 Chile earthquake. As summarized in Table 1, for this earthquake our preferred fault plane, which matches the data best, has a strike of 9°, a dip of 21° and a rake of 112°. The fault parameters of feasible

models actually span notable ranges. For example, the strike of 95% of feasible solutions captured during this inversion changes from 8° to 12°, though their mean is 10°, close to the preferred model. We point out that this approximation could only disclose the relative sensitivity of each parameter with respect to the observations. For example, the range of parameter value is smaller if we use a tolerance range less than 5%. It is a future effort to determine the tolerance range statistically by analyzing the data.

Using this ensemble of feasible models, we could also estimate the correlations among fault parameters. If defining the expected value of each parameter as the mean of all feasible models, we can calculate the correlation of two fault parameters *a*, *b* using the formula

$$Cor(a,b) = \frac{\sum_{i=1}^{N}(a^i - \bar{a})(b^i - \bar{b})}{\sqrt{\sum_{i=1}^{N}(a^i - \bar{a})^2}\sqrt{\sum_{i=1}^{N}(b^i - \bar{b})^2}} \quad (6)$$

Here, i=1, 2, .. N is the index of the feasible models. a^i and b^i are parameter values of the i-th model. $\bar{a}$ and $\bar{b}$ represent their means of whole ensemble. Figure 2.4 shows the results of event No. 2. Clearly, correlations between many parameters are significant. For example, the large positive correlations between half-duration (th) and seismic moment, strike and dip; the large negative correlations between dip angle and seismic moment, dip angle and half-duration. Some of these significant correlations are expected. As mentioned above, the half-duration in this study is calculated using its empirical relationship with seismic moment. The 1995 Mw 8.0 Chile earthquake is a shallow thrust earthquake on the subducted plate interface. The amplitudes of long-period Rayleigh waves excited by the shallow thrust earthquakes is directly proportional to the Mo*sin(2δ), where δ denotes dip angle and Mo is scalar seismic moment [*Kanamori and Given*, 1981]. This is presumably

caused by the fact that at the shallow depth, the response of 90° dip slip fault is much smaller than the responses of 45° dip slip fault and 90° strike slip fault. This leads to the well-known trade-off between the scalar moment and fault dip. As the half-duration is related with the seismic moment, it becomes correlative with fault dip as well. Another issue associated with the low angle thrust earthquake is the trade-off between fault strike and rake

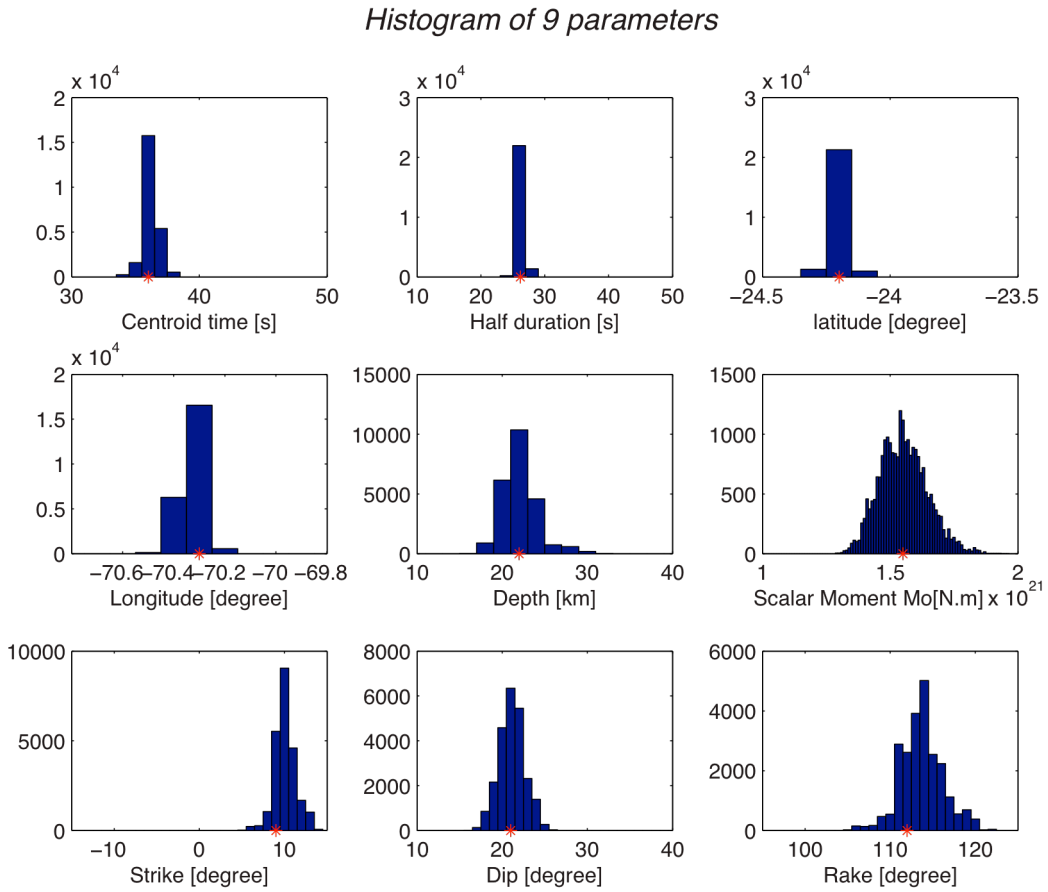

Figure 2.3. Histograms showing the approximate marginal posterior probability distribution of inverted nine source parameters for 1995 Chile earthquake. x axis represents the value of different source parameters, y axis represents the frequency of various value within acceptable misfit. Red points denote the best value of each parameter for the minimum misfit.

angle. Let's assume that the seismic moment, dip angle and source location are fixed. Then the ground displacement only depends on fault strike (stk) and fault rake (λ). The differentials of geometric coefficients around λ=90^o are,

For m=1 (90^o strike slip)

$$dA_1 = -\sin(\delta)\sin(2\varphi)\,\mathrm{d}\lambda - \sin(2\delta)\sin(2\varphi)\,d\varphi$$

$$dA_4 = -\sin(\delta)\cos(2\varphi)\,d\lambda - \sin(2\delta)\cos(2\varphi)d\varphi$$

For m=2 (90^o dip slip)

$$dA_2 = -\cos(\delta)\cos(\varphi)\,d\lambda + \cos(2\delta)\cos(\varphi)\,d\varphi$$

$$dA_5 = \cos(\delta)\sin(\varphi)d\,\lambda + \cos(2\delta)\sin(\varphi)\,d\varphi$$

For m=3 (45^o dip slip)

$$dA_3 = 0$$

Here, $\varphi = Az - stk$. Thus $d\theta$ is equal to $-d(stk)$. Thus in the first order, the coefficient associated with 45^o dip slip (m=3) is insensitive to the small change of fault strike and fault rake. The coefficients associated with other two basic faults are sensitive to these changes. Note that for the coefficients associated with 90^o dip slip (m=2), $dA_2 = dA_5 \sim 0$, if $d\lambda = \cos(2\delta) / \cos(\delta)\, d(stk)$; for the coefficients associated with 90^o strike slip (m=1), $dA_1 = dA_4 \sim 0$, if $d\lambda = 2\cos(\delta)\, d(stk)$. When the response of 90^o dip slip (m=2) is significant in compared with the responses of 90^o strike slip (m=1), there is no trade-off between the strike and the rake. However, if the response of 90^o dip slip (m=2) is negligible, a trade-off between strike and rake exists. The error in fault strike results in the error in fault rake, i.e., $d\lambda \sim 2\cos(\delta)\, d(stk)$.

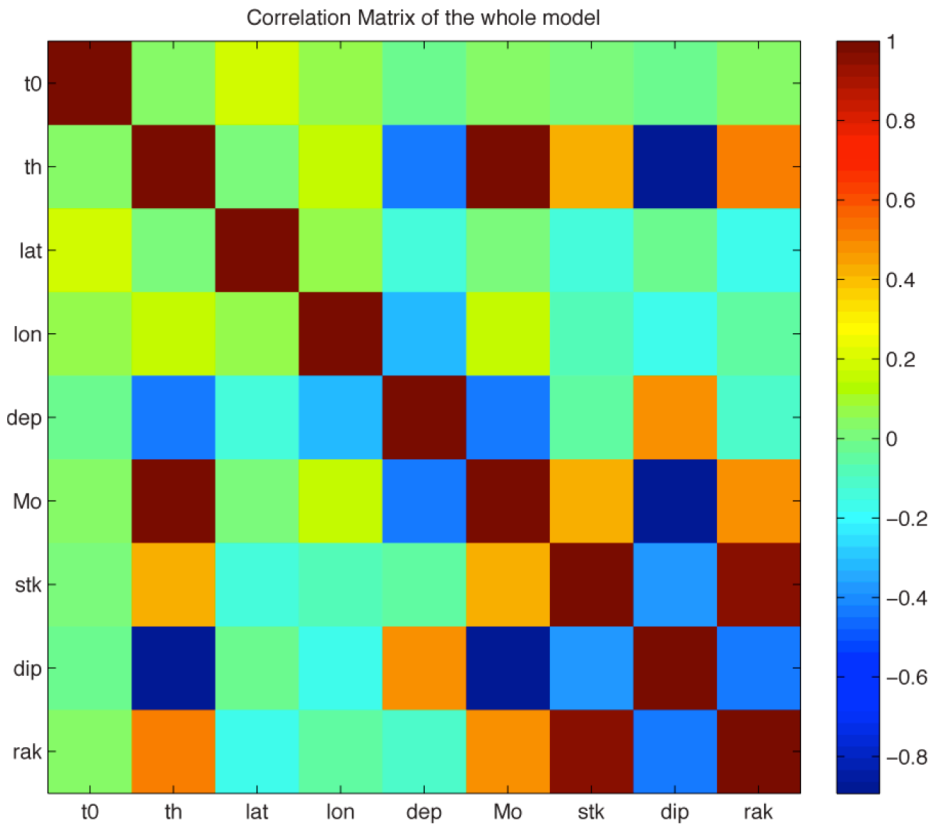

Figure 2.4. Correlation matrix of 1995 Chile earthquake computed from 240000 feasible models which are associated with objective functions less than 5% larger than the minimum objective function value found in this inversion. Note the strong positive correlations between strike angle (stk) and rake angle, as well as negative correlation between fault dip and seismic moment (M_0), Half duration is determined by Mo and therefore has similar pattern.

In Figure 2.5, we compare our solution with the GCMT best double-couples in terms of eight inverted fault parameters. Note that for each event, there are two GCMT best double-couple nodal planes. We have selected the one that is closer to our solutions for this comparison and highlight it in Table 1 using bold font. Within each subplot, the red dots are used to indicate one of 18 earthquakes. The horizontal axis shows its value in its single-

double-couple solution. The vertical axis denotes its value of GCMT best-double-couple solution. Thus if two solutions are equal, the cross will lie right on the diagonal line. It can be seen that most red stars fall near the diagonal lines in these subplots, while outliers with large discrepancies indeed exist.

The centroid locations of two solutions are very close (the first two subplot in Figure 2.5). The average offset between two results is 35 km, with a standard deviation of 20 km. In fact, for these 18 earthquakes, only 3 events are associated with offsets larger than 50 km. Their event numbers are 5, 17, and 18. As discussed later, all of them are associated with a complex rupture process for which we need use more than one source to model their long period observations. The centroid depths of two solutions agree with each other well. Our solutions on average are 1.4 km shallower than the GCMT centroid depths. The standard deviation is 6 km. We note that the two earthquakes with more than 12 km ($>2\sigma$) difference in centroid depth are Dec. 26, 2004 Sumatra earthquake (No. 9), March 5, 2005 Nias earthquake (No. 10). Again, both of them are associated with more complicate source mechanisms. Without considering these two outliers, the standard deviation is 4.3 km.

Our inverted centroid time typically shows a slightly higher value than GCMT solution. This difference has an average of 4.8 s with a 2σ standard deviation of 9 s and may be due to the different frequency band (167 s to 500 s) we use. It is possible that the complex source and the long-period slip features also can give rise to the generally higher value of our results compared to the GCMT solution.

The solutions of event No. 13, 2007 Kuril island outer-rise earthquake (underlined in Table 1) has a nearly 180^{o} discrepancy in strike and will be addressed separately. For the

rest of the earthquakes, the average differences in terms of strike, dip and rake angles are 0.5°, -2.8°, -3.2°, respectively. The standard deviations of these three parameters are 8.5°, 8.6° and 18.4° respectively. The outliers can be explained with various trade-offs discussed above. For example, there are notable difference between the GCMT and our solutions of event No. 2, 1995 Mw 8.0 Chile earthquake. In GCMT solution it has a strike of 354°, a dip of 22° and a rake of 87°, while our solution shows a strike of 9°, a dip of 21° and a rake of 112°. Hence, two solutions have discrepancies of 16^o and 25^o in strike and rake, respectively. *Ruegg et al*. [1996] studied this earthquake using teleseismic and local geodetic data together. The causative fault plane they defined has a strike of 8°, a dip of 19° and a rake of 110°, closer to our solution. It is of interest to note that the differences between our and GCMT solutions in strike and rake are consistent with the trade-off discussed above, i.e., $2*\cos(21^o)*16^o=30^o \sim 25^o$.

The largest discrepancy in strike between two solutions is associated with event No. 13, the 2007 Mw 8.1 Kuril island earthquake. This is an outer-rise normal fault earthquake. The focal mechanism we obtain is (strike=83^o; dip= 30^o; rake=-51^o). The closer GCMT nodal plane is (strike=266^o; dip= 39^o; rake=-54^o). Hence, the two solutions have similar fault dip and rake angles, but are nearly opposite in the dip direction. *Lay et al.,* [2009] studied this earthquake using a W-phase algorithm, they found a fault plane solution (strike=92^o; dip= 43^o; rake=-43^o). This solution is close to our result. Without local observations, it is difficult to judge which solution is more plausible. It illustrates that the source mechanism of this large rare outer rise normal fault is not well determined. We could also intuitively explain this uncertainty using the fact that at the shallow depth, response of the 90^o dip slip fault is significantly smaller than the responses of the other two fault types. Looking at the

geometric coefficients formula given in equation 2, the response of 45^o dip slip is independent of θ, the difference between station azimuth and strike. The response of 90^o dip slip is related with sine or cosine of θ. The response of 90^o strike slip is related with sine or cosine of 2θ. Thus, if the contribution of the 90^o dip slip can be ignored, there is an 180^o ambiguity embedded in the fault strike constrained by seismic data.

In the end, it is noteworthy that even using single double-couple approximation, the average variance reduction between synthetics and observations of 18 earthquakes is as high as 80.55% with a standard deviation of 7.6%. We notice that the 2004 Mw 9.1 Sumatra earthquake and 2009 Mw 8.1 Samoa earthquake are associated with the lowest variance reductions of 61.4% and 61.8%, which indicate their source complexity, which will be further discussed later.

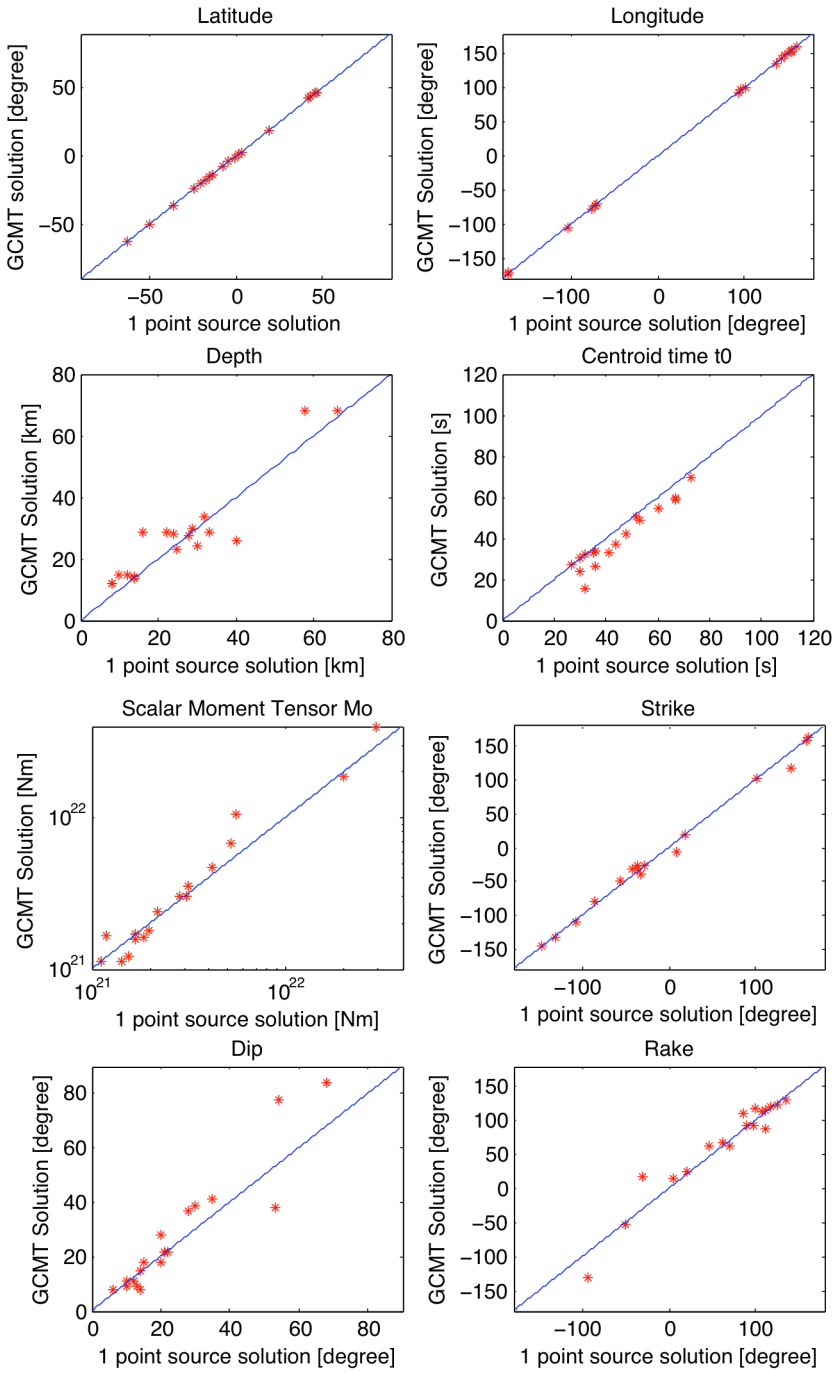

Figure 2.5: Comparison of source parameters of 18 earthquakes (red stars). The horizontal axis denotes the solutions of single double-couple analysis, while vertical axis shows the solutions inferred from the corresponding Global CMT solutions.

2.3 Multiple double-couple inversion (MDC)

We subsequently use two and more double-couples to approximate the rupture processes of these events and simultaneously invert for their locations, focal mechanisms, seismic moments, and centroid times, which we have named as the multiple double-couples inversion (MDC) in Chapter 1. The same initial search ranges of each parameter are used for different point sources in multiple point sources inversion. With respect to the preliminary inversion with a wide search range, a further optimization for a multiple double-couple model is sequentially performed, with appropriate and denser search ranges for corresponding parameters of various point sources. The ensemble of all possible models within an acceptable fit, i.e. misfit value is no greater than 5% of the minimum value we found, are kept and used to describe the approximate posterior probability distribution.

It is no doubt that using more double-couples (or more free parameters) will improve the waveform match. Of equal importance is to determine a suitable number of double-couples for each earthquake. The most straightforward way is to compare of waveform matches associated with the models from different numbers of double-couples. Typically the net improvement in waveform fits by adding another double-couple gradually becomes less significant as the total number of double-couple subevents increases. To quantitatively determine the proper number of the point sources, we use the F-test as a statistical aid to determine whether the additional free parameters of a complex MDC model improve the inversion results more significantly than a random process with more parameters. The F is defined as the ratio of the variances associated with models that have different degrees of freedom for identical input data:

$$F_{ratio} = \frac{\sigma_{n1}^2}{\sigma_{n2}^2} \tag{7}$$

where n1 and n2 denote the number of double-couples. Suppose that during an inversion, we have used L seismic waveforms, the variance is then defined as:

$$\sigma^2 = \frac{1}{K-M}\sum_{i=1}^{L}\int (o_i(t) - s_i(t))^2 dt \tag{8}$$

Here, o_i and s_i denote the observation and synthetic seismogram at the i-th station. M is the degrees of freedom of the inverted model. If we use N double-couples, M is equal to 8xN. K represents the total number of independent observational points. Critical values of F for different confidence levels follow the F distribution; the critical values depend on the degrees of freedom, i.e., uncorrelated data used in inversion. Given that the calculated F value is greater than the critical value, we can argue that the better fit of waveform is supposed to be attributed to the significant improvement in signals rather than to the random fluctuations in the data.

The number of independent data points shall not be simply equal to the number of sampling points. In principle, we can represent the observed time series $\underline{o_i}$ at the i-th station as

$$o_i(t) = o_i^0(t) + n_i(t) \tag{9}$$

Here, we use $o_i^0(t)$ to denote the signals that can be modeled. $n_i(t)$ represents the error caused by ambient earth noise and heterogeneous earth structure. We simply assume the noise at different stations can be treated as uncorrelated white noise and use the fact that Fourier transform will not change the amount of information. The maximum amount of independent data can be represented as

$$K_i = 2 \cdot [f_{max} - f_{min}]/df \tag{10}$$

Here f_{max} and f_{min} define the bandwidth of filter; df is the sampling interval in frequency domain and is equal to *1/T*, *T* is the duration of signals used in the inversion. The constant 2 is used because we need two variables to represent one complex variable. Suppose we use a duration of 3600 s and filter the data from 2 mHz to 6 mHz, the maximum amount of the independent information embedded in this waveform is 28.8. In this analysis, we assume $K = \sum K_i$. For the earthquakes studied here, K varies from 1000 to 4000. The corresponding critical value of the 95% confidence level that coincides with this range is from 1.11 to 1.16. The F-test results of each earthquake are presented in Table 2 and only the confidence levels greater than 95% are shown. According to the results of F-test, we conclude that single double-couple models are sufficient to explain the long period observations of 13 large events. On the other hand, the observations of events 5, 9, 10, 17, and 18 require are better represented as events with multiple double-couples, these are predominantly discussed in this paper. The variance reductions of all the MDC models are list in Table S1. Take the 5 earthquakes with complex rupture process apart, all other 13 earthquakes can be adequately approximated as a single double-couple event with respect to our F-test prediction. The single double-couple model of these earthquakes with their station distribution as well as amplitude ratio are shown in supplementary materials from Figure S2.2 to Figure S2.14. We notice that the regional fault geometry of these 13 earthquakes is relatively simpler than that of 5 complicate earthquakes. For simplicity, we would mainly focus on discussing the 5 complicate earthquakes in the following part.

Table 2: F-test of our multiple point source analysis.

Events	F ratio & Confidence level				Best model
	1point to 2point	2point to 3point	3point to 4point	4point to 5point	
1	-	-	-	-	1 point source
2	-	-	-	-	1 point source
3	-	-	-	-	1 point source
4	-	-	-	-	1 point source
5	1.41 > 99%	-	-	-	2 point source
6	-	-	-	-	1 point source
7	-	-	-	-	1 point source
8	-	-	-	-	1 point source
9	1.52 > 99%	1.13 > 95%	1.25 > 99%	1.12 > 95%	5 point source
10	1.37 > 99%	-	-	-	2 point source
11	-	-	-	-	1 point source
12	-	-	-	-	1 point source
13	-	-	-	-	1 point source
14	-	-	-	-	1 point source
15	-	-	-	-	1 point source
16	-	-	-	-	1 point source
17	1.69 > 99%	1.15 > 95%	-	-	3 point source
18	1.16 > 99%	-	-	-	2 point source

2.3.1 The 1998 Antarctic earthquake

Event No. 5, the 1998 Mw 8.1 Antarctic earthquake, is temporally the first event in our catalog, which needs more than one double-couple to explain its long period observations. Figure 2.6 shows its GCMT focal mechanism on a bathymetry map. The double-couple focal mechanism suggests that this earthquake is a strike-slip event with a substantial large CLVD component (0.411). It is noteworthy that when this earthquake occurred, it was the largest intra-plate submarine strike-slip earthquake ever recorded.

We have used 64 long period seismic waveforms in vertical and transverse components. The station distribution is shown in Figure 2.6. Our single double-couple model explains these long period waveforms well with a variance reduction of 73.9%, 6% worse than the global average of the waveform fits to the long period waves excited by the Mw>8 earthquakes. However, when we use two double-couples to approximate this source, the waveform fits have improved significantly. The new variance reduction becomes 84.0%. The F-ratio is 1.41. The critical value of 99% confidence is 1.17. Further using three double-couples, the variance reduction further improves to 86%, the corresponding F-ratio is 1.09, smaller than critical value for 95% confidence of 1.11. Thus the two double-couple model is selected as the preferred solution. The GCMT solution and our best multiple double-couples model from the F-test as well as the amplitude ratio, which is defined as the natural logarithm of the ratio from amplitude of synthetics to observations, are shown in Figure 2.3. As the long-period seismic waveforms are dominated by Rayleigh and Love fundamental waves, we also compare the peak amplitudes of observations (A_d) and synthetic seismograms (A_s). As shown in Figure 2.6, the average value of $\ln(A_s/A_d)$ is -0.11 and the 2σ standard deviation is 0.41, suggesting that 95% of peak amplitude ratios (A_s/A_d) falls between 0.60 to 1.36.

The locations and focal mechanisms of our two double-couple solution are also shown in Figure 2.6. These two subevents distribute longitudinally, which suggests the east-striking nodal planes of these two subevents are likely the causative fault planes. Two subevents have nearly same strike-slip focal mechanisms. The causative faults dip 71° to the south. The first subevent had a seismic moment of 1.45×10^{21} Nm (Mw 8.1). Its centroid (62.95°S, 147.90°E) locates at about 83 km west of the USGS hypocenter (62.88°S, 149.53°E). Its

rupture has a centroid time of 32 s. The centroid of the second double-couple (63^{o}S, 144.80^{o}E) locates about 253 km west of the epicenter. Its rupture has a centroid time of 88 s and a seismic moment of $0.77x10^{21}$ Nm (Mw 7.9). The total seismic moment is then $2.2x10^{21}$ Nm (Mw 8.2). The spatial distribution of these two subevents and the USGS epicenter implicates that the rupture propagates unilaterally 250 km to the west with an average rupture velocity larger than 2.9 km/s, which agrees well with the locations of relocated aftershocks.

For the first double-couple, the centroid time and centroid location are well resolved. For the 95% of all feasible models found during this inversion, the latitude and longitude of their inverted centroid locations change from -63.1^{o} to -62.9^{o} and from 147.6 ^{o} to 148.1^{o}, respectively. Or in another word, they change by only 22 km latitudinal and 25 km longitudinally. The centroid depth changes within a 4 km range from 15km to 19km. Their inverted centroid times fail between 30s and 35s. Their seismic moment changes from $1.3x10^{21}$Nm to $1.6x10^{21}$Nm. Their strike, dip and rake varies within 94°~95°, 65°~77° and 320~333°, respectively. The constraints on the latter two fault parameters are apparently worse than that on the strike. Our correlation analysis further reveals trade-offs among seismic moment, dip angle, rake angle. There are negative correlations between the rake angle and dip angle as well as rake angle and seismic moment. The correlation between the dip angle and seismic moment is, however, positive.

As the seismic moment of the second subevent is much smaller than the first one, it is not surprising that the constraints on the second double-couple are worse as it shows a relative more broaden ranges for the inverted parameters. The range of the centroid time becomes 8 s, changing from 84s to 92s. The latitude and longitude of their centroid locations

change from -63.2° to -62.9° and from 144.3° to 145.0°, corresponding to changes of only 33 km in latitude and 35 km in longitude. Their centroid depths vary from 26 km to 34 km, notably deeper than the first subevent. Their seismic moment changes from 6.5×10^{20}Nm to 9.5×10^{20}Nm. Their strike, dip and rake varies within 91°~93°, 65°~80° and 320~340°, respectively. Fault strike is again the best-constrained fault parameter.

Henry et al [2000] studied this earthquake using long period seismic data and teleseismic body waves separately. They also found that this earthquake has two subevents. The first subevent has a length of 140 km on a fault orienting N96°E, dip of 69° to the north. The inverted seismic moment is 1.2×10^{21} Nm. The second event extends from 210 km to 270 km east of the epicenter with a seismic moment of $0.3\text{-}0.6 \times 10^{21}$ Nm. The spatial distribution and focal mechanisms of our two double-couples are consistent with their result, though our cumulative seismic moments are larger. This is consistent with the result of *Hjörleifsdóttir et al.* [2009] using 3-D earth model. They found that they have to use a larger seismic moment (2.2×10^{21} Nm) to match the long period (0.025 mHz) seismic data.

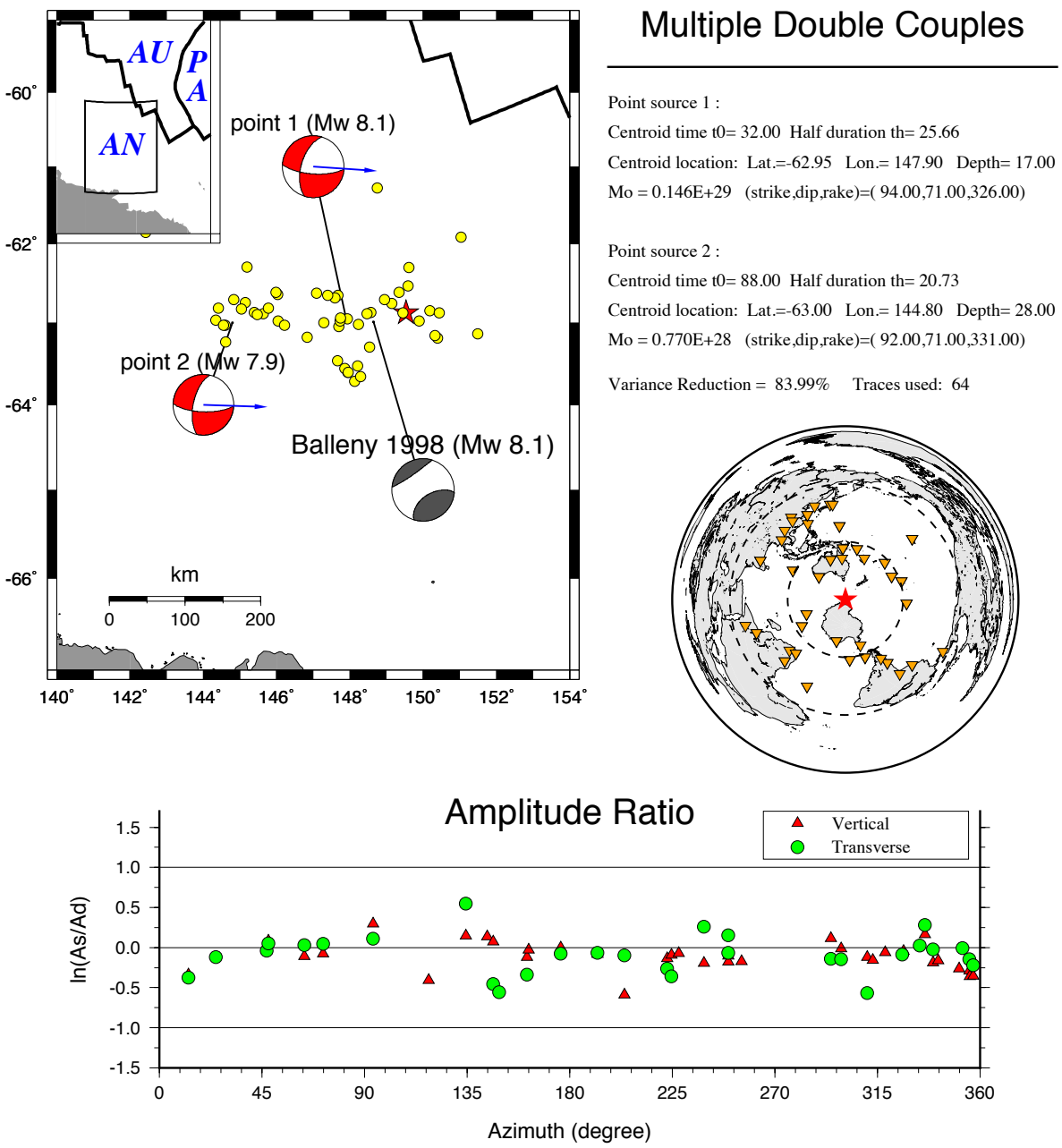

Figure 2.6: Summary of the result of MDC analysis for the 1998 Antarctic earthquake. The location of preferred point source as shown on the bathymetric map for the area., The USGS PDE location is the red star. The red focal mechanisms show the preferred MDC solution while the black one represents the GCMT solution. Blue arrow denotes the strike of the

inferred low angle fault plane. Yellow dots denote the aftershocks within one week. The azimuthal variation of $\ln(A_s/A_d)$ is shown in (b) with red triangles and green circles for vertical and transverse components, respectively. The values of inverted parameters of each point source are summarized on the right side as well as the average variance reduction and number of traces.

2.3.2 The 2004 Sumatra eathquake and the 2005 Nias earthquake.

The devastating Sumatra-Andaman earthquake of 26 December 2004 was the largest earthquakes ever recorded with modern instruments. This earthquake had a long rupture duration of 500 s with rupture propagating northward along the subduction interface over 1300 km [*Ammon et al.*, 2005]. *Ammon et al.* [2005] present 3 slip models obtained by combining surface waves and body waves and estimate a total moment release of 6.5×10^{22} Nm, which is approaching that found by using normal mode spectral data [*J Park et al.*, 2005]. The variance reduction of 61.4% from a single point source inversion for this giant earthquake illustrates that, as might be expected, simplifying this earthquake as a point source led to large errors in matching the long period seismic waves. Using an iterative approach, *Tsai et al.* [2005] found that as many as five point sources with a total moment of 1.17×10^{23} Nm are required to explain the observations. Here, we study this event using the multiple point sources analysis without knowing any prior location and focal information about each point source and invert them simultaneously.

In this study, we have selected the long period waveforms recorded at 53 vertical components and 37 transverse components. The station distribution is shown in Figure S2.1. The azimuth coverage is excellent. We initially employed a global range search for each

parameter and then gradually limited their ranges to obtain an accurate solution. Our F-test reveals that up to five point sources with a total moment of 7.0×10^{22} Nm and a duration of 500 seconds are required to interpret the observations (Figure 2.5). This seismic moment is 35% lower than results of *Tsai et al.* [2005] but slightly larger than the estimate of 6.5×10^{22} Nm, [*Ammon et al.*, 2005]. Difference in total moment between the two results is probably due to the larger dip angle and flexible depth of each point source for which we inverted. We also note that the additional shorter period band from 167 s to 200 s in our inversion has a significant impact on constraining the long-period amplitude compared to the cutoff period of 200 s used for GCMT. Here, care must be taken because a robust result highly depends on the appropriate time window we implement for source inversion. Although the 3D effects might be significant as the ray path leaves the source along the subduction zone, it is a surprise to find that our five point sources model derived only from long period seismograms displays an excellent agreement with the trench axis.

Our model shows three dominant discrete regions of energy release roughly consistent with the patches of high slip observed in geodetic data [*Subarya et al.*, 2006] from 3°N to 5°N, 6°N to 8°N, and 13°N to 14°N. The first patch in the southern part comprised of two Mw 8.9 subevents (point source 1 and 2) separated by 60 seconds accounts for almost 70% of the total moment. Both have similar source duration about 135s and depth of 26 km. The first thrust event initiated northwest of Simeulue island along a fault plane dipping 6.4° with a strike of 310°. The rupture then propagated about 200 km to the NW on a fault striking 339° with a dip angle of 8°, where forms the second thrust subevent. Nearly 30° change in the strike direction between them as well as their location coincides with the characteristics of regional subduction interface. Point source 5 with a magnitude of 8.4 was located on a

Northeast-striking fault dipping 9° close to the Andaman island. The time, focal mechanisms, and centroid locations of southern asperity composed of point source 1 and point source 2, and northern portion composed of point source 5 in our model are consistent with previous studies [*Ammon et al.*, 2005; *Ishii et al.*, 2005; *Tsai et al.*, 2005]. Primary discrepancies occur along the subducted interface near the Nicobar island. Our model shows that two subevents having the same magnitude of Mw 8.6 and depth of 32 km took place between 6°N and 8°N, with the centroid time of 244 s and 336 s (Figure 2.7) These two subevents are similar in space and time to the normalized peak amplitude as a function of time in the results of *Ishii et al.* [2005]. The slight change of the dip angle (2.5°) between them may imply the multiple fault segments in this region and hence lead to the distinct process of the moment release. The relative location and time of these five events allow us to approximately estimate an average rupture velocity of 3.4 km/s for this giant earthquake.

Source time function and uncertainty estimates of each parameter of our five point source model are shown in Figure 2.8. Note that centroid times and locations of five events are well determined, while some acceptable variations are present in focal mechanisms. Larger dip angles (10.5° and 8.5°) of the subevents 3 and 4 compared to that of the south portion (6.4° and 8.0°) may result from the increasing depth as found in their related correlation matrix. Besides the trade-off between dip and scalar moment, evident in the positive relationship between strike and rake angle from their correlation matrix shows that the rupture propagation highly correlates with the irregularity of trench geometry along the subduction zone. Our results are pretty close to the Model II of *Ammon et al.* [2005] obtained from long-period seismograms and teleseismic surface waves. The total moment

release is equivalent to moment magnitude Mw 9.2 with about 90% of the moment released in the southern part from 3°N to 8°N mainly in terms of pure thrust components.

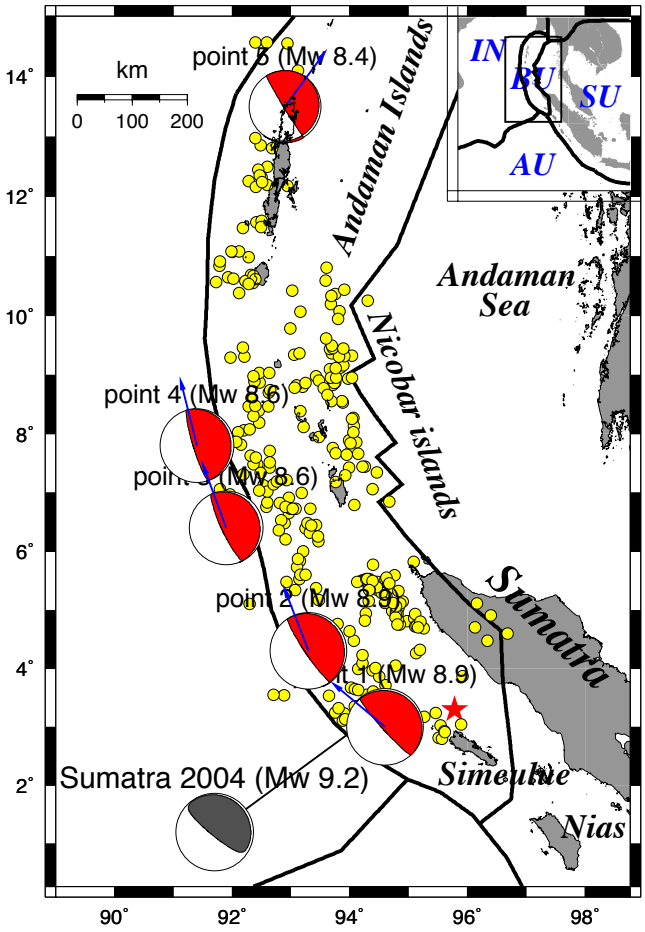

Multiple Double Couples

Point source 1 :
Centroid time t0=102.00 Half duration th= 65.52
Centroid location: Lat.= 3.00 Lon.= 94.60 Depth= 26.00
Mo = 0.243E+30 (strike,dip,rake)=(310.00, 6.40, 82.00)

Point source 2 :
Centroid time t0=161.00 Half duration th= 67.44
Centroid location: Lat.= 4.30 Lon.= 93.30 Depth= 26.00
Mo = 0.265E+30 (strike,dip,rake)=(339.00, 8.00,103.00)

Point source 3 :
Centroid time t0=244.00 Half duration th= 48.41
Centroid location: Lat.= 6.40 Lon.= 91.90 Depth= 33.00
Mo = 0.980E+29 (strike,dip,rake)=(340.00,10.50, 95.00)

Point source 4 :
Centroid time t0=336.00 Half duration th= 48.41
Centroid location: Lat.= 7.80 Lon.= 91.40 Depth= 32.00
Mo = 0.980E+29 (strike,dip,rake)=(346.00, 8.50, 93.00)

Point source 5 :
Centroid time t0=484.00 Half duration th= 38.16
Centroid location: Lat.= 13.50 Lon.= 92.90 Depth= 28.00
Mo = 0.480E+29 (strike,dip,rake)=(36.00, 9.00,157.00)

Variance Reduction = 86.70% Traces used: 90

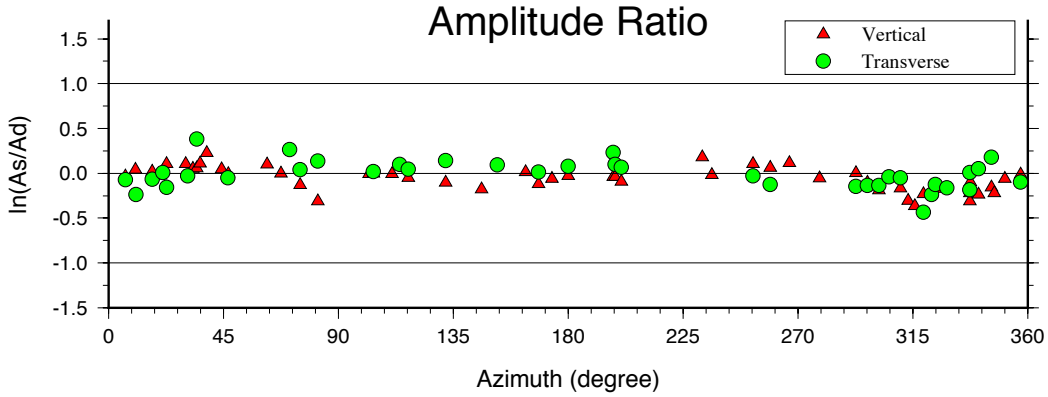

Figure 2.7: Summary of the result of MDC analysis for the 2004 Sumatra earthquake. The location of preferred point source as shown on a bathymetric base map, with USGS PDE location (red star) on. Yellow dots denote the aftershocks in one week. The average value of $\ln(A_s/A_d)$ is -0.04 and the 2σ standard deviation is 0.29, suggesting that 95% of peak amplitude ratios (A_s/A_d) falls between 0.72 to 1.28.

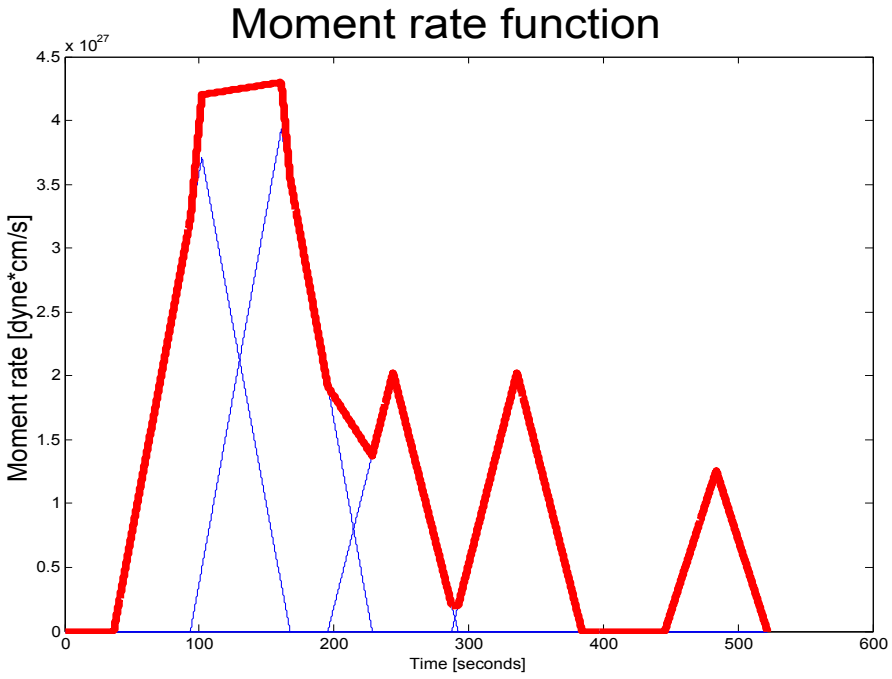

Figure 2.8: Moment rate function of the 2004 Sumatra earthquake using our best double-couple model. The thin blue solid lines denote the individual point source. The heavy red line denotes the overall model. The source durations are determined by the scalar moment.

The 2005 Mw 8.6 Nias earthquake (Figure 2.9) occurred three months after the 2004 Sumatra earthquake. The long period waveforms of 55 vertical components and 43 transverse components are used to study its source in terms of multiple double-couples. Our single double-couple solution (Table 2.1) in fact already matches the data well with a

variance reduction of 82.7%. But we notice that the synthetic seismograms generally overestimate the observed amplitudes near the strike of 320˚ and underestimate in the opposite direction, 140˚. This would suggest a southeastward directivity effect. Using two double-couples, the variance reduction increases to 90.5%. And there is no azimuthal variation in fitting the peak amplitudes (Figure 2.9). F-test suggests that three double-couple cannot significantly improve the waveform fits at a confidence of 95%. So the two double-couple model is selected as the preferred solution.

The centroids of two double-couples are separated by 35 s temporally and 140 km spatially. The first subevent has a moment magnitude 8.5 (is 6.0×10^{21}Nm). Its centroid (2.0°N, 97.0°E) locates slightly southwest of the USGS epicenter (2.09°N, 97.11°E) with a depth of 25 km. The fault plane has a strike of 319° and dips 8^{o} to the northeast. The centroid time is 43 s. The second subevent has a moment magnitude 8.4 (5.0×10^{21}Nm). Its centroid (0.9°N, 97.6°E) is 140 km south-southeast of the first subevent. This location is in the vicinity of Nias Island and closer to the trench axis than the first subevent. This is consistent with the inverted centroid depth (13 km), 11 km shallower than that of the first subevent. The fault plane has a strike of 340^{o} and dips 9^{o} to the north-northeast. The centroid time of this second subevent is 78s. The cumulative seismic moment is 1.1×10^{22}Nm, much larger than our single couple solution (5.6×10^{21} Nm, table 2.1) but consistent with GCMT estimate (1.06×10^{22}Nm). The 21^{o} difference in fault strike is consistent with change strike of the nearby trench axis.

Unlike the 2004 Sumatra earthquake, substantial near-field observations and geodetic data [*Briggs et al.*, 2006] provide valuable local information to constrain the slip distribution of the 2005 Nias earthquake. Using the continuous GPS observations, Hsu et al. [2006]

found that the 2005 Nias earthquake resulted from two distinct ruptures along the strike : a Mw 8.2 event to the north of the hypocenter and a Mw8.5 event to the south. This result is further confirmed by the joint analysis of teleseismic body waves and geodetic data by *Konca et al.* [2007]. We point out that the locations of two double-couples are inconsistent with the locations of two subevents constrained by the local data. Hence, we need cautions in interpreting the results of MDC analysis. Our results reveal that the early portion of rupture (with a centroid time of 43 s) is dominated by the slip on the relatively deeper portion of the fault (with a centroid depth of 25 km). The later rupture (with a 78 s centroid time) is dominated by the slip on the relatively shallower portion of fault and 150 km southwest of the epicenter. Both are consistent with the inverted slip history of *Konca et al.* [2007].

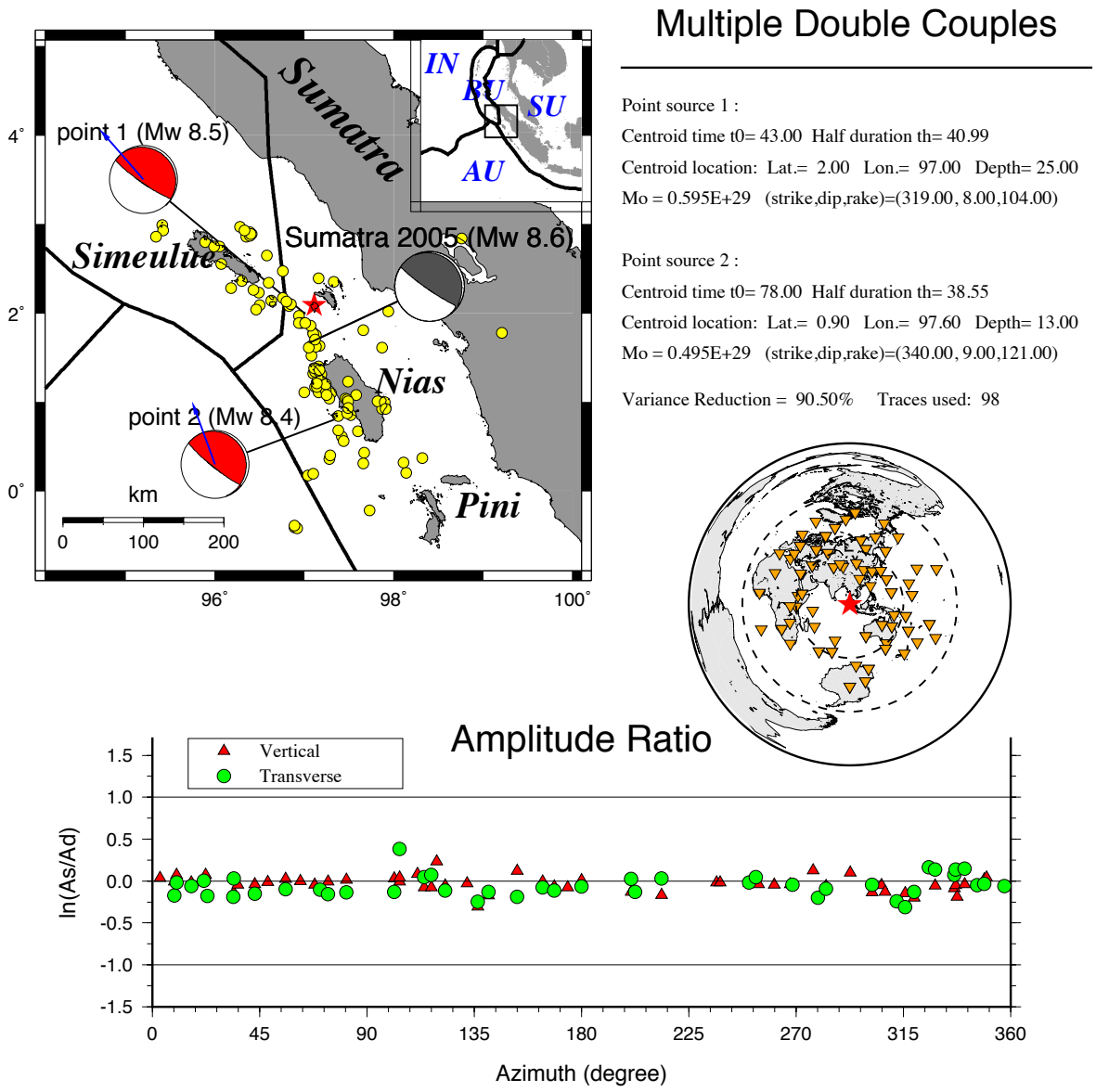

Figure 2.9: Summary of the result of MDC analysis for the 2005 Nias earthquake. The average value of $\ln(A_s/A_d)$ is -0.04 and the 2σ standard deviation is 0.22, suggesting that 95% of peak amplitude ratios (A_s/A_d) falls between 0.77 to 1.19.

2.3.3 The 2009 Samoa earthquake

The 2009 Mw 8.1 Samoa earthquake initiated in the outer rise region of the Tonga subduction zone, where the Pacific Plate descends beneath the Australia Plate at a speed of 86 mm/yr to the west. This earthquake was the largest earthquake in year 2009 and also the largest normal fault earthquake according to the GCMT solution since the 2007 Mw 8.1 Kuril island earthquake. However, there were big controversies among the preliminary seismological solutions in terms of the size of non-double-couple component and the causative fault plane. The poor long-period waveform fits using a single point source originally prompted us to develop the approach for multiple point source analysis. In an early report [*Li et al., 2009*], we roughly find that at least two major subevents, a normal fault event and a thrust event, should be involved to interpret the observations (Figure 2.10). In this paper, we further investigate the properties of long-period waveforms as well as the uncertainty of source parameters using the long period waveforms recorded at 49 vertical components and 43 transverse components. The F-test suggested that an additional possible strike-slip event occurred on the overriding plate about 200 km to the west at a time that is between the major two events. The best MDC model with a variance reduction of 88.1% of this earthquake is shown in Figure 2.11. The strike direction of each subevent is consistent with adjacent plate boundary. The total moment release of 3.27×10^{21} Nm is twice the GCMT solution.

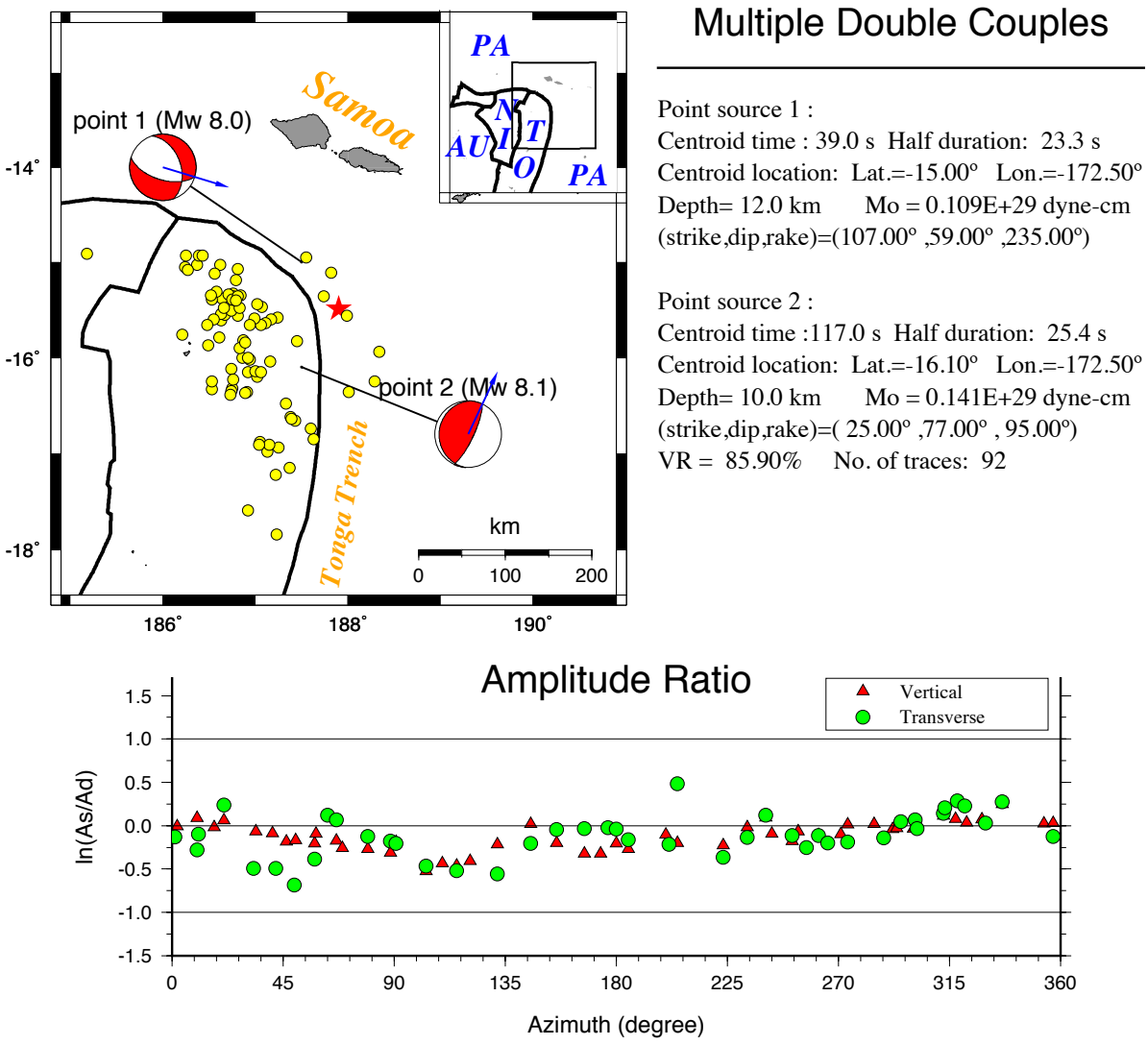

Figure 2.10. Summary of the best two double-couple model of MDC analysis for the 2009 Samoa earthquake. The average value of $\ln(A_s/A_d)$ is -0.11 and the 2σ standard deviation is 0.42, suggesting that 95% of peak amplitude ratios (A_s/A_d) falls between 0.59 to 1.36.

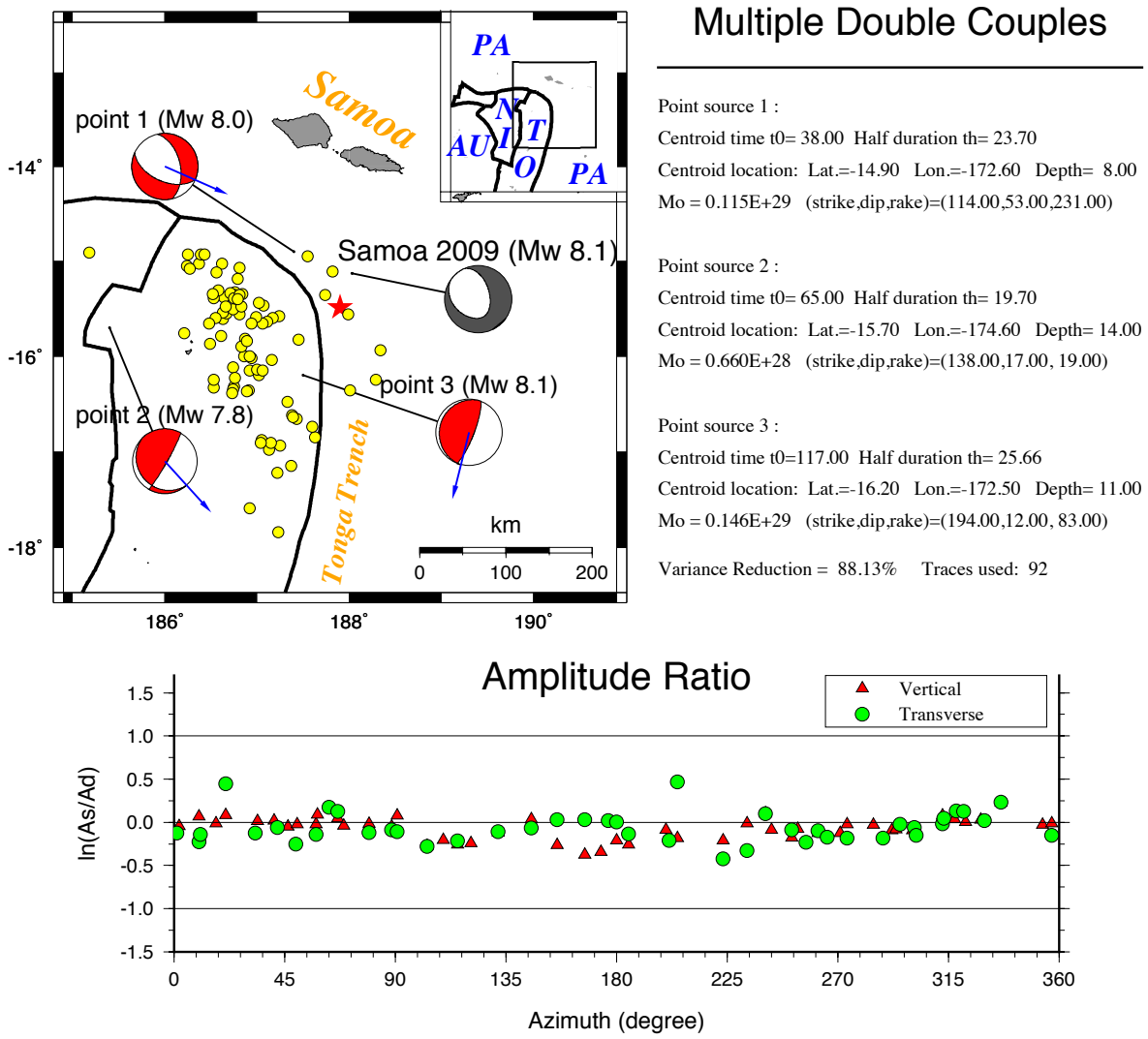

Figure 2.11: Summary of the best three double-couple model of MDC analysis for the 2009 Samoa earthquake. The average value of $\ln(A_s/A_d)$ is -0.06 and the 2σ standard deviation is 0.30, suggesting that 95% of peak amplitude ratios (A_s/A_d) falls between 0.69 to 1.27.

Our result suggests that a shallow (centroid depth of 8 km) high angle (~53°) oblique

normal fault event of magnitude Mw 8.0 strike southeast initiated on the outer wall of the Pacific Plate with a centroid time at 38 s. The rupture plane is parallel to the trench axis and the centroid locates at 70 km northwest of the USGS hypocenter (15.49°S, 172.1°W). Eighty seconds later, another Mw 8.1 pure thrust with a shallow dip angle 12° was triggered about 140 km south along the subduction zone with its strike direction rotated by 80° to the southwest to accommodate to the geometry of Tonga trench. Another point source of Mw 7.8 from our model took place on the overriding plate 270 km to the west with the centroid time at 68 seconds. We prefer its focal mechanism as a strike-slip event containing slight thrust component. From the approximate posterior probability distribution, the normal fault subevent has an overall solid constraint for each source parameter using long-period records. The centroid time and location of the under-thrusting event are well resolved but the strike and dip angle show a typical higher uncertainty of 10° ~ 15° from our best model. Taking the trade-off between dip and seismic moment into account in this event, the seismic moment ranges from 1.0×10^{21} to 1.5×10^{21} Nm and the dip varies from 15° to 12°. These two main events contribute to the approximate 86% of the variance reduction in the synthetics. In the case of the additional strike-slip subevent, each parameter commonly manifests a broader range of uncertainty, which implies that the data is unable to provide sufficient restraint on the source parameters of this subevent.

The two principal normal fault and thrust events are explicitly detected in teleseismic body waveforms. The peak time of power obtained from back projection method using the Japanese F-net stations [*Lay et al.*, 2010b] strongly verifies the two predominant subevents in our model. Particularly, the interaction of these two events uniquely causes prominent CLVD component (0.165) in GCMT solution and results in an ambiguously illusive centroid

location based on a single point source model. Our model has substantiated that this composite source with entirely different focal mechanisms can be resolved from long-period waveforms. However, care must be taken in interpreting the extra source such as the third point source (Point source 2 in Figure 2.11) because it is far from the Tonga subduction zone and near a complicated plate boundary, involving a continental rift, an oceanic transform fault and an oceanic spreading ridge. No plausible mechanism can explain how this subevent was so quickly triggered 270 km away just about 30 s after the first subevent. Moreover, there is no evidence of related aftershocks present in this region. Nevertheless, without the third point source, the amplitude of both vertical and transverse components of long-period synthetics with azimuth from 45° to 135° are typically smaller than observations. We notice that our station distribution notwithstanding the good azimuth coverage, is asymmetric and all the seismograms within azimuth between 45° and 135° are recorded about 90° far away from hypocenter and evenly distributed along the America Plate. This asymmetric feature of distance may introduce systematic bias in our inversion. The relatively high amplitude of these observations may indicate the effect of lateral heterogeneity in this azimuth range. Accordingly, we continue to accept that the third point source derives from the uncertainty of structure, bias in data and some systematic artifacts in inversion rather than the source complexity. We propose that strong-motion data and potential geodetic data can provide further constraints and help better resolve the source complexity of this earthquake. As a whole, a comprehensive combination of various available datasets and associated evidence should be involved before we safely build a rational and valid MDC model.

2.3.4 The 2010 Chile earthquake

The 27 February 2010 Chile (Mw 8.8) earthquake is a shallow low angle underthrust occurring offshore the Maule, Chile area and ruptures nearly 500 km along the subducting interface in central Chile. Various types of data are available and used to study this earthquake [*Delouis et al.*, 2010; *Lay et al.*, 2010a; *Moreno et al.*, 2010]. One of the most typical and important attributes of this earthquake revealed by these studies is the main slip being concentrated in two asperities to the north and south of the hypocenter with a possible seismic gap between them. A single point source inversion of this earthquake has a variance reduction of 84.6% but suggests a directivity effect with generally lower amplitude ratios near the strike direction of 18° and higher ones in the opposite direction of 200°. A multiple double-couple analysis using long period waveforms recorded at 49 vertical components and 43 transverse components was subsequently performed. Our F-test suggests that a two point source model (Figure 2.12) with a total moment release of 2.2×10^{22} Nm, about 20% greater than the GCMT solution, can sufficiently account for the long-period waveforms of this earthquake with a variance reduction of 90.2%.

As shown in Figure 2.12, the first subevent has an Mw of 8.6. Its centroid location is at (-36.6^{o}, -73.6^{o}), south of the USGS epicenter. The preferred fault plane has a strike of 10° and a dip angle of 13°. The centroid depth is 14 km beneath the upper plate, The second point source with a magnitude of Mw 8.7 occurred 160 km north at a depth of 24 km about 40 seconds later and probably ruptured a new fault zone with a strike of 18° and dip of 17°. Strike directions of two point sources as well as the mild change of 8° between them coincide with the trench geometry, the dip angle increasing from 13° to 17° can be associated with the growing depth from 14 km to 24 km.

Note that the centroid location of our model lies to the east of USGS hypocenter, which is likely due to the 3D variations in velocity structure of regional subducted plate. The waveform fits are nearly perfect and all the source parameters for both events seem stable and well determined in our uncertainty estimate. Our MDC model displays a good agreement with the model based on geodetic data and tsunami data [*Lorito et al.*, 2011]. The latitudes of the centroid locations highly correlate with the two asperities claimed in the previous studies. This example indicates that, besides interpreting the potential source complexity, our MDC analysis can also use point source solutions to approximate the asperities and derive their possible changes in the source parameters.

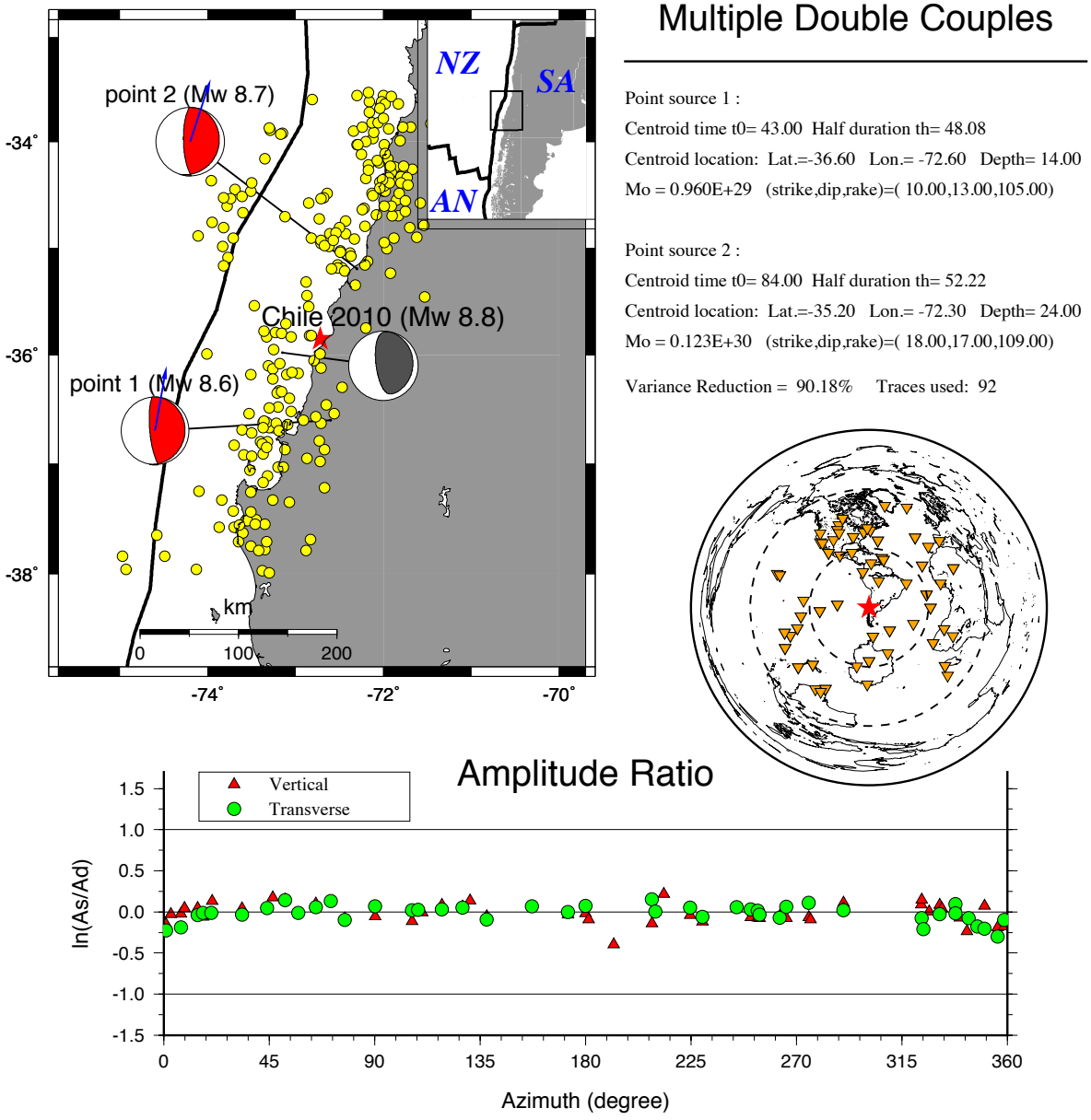

Figure 2.12: Summary of the result of MDC analysis for the 2010 Chile earthquake. The average value of $\ln(A_s/A_d)$ is -0.02 and the 2σ standard deviation is 0.22, suggesting that 95% of peak amplitude ratios (A_s/A_d) falls between 0.79 to 1.23.

2.3.5 The 2011 Tohoku earthquake

We also apply our method to study the 11 March 2011 giant earthquake shaking the offshore region (38.1°N, 142.86°E from Japan Meteorological Agency) near Tohoku. In this case, the first hour of continuous real-time broad-band seismic data automatically downloaded from global seismic network (GSN) within distance from 30° to 110° were initially used to quickly invert for our multiple double-couple model, which was obtained just 2 hours after the earthquake happened. A total of 91 waveforms recorded at 47 vertical components and 44 transverse components provide good azimuth coverage (Figure 2.13). We find a single point source model can explain the data with a variance reduction of 89%. According to F-test, using models with two double-couples cannot significantly improve the waveform fits. The focal mechanisms of GCMT, USGS Wphase moment tensor solution, USGS centroid moment tensor solution and our MDC model are shown in Figure 2.13.

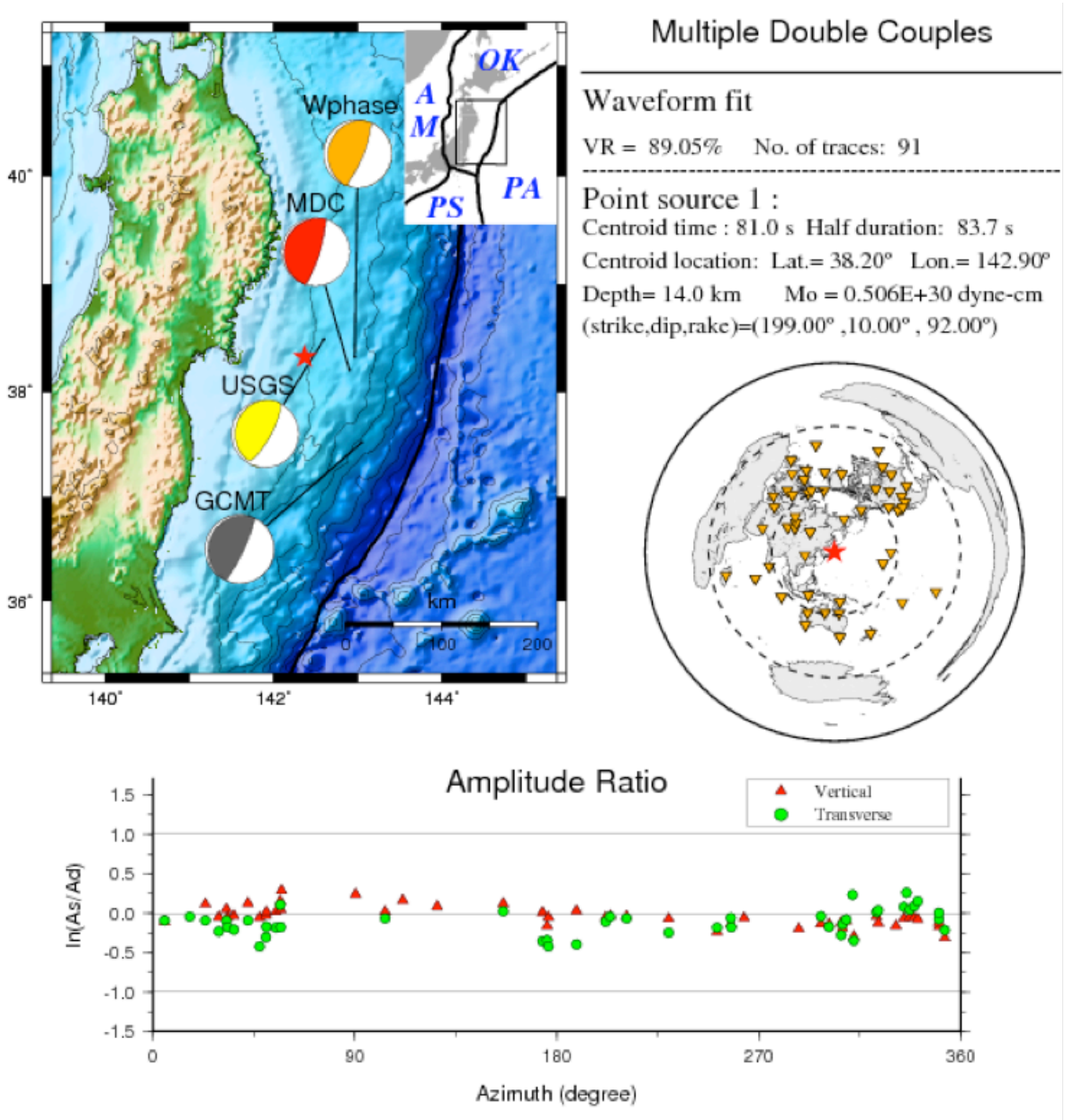

Figure 2.13: Summary of the result of MDC analysis for the 2011 Japan earthquake. The solution of GCMT, USGS cmt and Wphase cmt are also plotted in the map. The average value of $\ln(A_s/A_d)$ our model is -0.077 and the 2σ standard deviation is 0.30, suggesting that 95% of peak amplitude ratios (A_s/A_d) falls between 0.74 to 1.35. The station locations are summarized in as orange inverted triangles. The dashed contours denote 60^o and 120^o iso-distances.

Our MDC solution [*Shao et al.*, 2011] shows that the total moment release is about 5.0 x 10^{22} Nm, equivalent to a magnitude of Mw 9.1, and the preferred nodal plane has a strike of 199°, a dip angle of 10°, and a rake angle of 92°. The conspicuous agreement in focal mechanisms between our solution and the updated GCMT solution with a best-fitting fault plane having a seismic moment of 5.31 x 10^{22} Nm, a strike of 203°, a dip of 10° and a rake of 88°, further corroborates that our approach is applicable for a fast real-time point source inversion to provide useable MDC solutions. We want to highlight that a real-time quick and stable MDC model is extremely important for subsequent detailed analysis of the rupture model such as building real-time finite fault model. Notice that the centroid location of 38.2°N, 142.9°E in our model is quite different from that of 37.52°N, 143.05°E in GCMT solution but pretty close to that of the USGS Wphase and centroid moment tensor solution, as well as the location released by JMA. It is also noteworthy that the low angle fault plane coincides with the plate interface constrained with wide-angle reflection and refraction profile across the source region [*Miura et al.*, 2005].

Another attractive characteristic of this earthquake is that it includes two identifiable subevents: one Mw 7.9 thrust event, and one Mw 7.6 normal fault event about 30 and 40 minutes, respectively, after the occurrence of the mainshock in response to GCMT solution. The source mechanism of aftershocks, in principle, should be dramatically contaminated by the mainshock. In previous examples, we have primarily focused on exploring the source complexity in the mainshock with the maximum time range of no more than 500 s after the earthquake initiates. Despite the much smaller peak wave amplitude of two aftershocks compared to the mainshock of this Japan earthquake, we seized the opportunity to extend

our search range for the time window and test whether we can extract the source information of these two aftershocks based on our MDC analysis with the intention of determining the possible interaction of source parameters between them. We use almost the same data but extend the length of waveforms to 5600 s to accommodate the later waveforms generated by aftershocks. Given the prior time information of aftershocks from GCMT, a three point source inversion is performed; the results are shown in Figure 2.14. We find that the solution of mainshock has changed slightly. The scalar moment increases by 15%, accompanied by a slight decrease in dip angle (from 10^{o} to 9°). Latitude changes from 38.2°N to 38.1°N.

For the Mw 7.9 aftershocks, we obtain a centroid location of 35.7°N, 141.4°E and depth of 34 km, agreeing with that of GCMT solution (35.92°N, 141.38°E, 29 km). Our scalar moment is $7.9*10^{20}$ Nm, similar to that of $8.4*10^{20}$ Nm in GCMT. This is an underthrusting event occurring on a fault dipping 13° with a strike of 210° and a rake angle of 98°, again consistent with that of 17°, 199° and 84° in GCMT solution. For the Mw 7.6 event occurring on the outer rise region about 40 minutes after the mainshock, there is difference of around 45 km present between the centroid locations of our model and the GCMT. Our scalar moment of $3.1*10^{20}$ Nm is same as that of GCMT result. Our focal mechanism has a strike of 191°, a dip of 30° which agrees well with that of 182° and 42° in GCMT solution.

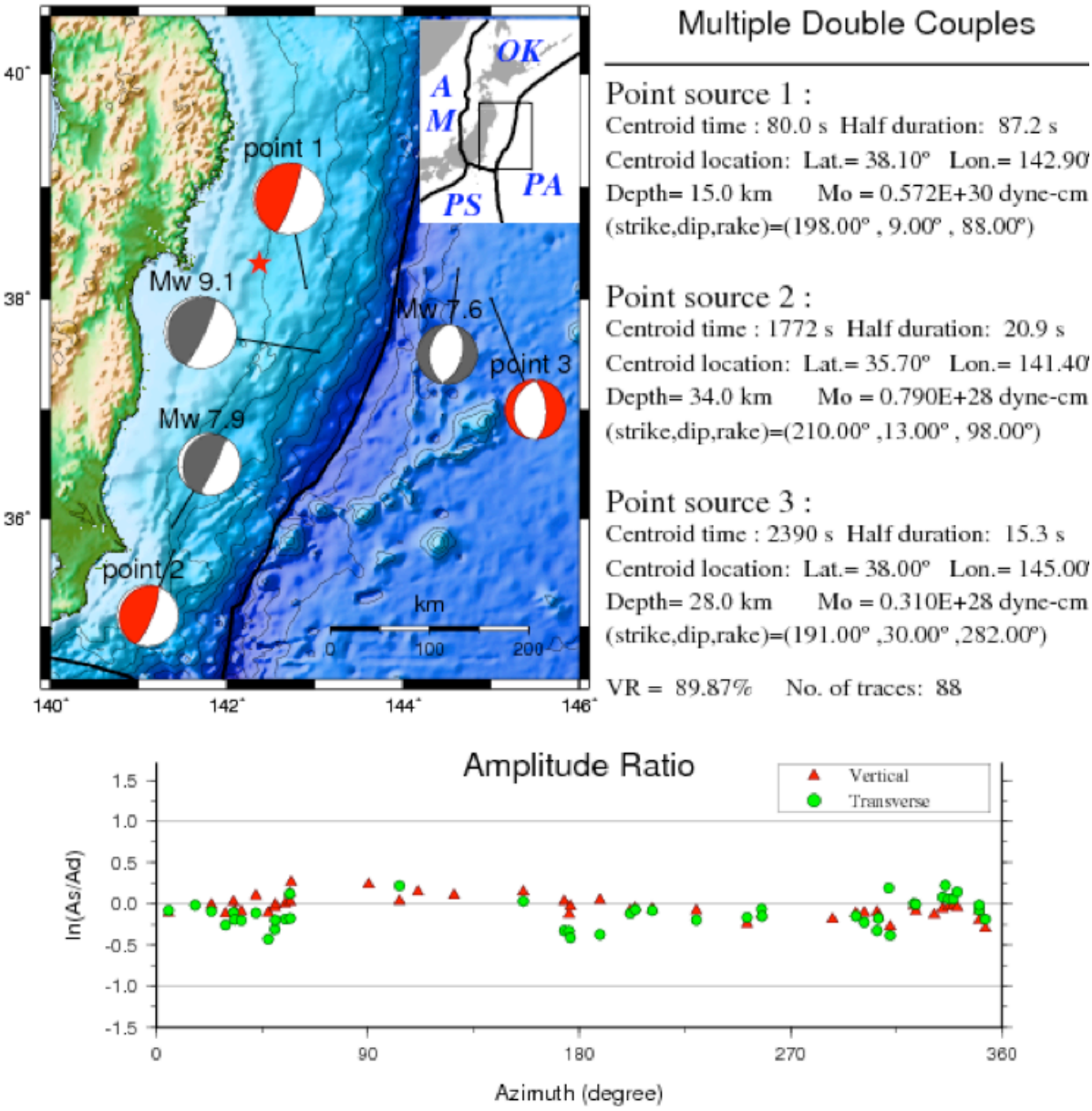

Figure 2.14: Summary of the result of MDC analysis involving two aftershocks for the 2011 Japan earthquake. The average value of $\ln(A_s/A_d)$ is -0.083 and the 2σ standard deviation is 0.30, suggesting that 95% of peak amplitude ratios (A_s/A_d) falls between 0.68 to 1.24.

2.4 Conclusion

We have developed a fast algorithm to constrain the focal mechanisms of global large earthquakes using long-period seismic records. We demonstrated its successful application in the study of the source complexity of the great earthquakes (> Mw 8.0) in the past two decades. The sources are approximated as either single or multiple double-couples. The number of point sources is determined by performing an F-test to see if additional double-couples are warranted by the data. Long-period waves inherently fail to provide details of the slip history. In contrast, high-frequency body waves are insensitive to long-period characteristic of source process and thus tend to underestimate the scalar moment of large earthquakes.

Greatly benefitting from the modern digital seismograph network with good azimuth coverage, we apply this method to investigate the long-period complexity of 19 Mw>8 shallow earthquakes since 1990. Our F-test analysis shows that with 95% of confidence, it is better to use more than one point source to approximate five of these 19 earthquakes to explain their long period waveforms. It is impressive that all of our multiple double models particularly agree well with the regional fault geometry. The confidence levels of all of them are larger than 99%. It demonstrates the importance to consider the finiteness of rupture and source complexity for large earthquakes. This is because the possible difference in the source mechanism of distinct subevents results in directivity and compound rupture characteristics, which can be reflected in the long-period waveforms. However, we should point out that the F-test can not cover all kinds of source complexity of distinct earthquakes. A reasonable and valid MDC model is supposed to satisfy the source features of other accessible observations and geological information. The last example of 2011 Japan

earthquake explicitly illustrates that long-period waveforms can possibly be used to invert for the source mechanisms of smaller aftershocks hidden in the mainshock despite the large uncertainty of some parameters. What's more, the MDC method can isolate the focal mechanisms of events that occasionally emerge at the same rupture time yet far from the location of mainshock. In this case, multiple double-couple analysis can potentially help reduce or eliminate the contamination of such unrelated events.

A corresponding fast multiple double-couple inversion system based on real-time broadband seismic data has been designed for the purpose of routine MDC analysis for new earthquakes. We find that our method can well resolve the source mechanism of earthquakes with moment magnitude greater than 7.5. The focal mechanism of the earthquake with a magnitude between 6.5 and 7.5 can also be determined by using a narrow band (167s to 333s) and selecting stations with a high signal to noise ratio (SNR). The long-period signals of Mw < 6.5 earthquakes are usually too noisy to constrain the source parameters. Another possible way is to involve the teleseismic records of stations close to the source (within 30°) in inversion to improve the SNR. However, this is usually not realistic in case of earthquakes larger than Mw 8, because the signals recorded in this distance region appear so strong that they saturate the range of the instrument.

We admit that our method still needs further improvement. After carefully optimizing the algorithm and taking advantage of the multi-thread capability of conventional CPUs, the entire inversions could be accomplished in a few minutes in a regular single-CPU PC workstation, depending on the number of point sources used. As mentioned above, in this study, we approximate the Earth structure as the 1-D PREM model and ignore its 3-D lateral variations. This approximation might not be correct if the great circle paths from source to

stations go through the regions with extremely large lateral variations. The further improvements include the use of 3-D Green's functions and the calibration using nearby large earthquakes, such as large aftershocks. These in-depth approaches might also allow us to model the surface waves with higher frequency and then improve the resolution of centroid depth.

Supplementary material.

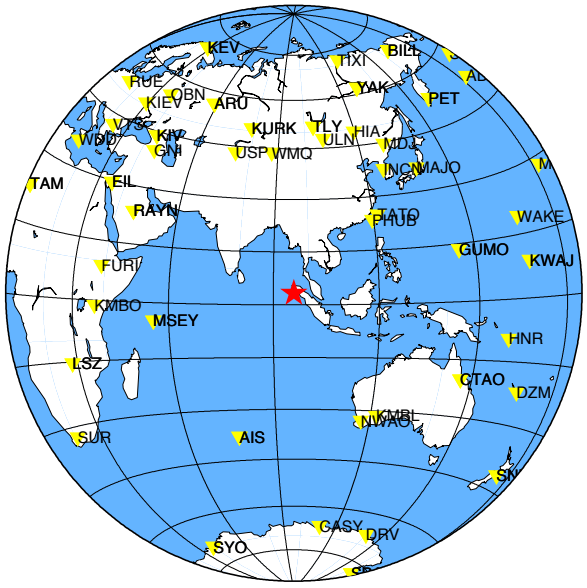

Figure S2.1. Station distribution of the 2004 great Sumatra earthquake.

Table S1. Variance reduction of our multiple double-couple analysis of 18 earthquakes.

Events	Variance Reduction				Best model
	1 double-couple	2 double-couple	3 double-couple	4 double-couple	
1	78.7%	80.1%	81.7%	-	1 DC (78.7%)
2	84.3%	84.6%	84.8%	-	1 DC (84.3%)
3	83.0%	83.6%	85.4%	-	1 DC (83.0%)
4	82.5%	85.5%	86.7%	-	1 DC (82.5%)
5	73.9%	84.0%	86.0%	-	2 DC (84.0%)
6	85.1%	85.9%	86.3%	-	1 DC 85.1%)
7	82.1%	84.4%	85.4%	-	1 DC (82.1%)
8	80.2%	80.8%	81.8%	-	1 DC (80.2%)
9	61.4%	77.3%	79.8%	83.2%	5 DC (86.7%)
10	82.7%	90.5%	90.9%	-	2 DC (90.5%)
11	84.5%	85.4%	85.9%	-	1 DC (84.5%)
12	83.5%	87.9%	88.6%	-	1 DC (83.5%)
13	82.1%	84.9%	85.9%	-	1 DC (82.1%)
14	83.7%	84.5%	85.5%	-	1 DC (83.7%)
15	87.8%	88.4%	89.3%	-	1 DC (87.8%)
16	88.0%	88.9%	89.3%	-	1 DC (88.0%)
17	61.8%	85.9%	88.1%	88.9%	3 DC (88.1%)
18	84.6%	90.2%	90.8%	-	2 DC (90.2%)

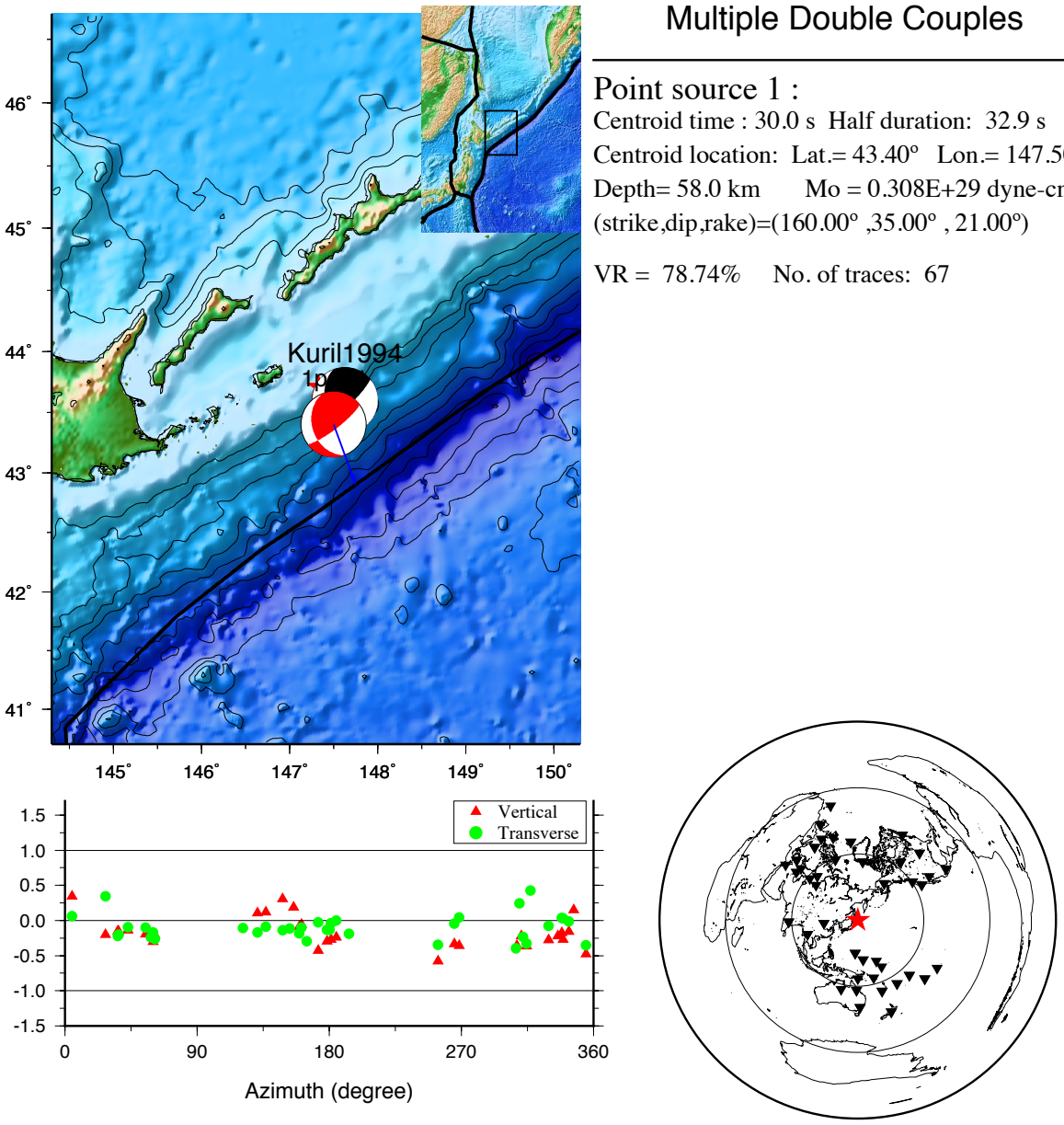

Figure S2.2. The best MDC model for the 1994 Mw 8.3 Kuril Island earthquake. The amplitude ratio (in log scale) and station distribution are shown below.

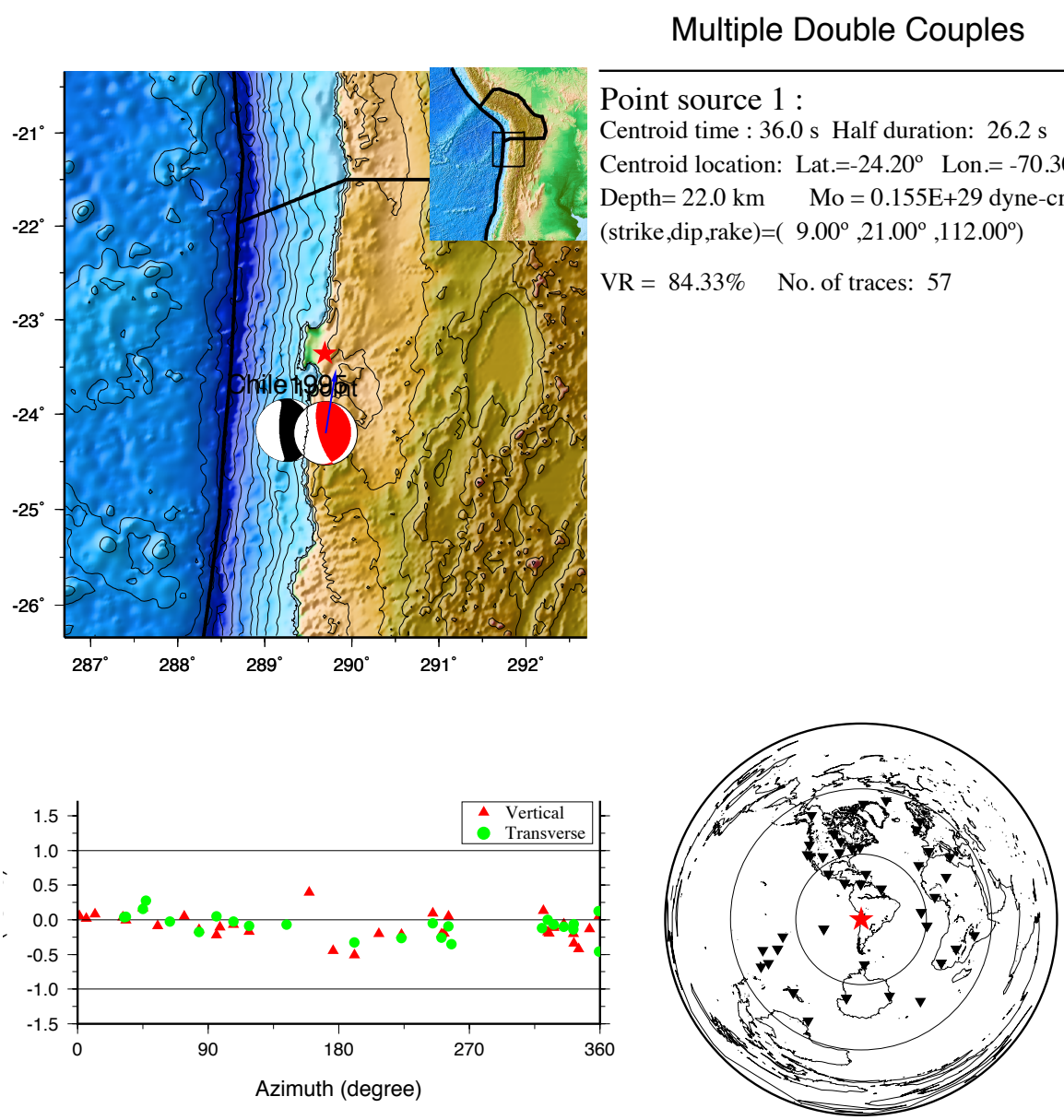

Figure S2.3. The best MDC model for the 1995 Mw 8.0 Northern Chile earthquake. The amplitude ratio (in log scale) and station distribution are shown below.

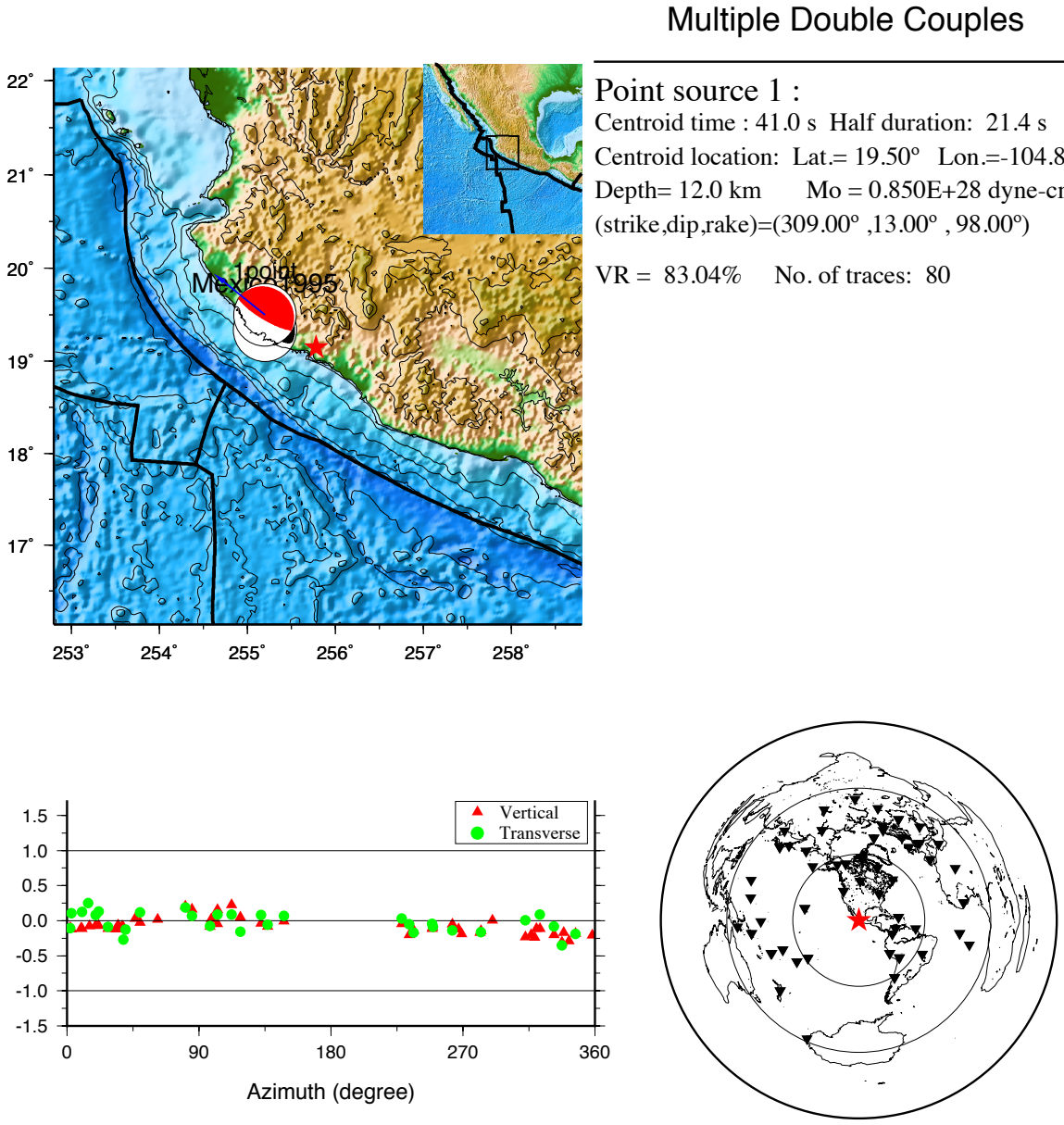

Figure S2.4. The best MDC model for the 1995 Mw 8.0 Mexico earthquake. The amplitude ratio (in log scale) and station distribution are shown below.

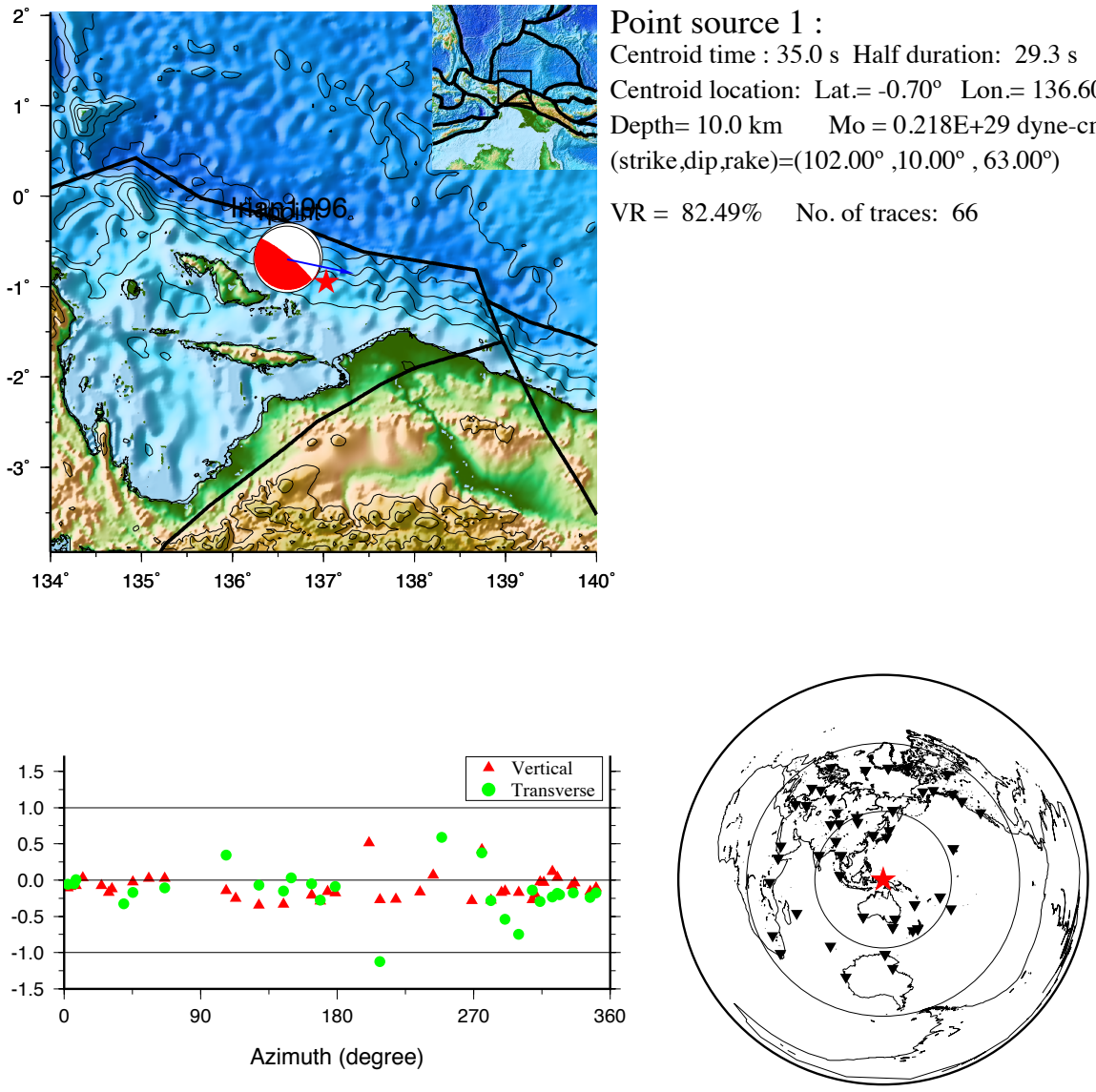

Figure S2.5. The best MDC model for the 1996 Mw 8.2 West Irian earthquake. The amplitude ratio (in log scale) and station distribution are shown below.

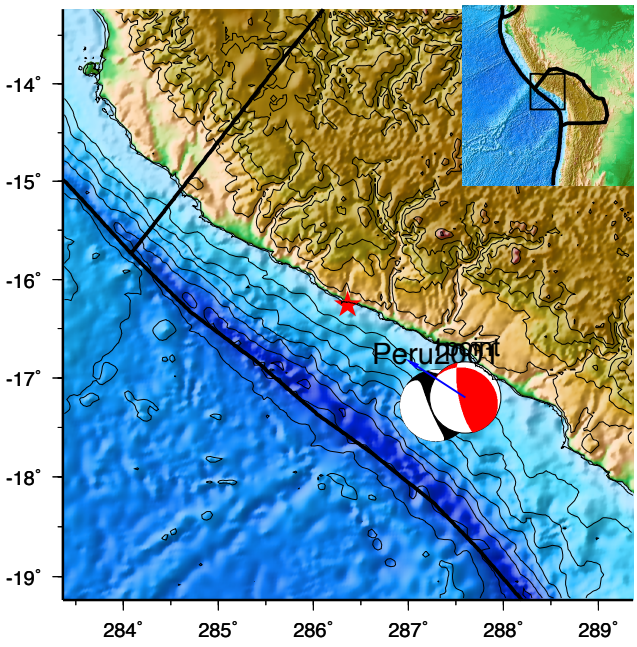

Point source 1 :
Centroid time : 73.0 s Half duration: 36.4 s
Centroid location: Lat.=-17.20° Lon.= -72.40°
Depth= 29.0 km Mo = 0.418E+29 dyne-cm
(strike,dip,rake)=(303.00° ,20.00° , 47.00°)

VR = 85.06% No. of traces: 68

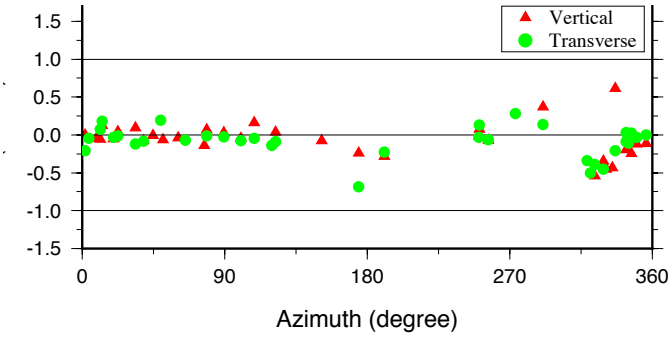

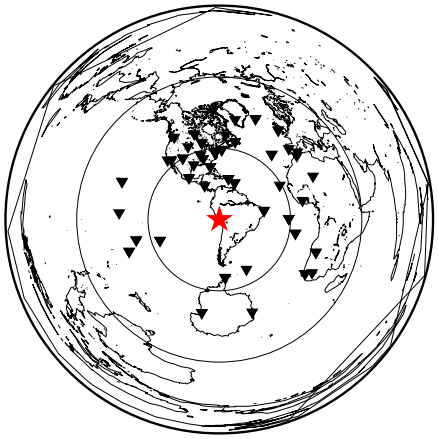

Figure S2.6. The best MDC model for the 2001 Mw 8.4 offshore Peru earthquake. The amplitude ratio (in log scale) and station distribution are shown below.

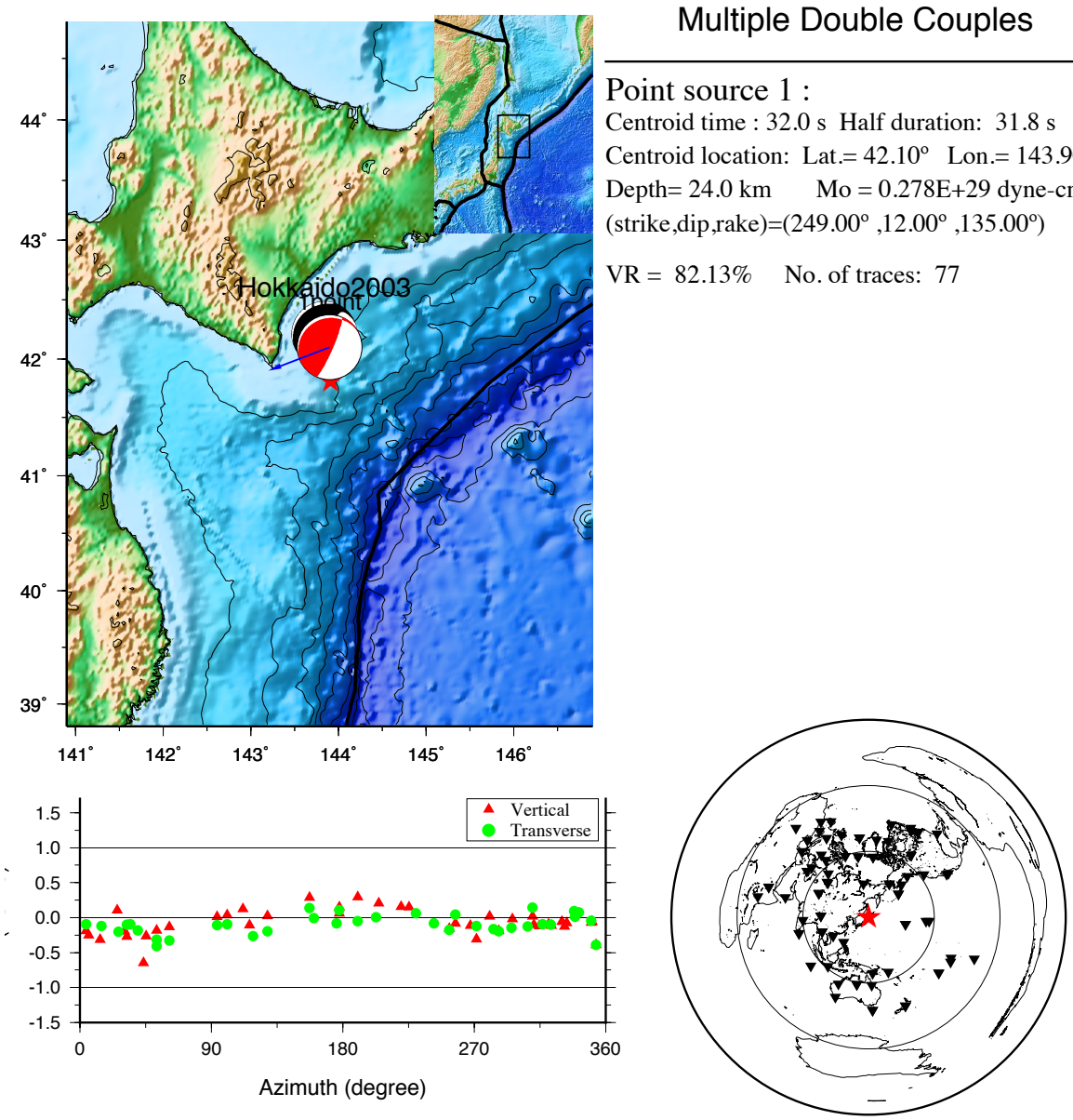

Figure S2.7. The best MDC model for the 2003 Mw 8.3 Hokkaido earthquake. The amplitude ratio (in log scale) and station distribution are shown below.

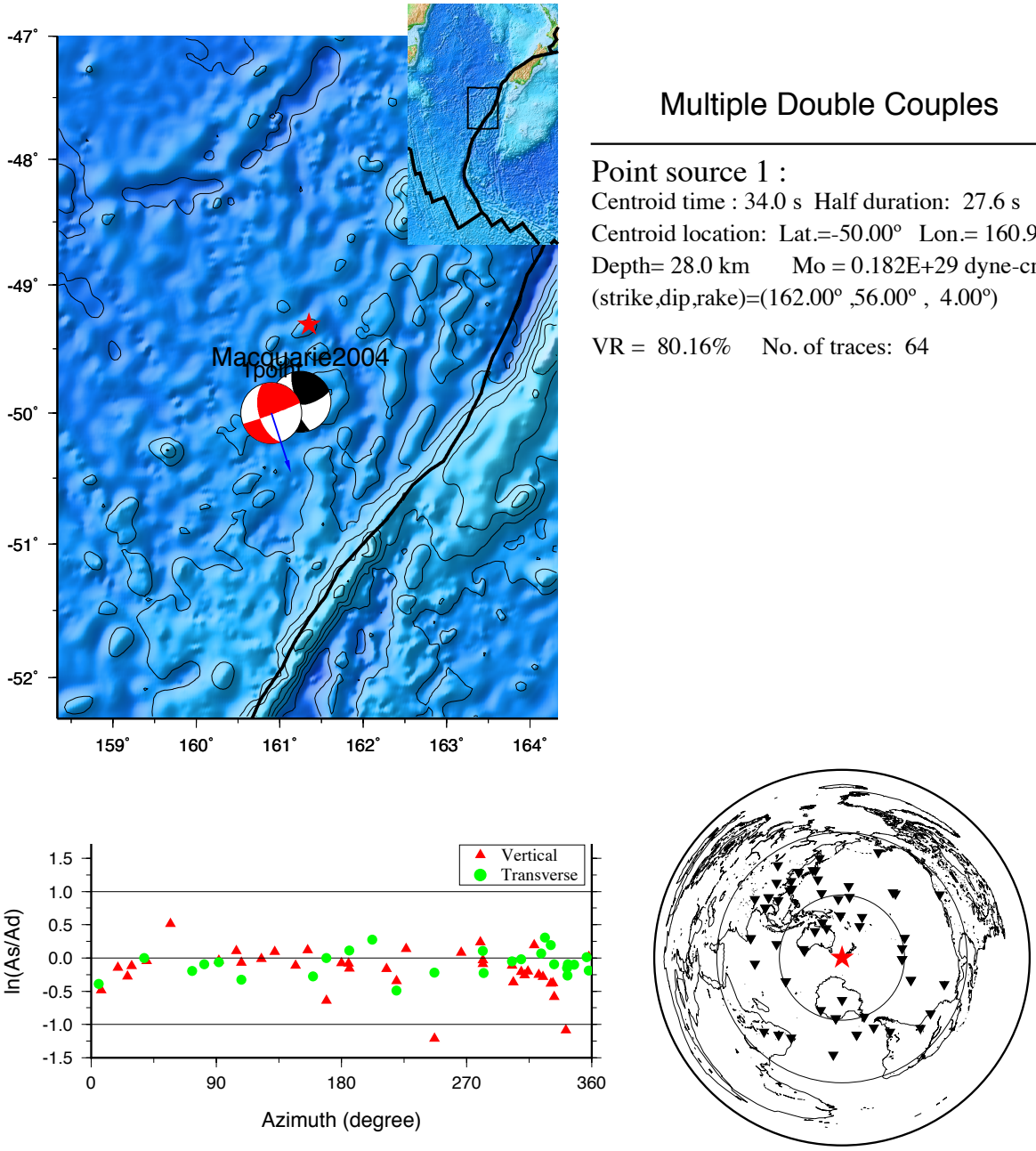

Figure S2.8. The best MDC model for the 2004 Mw 8.1 Northern Macquarie earthquake. The amplitude ratio (in log scale) and station distribution are shown below.

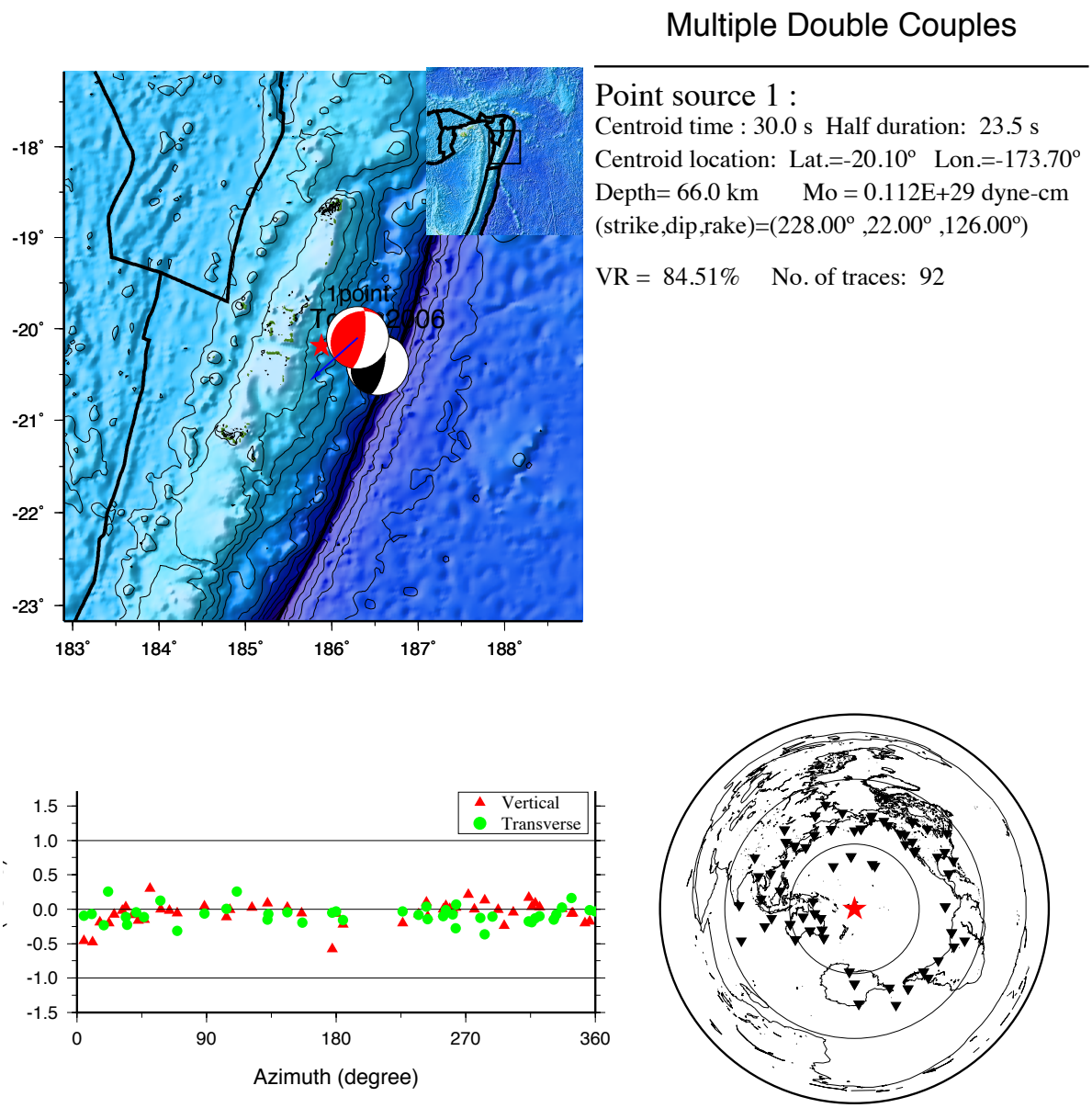

Figure S2.9. The best MDC model for the 2006 Mw 8.0 Tonga Island earthquake. The amplitude ratio (in log scale) and station distribution are shown below.

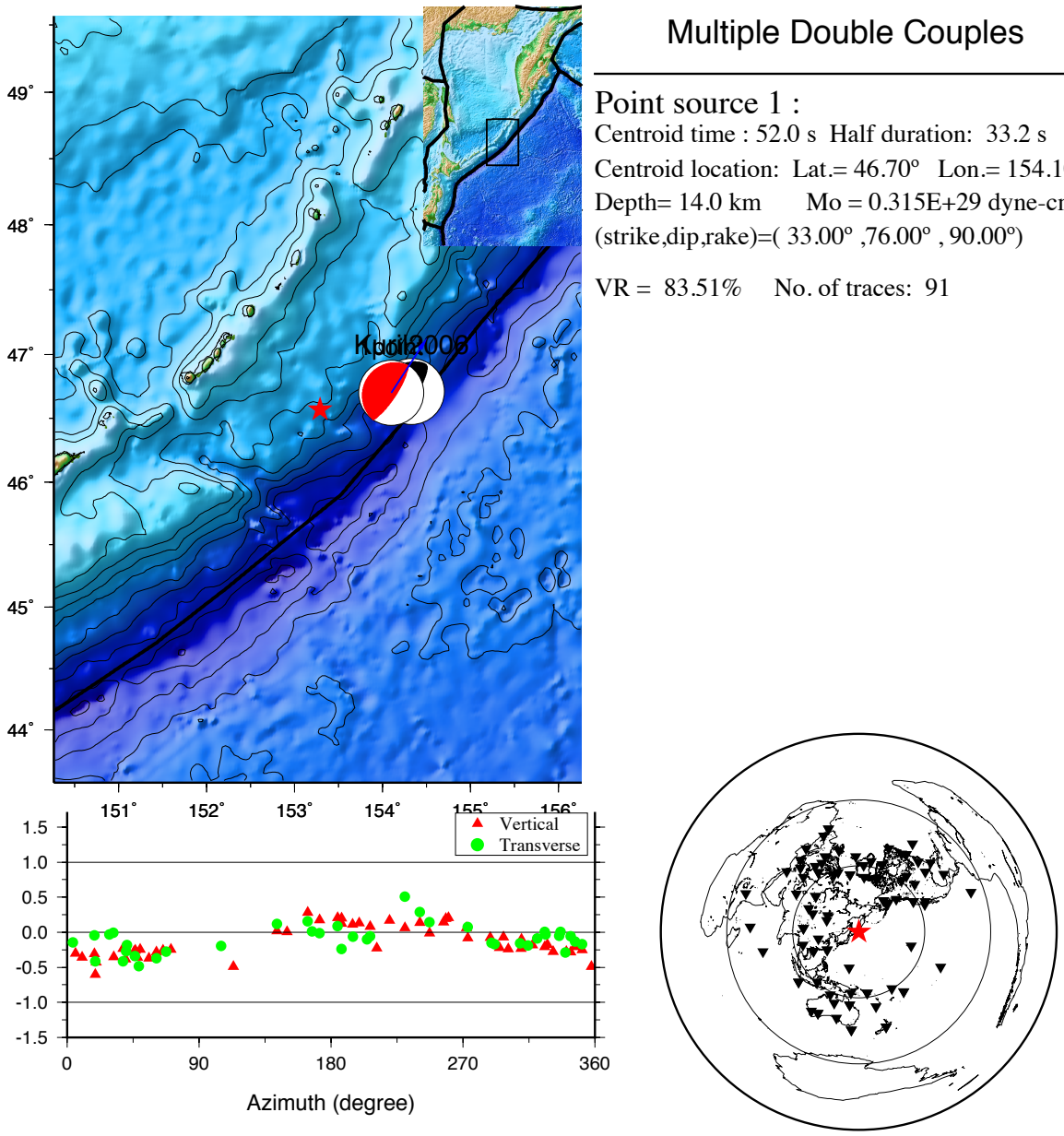

Figure S2.10. The best MDC model for the 2006 Mw 8.3 Kuril island earthquake. The amplitude ratio (in log scale) and station distribution are shown below.

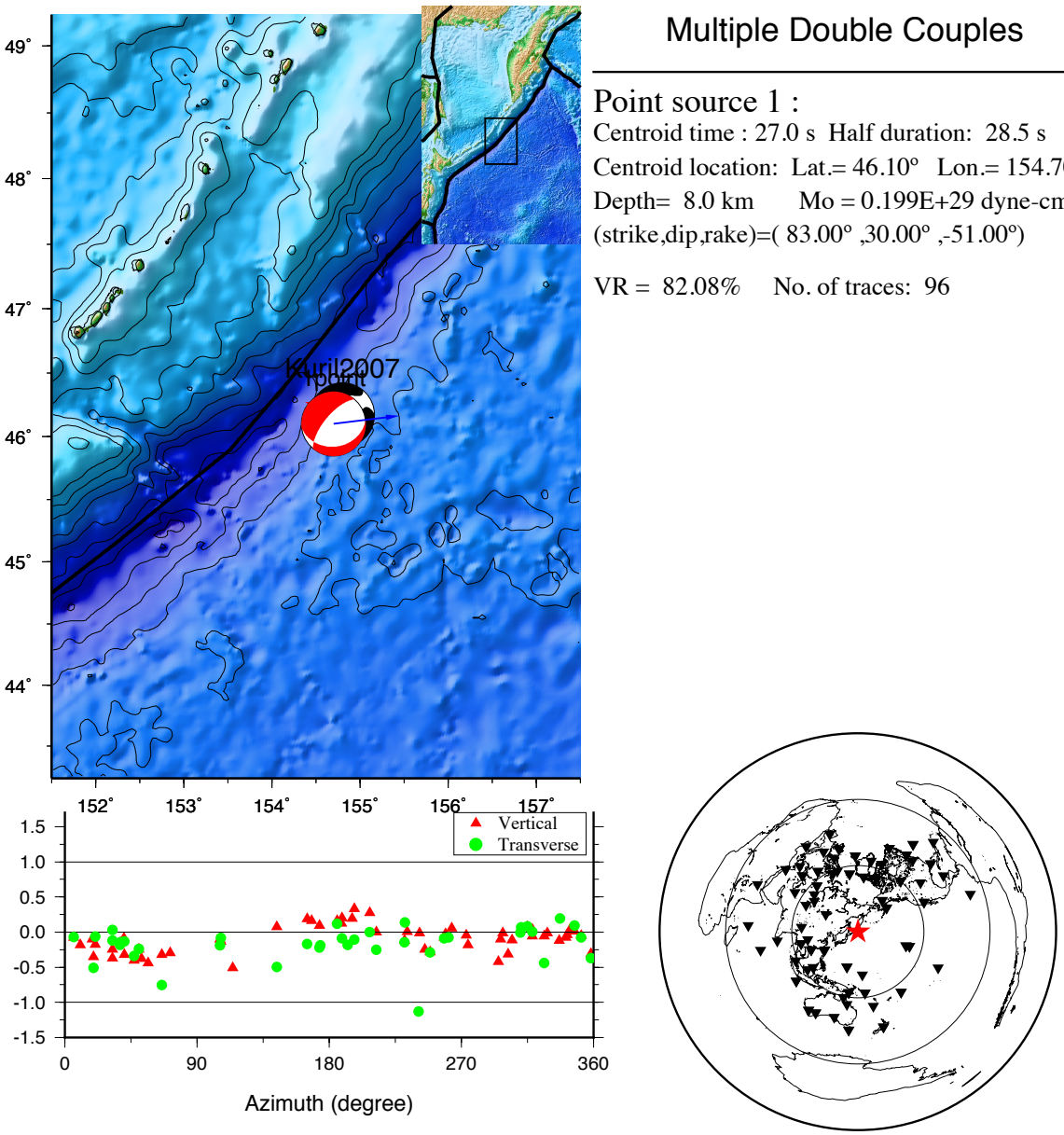

Figure S2.11. The best MDC model for the 2007 Mw 8.1 East Kuril island earthquake. The amplitude ratio (in log scale) and station distribution are shown below.

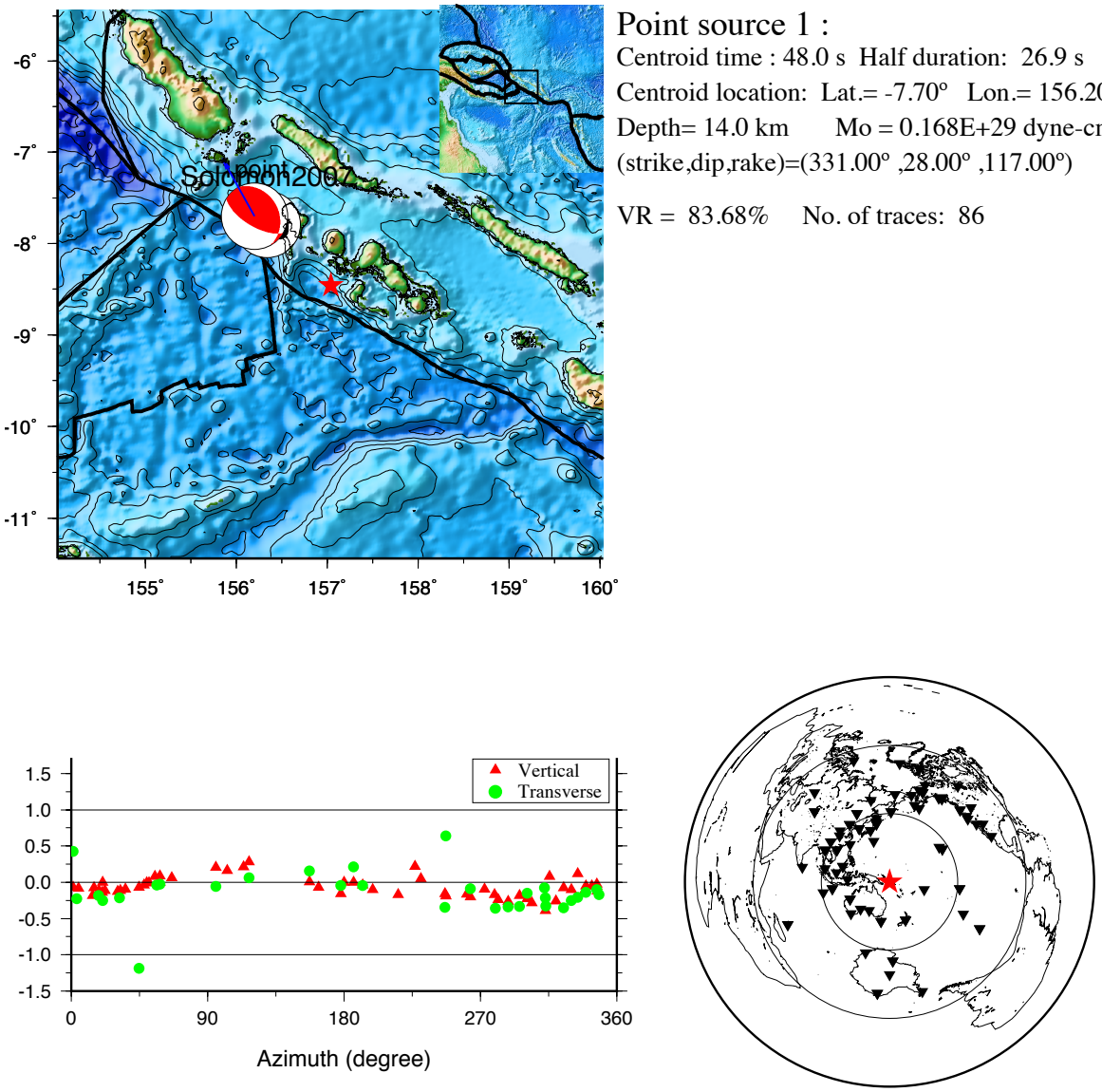

Figure S2.12. The best MDC model for the 2006 Mw 8.1 Solomon island earthquake. The amplitude ratio (in log scale) and station distribution are shown below.

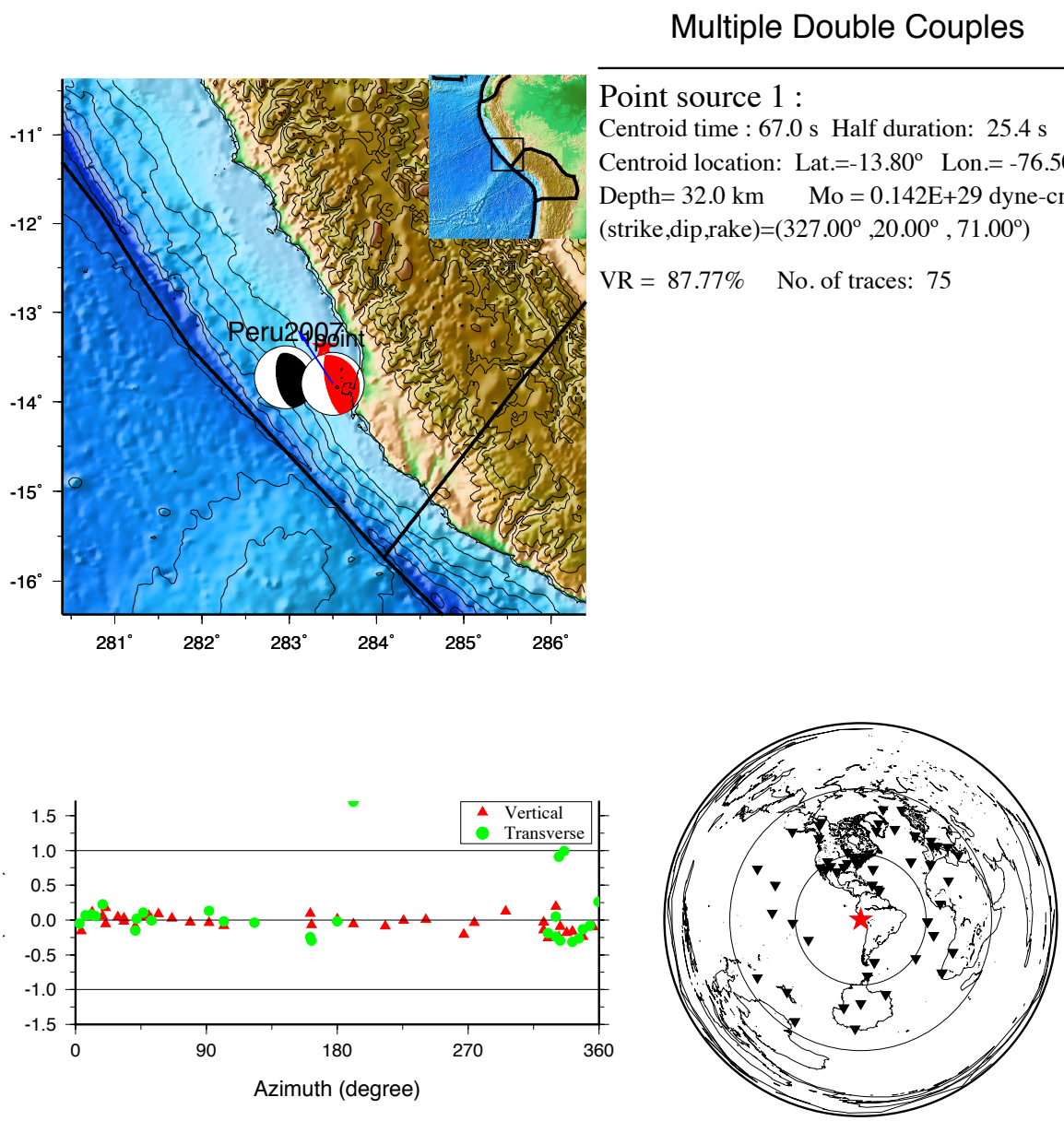

Figure S2.13. The best MDC model for the 2007 Mw 8.0 Peru earthquake. The amplitude ratio (in log scale) and station distribution are shown below.

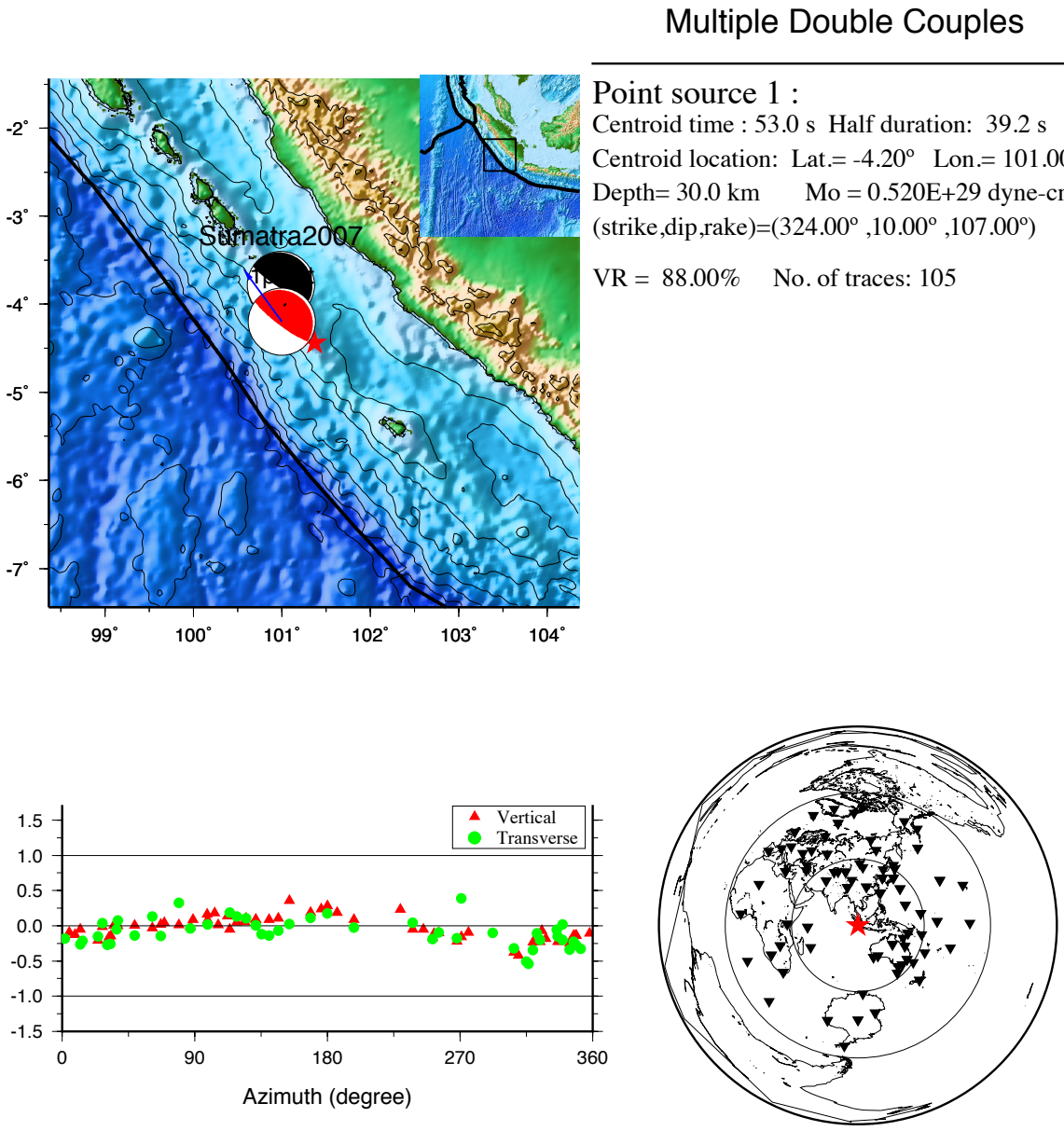

Figure S2.14. The best MDC model for the 2007 Mw 8.5 Southern Sumatra earthquake. The amplitude ratio (in log scale) and station distribution are shown below.

Chapter 3

Multiple point source modeling of the 2012 Mw 7.4 Honshu doublet using teleseismic data.

Abstract:

The 7 December 2012, Mw 7.3 Honshu earthquake doublet is studied with multiple double-couple and finite fault analyses using the teleseismic body waves and long-period waveforms. Our results reveal that this doublet initiated as an Mw 7.3 oblique thrust earthquake east of the Japan trench axis at a depth of ~50km. It was followed 12-13 s later and 45-50 km from the first event by a Mw 7.3 pure normal fault rupture at a depth 25-30 km west of the trench axis. The latter is located in the vacancy of its one-day aftershock region. The initial stage of the subevent rupture is well constrained, suggesting either abnormal large co-seismic stress drop even for intraplate earthquakes or abnormally fast rupture velocity. Further stress calculation indicates that the rupture of the 2011 Mw 9.1 Tohoku earthquake induced significant positive static Coulomb stress on the hypocenters of both events. However, the rupture of the first subevent produced a negative Coulomb stress perturbation at the hypocenter of the second subevent. While there is a good temporal correlation between the arrival of S wave radiated by the first subevent and initiation of the second subevent, the resulting dynamic stress is negative.

3.1 Introduction

On 7 December 2012, a large earthquake occurred near the Japan trench, 250 km east of the coast of Honshu. The epicenter was located ~20 km seaward (east) of trench axis by both United States Geological Survey (USGS) and Japan Meteorological Agency (JMA) (Figure 3.1). This location places the epicenter east of the portion of the plate interface where more than 50 m of coseismic slip occurred during the 2011 Mw 9.1 great Tohoku earthquake (e.g., *Shao et al.,* [2011]). White circles in Figure 3.1 represent the JMA aftershocks occurring within the first day. Besides a small cluster near the JMA mainshock epicenter, most are located at island side (west) of the trench axis 20-70 km to the west or west-southwest of the JMA mainshock epicenter. Earth Science and Disaster Prevention (NIED) further studied the moment tensors of large aftershocks in the next few months; most of these have normal-faulting focal mechanisms [*Lay et al.*, 2013].

It was quickly recognized that this event was doublet that included two subevents with different focal mechanisms; though the location of the second subevent is still debated. For instance, the JMA epicenter of the second subevent locates to the northwest (NW) of the epicenter of the first subevent (Figure 3.1). And according to the best double-couple solution inferred from its Global CMT (GCMT) solution, the first subevent is an Mw 7.2 inter-plate oblique thrust event with a centroid depth of 57.8 km, and the second subevent is an Mw 7.2 pure normal fault earthquake with a centroid depth of 19.5 km (Table 3.1). The difference in centroid times of these two subevents is less than 9 s. The GCMT centroid of the second subevent is directly beneath the trench axis, 35 km southwest (SW) of the centroid of the first subevent (Figure 3.1). *Lay et al.,* [2013] studied this earthquake using teleseismic P waves and W-phases. They found that an initial Mw 7.2 thrust faulting subevent with a

centroid depth of 60.5 km, followed 14.1 s later by an Mw 7.1 normal faulting subevent at centroid depth 19.5 km located 27 km to the south-southwest. The centroids of both subevents are seaside of Japan Trench axis and far from the locations of most aftershocks.

The occurrence of large thrust-faulting earthquakes within subducting plates in the outer rise (within the plate before it is subducted) are rare and have been observed to correlate with subsequent occurrence of great thrust events on the adjacent mega-thrusts [*Christensen and Ruff*, 1988]. The 2012 Honshu earthquake doublet provides a unique opportunity to study the relationship between the megathrust and such compressional outer-rise earthquakes. The dynamic interaction between these two subevents is also interesting. While recent studies suggest that the passing seismic waves can immediately trigger micro-earthquakes and non-volcanic tremor [*Gomberg et al.*, 2003; *Kilb*, 2003; *Rubinstein et al.*, 2007]. But temporal association between the arrivals of seismic waves excited by distant events and relatively large (M>5) earthquakes is rare [*Parsons and Velasco*, 2009]. In the region near the source, it is often difficult to distinguish the effects of static and dynamic Coulomb stress perturbations in triggering larger aftershocks, because they often rupture minutes to days after the mainshock. The importance of near-field dynamic stress change on modeling spontaneous ruptures of multi-fault has been emphasized by [*Harris*, 1998]. However, the accurate prediction of the induced time-dependent stress evolution highly depends on the spatial-temporal resolution of the source model, which might be extensively contaminated by the impending interaction between subevents. In this article, we tend to derive a model with the uncertainty of the most source parameters under sufficient control based on our recently developed inversion method. The computation of related static and

dynamic stress change would then shed light on whether the stress transfer and triggering mechanism could explain this interesting doublet.

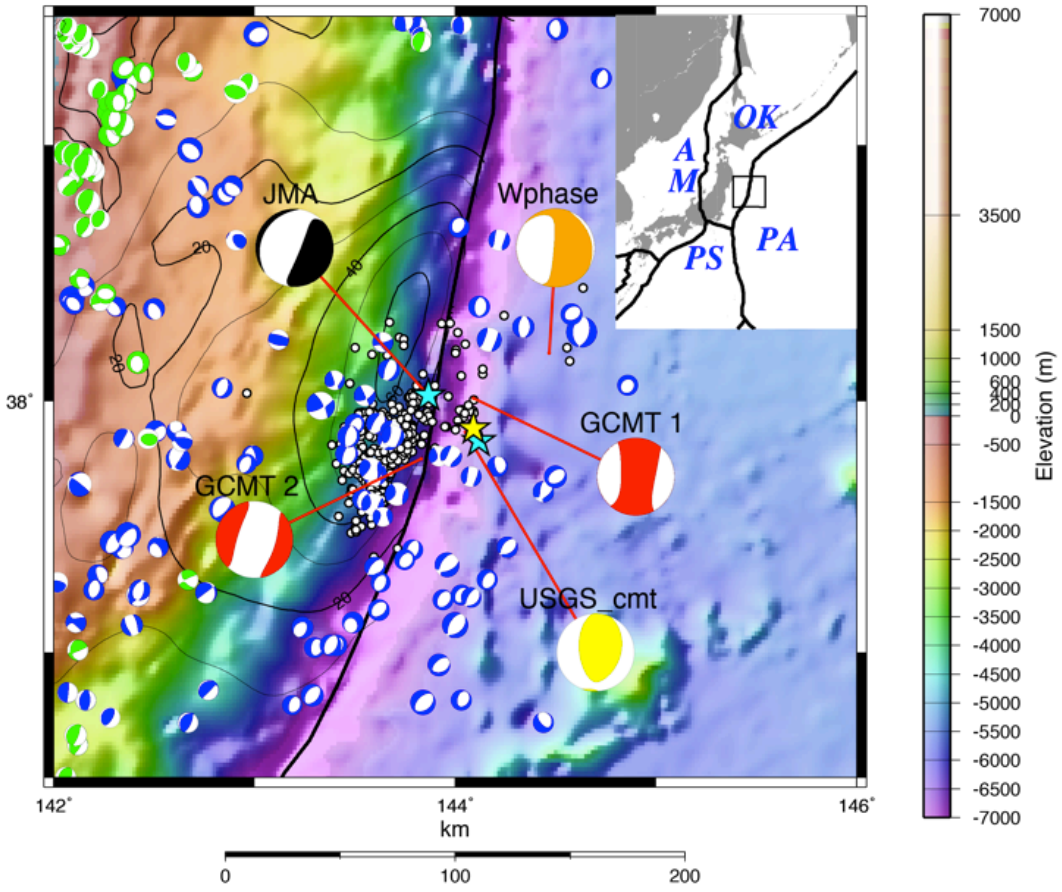

Figure 3.1: The December 7th 2012 Japan Trench earthquake doublet and background tectonic setting. The black contours indicate the co-seismic slip of the 2011 Mw 9.1 Tohoku earthquake with a maximum slip about 60 m. Small focal mechanisms represent Mw>5 events from GCMT catalog occurring from March 11, 2011 to December 7, 2012. The blue or green color denotes their centroid depths shallower or deeper than 30 km, respectively. The JMA and USGS hypocenters of the December 7th event are shown with red and blue stars. White circles represent the JMA aftershocks occurring within the first day after this event. Large "beach balls" are its inverted focal mechanisms reported by different agencies.

Note the big discrepancies among these solutions. Related plates including Okhotsk Plate (OK), Amur Plate (AM), Philippine Sea Plate (PS) and Pacific Plate (PA) are shown upper-right.

3.2 Multiple Double-couple (MDC) Analysis

Broadband records of 34 teleseismic stations of Global Seismographic Network (GSN) were downloaded from Incorporated Research Institute of Seismology (IRIS) data center. After removing their instrument responses, 26 vertical components and 20 transverse components were selected, according to signal to noise ratio and azimuthal coverage. The GCMT solution of this doublet shows pronounced CLVD components of 40% and 25% for its two subevents, respectively. It is then interesting to explore whether these abnormally large CLVD components are truly required to match the observations. Here we simply assume the complex rupture process of this doublet can be decomposed into one or two subevents with different double-couple mechanisms. By matching the teleseismic waveforms, we simultaneously invert for the centroid location, centroid time, strike, dip, rake and scalar moment M_o of each double-couple source.

3.2.1 Inversion of long-period waveforms

We start our investigation using long-period (3-6 mHz) seismic waveforms. While these data are less sensitive to the 3D heterogeneity in structure, they are also less sensitive to the details of the moment rate function. So we approximate moment rate function as a symmetric cosine function [*Ji et al.*, 2002a; b] with an empirical half duration of $2.26 \times 10^{-}$

$^{6}M_0^{1/3}$, where M_0 is the scalar moment in Nm [*Ekstrom et al.*, 2005a]. The total number of free parameters is $8N$, where N is number of point sources. We assume an anisotropic PREM Earth and calculate the synthetic seismograms using a normal mode superposition algorithm [*Dahlen and Tromp*, 1998].

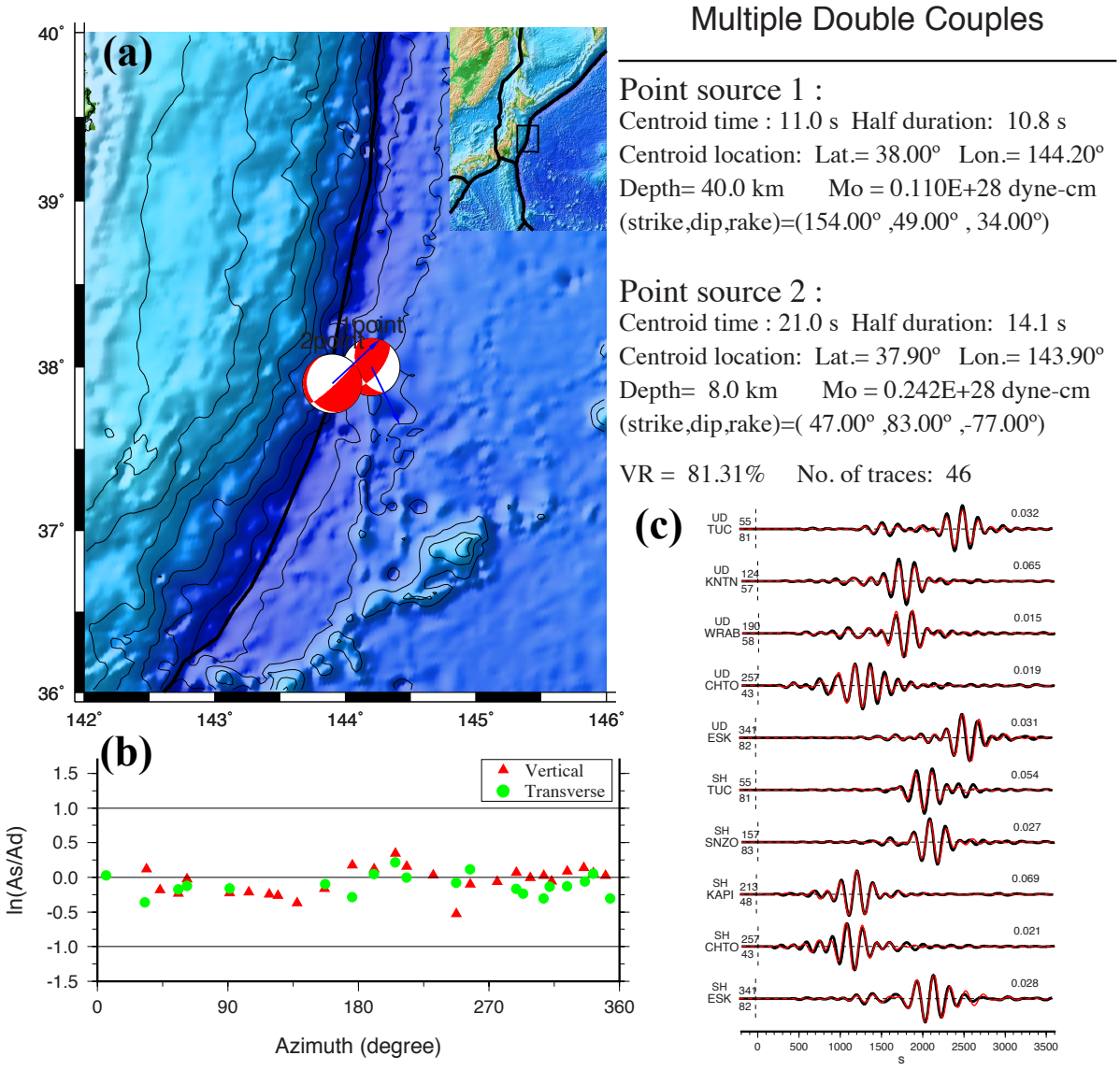

Figure 3.2: (a) Multiple double-couple (MDC) analysis using long-period (167s - 333s) waveform. The red beach balls represent the preferred MDC solution. Blue arrow denotes

the strike direction of the inferred fault plane. (b) The azimuthal variation of amplitude ratio in logarithmic format (ln (As/Ad)). Red triangles and green dots denote the vertical and transverse components, respectively. (c) Selected long-period waveform fit. The data are shown in black and the synthetics are plotted in red. The number at the end of each trace is the peak amplitude in millimeters. The number above the beginning of each trace is the source azimuth; the number below is the epicentral distance. Details of inverted focal mechanism of each point source using 46 traces with a variance reduction of 81.3% are summarized on the top right.

We first approximate the source with single double-couple, i.e., N=1, and soon find out that such an approximation is too simple to fully explain the long period observations. The best waveform fit achieved during this study has only a 37% variance reduction. As shown in Chapter 2, with an appropriate focal mechanism and 1D PREM synthetic response, such long period seismic waveforms should have a variance reduction of ~81%. This poor waveform match is, therefore, the strong evidence that the December 7th earthquake must have a source more complex than a single double-couple. We subsequently find by using just two double-couple sources to approximate this earthquake, the variance reduction dramatically increases to 81.3%. In contrast, our forward calculation suggests that the source model consisting of the best double-couples from GCMT solutions achieves a variance reduction of 70%.

The two double-couples obtained from this MDC inversion are hereafter referred as Point 1 and Point 2, summarized in Table 3.1 and shown in Figure 3.2. The model shows focal mechanisms and a temporal-spatial relation between two subevents similar to the

GCMT solutions, but the model has a larger total seismic moment (factor of 2.2) (Figure 3.2). Relative to the first thrust subevent, the second normal fault subevent initiated about 10 seconds later ~30 km southwest and ~30 km shallower. By extensively collecting the inverted solutions similar to the global optimal solution, we can approximate posterior a probability density of each parameter. We notice that the solution for each parameter of the first subevent (Point 1) is fairly stable. Similarly, most of parameters of the second subevent (Point 2) are fairly well resolved except for the depth and seismic moment, which display a significant trade-off. This trade-off can probably be attributed to the opposite focal mechanisms of the two subevents as well as the inherent insensitivity of long-period waveform inversion in determining the focal depth at a relatively short distance and with a short time window. Consequently, for this specific doublet, the long-period waveform inversion alone is unable to accurately constrain the focal mechanisms. Nevertheless the long period waves demonstrate the necessity for two subevents with different focal mechanisms.

Table 3**.** Source parameters of different solutions

Source of solution	**Centroid time (s)**	**Lat(°)**	**Lon(°)**	**Depth (km)**	**Mo (N.m)**	**Strike (°)**	**Dip (°)**	**Rake (°)**
GCMT #1	10.6	38.01	144.09	57.8	$7.9*10^{19}$	158	59	48
						38	51	138
GCMT #2	19.5	37.77	143.83	19.5	$7.7*10^{19}$	18	40	-90
						198	50	-90
Point #1	11.0	38.00	144.20	40.0	$1.1*10^{20}$	154	49	34
						40	65	134
Point #2	21.0	37.90	143.90	8.0	$2.4*10^{20}$	47	83	-77
						165	15	209
Source #1	2.0*	37.89	144.09	52.0	$2.0*10^{20}$	168	58	71
						21	37	117
Source #2	12.8*	37.82	143.54	25.0	$2.1*10^{20}$	26	47	-91
						207	43	-89

***** For Source #1 and Source #2, this is the inverted initial time rather than centroid time.

3.2.2 Inversion of teleseismic body waves

Our second analysis uses the teleseismic P and SH broadband waveforms. We have made two special changes to the model parameterization so that this inversion can take full advantage of the better spatiotemporal resolution provided by broadband seismic waveforms. First, the location of the *i-th* subevent is defined as (r_i,θ_i,h_i), where r_i and θ_i denote the offset and azimuth, respectively, of this subevent relative to the epicenter. h_i represents its depth. Using this representation and properly aligning the body wave arrivals from the hypocenter, the error caused by unmodeled 3D Earth structure can be limited. Such relative locations are then more precise than the absolute locations. Second, with broadband waveforms, it is possible to constrain the details of the moment rate function to some extent. So we have adopted a multiple time window approach. For the *i-th* subevent, its moment rate function $\dot{M}_0^i(t)$ is represented as $M_0^i * D_i(t)$:

$$D_i(t) = \frac{1}{\sum_{j=1}^{N} A_i^j} \sum_{j=1}^{N} A_i^j T[t - (j-1) * L - t_i^0] \qquad (11)$$

M_0^i is the scalar seismic moment of the i-th subevent; $D_i(t)$ is the normalized moment rate function; $T(t)$ is a symmetric triangle function with duration of $2 \cdot L$ and peak amplitude of $1/L$. N is the total number of triangles used. The maximum source duration is then $(N+1) \cdot L$. Both L and N need be assigned in advance. t_i^0 denotes the initial time of this subevent relative to the original time and A_i^j is amplitude coefficient. The inversion searches for appropriate t_i^0 and A_i^j using the same heat-bath algorithm mentioned earlier.

In this analysis, we adopt the USGS epicenter location as the reference point and use the waveforms of 24 P waves and 24 SH waves recorded at teleseismic distances ($30^o<\Delta<90^o$)

to constrain the MDC model. After removing the instrument response, we band-pass filtered these data from 2s to 330s. To enhance the resolution of SH waves, we use their velocity waveforms rather than displacement. We first align the P and SH waves by their first arrivals using USGS hypocenter and IASPEI91 travel-time table [*Kennett and Engdahl*, 1991] and later adjust the first arrivals according to the results of preliminary inversions. We doubly weight the P wave records during the inversion because SH waves usually have lower signal to noise ratio and an ambiguous arrival time. The synthetic waveforms are calculated using a 1-D layered velocity model (Figure 3.3) interpolated from the global CRUST2.0 [*Bassin et al., 2000*] with a 5.5 km water layer at the top.

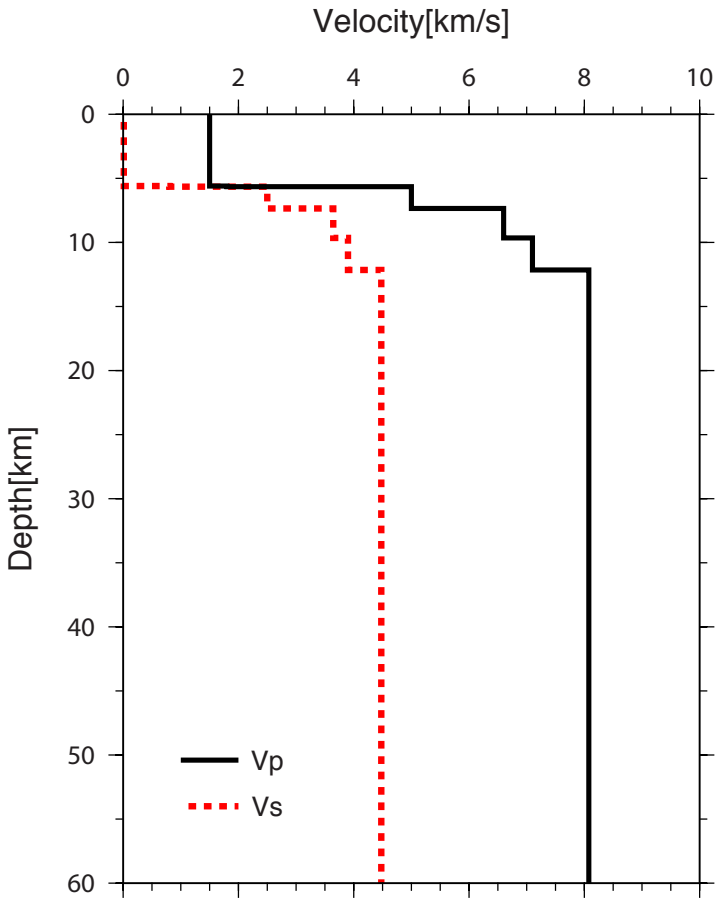

Figure 3.3: Velocity model for the crust.

The preferred MDC model is composed of two point sources (Source #1, Source #2), which are listed in Table 3; their centroid locations are converted into latitude and longitude. The focal mechanisms of the Source #1 and #2 are depicted in Figure 3.4, accompanied by examples of waveform comparison between synthetics and observation. The results suggest that this earthquake doublet initiated as an Mw 7.3 outer rise thrust subevent at 52 km depth. It was followed by an Mw 7.3 pure normal fault earthquake 45-50 km to the N261^{o}E, at a shallower depth of 25-30 km. The moment rate functions of the two subevents are shown in Figure 3.4. Temporally the rupture of the first subevent includes two well separated stages: a sharp pulse within first 10 s, followed 5 s later by a 30 s wide pulse (15 s to 45 s). The cumulative seismic moment during the first stage is 0.95×10^{20} Nm (Mw 7.25), just slightly smaller than that of the second stage (1.05×10^{20} Nm, Mw 7.28). Temporally the rupture of the Source #2 has three separate stages. The first stage starts at 12.8 s and ends 8 s later. The second stage starts subsequently and has a duration of 15 s. The third stage starts at about 39 s and ends 10 s later. The peak moment rates of these three stages are roughly the same. The seismic moment of the first stage is 0.5×10^{20} Nm (Mw 7.07). We notice two significant uncertainties associated with this solution. First, the starting time of the first stage is not well constrained. The rupture can initiate as early as 6 s but no later than 14 s. This reflects the fact that the seismic waveforms are insensitive to the slow onset. The range of this starting time can be significantly reduced if we define the rupture initiation time as time when the cumulative seismic moment is 5% of total subevent seismic moment. Furthermore, there is a trade-off between this rupture initiation time and the hypocenter depth of this second event. If we use a depth of 30 km instead, the initiation time will increase about 0.6 s. Secondly,

the moment release during the period 21 s to 40 s is composed of the second stage of two subevents. Their moments are then not well constrained, presumably due to the cancellation between thrust and normal fault responses. Finally, as shown in Figure 3.4, the second event yields strong P wave waveforms but its SH response is ignorable. The source parameters could be better constrained by combining the P wave and SH wave records.

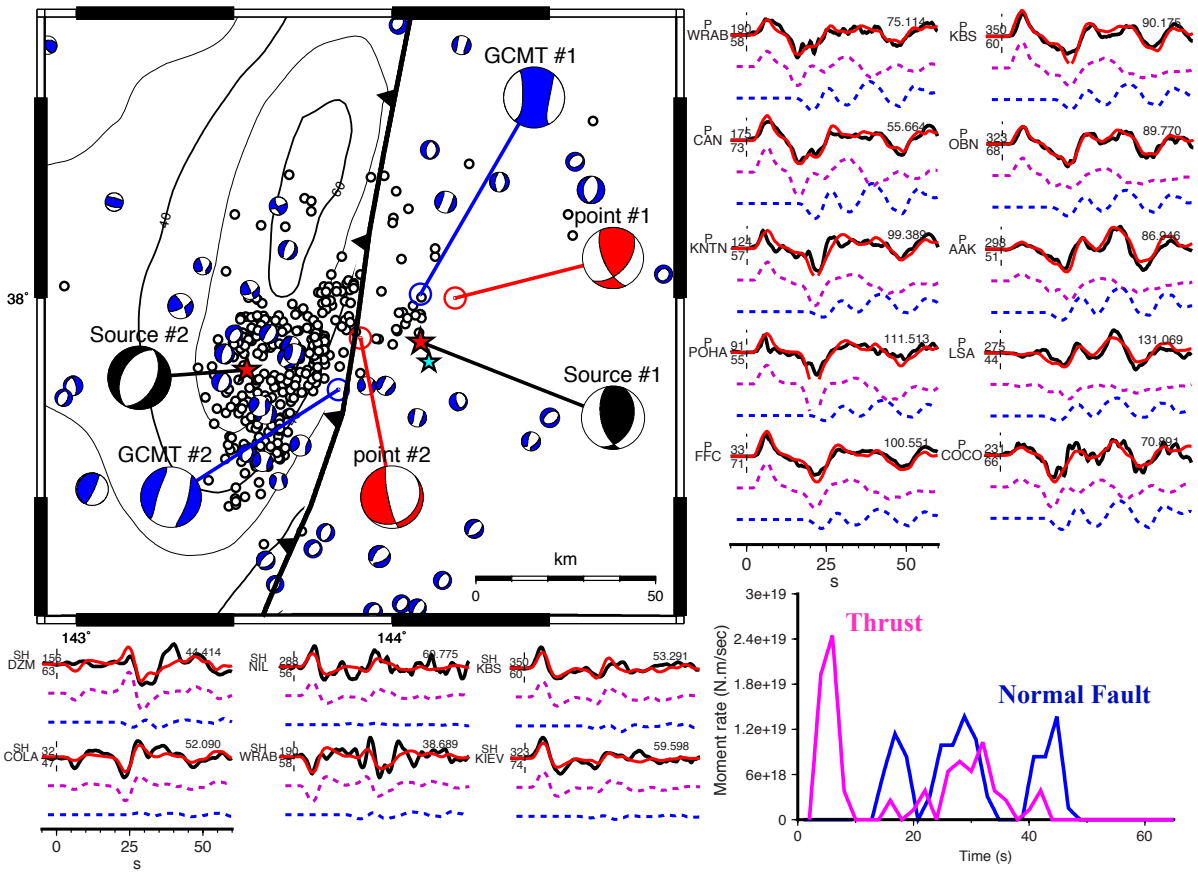

Figure 3.4: Inverted MDC focal mechanisms (black) and teleseismic waveform fit for the December 7, 2012 Mw 7.3 earthquake using broadband body waves. Corresponding MDC solutions of long period waveforms and GCMT moment tensor solutions are shown with red and blue beach balls. White circles represent the JMA aftershocks occurring within the first day after this event. The black contours indicate the co-seismic slip of the 2011 Mw 9.1 Tohoku earthquake. Small blue focal mechanisms represent Mw>5 events from GCMT catalog occurring from March 11, 2011 to December 7, 2012. Blue star and red stars represent the JMA hypocenters and our inverted centroid locations of two subevents using body waves. Waveform comparison of selected P wave (right) displacement seismograms and SH wave velocity seismograms (bottom) are given. Data and synthetics are plotted in black and red, respectively. The contributions of the first and second subevent are plotted in

pink and blue, respectively. The representative moment rate function is shown at the bottom right.

The cumulative moment release is 4.1×10^{20} Nm, which is similar to the results based on long-period waves, i.e., Point 1& Point 2, but about 2.5 times greater than that of GCMT solution. Because of the uncertainty mentioned above, this discrepancy is not robust. The seismic moment estimates of the first stage of the two subevents are relatively robust.

The focal mechanisms of the Mw > 5 events from GCMT catalog occurring from March 11, 2011 to December 7, 2012 are shown in Figure 3.4. Note that the extensional faulting is predominant beneath the high slip region (black contour) after the 2011 great Tohoku earthquake. Moreover, the epicenter of the second subevent of the body wave solution, which is more precise in location than the above solution based on long period data, fills in the vacant area that was surrounded by the first-day aftershocks and Mw>5 extensional faulting aftershocks of the 2011 Tohoku earthquake (Figure 3.4). In fact, considering the small offset between JMA and USGS epicenters (Figure 3.4), this argument holds even if we use the JMA hypocenter.

3.3 Finite fault inversion

We subsequently conduct a finite fault inversion using teleseismic body waves and long-period surface waves as used in the MDC analyses. Guided by the results of MDC body waves inversion, two rectangular fault planes are assigned. For the first subevent, we choose the nodal plane with a smaller dip angle of 37° (Table 3.1). Note that the orientation of this plane (strike = 21°) matches the strike of the adjacent trench axis better than auxiliary plane,

which has a strike of 168^{o} and a dip angle of 58^{o}. The fault plane has a dimension of 60 km (along strike direction) by 40 km (along dip direction), spanning a depth range from 39.0 to 62.7 km. The hypocenter depth is 52 km. For the second subevent, we use a 60 km (along strike direction) by 48 km (along dip direction) rectangular fault plane with a strike N26°E and dipping 47° east-southeast. The depth of hypocenter is 25 km. Each fault plane is discretized into 5km by 4km subfaults. The first fault has 120 subfaults, the second 144. Each subfault is sampled with 63 evenly allocated point sources to take into account the rupture across the subfault.

The waveform inversion was conducted in the wavelet domain. The same simulated annealing method was applied to simultaneously invert for the rake angle, slip amplitude, rupture initiation time and the source time function of each subfault [*Ji et al.*, 2002b; *Ji et al.*, 2003]. The synthetics of long-period waveforms are generated by means of the normal mode superposition algorithm. During the inversion, we assigned equal weight to the teleseismic P waves and long-period waves; we gave SH waves half the weight of the P wave and long-period waves.

Figure 3.5(a) shows a representative slip distribution. It reveals that the rupture of the first subevent is divided into two stages temporally. The rupture of the first stage is energetic. It nucleated at 52 km depth and then broke the surrounding area in less than 10 s. The cumulative seismic moment during this period is 6.7×10^{19} Nm, yielding an Mw of 7.15. The rupture has essentially ceased from 10 s to 23 s. The second stage initiates at 23 s and extends in the up-dip direction for another 17 s. The peak moment rate duration this stage is only 20% of that during the first stage. The cumulative seismic moment during this period is 3.0×10^{19}, or a moment magnitude of 6.9. The peak slip is 3m.

The rupture of the second subevent is complicated. Most fault slip is distributed on two isolated asperities, right beneath the high-slip region of the 2011 great Tohoku earthquake (Figure 3.5(b)). The failure of the first asperity initiated at about 12 s and temporally includes two stages. The first stage is energetic. It has duration of 8 s and seismic moment of 2.5×10^{19} Nm (Mw 6.86). The second stage initiates roughly at 22 s and has duration of 10 s. The seismic moment is 4.0×10^{19} Nm. The second asperity locates 20-30km northeast of the first one, with a centroid depth of 40 km. Its rupture occurs between 40 s and 50 s. The peak slip of both asperities is about 2.5m. We should highlight that the rupture history of the finite fault model is consistent with our MDC analysis using body waves, though the cumulative seismic moment is smaller. Total seismic moment is 2.87×10^{20} Nm. Nevertheless, the passive interaction between two subevents is amplified by the spatial-temporal proximity of their slip distributions in our model, which again inhibits us from better constraining their slip history after 20 s. The structural heterogeneity near the trench axis and water reverberation also increase the uncertainty of inverted late slip. Thus further discussion focuses on the first rupture stage of two subevents.

Lay et al. [2013] studied this earthquake using teleseismic P wave and W-phase. Their P wave analysis revealed three subevents. Though there are big discrepancies in the subevent locations and focal mechanisms, the centroid times and magnitudes of their first two subevents are consistent with the first rupture stages of our two subevents. The centroid time and magnitude of their third subevent is consistent with the failure of the second asperity of the second subevent. The location of their second subevent is at 27 km N208.4^{o}E of the USGS epicenter.

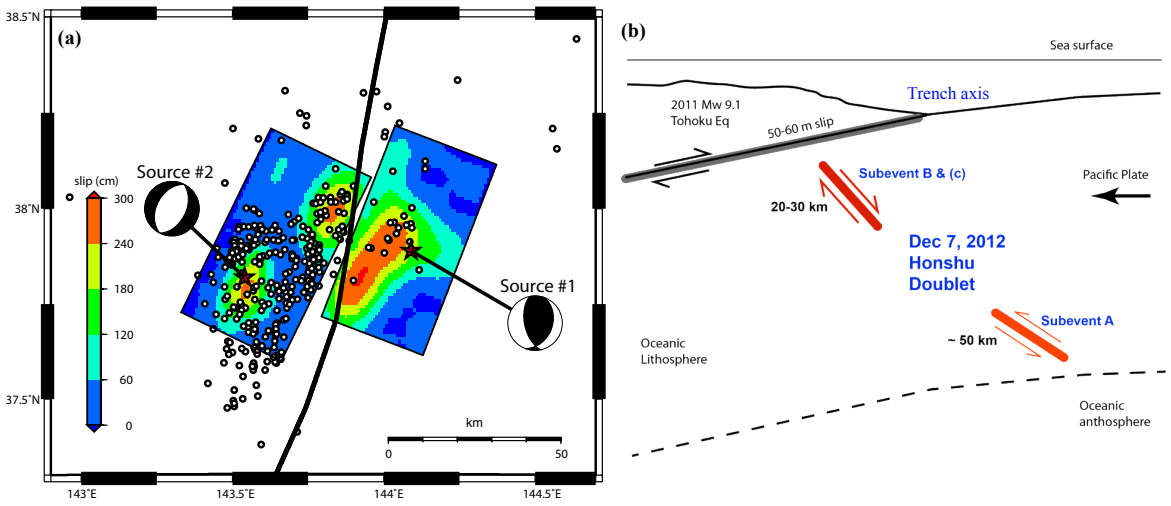

Figure 3.5: (a) Surface projection of the slip distribution. The black line indicates the major plate boundary [*Bird*, 2003]. Red star, white circles and beach balls are the same with Figure 1. (b) Synopsis of the December 7th Mw 7.3 doublet.

3.4 Coulomb stress calculation

Based on the finite fault model of the specified master fault plane, the Coulomb failure function (CFF) at a receiver point on a target fault plane can be calculated to evaluate the possibility of static or dynamic triggering.

3.4.1 Static stress change caused by the 2011 great Mw 9.1 Tohoku earthquake

Since the 2012 December 7th Japan trench doublet took place in the vicinity of the high-slip region of the 2011 great Mw 9.1 Tohoku earthquake, we first calculated the static Coulomb stress perturbation caused by this great earthquake with respect to the fault planes used in our inversion of the 2012 doublet. We use the slip model of Phase 3 in [*Shao et al.*,

2011] for the 2011 Mw 9.1 master event. For the target faults, we apply the source mechanisms and hypocenters of Source #1 and Source #2 (Table 3.1). The static stress change was computed using the Coulomb 3.3 software [*Lin and Stein*, 2004; *Toda et al.*, 2005] with a homogeneous half-space model. We used a generic value of 0.4 for the apparent friction coefficient μ′;Young's modulus was adjusted from 8.0×10^4 MPa to 1.7×10^5 MPa to reconcile with the adopted velocity structure. Hence, the amplitude of calculated stress perturbation has an ambiguity of 2.1.

Our calculation indicates that the 2011 Tohoku earthquake produced a positive static Coulomb failure stress perturbation at the hypocenters of the two subevents of the 2012 Honshu doublet (Figure 3.6(a) and 3.6(c)). The estimated stress increases are approximately 3 MPa at the hypocenter of the thrust subevent and 15 MPa at the hypocenter of normal fault subevent. We have also investigated the effect of the apparent friction coefficient μ′. We found that because the induced shear stress changes are much greater than the normal stress changes, the final Coulomb stress changes are not sensitive to the selected value of the apparent friction coefficient. With the value of μ′ ranging from 0.1 to 0.7, the stress change at the hypocenter of the first event would change from 2.9 to 3.2 MPa; at the second hypocenter the change is from 15.6 to 14.6 MPa. Such large positive Coulomb stress changes induced by the great 2011 Tohoku earthquake will facilitate the failure of these two subevents.

Figure 3.6 (b) and Figure 3.6 (d) show the corresponding Coulomb stress perturbations along vertical cross-section AB and A'B', which are perpendicular to the strike of the 2010 Tohoku earthquake but across the epicenters of two subevents, respectively**.** For the oblique thrust focal mechanism of the first subevent, the static Coulomb stress increase occurs

beneath the up-dip edge of the high slip patch, at depth below about 20 km. The prominent Coulomb stress increase that facilitates the rupture of the second subevent occurs in the region adjacent to the trench axis at a depth shallower than 25 km. The region then bifurcates into two zones laterally and extends to deeper region with gradually decreasing amplitude.

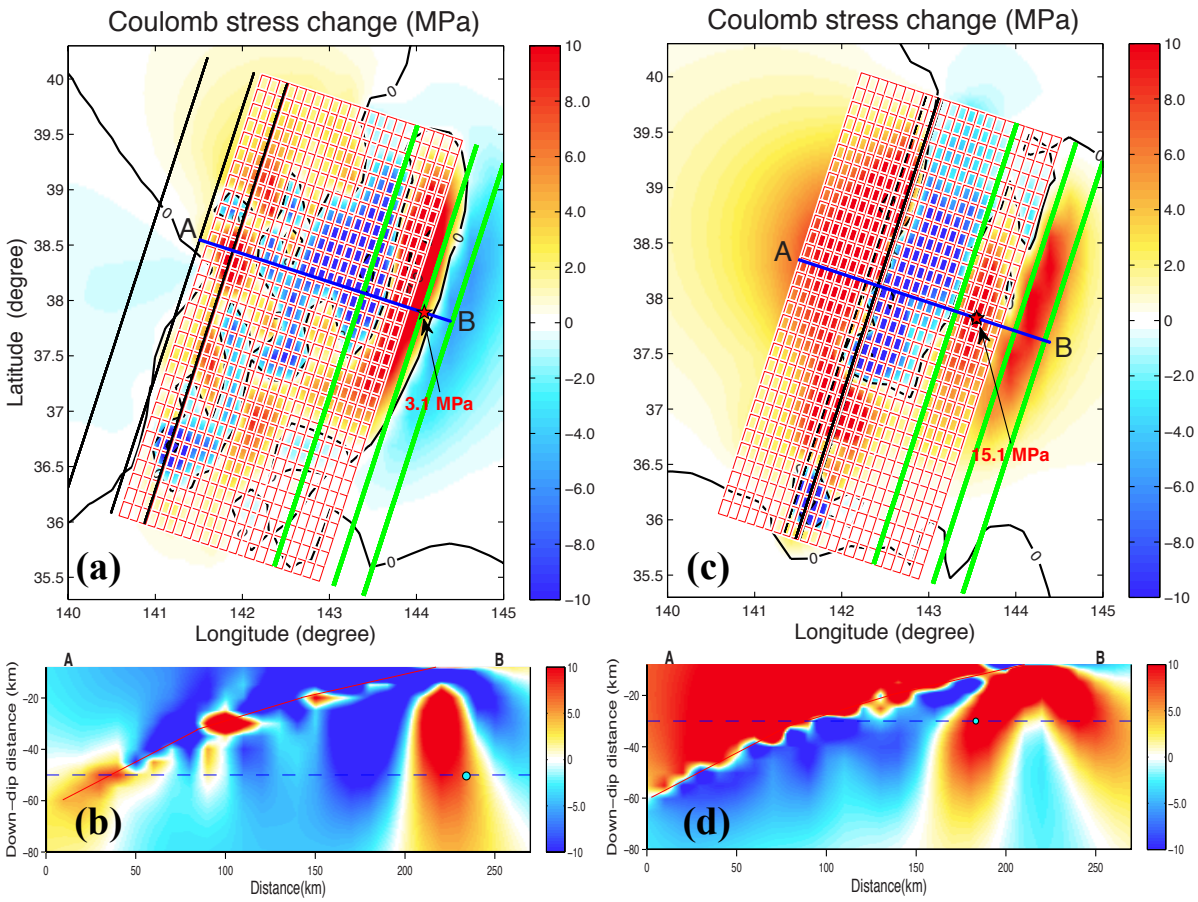

Figure 3.6: (a) Static Coulomb stress change caused by the 2011 Mw 9.1 Tohoku earthquake. The target receiver fault plane has the same focal mechanism with the first thrust subevent and locates at a depth of 50 km. The red star indicates its hypocenter, at

which the static Coulomb stress increases about 3 MPa. The contour indicates the static Coulomb stress change of zero and the grids show the fault plane structure. (b) Cross section view of static Coulomb stress change caused by the first subevent from A to B. The blue dot denotes the hypocenter. Coulomb 3.3 software package and half-space earth model are used in this calculation. (c) Similar to (a) but uses the focal mechanism of the second normal fault subevent as the target receiver fault plane. The static Coulomb stress increases about 15 Mpa at the corresponding inverted centroid location with a depth of 30 km. (d) Similar to (b) but uses the focal mechanism of the second normal fault subevent as the target receiver fault plane.

3.4.2 Static and dynamic stress perturbations excited by the first thrust event (Source #1)

In order to probe the dynamic stress evolution exerted by the first thrust event on the fault plane of the second normal fault event, we used the FK method [*Zhu and Rivera*, 2002] and our slip model of the first thrust event to compute seismograms at points surrounding the hypocenter of the second subevent. We used the oceanic homogeneous layered velocity structure (Figure 3.3) to compute the Green's functions, which were low-passed at 1s. We then calculated the strain in the vicinity of source region. The spatial interval was 2 km in the horizontal direction and 0.5 km in the vertical direction. The six components of the stress tensor were subsequently computed and projected onto the direction of normal stress and shear stress, based on the strike, dip and rake angle of the target fault. Consequently, we can obtain the time-dependent Coulomb failure function using equation 5.

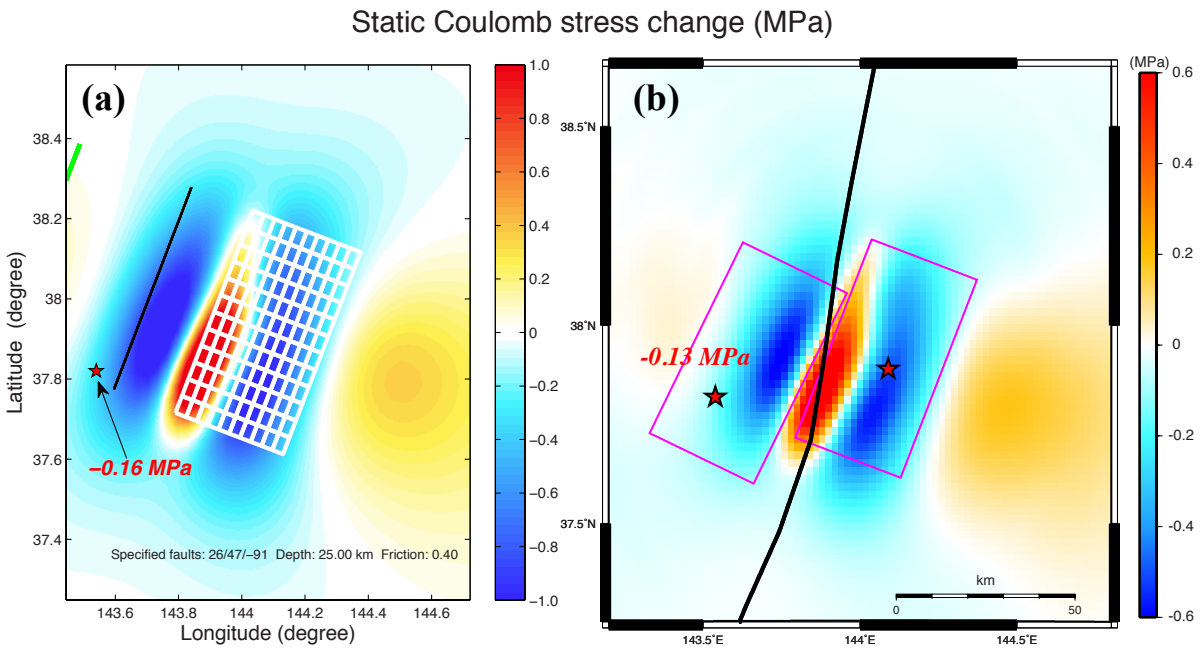

Figure 3.7: Comparison of the static Coulomb stress change caused by the first thrust subevent of 2012 Japan Trench doublet. The inverted slip model in Figure 2a is used. The target receiver fault plane, at a depth of 25 km, has the same focal mechanism as the second normal fault subevent. The red star indicates its inverted centroid location. (a) The results are calculated by the Coulomb 3.3 software package. The static Coulomb stress decreases about 0.16 MPa based on the half-space model. (b) Using the FK method and the homogeneous layered model, we compute a static stress change of -0.13 MPa. Note this approach also could compute the dynamic stress change.

First we investigate the static Coulomb stress change caused by the first subevent on the normal faulting fault plane at depth of 25 km. Figure 3.7 (a) shows the static Coulomb stress calculated using Coulomb 3.3 software. Figure 3.7(b) shows the results using the layered Earth model. It can be seen that the difference in velocity model does not change the spatial pattern of static Coulomb stress field. And in both cases, the hypocenter of the normal fault

subevent falls in the regions with negative Coulomb stress change (Figure 3.7). However, the amplitudes predicted using the layered model is smaller.

In Figures 3.8(a) and 3.8(b), we inspect the dynamic stress perturbation at the hypocenter of the second subevent, calculated using more realistic layered velocity model (Figure 3.3). Two solutions are presented. According to our kinematic analysis, the initiation of the second subevent is 12.8 s in our preferred model and cannot be later than 14 s. Further accounting on the propagation time of P wave (~6.8 s), it is clear that only the first 5 or 8 s rupture of the first subevent needs be considered. First we simply assume that the first subevent is a point source at its PDE location with seismic moment of 6.7×10^{19} Nm. The moment rate function is a truncated cosine function with duration of 10 s (Figure 3.8(c)). Both are simplified from the inverted slip model. Figure 3.8 (a) shows the waveform of the Coulomb stress perturbation using an apparent friction coefficient of 0.4. The vertical solid and dotted lines represent the predicted arrival time of P wave (7 s) and S wave (12.5s), respectively. Following the arrival of P wave, the Coulomb stress perturbation starts to gradually decrease and reach its maximum amplitude of -0.2 MPa slightly after S wave arrives. It then increases quickly and reaches a maximum amplitude of 0.18 MPa at 16 s. However, when the second subevent is initiated at 12.8 s, the dynamic Coulomb stress has its negative peak amplitude. Next we use the finite fault model of the first subevent to calculate the dynamic stress perturbation. The result is shown in Figure 3.8(b). The waveform of Coulomb stress perturbation has more structure and much larger peak amplitude than the estimate from the point source model. The Coulomb stress reaches its negative peak of -0.25 MPa at 13.5 s. From there it increases to 0 MPa at 14 s and reaches the first positive pulse of 0.6 MPa at 14.5 s—1.7 s after the initiation of the second subevent.

While it is important to take into account the fault geometry, rupture complexity and slip distribution in calculating the induced dynamic stress evolution, the conclusion here is that the initiation of the second subevent is temporally correlated with negative dynamic Coulomb stress perturbation.

In Figure 3.8(b), we also present waveforms for shear (blue dotted line) and normal (red dotted line) stress changes. The Coulomb stress perturbation is dominated by the shear stress change. It is noteworthy that for the time period for which we are interested (t<14s), the polarity of shear stress and extensional normal stress waveforms are same. Therefore, the value of μ' would not affect the analysis.

We have to point out that the 1.7 s difference between the initiation of the second subevent and the peak of the first positive stress pulse is, in fact, compatible with the uncertainty of our above kinematic modeling. For instance, if the hypocenter of the second subevent is set at a possible greater depth of 30 km and closer distance of 45 km, the arrival time of S wave would be 1.1s earlier at 13.4 s. Because of the trade-off between the hypocenter depth and initiation time, the inverted rupture initiation time of the second subevent would be 0.6 s later at 13.4 s. Thus the initiation of the second subevent is coincident with the peak of positive Coulomb stress peak carried by S wave. Furthermore, increasing the mantle velocity would reduce the discrepancy by 0.25 seconds per 0.1 km/s change in the mantle velocity.

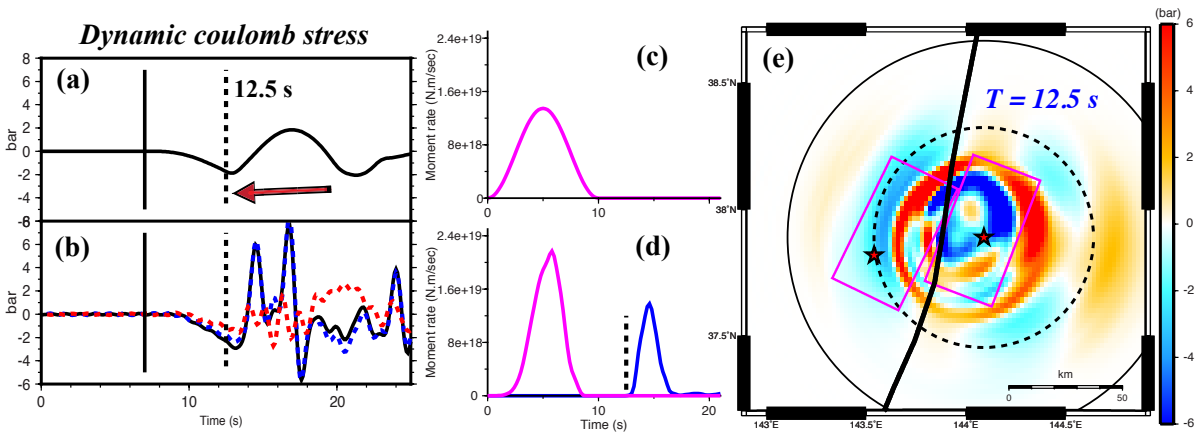

Figure 3.8: (a) Time series of the dynamic Coulomb stress caused by the first thrust subevent (modeled as a point source) experienced at the centroid location (37.82°N, 143.54°E) of the second normal fault subevent. Layered model (Figure S3) is used. The vertical solid line and dotted line represent the predicted arrival time of P wave and S wave. We assume a single point source with duration of 10s having the same focal mechanism, hypocenter and seismic moment as the first 10s of the thrust subevent. The corresponding moment rate function is given in (c). (b) Similar to (a) but caused by the finite fault model for the thrust event. The red and blue dotted time series denote the related normal and shear stress. The moment rate function of the first 20 seconds is given in (d). (e) Dynamic Coulomb stress field generated from the first thrust subevent about 12.5 seconds after its nucleation using the fault plane solution of the second normal fault subevent. The dotted and solid circles represent the predicted wavefront of S wave and P wave at 12.5 s..

3.5 Discussions

The 2012 Honshu doublet provides a unique opportunity to study the dynamic interaction between the megathrust and compressional outer-rise earthquakes. The occurrence of large thrust-faulting earthquakes within subducting plates seaward of the trench are rare. Such events have been observed to correlate with subsequent occurrence of great thrust events on the adjacent megathrusts [*Christensen and Ruff*, 1988]. Our stress calculation indicates that the 2011 Tohoku earthquake induced a large positive stress perturbation of 3.5 MPa at the hypocenter of the outer rise thrust earthquake. This stress perturbation is of the same order as the global average stress drop during earthquakes—3 MPa, [*Kanamori and Anderson*, 1975]. Of course, the exact value of the perturbation will depend on the velocity model and finite fault model used. The Coulomb stress perturbation at the second normal fault subevent is more than four times larger. We are curious whether such large an induced stress perturbation reversed the local stress field and led to these events. To answer this question, it is crucial to understand the coseismic stress drop of two subevents.

Because of the strong interference between these two subevents, estimates of the stress drop based on the inverted slip distribution could be biased. Here, we limit our attention to the rupture during the first 20 s and use an empirical relationship between seismic moment and stress drop. For the first subevent, the inverted seismic moment for the first 10 s is 0.67-0.95x10^{20} Nm. Using the empirical half duration formula (2.26x$10^{-6}M_0^{1/3}$, where M_0 is the scalar moment in Nm, [*Ekstrom et al.*, 2005b]), the estimate of the empirical duration of this subevent is 18.3-20.6 s. The apparent duration of moment rate function is about 9 s. Further adopting a circular fault approximation [*Brune*, 1970], the stress drop is proportional to T^{-3},

T is rupture duration. The stress drop is then 8.4-12.0 times the global average stress drop (~ 3 MPa), or about 25-36 MPa. This co-seismic stress drop is one order of magnitude larger than the induced Coulomb stress due to the 2011 great Tohoku earthquake. Hence, the most of the stress loading in this region occurred before the Tohoku megathrust earthquake. For the second subevent, the inverted seismic moment during the rupture from 12s to 20 s is $0.25\text{-}0.5\text{x}10^{20}$ Nm. Using the same empirical approach the stress drop during this period is 13.5-26.8 MPa. This estimate of co-seismic stress drop is considerably larger than the induced Coulomb stress but similar to the first event (in the same order).

It is noteworthy that these estimates are significantly larger than the globally average stress drop of intraplate earthquakes (~6 MPa, [*Allmann and Shearer*, 2009]). The estimated stress drop of the first subevent is abnormally high even compared with three other Mw>7 intraplate deep thrust earthquakes since 2006 beneath outer rise region of subducting plates [*Lay et al.*, 2013]. The biggest uncertainty associated with these estimates is the assumption of the rupture velocity, which is 3 km/s. If we use mantle shear wave velocity (4.5 km/s) for the rupture velocity, the estimated stress drop would be divided by 1.5^3~3.4. After this correction the estimates are roughly equal to globally average stress drop of intraplate earthquakes. Hence, the ruptures of these two subevents are associated with either abnormally high stress drop or abnormally high rupture velocity. Unfortunately we cannot differentiate between these two possibilities. It is of interest to note that the value of USGS energy magnitude (M_e) is 8.3 for this earthquake [*Lay et al.*, 2013]. It suggests that the seismic radiated energy of this event is 32 times larger than the global average of Mw 7.3 earthquakes.

Note that the blue focal mechanisms (Figure 3.4) are the Mw>5 earthquakes occurring during the period of March 11, 2011 and December 7, 2012, i.e. the aftershocks of the 2011 great Tohoku earthquake. Nine events surround the epicenter of the second subevent. Most have normal faulting focal mechanisms. *Lay et al.* [2013] further pointed out that most aftershocks (open circles) have normal faulting focal mechanisms according to NIED CMT catalog. The observations that the second subevent is associated with high stress drop and is surrounded by the foreshocks and aftershocks with similar focal mechanisms are likely correlated. It might suggest that its co-seismic fault plane might have relatively high yield stress. The occurrence of 2011 great Tohoku earthquake dramatically increases the stress level and brought this region of the subducting plate closer to failure. The regions that are relatively weak could fail earlier in either seismic events or aseismic creeping; both processes could further increase the stress level of this stronger part of the system. The passage of seismic wave excited by the first subevent then eventually led to its rupture.

3.6 Conclusions

We implemented the multiple double-couple (MDC) analysis for the 2012 December 7th Japan Trench earthquake doublet. Long-period surface wave and teleseismic body waves were independently employed in the MDC inversions. For the long-period seismograms, the waveform fit could be significantly improved by using a double-couple model consisting of an outer-rise thrust subevent and an intra-plate normal fault earthquake about 10s later. The strong negative interference between the focal mechanisms of these two events prevents us from accurately deriving the relevant source parameters from the long-period waveform inversion alone. This difficulty can, to a large extent, be settled by performing the MDC

inversion using teleseismic P and SH waves. The proposed MDC model based on the teleseismic body waves indicates that this earthquake doublet is composed of a Mw 7.3 outer rise thrust dominated subevent at 52 km depth and a Mw 7.3 intra-plate pure normal fault earthquake 45-50 km west-southwest at a shallower depth between 25 and 30 km. The inverted initial time of the second subevent is about 12.8s, but it has an uncertainty range from 6 to 14s.

Details of the slip history and rupture complexity were further resolved by our finite fault inversion. The source model with a total moment release of 2.87×10^{20} Nm revealed that the second normal fault subevent probably initiated about 12.8s after the first thrust event. The first event had an energetic moment release during the first 10s and then slowly ruptured upwards. The slip distribution of the second subevent right beneath the high slip region of the 2011 Mw 9.1 Tohoku earthquake can be divided into two asperities. The first initiated southwest at a depth of 25km was well determined, while the second event ruptured 20-30 km northeast at a deeper part about 20 s later. The relative location of the two patches agrees well with their aftershock area. We should point out that the slip history about 20s after the initiation of the first event has large uncertainty due to the ambiguous passive interference between two subevents.

We have computed the static stress field produced by the 2011 Mw 9.1 Tohoku earthquake on the fault planes of these two subevents using a half-space model. The estimated Coulomb stress is significantly raised by about 3 MPa on the hypocenter of the first event and about 15 MPa on the hypocener of the second normal fault subevent. We note that the aftershocks of this doublet and the extensional faulting of Mw >5 after the Mw 9.1 earthquake are all located in the regions of high static stress increase. With this perspective,

we infer that the intra-plate and outer-rise extensional faulting as well as the deeper inter-plate compressional thrust are spatially favored by the positive static stress pattern after the great megathrust. Nevertheless, the static stress change caused by the first thrust subevent on the fault plane of the second normal fault earthquake using the half-space and homogeneous layered velocity structure both render gentle negative value of the order of -0.1 MPa adjacent to the nucleation region of the second subevent. This result, as well as the comparable short spatial-temporal separation between two subevents, motivates us to further investigate the dynamic stress evolution in response to the rupture of the first thrust. The calculation of the corresponding time-dependent Coulomb failure function reveals an unequivocal correlation between the rupture initiation of the second subevent and the arrival time of S waves radiated by the first subevent. The predicted Coulomb stress change at the hypocenter of the second subevent during the passage of the S wave is negative with amplitude of about -0.3 MPa; this is followed by a positive peak amplitude of 0.6 MPa two seconds later. Small adjustments of the depth and location of the receiver point of the second subevent would not affect this characteristic. However, we should admit that our results are band-limited with frequencies less than 1 Hz. Thus we could not rule out the potential positive stress perturbation at higher frequencies that we cannot resolve. Based on our modeling results, it is explicit that the 2011 great Tohoku megathrust induced strong background static stress increase in the source region of the 2012 December 7 Japan Trench doublet, and therefore brought the specified faults close to failure. The first Mw 7.3 inter-plate thrust mainshock at the bottom of the subducting plate dynamically triggered the impending Mw 7.3 normal fault event 50 km away inside the trench with a negative Coulomb stress perturbation.

Chapter 4

Dual ruptures during the 2000 Mw 8.0 New Ireland earthquake: evidence of dynamic triggering of a normal fault earthquake by a strike-slip event

Abstract

We revisit the 16 November 2000 Mw 8.0 New Ireland earthquake and aim to explain an abnormal later phase that dominates nearly all of its teleseismic P wave records. Our result reveals that the 2000 New Ireland earthquake is a doublet. We first adopt a P wave back-projection analysis to estimate its centroid location and centroid time. Next we use long period (2-6 mHz) seismic waves to constrain its focal mechanism using MDC analysis. Finally we combine broadband body waves and long-period surface waves to retrieve a plausible slip model. In the doublet the first event propagates primarily southeastward ~130-km on the Weitin transform fault. This event has a duration ~73 s with an average rupture velocity ~2.5 km/s. It has a seismic moment of 1.1-1.2×10^{21} Nm (M_w = 8.0), with two-thirds of its moment released between 25 and 60 s on a 70-80 km long asperity, coincident with the New Ireland segment of the Weitin Fault. The second event, with a moment of 0.15×10^{21} Nm (M_w = 7.4), initiated about 263 km south-southeast of the epicenter of the first event. About 90 s - 105 s with respect to the initiation of the first subevent, the second subevent occurred on a normal fault located on the outer-rise region of the Solomon Sea Plate next to San Cristobal Trench. The hypocenter of the second event locates in a region with negligible

static Coulomb failure stress resulting from the first event. However, the dynamic stress perturbation caused by the first event caused a nearly instantaneous triggering of the second event with a negligible delay.

4.1 Introduction

Eastern Pagua New Guinea locates near the triple junction of the north and south Bismarck Plates, and Solomon Sea Plate (upper-inset, Figure 4.1). Geodetic studies revealed fast subduction of the Solomon Sea Plate along the New Britain Trench and San Cristobal Trench, as well as quick left-lateral strike-slip motion between the North and South Bismarck Plates along the Weitin-Kamadaru fault system [*Bird*, 2003; *Tregoning et al.*, 1999]. Accompanied with the fast and complicated tectonic motions, eastern Pagua New Guinea is one of the seismically most active regions in the world.

November 16, Mw 8.0 New Ireland earthquake was the globally largest earthquake in year 2000. According to the Global Centroid Moment Tensor catalog (GCMT, *www.globalcmt.org*), the New Ireland earthquake was dominated by left lateral strike-slip motion on a fault plane orienting N328^{o}W and dipping 42^o northeast. The strike is consistent with the segment of the Weitin Fault inside the New Ireland Island. *Finlayson et al.* [2003] reported a 5.5 m surficial slip across this fault. The GCMT solution includes a notable non-double-couple component with a $\boldsymbol{\varepsilon}$ of -0.15 (ε here is defined as $-\lambda_2/\max(|\lambda_1|, |\lambda_3|)$, $\lambda_1, \lambda_2, \lambda_3$ are eigenvalues of the moment tensor, ordered such that $\lambda_1 > \lambda_2 > \lambda_3$, *Nettles* and *Ekstrom* [1998]). The mainshock followed one of most energetic aftershock sequences, that included two Mw 7.8 thrusting aftershocks in the New Britain subduction zone. Their

relationships with mainshock had been interpreted using static [*Geist and Parsons*, 2005; *S C Park and Mori*, 2007] or dynamic [*Gomberg et al.*, 2003] Coulomb trigger mechanisms.

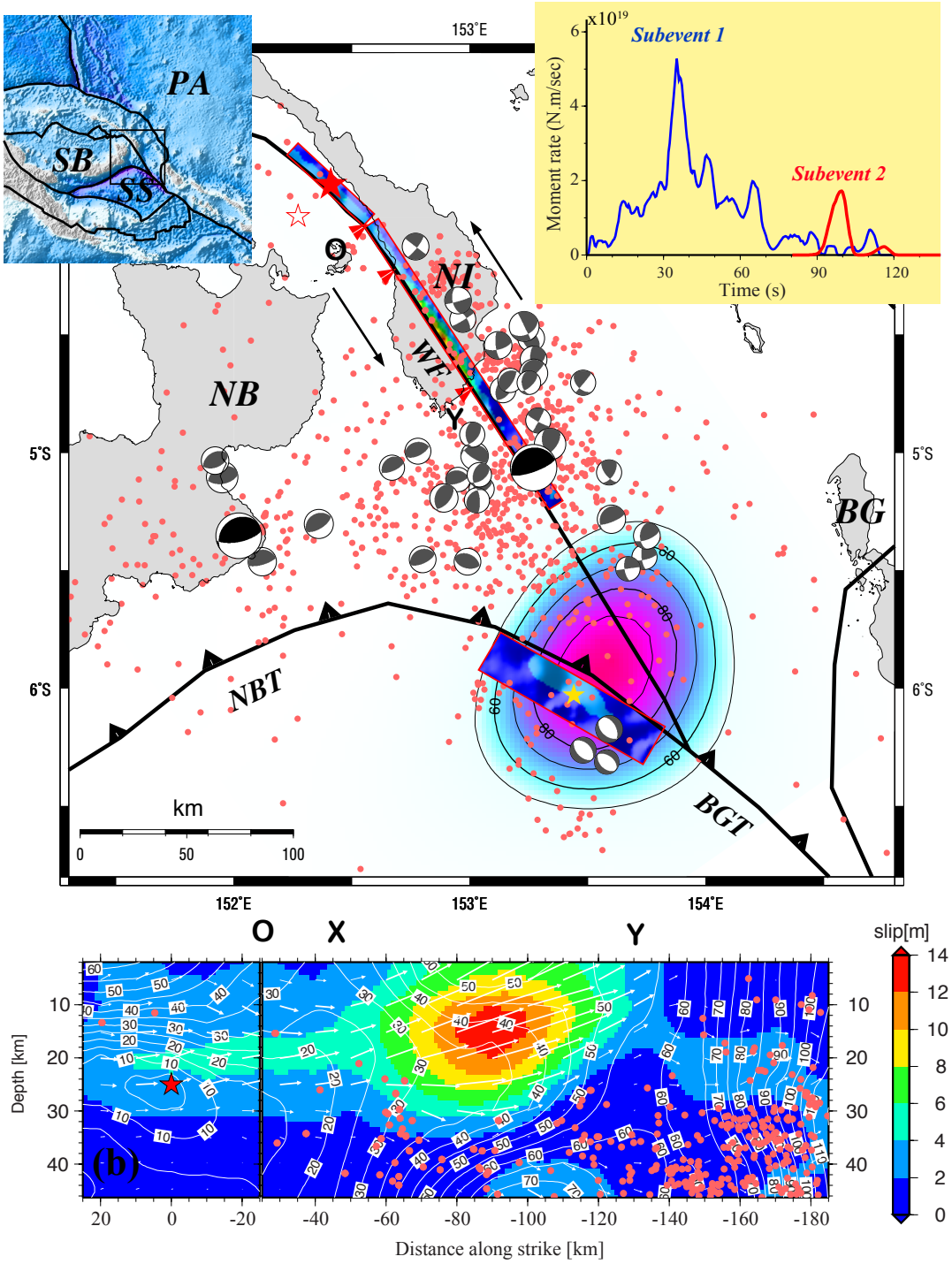

Figure 4.1: (a) Map of eastern Papua New Guinea region with associated tectonic plate boundaries [*Bird*, 2003]. Surface projection of the slip distribution of the 2000 Mw 8.0 New Ireland earthquake with its triggered normal fault event is superimposed on the map. Red and yellow stars represent the corresponding hypocenters for the two events. Focal mechanisms from Global Centroid Moment Tensor (GCMT) of the two largest aftershocks with moment magnitude of 7.8 that occurred on 2000 November 16 and 17 are shown using the black beach balls. Gray beach balls denote the focal mechanisms of aftershocks (from GCMT but relocated based on the EHB catalog) in the two weeks following the mainshock. X and Y highlight where the Weitin Fault intersects the coastline of New Ireland Island. NB, NI, WF, BG, NBT and BGT denote New Britain, New Ireland, Weitin Fault, Bougainville, New Britain Trench and Bougainville Trench, respectively. Surrounding plates such as Pacific Plate (PA), South Bismarck Plate (SB) and Solomon Sea Plate (SS) are shown on the top left. (b) Cross-section of slip distribution of the strike-slip event. Star denotes the hypocenter and white arrows indicate the slip direction of the hanging wall relative to the footwall. The slip amplitudes are shown with color; contours denote the rupture time in seconds. The red dashed line represents the position of the subducted Solomon Sea Plate.

Because the close-fault records were saturated due to the strong shaking [*Tregoning et al.*, 2005], the studies of the 2000 New Ireland earthquake relied on the distant records [e.g., *Park and Mori*, 2007]. Figure 4.2(a) shows a profile of P-waves within the epicentral distance range 30^{o} to 90^{o}. These 150 s long displacement waveforms are aligned by the P wave first arrivals and sorted by the azimuths of stations. For the first 80 s the polarity of the P-wave waveform changes with azimuth in a pattern consistent with what is expected for a

strike-slip earthquake. The peak amplitudes of these records, however, associate with an energetic narrow pulse, which appears at about 80-120 s, dependent of azimuth. This pulse always has positive polarity. Figure 4.2(b) shows a similar record section of teleseismic SH wave. We cannot identify any coherent phase around 100 s.

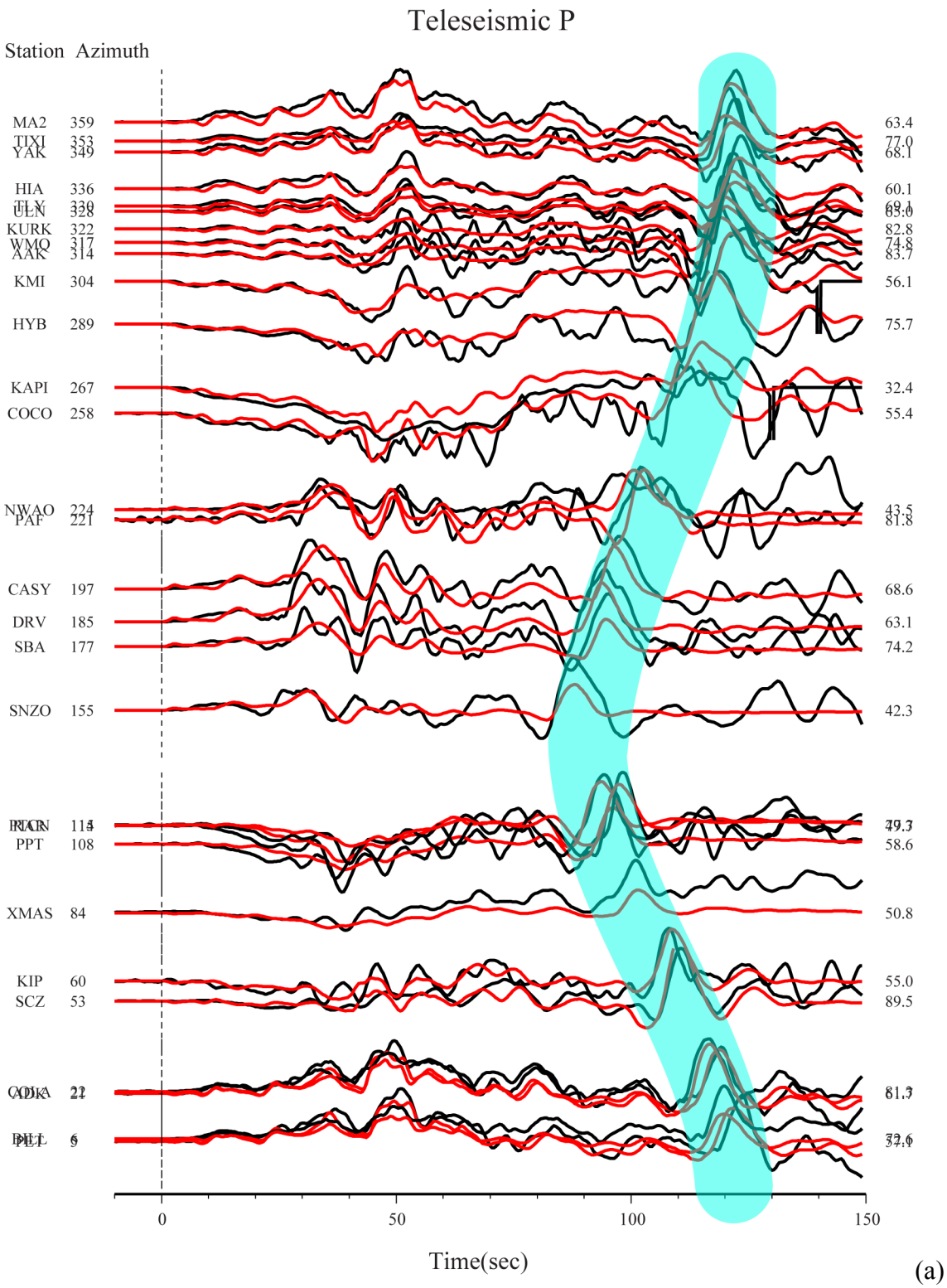
Teleseismic P
Station Azimuth
MA2 359
TIXI 353
YAK 349
HIA 336
KURK 322
WMQ 317
AAK 314
KMI 304
HYB 289
KAPI 267
COCO 258
NWAO 224
PAF 221
CASY 197
DRV 185
SBA 177
SNZO 155
PPT 108
XMAS 84
KIP 60
SCZ 53
63.4
77.0
68.1
60.1
82.8
74.8
83.7
56.1
75.7
32.4
55.4
43.5
81.8
68.6
63.1
74.2
42.3
58.6
50.8
55.0
89.5
0
50
100
150
Time(sec)

(a)

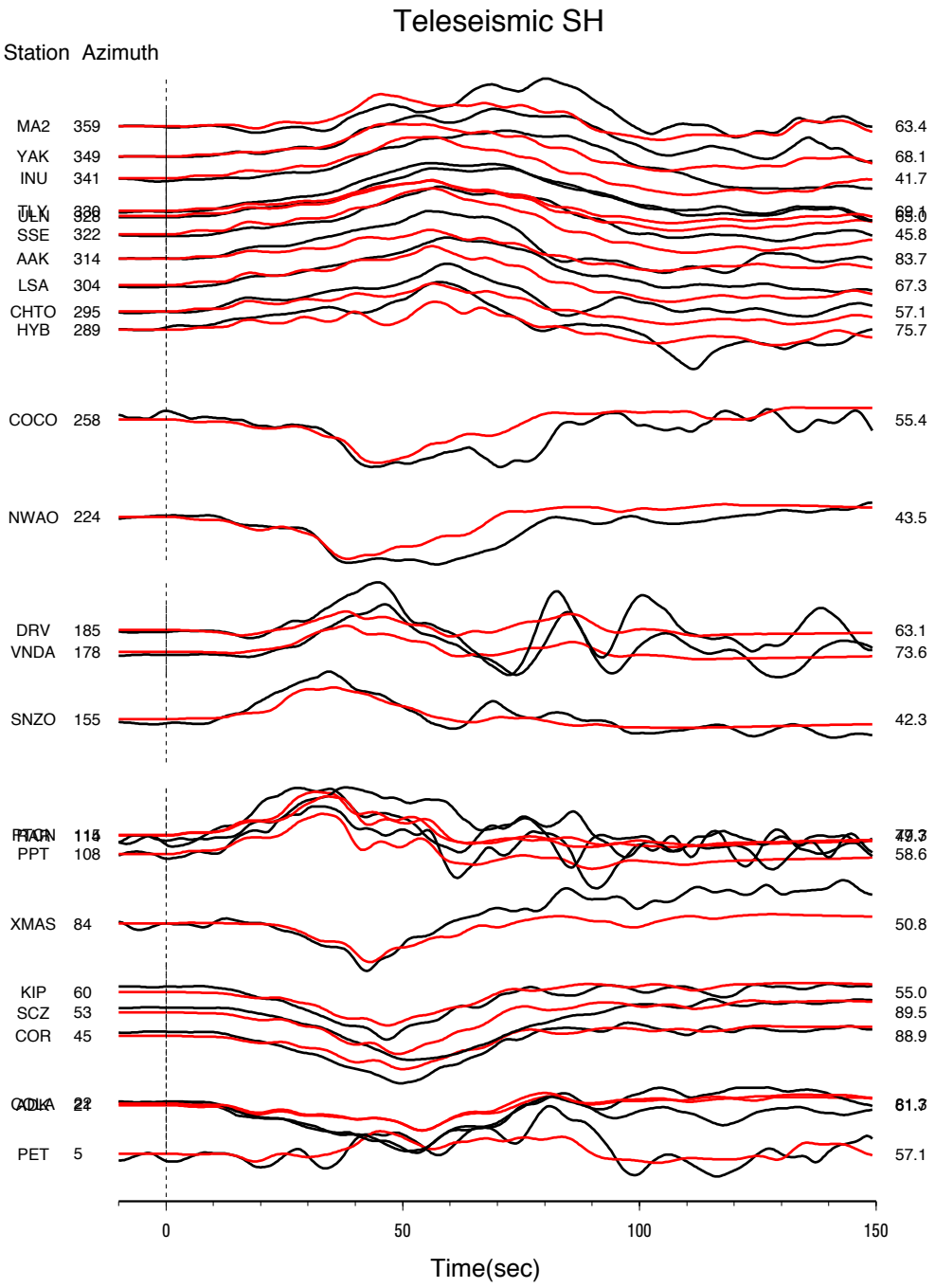

(b)

Figure 4.2: (a) Azimuthal profile of teleseismic P waves (black traces), which are aligned by the P first arrivals. The synthetic seismograms are calculated using the preferred finite fault model. Note that we could easily identify a strong phase arriving 80-120 s after the P first arrivals. (b) Similar to (a) but for SH wave.

A teleseismic P-wave pulse with azimuthally independent polarity is strong evidence that the causative rupture has either a thrust or normal fault focal mechanism. In fact, the lack of SH wave radiation supports such a hypothesis. Rupture complexity of the 2000 Mw 8 New Ireland earthquake has been previously investigated [e.g., *Park and Mori*, 2007], but the cause of this abnormal phase has not been fully explained. *Yagi and Kikuchi* (EIC note 94, 2000) suspected the possibility of a thrust earthquake two minutes after the initiation of the strike-slip rupture, but they did not conduct any further analysis. *Park and Mori* [2007] studied this earthquake using teleseismic body waves. They assumed a single fault plane orienting N320^{o}E and dipping 70^{o} to the northeast. Their solution has large thrust motion on the southeast end of the fault plane. However, this solution failed to explain the observed large P wave amplitudes arriving 80-120 s. Because this phase arrived much later than the first P arrival from the mainshock hypocenter, one might ask whether this pulse is a mantle reflection phase, such as PcP or PP, which usually has a radiation pattern different from that of direct P waves. We rule out this possibility by inspecting the observations at stations PTCN and RAR (Figure 4.3). These two stations have similar azimuths (115^{o} vs. 114^{o}) but quite different epicenter distances (77.3^{o} vs. 49.7^{o}). For the phase we are interested, its peak reached stations PTCN and RAR at 95 s and 99 s, respectively, after corresponding P first arrivals. The difference is only 5 s. In contrast, if this phase were a PcP wave or PP wave, the difference would be about 70 s.

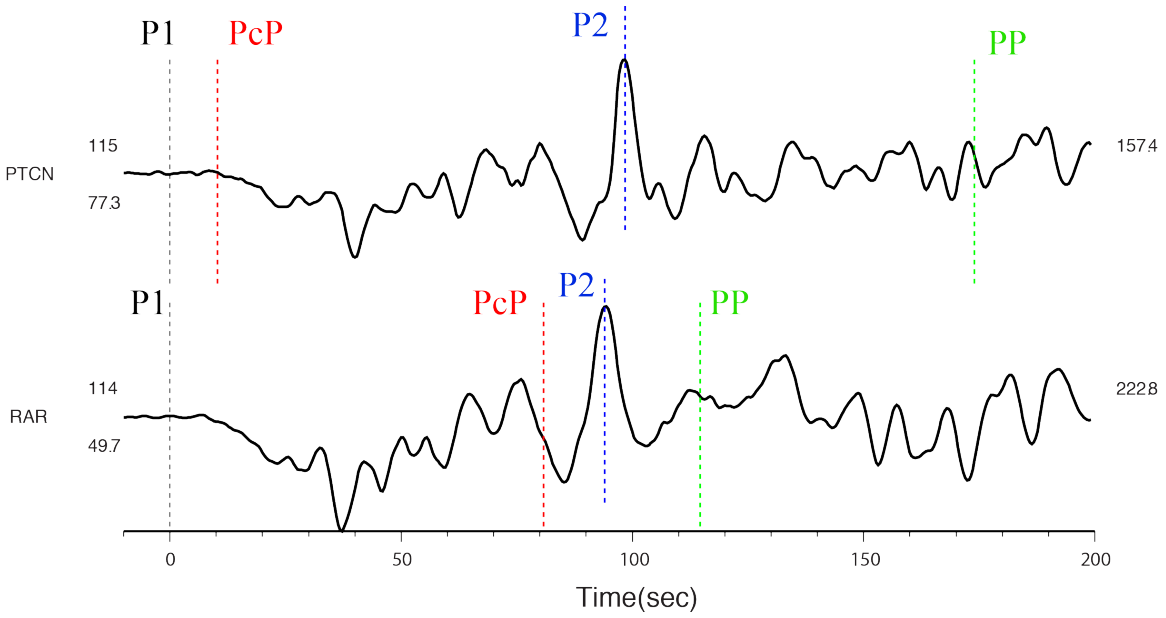

Station	*Distance (°)*	*PcP – P1 (s)*	*PP – P1 (s)*	*P2 – P1 (s)*
RAR	**49.7**	**80.8**	**114.7**	**99**
PTCN	**77.3**	**10.3**	**173.95**	**94**

Figure 4.3: Comparison of P wave records at stations RAR and PTCN. Their azimuths and epicentral distances are indicated above and below the beginning portion of waveform. P1 denotes the first arrival from the hypocenter. P2 indicates the time when the abnormal phase reaches its peak amplitude. Predicted relative arrival times of P, PcP, and PP phases from the mainshock hypocenter are indicated by gray, red, and green dotted lines, respectively, and are summarized in the table. Blue dotted line denotes the time associated with the peak amplitude of the anomalous phase**.**

In this study we use body waves and surface waves together to constrain the location and focal mechanism of the causative fault of the abnormal P wave. We find that the 2000 Mw 8.0 New Ireland earthquake was composed of two subevents, i.e., it is a doublet. The well-known Mw 8.0 strike-slip earthquake was followed by a Mw 7.4 normal faulting

earthquake, which is located 263 km southeast of the epicenter of the strike-slip subevent and near the San Cristobal Trench and initiated about 90 s after the strike-slip subevent. To our knowledge this is the first evidence of a distant Mw >7 normal fault earthquake being initiated nearly instantaneously after the SH waves of a Mw 8 strike-slip earthquake passed by. For convenience of further discussion, we hereafter refer to the earlier rupture as the strike-slip (SS) subevent and the event associated with later anomalous phase as the non-strike-slip (NSS) subevent.

4.2 Modeling

Because the seismic moment of the NSS subevent is much smaller than that of the SS subevent, it is hard to resolve unambiguously its focal mechanism and location using a regular method. In this section, we will first estimate the centroid location and centroid time of the NSS subevent using a back-projection approach [e.g., *Ishii et al.*, 2005] and then use the results to constrain a subsequent long-period, multiple double-couple (MDC) analysis. Finally we carry out finite fault modeling to demonstrate that our solution explains the teleseismic body and surface waves simultaneously.

4.2.1 Back-projection Analysis

Figure 4.2(a) shows the organized arrival times of the abnormal P phase, suggesting that the NSS subevent has a distant and spatially compact source. Taking advantage of the constant polarity of the abnormal P phase, we can locate it using a simple back-projection approach [e.g., *Ishii et al.*, 2005]. We assume that the centroid location of the NSS subevent

could be anywhere within a rectangle 400 km by 300 km at a depth of 25 km, same as the hypocenter depth of the SS subevent (Figure 4.4). We discretize this region with 10 km by 10 km uniform grid and treat every grid as a hypothetical source.

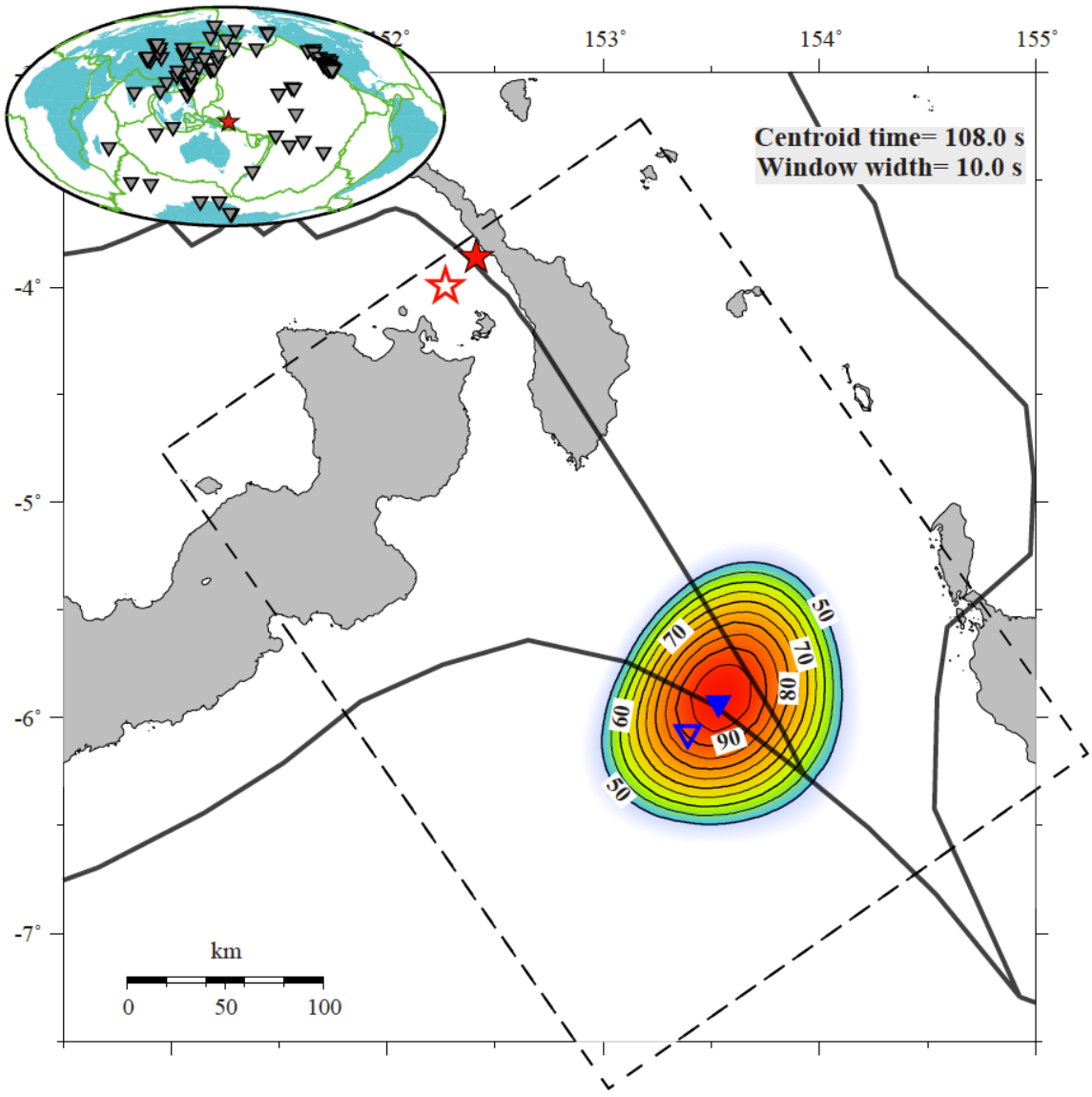

Figure 4.4: Distribution of relative energy radiation (the squared amplitude of stacked seismograms) obtained by integrating the teleseismic P waves in a time window between 103 and 113 s after hypocentral time corrections. Red solid and open stars denote the

relocated epicenter (3.86°S, 152.41°E) and the EHB epicenter (3.996°S, 152.268°E), respectively. Dashed box denotes the back-projection region of 400km by 300km. Inverted blue solid triangle shows the energy centroid (5.93°S, 153.56°N). The black contours are plotted at 5% intervals, starting at 50% of the normalized peak amplitude. Thick black lines show the plate boundaries. Upper-left insert panel shows the distribution of 108 selected teleseismic stations (grey triangles). The location of the 2000 New Ireland earthquake is denoted as a red star.

We project the observed waveforms back to the source region and sum them together at every hypothetical source. For the *i-th* grid, the stacking time series is

$$s_i(t) = \frac{1}{c}\int_{t-w/2}^{t+w/2}\left[\sum_{k=1}^{N}\frac{1}{A_k}u_k(\tau - t_{ik}^{p} + \Delta t_k)\right]d\tau \qquad (12)$$

Where $u_k(t)$ denotes P wave seismogram recorded at the k-th station with A_k as its peak amplitude. t_{ik}^{p} is the predicted travel time from the *i-th* hypothetical source to the *k-th* station using the *Iasp91* travel-time table [*Kennett and Engdahl*, 1991]. Δt_k is the static time correction for the *k-th* station which is introduced to correct the predicted P wave first arrival based on 1D earth model. To stabilize the stacking result, a moving time window with the width of ***w*** is applied. *w* used in this study is 10 s. ***c,*** which is the largest stacking amplitudes, is a constant to normalize the final result . Because the back propagating signals will sum constructively at the target source location but destructively at other sites [*Ishii et al.*, 2005], we can locate the centroid location and "centroid time" of this hypothetical source by searching for the location of the maximum stacking amplitude.

Because the locations of imaged hypothetical sources are relative to the epicenter of the SS event, we discuss it first. The open red star in Figure 4.4 denotes the relocated ISC epicenter (EHB location, http://www.isc.ac.uk/ehbbulletin) [*Engdahl et al.*, 1998], which is tens of kilometers from the transform plate boundary [*Bird*, 2003]. We have shifted this location 21 km along the direction normal to the local Weitin Fault trace so that the finite fault plane discussed later is consistent with the location of Weitin Fault trace. Considering the lack of close-fault stations and complicated local velocity structure, such an offset will be within the location uncertainty. This modified EHB epicenter used in this study is –3.86°N, 152.41°E, indicated as a filled red star in Figure 4.4.

We select P-wave waveforms at 108 global seismic stations, which generate a complete azimuthal coverage and span epicentral distances from 36.8^{o} to 86.8^{o} (Figure 4.5(a)). After removing instrument response, we band-pass filtered each between 1s and 100 s. This large earthquake started with a weak initiation. To align the waveforms properly we first perform preliminary finite-fault modeling using only the data with reliable P wave picks. Then we adjust the P-wave alignments at other stations by conducting a waveform cross-correlation between the beginning portion of data and the synthetics of the preliminary slip model.

Figure 4.4 shows the distribution of stacking amplitudes at t=108 s when the stacking amplitude reaches its maximum. The grid with the maximum stacking amplitude locates at -5.93°N, 153.56°E–filled blue triangle in Figure 4.4. Note that this location is related to the epicenter. If we instead use the EHB epicenter rather than modified EHB location as the reference, the location weas the one that is denoted by the open blue triangle (Figure 4.4). Nevertheless this site is 263 km away from the SS epicenter and close to the San Cristobal

Trench axis. As shown in Figure 4.5(b), after correcting the arrival time by using the preferred source location, the abnormal P waves at these stations are aligned well.

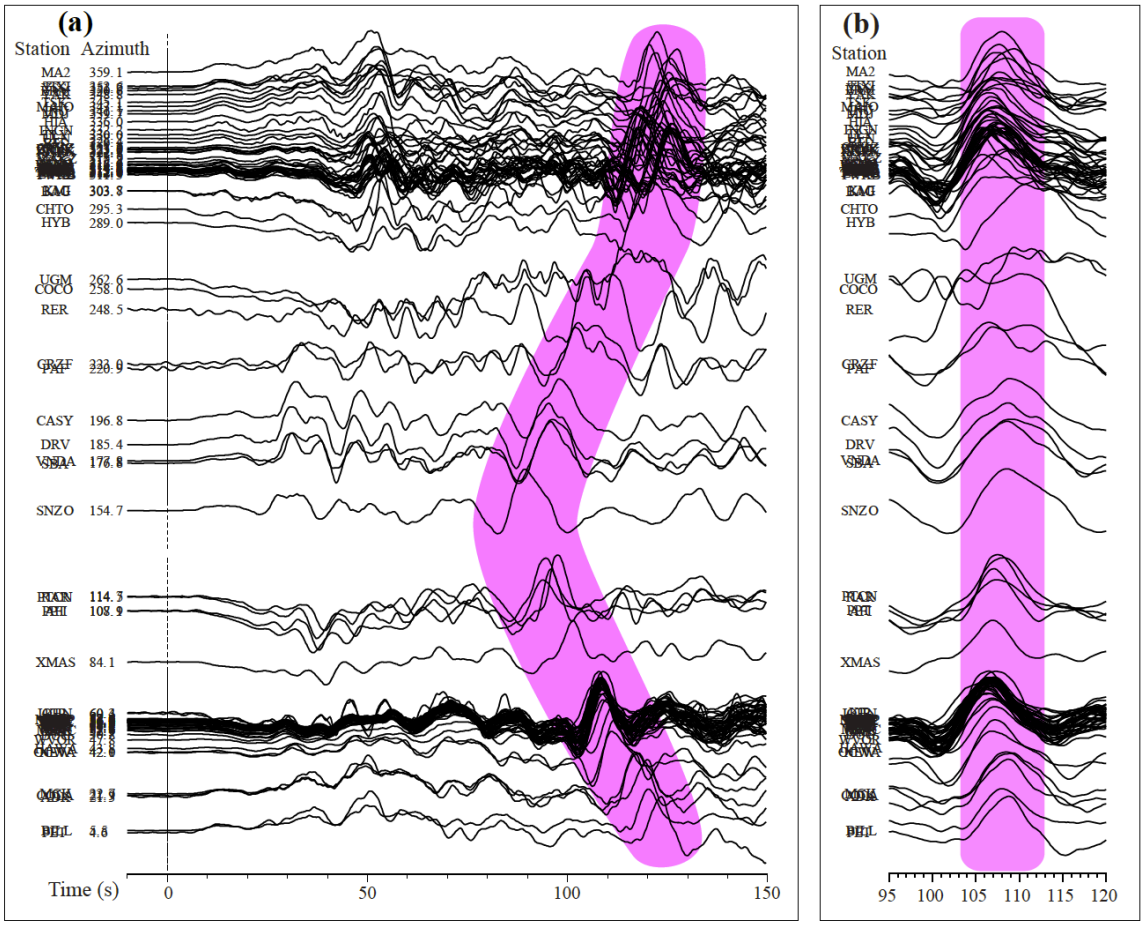

Figure 4.5: (a) Comparison of 108 teleseismic P waves from the 2000 New Ireland earthquake sorted by their azimuth. All the data are normalized by their amplitude and aligned by their P-wave first arrivals. Pink color highlights the energetic pulses, which have the similar polarity but different arrival times. (b) Cross-section of the energetic pulse after the time corrections at the preferred centroid location (solid blue triangles in Figure 4.4).

Figure 4.6 shows snapshots of stacking amplitude distribution from 104 s to 111 s. We can see that the location with the peak stacking amplitude shift from Solomon Sea to the

Cristobal margin along roughly northeast direction as the time continues. The locations at 107 s and 108 s are very close. But at time 106 s and 109 s, the peak locations shift 25-30 km away from the preferred location, accompanying with the relatively large decreases in the imaged peak stacking amplitude (Figure 4.6(i)).

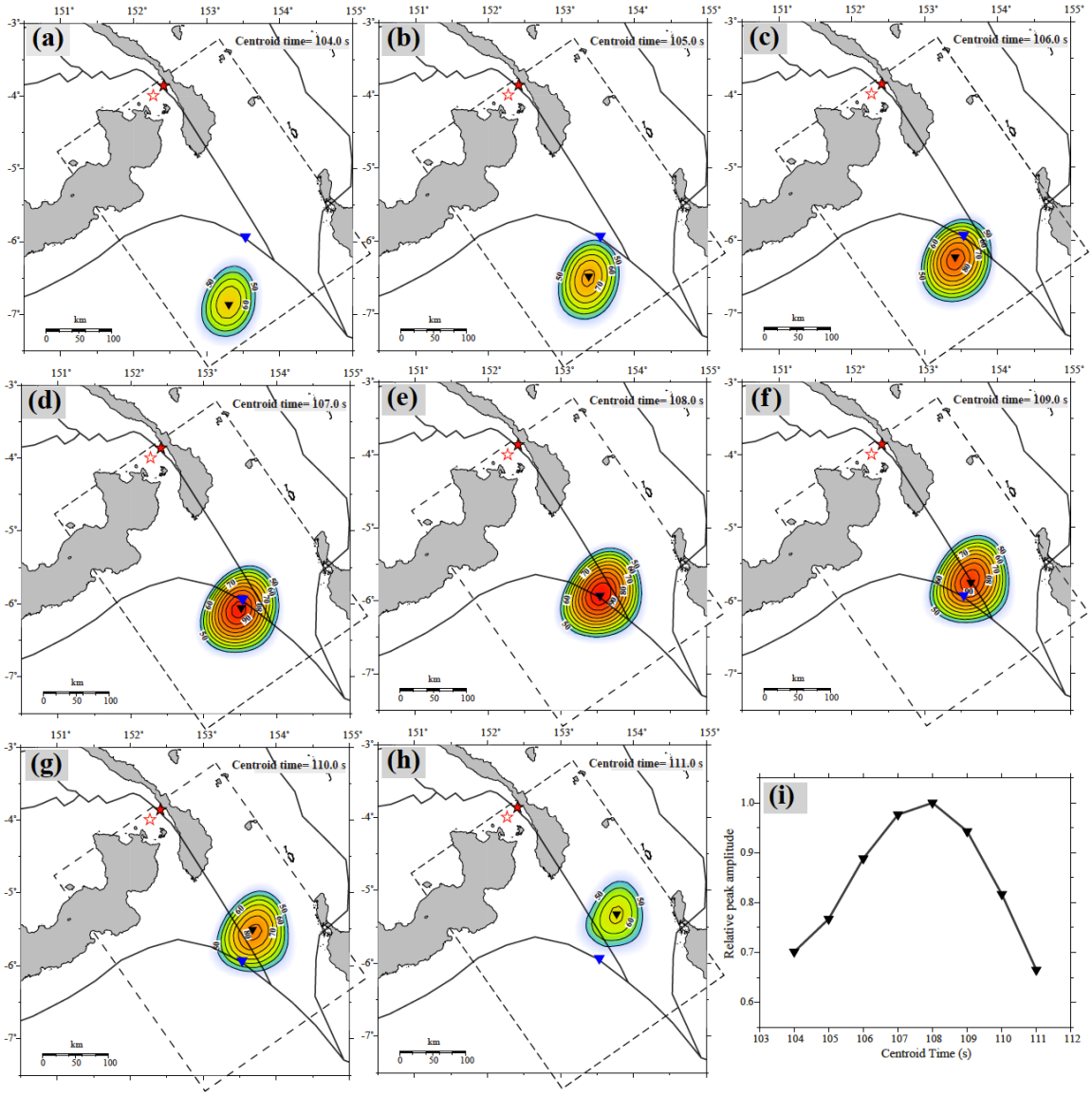

Figure 4.6: Snapshots of the normalized stacking amplitude from 104 s to 112 s. (a)-(h) shows the stacking amplitude distributions at centroid times 104 to 111 s in one second intervals. Black inverted triangle indicates the centroid at each time step and blue triangle

shows the centroid with the maximum amplitude in all time steps. Red solid and open stars denote the relocated epicenter and the EHB epicenter, respectively. (i) Variation of the peak amplitude relative to the centroid imaging time.

When interpreting above results, we also have to account for the near source response of teleseismic P wave. Surface reverberations, such as pP or sP, often dominate the teleseismic P records. The location associated with the maximum stacking amplitude should be close to the centroid location of the NSS subevent. But the time associated with the maximum stacking amplitude is 7-11 s earlier than the true centroid time of the NSS subevent if the centroid depth is 25 km. During our long period analysis discussed next, we simply use 100 s as a rough estimation of the centroid time.

4.2.2 Multiple double-couple analysis

We subsequently attempted to constrain the focal mechanisms of the SS and NSS subevents, using 2-6 mHz long-period seismic waves on 24 vertical and 24 transverse components. By matching the long-period waveforms, we simultaneously invert for source focal mechanisms, centroid locations, centroid times, and seismic moments using a heat-bath algorithm [*Shao et al.*, 2011]. The moment rate function is approximated as a symmetric cosine function [*Ji et al.*, 2002b] with an empirical half duration of $2.26 \times 10^{-6} M_0^{1/3}$, where M_0 is the scalar moment in Nm [*Ekstrom et al.*, 2005b]. The total number of free parameters is $8*N$, where N is the number of point sources. We assume an anisotropic PREM Earth and synthetic seismograms are calculated using a normal mode superposition algorithm.

Although the observed P-wave waveforms are dominated by the NSS response (Figure 4.3), these long-period data are well matched using just one strike-slip point source. The inversion result, if we only use one point source to approximate this doublet, reveals a nearly pure left-lateral strike-slip solution on a fault plane orienting N326^{o}E and dipping 48^{o} to the northeast. Its centroid locates at the southern portion of New Ireland Island, about 90 km southeast of the epicenter. The centroid time is 40 s. Synthetic seismograms predicted using this model match the data well with a variance reduction of 80.5%. This model is in excellent agreement with the best double-couple of the GCMT solution, which features strike-slip motion on fault plane orienting N328^{o}E and dipping 43^{o} to the northeast. Large strike-slip earthquake often occur on fault planes with high dip angles (e.g., 2001 Kunlunshan earthquake [*Lasserre et al.*, 2005], 2002 Denali fault earthquake [*Hreinsdottir et al.*, 2006]). It is then interesting to know how robust this result is. During another inversion we specifically force the dip angle to be 80^{o}; the variance reduction associated with the inverted model reduces to 78.3%. We also observe the trade-off between inverted seismic moment and inverted fault dip. For the inverted point source the seismic moment is 1.32x10^{21} Nm for a dip angle of 48^{o} and becomes 1.0x10^{21} Nm for a dip angle of 80^{o}.

Next we approximate the source as two point sources. The total number of free parameters is now 16. Many inversions were preformed to explore the uncertainty of result. We summarize them here:

1) Using two point sources to approximate this earthquake improves the waveform fits. The variance reduction increases by 3.5-3.7% relative to single point solutions.
2) The inverted results of the first subevent are all identical with the single point source solution, as expected.

3) The focal mechanism of the second subevent, however, is less well constrained. Although all solutions have large normal fault components, the amplitude of strike-slip component changes with the centroid time. However, if we limit the centroid time within a 10 s period –95 s to 105 s– the inverted strike angles and rake angles are very stable, changing slightly around 120^o (or 300^o) and -90^o, respectively. Note that this fault plane is parallel to the axis of the San Cristobal Trench. It is also noteworthy that adding the constraint of centroid time has nearly no impact on the waveform fits. The variance reduction varies negligibly from 84.18% to 84.00%.
4) The inverted centroid locations of second subevent are all beneath the Solomon Sea but are about 60-70 km south of what was inferred from the P wave back-projection analysis (Figure 4-6). The trade-off between fault dip and seismic moment has also been observed.

Nevertheless, combining the results of the P wave back-projection and long-period wave MDC analysis, we can reasonably argue that a normal fault subevent can explain both data sets simultaneously.

In the end, we force the fault dip of first event to be 80^o and the centroid location of second event at the result of back-projection (Figure 4.4). The result is shown in Figure 4.7. The synthetics predicted still match the data well with a variance reduction of 81.3%. For the second subevent we choose a dip angle of 45^o, which is consistent with GCMT solutions of three nearby aftershocks, and find a seismic moment of 1.5×10^{20} Nm, equivalent to Mw 7.4. It is noteworthy that the cumulative moment tensors of these two double-couple subevents still has a significant CLVD component with a ε of 0.13, agreeing well with the aforementioned GCMT solution ($\varepsilon = 0.15$). As we show next, such focal mechanisms can

explain both body and surface waves. One should keep the uncertainties in fault dips and seismic moments in mind.

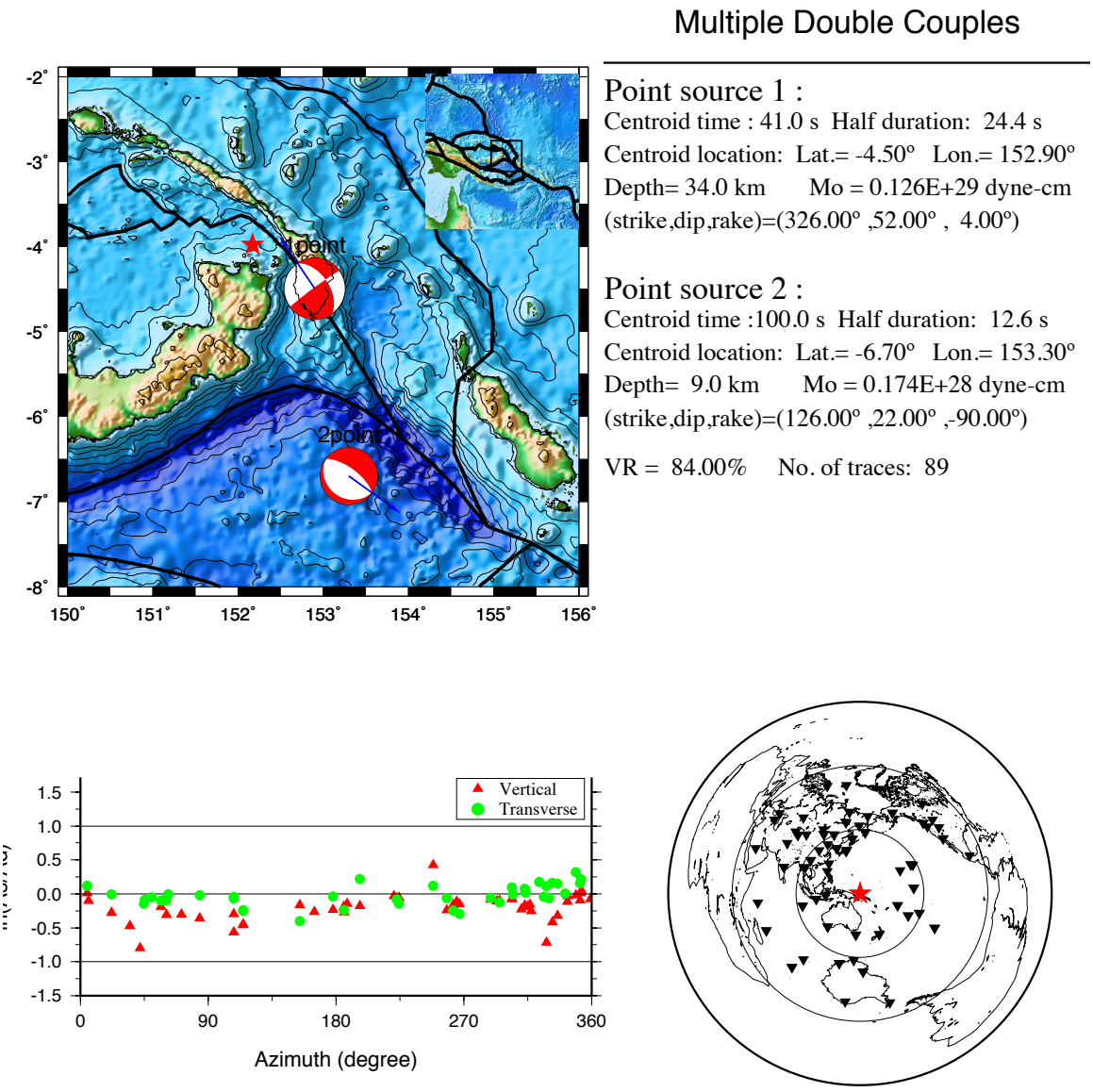

Figure 4.7: MDC solution of our two double-couple model with the dip angle of the strike-slip mainshock fixed at 80°.

4.3 Finite fault analysis

We end our kinematic analysis of the 2000 New Ireland earthquake by constraining its slip model with the waveforms of teleseismic body waves and long-period surface waves mentioned earlier. For the SS subevent, we use two rectangular planes to approximate the curved Weitin Fault (Figure 4.1, [*Bird*, 2003]), which turns 14^o from 313^o to 327^o southeast of its EHB epicenter (open star, Figure 4.1). We let both planes dip 80^o to the northeast and extend from surface to a depth of 45 km. We use the EHB hypocenter depth of 25 km. As mentioned earlier, we have to shift the EHB epicenter northeastward by 21 km to match this fault geometry. For the NSS subevent, we adopt a rectangular plane orienting N120^{o}E and dipping 45^o to the southwest-west. The epicenter (-6.03°N, 153.44°) has been slightly shifted to the ocean side so that the horizontal centroid location is consistent with the back-projection analysis. The hypocenter depth is 12 km. In the model discussed here, we let the rupture initiate at the middle of plane at 85 s after the origin time of the SS subevent. However, the result is similar as long as the initiation time is less than 90 s. We divide the fault plane into 243 subfaults (10 km x 5 km) and use a search-based finite fault inversion method to simultaneously constrain the fault slip, rake angle, rupture initiation time and the shape of slip rate function [*Ji et al.*, 2002b]. The slip distribution and cumulative moment rate function are shown in Figure 4.1.

Our study reveals that the 2000 New Ireland earthquake had a very unique rupture process. It initiated as a left-lateral strike-slip rupture under the Bismarck Sea. After a 5-s slow initial break, the rupture front propagated up-dip and unilaterally along the Weitin Fault to the southwest at an average velocity of 2.0-3.0 km/s. After the rupture front reached New Ireland Island, 50 km southeast of the epicenter (site X in Figure 4.1), at 25 s, the width

of slip zone expands to the entire crust, from surface to a depth of 35-40 km. The peak slip of 14 m occurred 90 km from the epicenter, close to the centroid location inferred from point source MDC inversion. The fault slip then becomes shallower as rupture front gradually moved away from New Ireland Island. The rupture front reaches the southeast coast of New Ireland at about 50 s, roughly 130 km away from the epicenter (site Y in Figure 4.1). The cumulative moment rate quickly decreases afterward and essentially becomes negligible after 73 s. The cumulative seismic moment of the SS subevent is 1.1-1.2x10^{21} Nm. The energetic rupture of the NSS subevent occurred at 90 s, though its initiation might be seconds earlier. The cumulative moment rate reached its peak at 100 s but quickly ceased at 105 s. The peak slip is 3 m. The cumulative seismic moment of the NSS subevent is 1.5x10^{20} Nm. The comparison of synthetic seismograms and observations is shown in Figure 4.2 and Figure S4.1. It can be seen that this model simultaneously explains teleseismic body waves and long period surface waves.

4.4 Discussions

4.4.1 New Ireland asperity

The slip distribution of the SS subevent is interesting. Most its seismic moment occurred on the southern New Ireland section of the Weitin Fault, which has a length of 70-80 km (between X and Y, Figure 4.1). Temporally, the rupture concentrated within a short time window between 25 s – 60 s after rupture initiation. The cumulative seismic moment during this period is 8x10^{20} Nm, about 66-70% of the total seismic moment of SS subevent. This is consistent with the results of long-period moment tensor or double-couple analyses (e.g.,

GCMT). As shown in Figure 4.1, the GCMT centroid location fell in the center of this segment, which is 90 km from the epicenter. We name this robust feature the New Ireland asperity.

Note that the down-dip extension of fault slip within this segment is 30-35 km. In contrast, the down-dip seismogenic zone extension of the continent strike-slip fault systems, such as San Andreas Fault, is about 15 km [*Scholz*, 2002]. The large down-dip extension is consistent with the locations of aftershocks [*Tregoning et al.*, 2005], which skirt around the edge of this high slip patch (Figure 4.1). The result is also consistent with the large centroid depth of the GCMT solution (24 km) as well as the down-dip extensions found in the previous studies based only on teleseismic body waves [*Park and Mori*, 2007]. Note that if we limit the down-dip extension to be 20 km, using a typical upper crust rigidity of 3.3×10^4 MPa and a fault length of 80 km, the average slip of this asperity is 15 m, about three times of the observed maximum surface slip (5.5 m). Using the Knopoff formula $\Delta\sigma = 2M_0(\pi W^2 L)^{-1}$ for shallow strike-slip fault [*Knopoff*, 1958] to estimate the average stress drop, here, M_o, W, L denote the seismic moment, width, and length of the fault. $\Delta\sigma$ is 15.9 MPa for w=20 km, and 7.1 MPa for w=30 km.

King and Wesnousky [2007] proposed that the base of the seismogenic zone does not result from the onset of viscous relaxation but rather a transition to stable sliding in a medium that remains stressed or close to failure. Subsequently, the rupture of a large earthquake like this event extends below the depth at which earthquakes can initiate. Our slip distribution appears to support such a hypothesis. However, the width of seismogenic zone in this region is not known. The background seismicity of this region has not been well

studied. The available solutions span a large depth region from 0 to 50 km and cannot clearly identify a fault plane [*Lindley*, 2006].

The correlation between this large asperity and the New Ireland Island might simply be coincidence. However, note that the velocity structure beneath the Bismarck Sea and New Ireland Island are quite different. The crustal thickness beneath the former is only 20 km but is 32 km beneath the latter [*Finlayson et al.,* 1972].

4.4.2 Distribution of background seismicity

The complex tectonic activity in this region leads to heterogeneous local velocity structure at shallow depth; this strongly affects the propagation of surface waves. This complex structure might have small impact on the propagation of teleseismic body waves, which leave the source downward with small take-off angles. Evidently, the distribution of GCMT centroid locations of 453 Mw>5 earthquakes from 1976 to 2007 (Figure 4.8(a)) are less consistent with local tectonic structures than the distribution of their EHB locations (Figure 4.8(b)). According to the former, some thrust earthquakes occurred beneath the Solomon Sea (Figure 4.8(a)), while their EHB locations are on the island side of the trench axes where we would expect them (Figure 4.8(b)). There is also a linear strike-slip cluster beneath the Bismarck Sea, following the curve of the nearby transform plate boundary. Furthermore, because all of our solutions are relative to a modified EHB epicenter of the SS subevent, we shifted all focal mechanisms 21 km northeast, same as what we had done for the SS epicenter. Note that the linear strike-slip cluster beneath the Bismarck Sea now visually overlays with the Bird's plate boundary (Figure 4.8).

Thrust earthquakes beneath the New Britain and San Cristobal subduction zones dominate the seismic activity in this region. Clusters of other focal mechanisms can be seen, such as normal fault earthquakes beneath Solomon Sea and strike-slip event earthquakes beneath the Bismarck Sea (Figure 4.8).

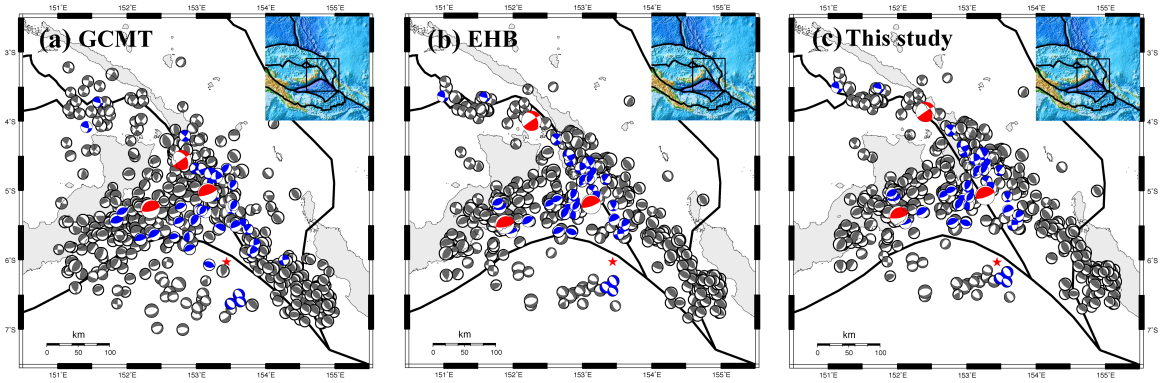

Figure 4.8: Distribution of 457 Mw>5 shallow earthquakes (depth<100 km) of eastern Papua New Guinea region from 1976 to 2007 (http://www.globalcmt.org). The black lines denote the plate boundaries [*Bird*, 2003]. The blue focal mechanisms are aftershock within first week; red focal mechanisms are the 2000 New Ireland earthquake mainshock and its two Mw 7.8 aftershocks. (a) The focal mechanisms are plotted at GCMT centroid locations. (b) The focal mechanisms are joined with corresponding epicenters in EHB Bulletin database. (c) Same as (b) but the locations have shifted 21 km in 45^{o}N direction so that they can be compared with the results obtained in this study.

The bending of subducted oceanic plate near the trench axis produces extensional stress environment at shallow depth that leads to normal-faulting earthquakes observed in subducted zones around the world [*Chapple and Forsyth*, 1979; *Christensen and Ruff*, 1983]. The location of the NSS subevent and its focal mechanism are consistent with this interpretation. However, the global survey of Christensen and Ruff [1988] revealed that the

outer-rise normal fault earthquakes located near a coupled subduction zone often occurred after a large mega-thrust event. This temporal characteristic is consistent with the background seismicity distribution in this region. Note that during this 31-year period 1976–2007, only three Mw>5 normal fault earthquakes occurred along the outer-rise region of San Cristobal Trench. All were aftershocks of the 2000 New Ireland sequence. Hence, the occurrence of the NSS subevent is not common.

Note the 100-km long linear cluster of normal faulting earthquakes in the middle of Solomon Sea (Figure 4.8(c)). This cluster elongates roughly in the east-west direction; the NSS subevent (red star) and three normal fault aftershocks (blue focal mechanisms) mark the east end of this cluster (Figure 4.8(c)). These earthquakes have similar focal mechanisms, but their strikes are not along the east-west direction. Thus the occurrence of this normal earthquake might also associate with some unknown tectonic activities that are deforming the Solomon Sea Plate.

4.4.3 Dynamic triggering Normal fault event by a strike-slip earthquake

The NSS subevent locates 263 km from the epicenter of the SS subevent and 150 km from the southeast end of the New Ireland asperity. Although we cannot rule out the scenario that the occurrence of these two events within 2 minutes was simply coincident, the probability is negligible, considering that only 15-17 Mw>7 earthquakes occur each year globally. Furthermore, background seismic activity mentioned above also suggests that it is uncommon to have a normal fault earthquake in the outer-rise region without a mega-thrust earthquake along the San Cristobal subduction zone.

To investigate their dynamic interaction, we calculate the perturbation of Coulomb static failure stress due to the rupture of the SS event. We first assume a half-space Earth and adopt Coulomb 3.3 software package [*Lin and Stein*, 2004]. We assume a friction coefficient of 0.4 and hypocenter depth of 12 km. The distribution of normal-faulting Coulomb stress perturbation on a fault plane orienting 120^o and dipping 45^o is shown in Figure 4.9(b). At the NSS hypocenter, the change in Coulomb stress is -4.8×10^{-3} MPa. Note that the NSS hypocenter locates within the transition zone where the change in Coulomb failure stress switches its sign. By definition, such a negative stress change shall delay rather than enhance its failure. As it will take about 40 s for S wave to propagate from the southeast edge of the New Ireland asperity to this site and the failure of the NSS subevent initiates earlier than 90 s. We also estimate the Coulomb stress perturbation caused by the slip occurring within first 50 s. We obtain a positive estimate but with an even smaller amplitude of 6×10^{-4} MPa (Figure 4.9(a)). In order to test the effect of the velocity structure, we calculate static Coulomb failure stress change using the 1D New Ireland layered structure [*Finlayson et al.*, 1972]. We first calculate the displacement field at a set of dense 3D grids using a FK algorithm and then calculate the strain field by interpolation. The distribution of stress variation (Figure 4.10(a)) in this case is similar to the result based on the half-space though the amplitude of the Coulomb failure stress change at the target site is smaller (-2.8×10^{-3} MPa). These estimates of static Coulomb failure stress are not significant. According to research for California earthquakes, it is hard to detect seismicity rate change when the static stress change is less than 10^{-2} MPa [e.g., *Hardebeck et al.*, 1998].

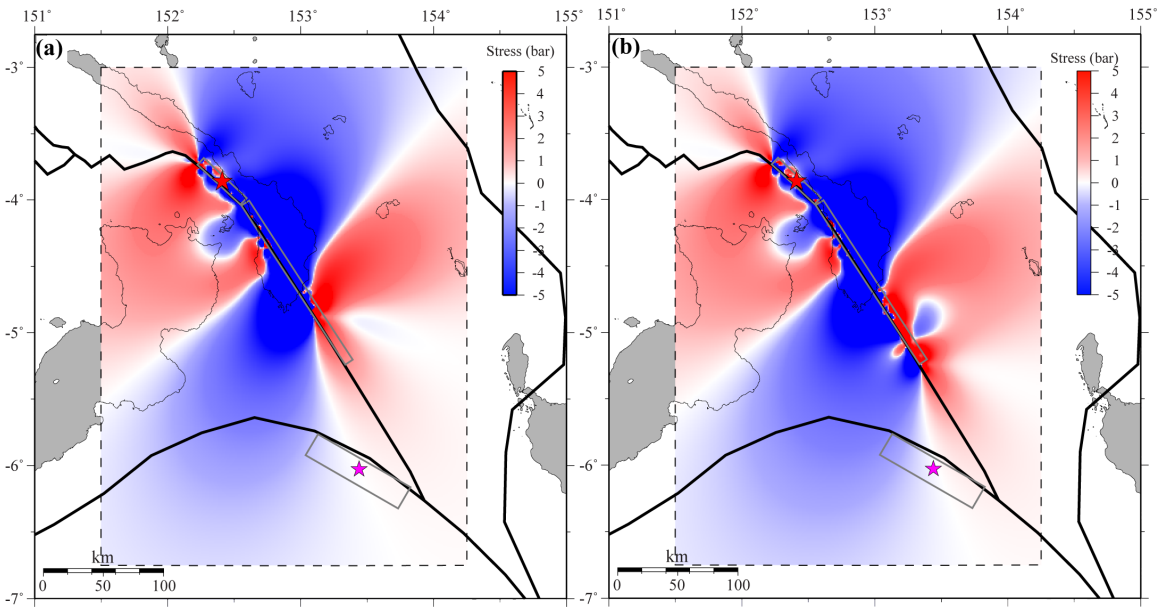

Figure 4.9: Coulomb stress change (depth =12km) on the NSS fault plane calculated using the Coulomb 3.3 software package. (a) The slip model used to excite static field only includes the strike-slip rupture occurring within the first 55 s. (b) The slip model of entire SS subevent is used. Red star indicates its epicenter and pink star denotes the epicenter of the normal subevent. Grey rectangles outline the surface projections of the fault plane. Thick black lines show the major plate boundaries in this region.

Next we consider the dynamic Coulomb failure stress. Figure 4.11 compares the synthetic displacement and velocity time history at the potential hypocenter of the NSS subevent as excited by the SS subevent. A band-pass filter with corner frequency of 1 Hz has been applied. We have projected the horizontal motion into the directions of N160^{o}E and N250^{o}E, which are essentially the radial and transverse components if the seismic waves are mainly radiated from the center of the New Ireland asperity. Because the NSS hypocenter locates close to the P wave nodal plane of SS subevent, the transverse component dominates

the displacement (Figure 4.11(a)). The motion in this component initiates right after the P wave arrives at 34 s as a near field drift. The energetic motion however started later after Sg phase from the SS hypocenter arrives at 70 s. It has two distinguished pulses centering at about 85 s and 95 s, respectively. The peak amplitude is 0.25 m, triple the peak amplitudes of radial and vertical components. It is of interest to note that the radial component has smaller peak amplitude but dominates the static displacement at this site. The domination of transverse component becomes even more obvious in velocity (Figure 4.13b), the peak amplitude of transverse component is 0.14 m/s, in contrast with the peak amplitude of 0.01 m/s in radial component.

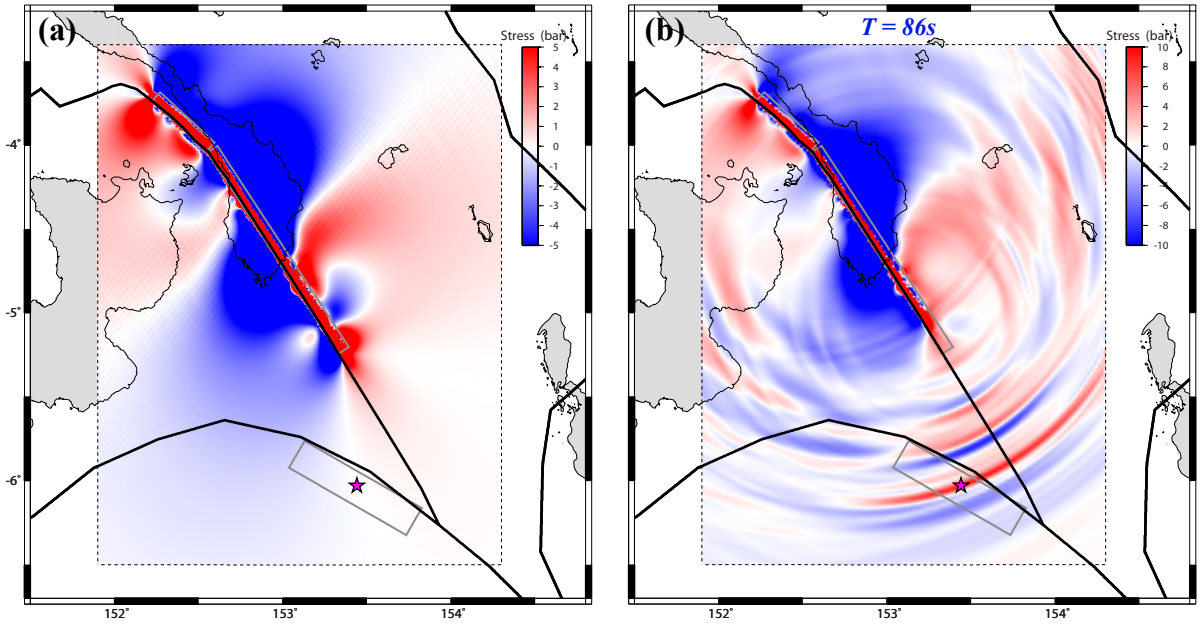

Figure 4.10: Coulomb stress change (depth =12km) on the NSS fault plane calculated using FK method and 1-D New Ireland layered structure. (a) The static stress change induced by the first strike-slip mainshock. The color bar scale is the same with Figure 4.9, -0.5 MPa to

0.5 MPa. (b) The dynamic stress change induced by the mainshock at 86s. The color bar scale is from -1MPa to 1MPa. Notice that the significant positive stress pulse with peak amplitude of 0.9 MPa is passing by the hypocenter of the second NSS fault plane at this moment. Red star indicates its epicenter and pink star denotes the epicenter of the normal subevent. Grey rectangles outline the surface projections of the fault plane. Thick black lines show the major plate boundaries in this region.

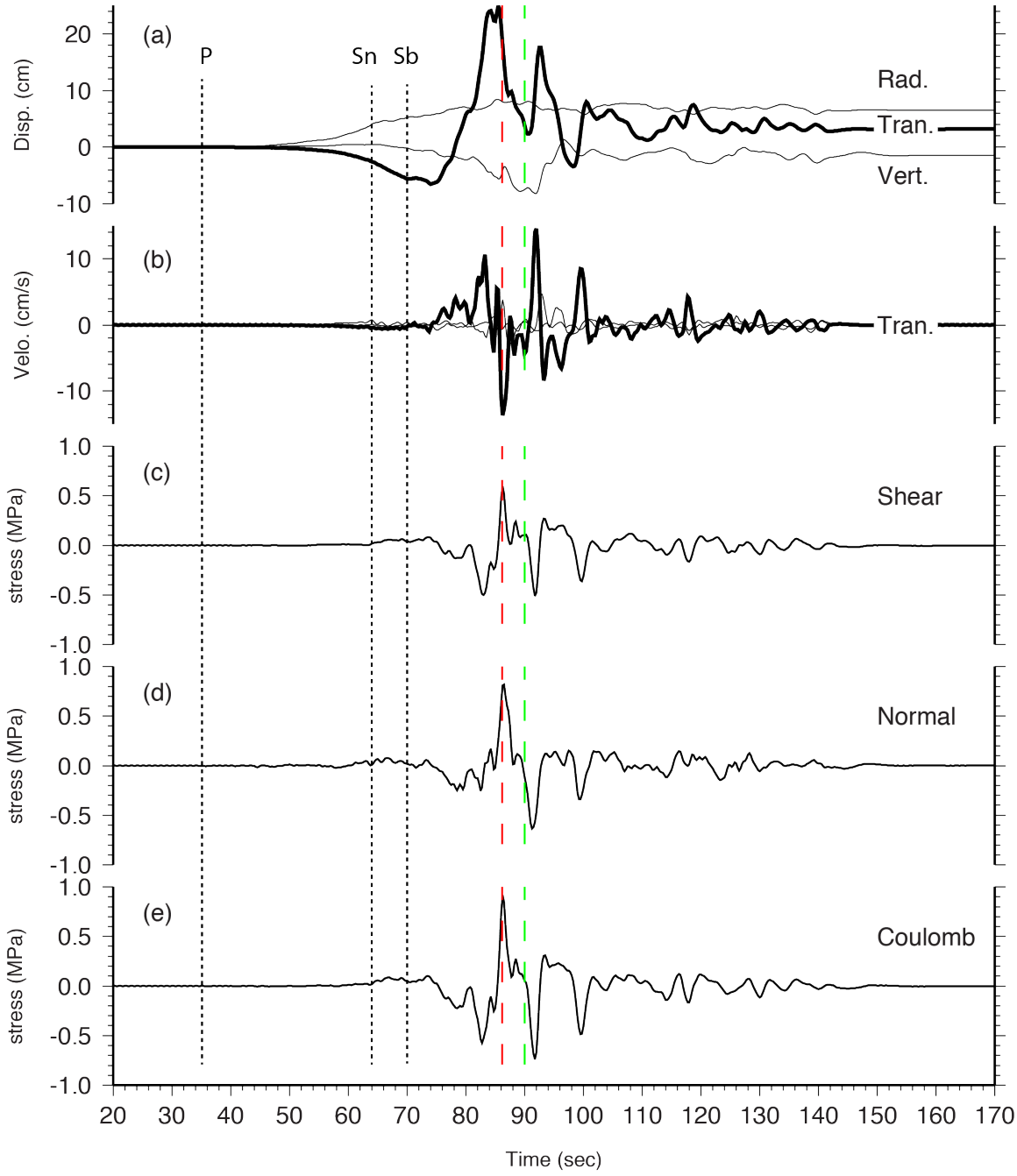

Figure 4.11: Displacement, velocity and stress waveforms at potential NSS hypocenter excited by the SS event. The red line indicates the time when the maximum positive Coulomb stress change occurs. The green dashed line denotes the starting time of detected energetic rupture on NSS fault plane. (a) Comparison of 3-component displacements. The

thick line depicts the displacement along transverse (N250^{o}E) direction. Thin lines show vertical or radial (N160^{o}E) components. (b) Comparison of 3-component velocity waveforms. Thick line depicts the transverse response and two thin lines show vertical or radial components. (c) The change of normal-faulting shear stress on the fault plane. (d) The change of normal stress on the fault plane. Here extensional stress is positive. (e) The change of Coulomb stress. Note the good anti-correlation between the velocity in transverse component and stress waveforms. See text for details.

The energetic motion however started much later as the Sb/Sg phase from the hypocenter arrives at 70 s. It has two distinct pulses centered at about 85 s (Figure 4.10(b)) and 95 s. The peak amplitude is 0.25 m, three times the peak amplitude of radial and vertical components. It is of interest to note that the radial component dominates the static displacement at the hypocenter. The dominance of the transverse component is more obvious in velocity (Figure 4.11(b)). The peak amplitude of the transverse component is 0.14 m/s, one order of magnitude larger than the peak amplitude of the radial component (0.013 m/s). Note that the largest amplitudes are associated with starting and ending of two SH wave pulses.

Figure 4.11(d) and 4.11(c) shows the dynamic normal and shear stress change. The shapes of their two waveforms are roughly anti-correlated to the shape of the velocity waveform at the transverse component. This is expected because the dynamic stress associated with the body wave is roughly proportional to particle velocity; in this case it is dominated by transverse motion. Figure 4.11(e) shows the dynamic Coulomb stress. We again use a friction coefficient of 0.4. However, as the dynamic normal stress and shear

stress change are highly correlated, using a different value of friction coefficient would only change the amplitude of the stress. In the frequency band we are using, the dynamic stress changes vary significantly with time. Note the positive stress change from 64 s to 74 s, negative stress drop from 74 s to 84 s, positive stress change from 84 s to about 90 s, and two more negative pulses at 92 s and 100 s. The stress variation gradually ceases at 150 s, leaving a small static Coulomb stress change of -2.8×10^{-3} MPa, which has been discussed earlier. The peak dynamic Coulomb stress change is 0.91 MPa, three hundred times larger than the static stress change. This dynamic stress change occurs at 86.2 s, only 3.8 s earlier than the initiation of the energetic rupture of the NSS event (Figure 4.10 (b)). The temporal difference between the arrival time of this positive stress peak on the subevent fault plane and the inferred origin time is well within the uncertainties. Note that our finite fault analysis only can resolve the beginning time of energetic rupture. The initiation time could be seconds earlier. Furthermore, the 3.8s difference in time might also be explained with a 15 km offset in NSS location, within the uncertainty of P wave back-projection analysis shown in Figure 4.6. Finally, it might also be questionable to use the New Ireland velocity structure to approximate the structure beneath New British margin and San Cristobal margin. Given all the uncertainties, our calculation suggests that the dynamic stress changes caused a nearly instantaneous triggering of the second subevent.

Radiation from large strike-slip earthquake that dynamically trigger distant ruptures has been previously reported [*Antonioli et al.*, 2002; *Henry et al.*, 2000]. *Henry et al.* [2000] and *Nettles et al.* [1999] reported that the 25 March 1998 great Antarctic Plate (M_W 8.1) earthquake was a doublet, composed of two subevents with seismic moment of 1.1×10^{21} Nm (Mw=8.0) and $0.3\text{-}0.6 \times 10^{21}$ Nm (Mw=7.6-7.8). *Henry et al.* [2000] model the first subevent

as westward-propagating rupture approximately 140 km in length, followed by a second strike-slip event starting approximately 70 s later and about 100 km from the termination of the first event. *Antonioli et al.* [2002] calculated the dynamic stress change excited by the first subevent. They found the largest positive dynamic stress peak on the second subevent fault plane was slightly less than 0.2 MPa at 60-65 sec depending on the velocity models. They suggested that the dynamic stress changes caused by the first subevent promoted a nearly instantaneous failure on the second subevent fault. The first subevent of the 1998 Antarctic Plate and the 2000 New Ireland doublet has roughly the same seismic moment. Our study of the 2000 New Ireland earthquake suggested that the triggered event can have a different focal mechanism and triggered distance could be 50% larger (150 km).

4.5 Conclusions

We revisit November 2000 Mw 8 New Ireland earthquake. Our results reveal that this earthquake was a doublet, composed of two distinct subevents— a Mw 8.0 left lateral strike slip event on the high angle Weitin Fault, and a Mw 7.4 normal fault event beneath the Solomon Sea Plate. The strike-slip rupture occurred first with seismic moment of 1.1-1.2x10^{21} Nm. It unilaterally propagated approximately 130 km to the southeast with an average speed of 2.5 km/s. The total duration is about 73 s and the peak slip is 14 m. Over two-thirds of seismic moment release occurred along a 70-80 km fault section where the Weitin Fault across the New Ireland Island. Energetic normal faulting rupture was detected at 90 s and located beneath the Solomon Sea 263 km south-southeast of the hypocenter of the first subevent. Most of its seismic moment (1.5x10^{20} Nm) occurred within a short duration of 15 s and the peak slip is 3 m. The existence of a normal fault event also explains

the large CLVD component of its GCMT solution. Its focal mechanism agrees well with the nearby aftershocks and the background seismicity. We demonstrate that the dynamic stress perturbation caused by the first subevent caused a nearly instantaneous triggering of the second subevent with a negligible delay.

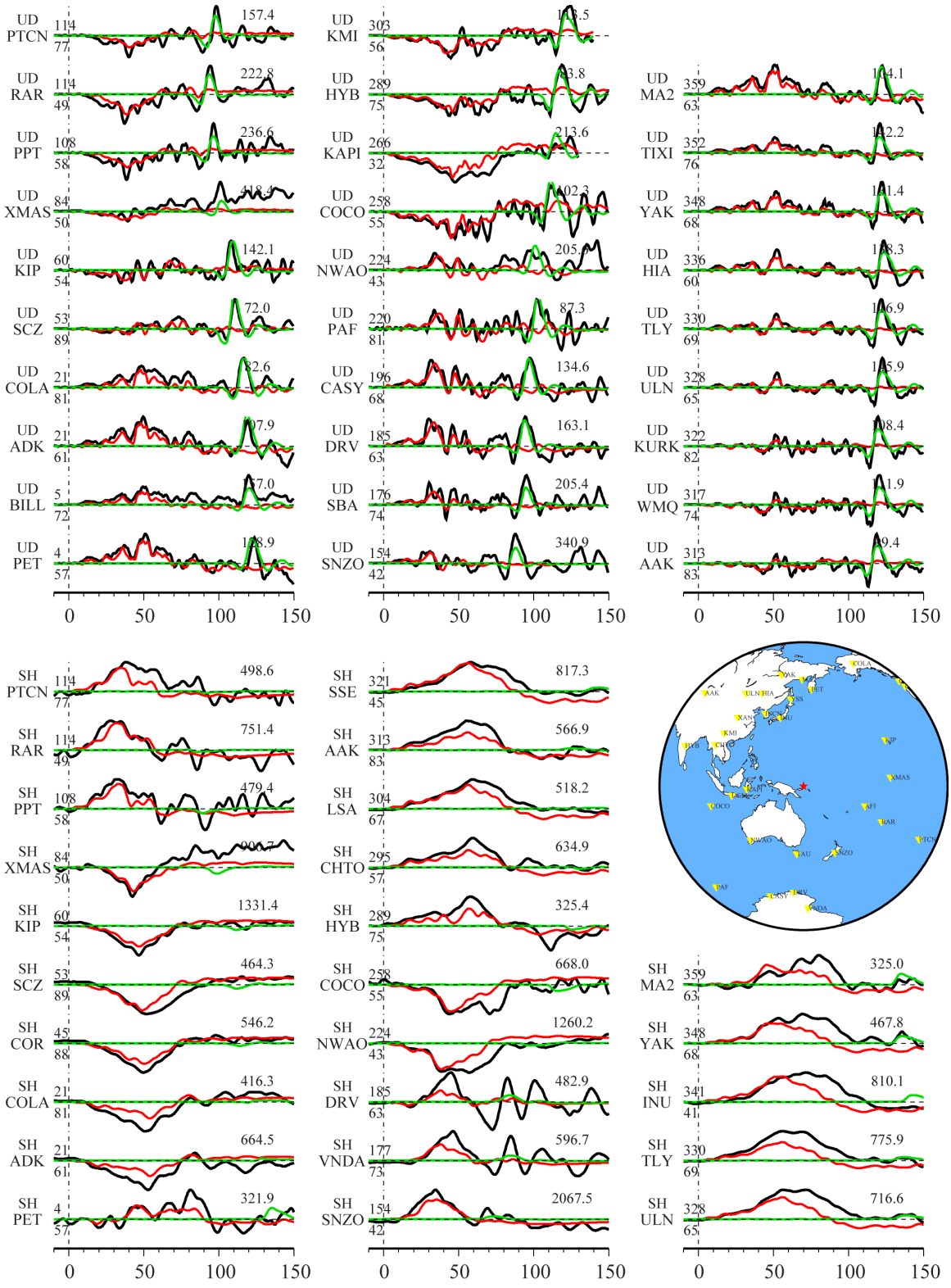
UD PTCN 114 77 157.4
UD RAR 114 49 222.8
UD PPT 108 58 236.6
UD XMAS 84 50
UD KIP 60 54 142.1
UD SCZ 53 89 72.0
UD COLA 21 81
UD ADK 21 61
UD BILL 5 72
UD PET 4 57
UD KMI 303 56
UD HYB 289 75
UD KAPI 266 32
UD COCO 258 55
UD NWAO 224 43
UD PAF 220 81 87.3
UD CASY 196 68 134.6
UD DRV 185 63 163.1
UD SBA 176 74 205.4
UD SNZO 154 42 340.9
UD MA2 359 63
UD TIXI 352 76
UD YAK 348 68
UD HIA 336 60
UD TLY 330 69
UD ULN 328 65
UD KURK 322 82
UD WMQ 317 74
UD AAK 313 83
SH PTCN 114 77 498.6
SH RAR 114 49 751.4
SH PPT 108 58 479.4
SH XMAS 84 50
SH KIP 60 54 1331.4
SH SCZ 53 89 464.3
SH COR 45 88 546.2
SH COLA 21 81 416.3
SH ADK 21 61 664.5
SH PET 4 57 321.9
SH SSE 321 45 817.3
SH AAK 313 83 566.9
SH LSA 304 67 518.2
SH CHTO 295 57 634.9
SH HYB 289 75 325.4
SH COCO 258 55 668.0
SH NWAO 224 43 1260.2
SH DRV 185 63 482.9
SH VNDA 177 73 596.7
SH SNZO 154 42 2067.5
SH MA2 359 63 325.0
SH YAK 348 68 467.8
SH INU 341 41 810.1
SH TLY 330 69 775.9
SH ULN 328 65 716.6
0 50 100 150

Figure S4.1(a): Waveform comparison of teleseismic body waves, green line denotes the waveform yielded by the second normal fault event.

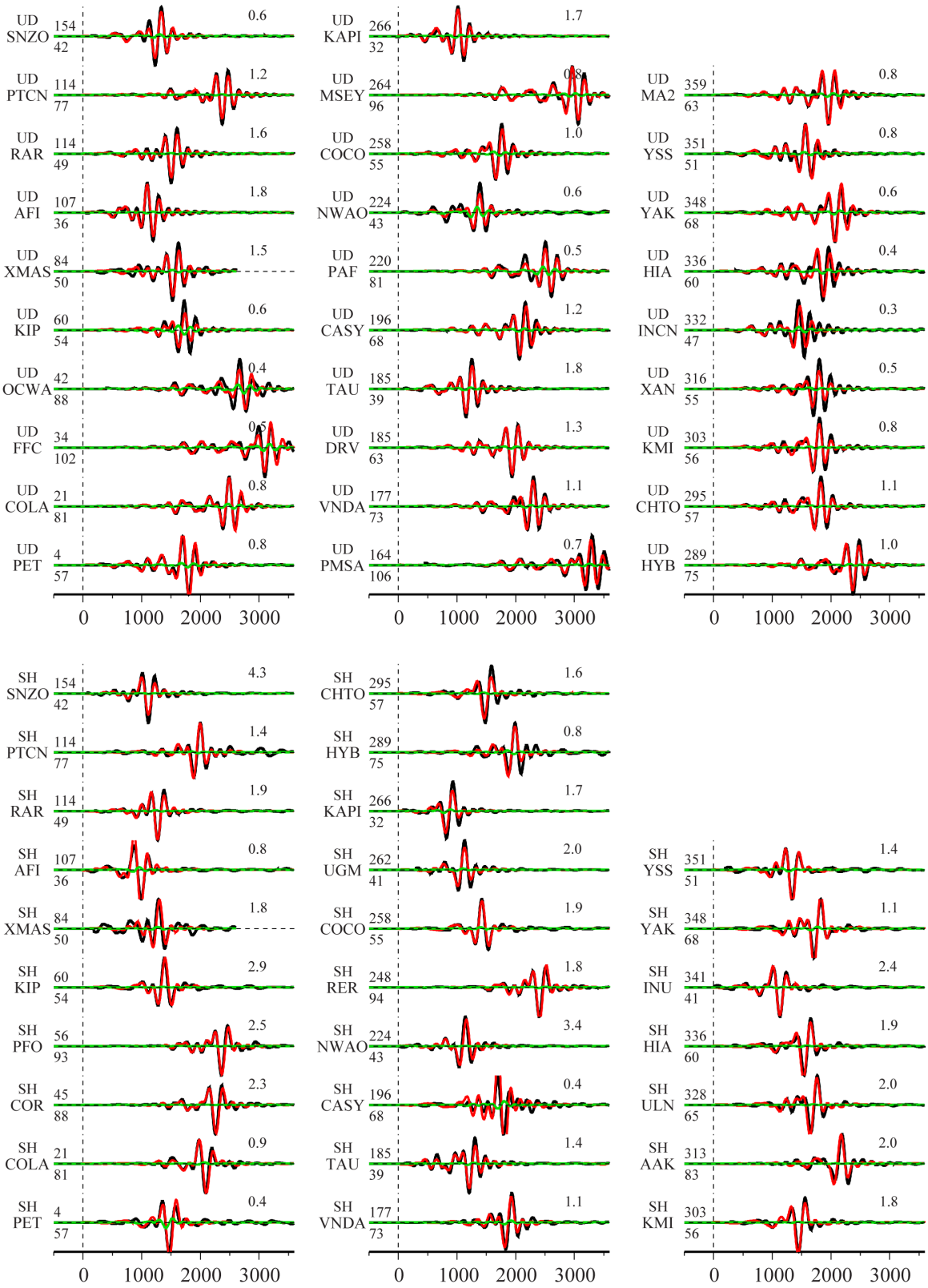

Figure S4.1(b): Waveform comparison of long-period waves.

Chapter 5

Rupture History of the 2013 Makran Earthquake and the Dynamic Stress Triggering of the Gwadar Mud Volcano

Abstract:

The slip history of the 24 September 2013 Mw 7.7 Balochistan earthquake is constrained by jointly inverting teleseismic body waves and long-period surface waves. The inversion results in a preferred rupture model where the rupture initiates on a sub-vertical north-dipping fault and unilaterally propagates 150 km southwest with an average rupture velocity of 3.0 km/s. The rupture duration is about 60s; most of the significant slip occurred in the top 15 km. The cumulative seismic moment is 5-6x10^{20} Nm. Using the preferred rupture model as input, we estimate the dynamic stress perturbation in the Pakistan coastal region. The peak amplitude of the induced transient volumetric stress and Coulomb stress are 0.2-0.3 MPa and 1-2 MPa, respectively, at the mud volcano eruptions near coastal cities Gwadar and Ormara. The static stress perturbation from the model cannot simultaneously explain the two mud volcano eruptions.

5.1 Introduction

Mud volcanoes are eruptions of mixtures of water, fine sediment, and gas at depth [*Manga and Bonini*, 2012]. The mud source typically occurs at depths of 1–3 km [*Davies and Stewart*, 2005; *Kopf*, 2002; *Mazzini et al.*, 2007] and is blocked by impermeable structures above the source depth. Mud volcanoes usually occur in regions of rock formations with high sedimentation rates that are in compressional tectonic settings. Observed mud volcanoe eruptions shortly after nearby earthquakes suggest a causal relationship. *Manga et al.*[2009] recently reviewed various triggering mechanisms of mud volcanoes due to earthquakes. They concluded that the triggering most likely results from dynamic strain perturbation. However, the amplitude of dynamic strain induced by earthquakes at mud volcano sites has not been calculated.

Pakistan is near the triple junction of Indian, Arabian, and the Eurasian Plates (Figure 5.1). To the south, the Arabian Plate obliquely subducts beneath the Eurasian Plate along the Makran Trench at a rate of 33 mm/yr in the N16^{o}E direction (GEODVEL, [*Argus et al.*, 2010]). To the east, the India Plate moves northwards and collides with the Eurasian Plate. As a consequence, Pakistan is one of the most earthquake prone countries in the world. On 24 September 2013, a powerful earthquake shook the Balochistan province of Pakistan. The United States Geological survey (USGS) locates the epicenter at 26.971^{o}N 65.520^{o}E—east vicinity of the central Makran mountain range (Figure 5.1). Quick moment tensor analyses (e.g., USGS W-phase solution: http://comcat.cr.usgs.gov/earthquakes/eventpage/usb000jyiv#scientific; GCMT http://www.globalcmt.org) revealed that this earthquake is M_w 7.7 dominated by left-lateral strike-slip motion on a NE-SW extending fault dipping 45°.

Although the earthquake occurred in the remote region of Pakistan, there were 825 fatalities with a Mw 6.8 aftershock occurring four days later that killed another 22 people.

Barely half an hour after the 2013 Balochistan earthquake, people of the Pakistan coastal town of Gwadar, 380 km away from the mainshock epicenter (Figure 5.1), saw a new island emerge in the sea, approximately 500 m away from the coastline. This oval-shaped island was named Zalzala Jazeera ("quick island"). According to a Pakistan Navy team which visited the island the day after it appeared, this new island is 18 m high, 30 m long, and 76 m wide. It has a rough surface, much of which is muddy and some parts are mostly made up of fine- to coarse-grained sand (BBC news, last retrieved on July 16, 2014). WWF-Pakistan also reported that near another coastal city Ormara, approximately 250 km away from the mainshock hypocenter and 200 km east of Gwadar, two smaller islands with a diameter of about 9-12 m and a height of 0.6-0.9 m above sea surface appeared.

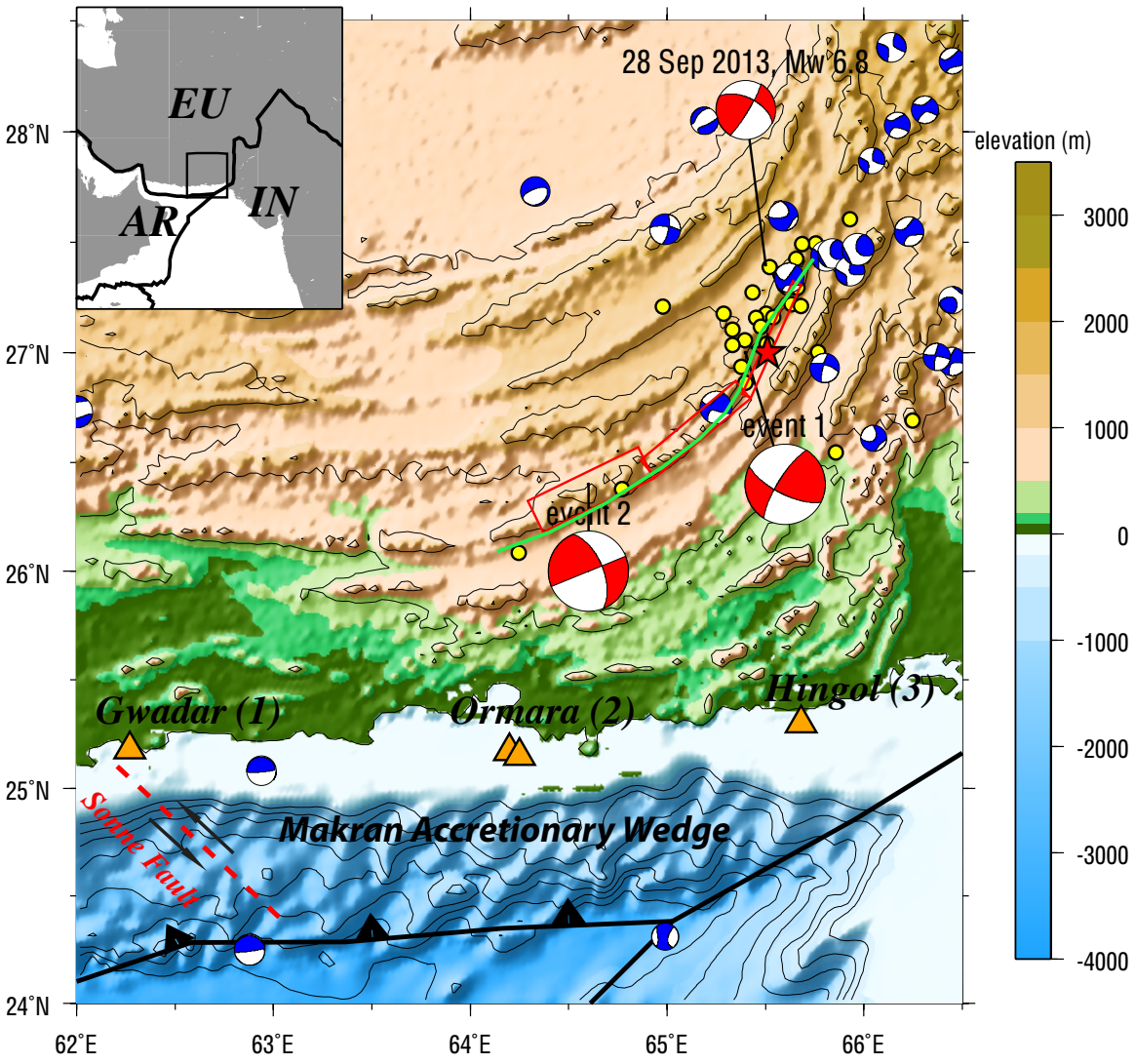

Figure 5.1: Basemap for the 24 September 2013 Parkistan earthquake. The locations of the sequential emerging mud volcanos in Gwadar and Ormara, as well as the historical mud volcanos in Ormara, Hingol are plotted with orange triangles. The red beachballs represent the focal mechanisms of two subevents during the mainshock resolved by our MDC analysis and the largest aftershock (Mw 6.8) on 28 September. The blue beachballs denote the surrounding focal mechanisms of historical earthquakes between 1976 and 2013 from the GCMT catalog. Yellow dots are epicenters of aftershocks of the 24 September mainshock within the following three weeks. The red rectangles show the location of the surface

projection of our slip model; red star marks the mainshock epicenter. EU, AR and IN indicate the Eurasia, Arabian and India Plate, respectively. The red dotted line signifies the approximate location of the left-lateral strike-slip Sonne fault in the Makran Accretionary Wedge [*Kukowski et al.*, 2000]

The formation of these islands is apparently the result of mud volcano eruptions, which are not unprecedented in this region. South of the Pakistan coast, Arabian Plate subducts beneath Makran margin with a dip angle of 2^{o}-3^{o}. Large portions of sedimentary layers above the Arabian Plate are scraped off to form a large geologic structure referred to as the Makran Accretionary Prism. Overpressurized fluids and possible gas hydrates have been trapped in this Makran prism, resulting in mud volcanoes reported both onshore and offshore. The reemergence of mud extrusion has been previously related with seismic activity. For instance, eruptions of mud volcanoes near coastal cities Gwadar, Ormara and Hingol were reported after the 1945 Mw 8.0 Makran megathrust earthquake [Sondhi, 1947]. However, we have found no report of mud volcano activity near Hingol after the 2013 Balochistan earthquake.

The temporal correlation between these new islands and the 2013 Balochistan earthquake motivates us to investigate their dynamic relationship. We first invert teleseismic records to obtain a kinematic finite fault rupture for the 2013 Balochistan earthquake. Next we predict the dynamic strain and stress field along the coast of Pakistan, particularly for sites near Gwadar, Ormara and Hingol. We limit our discussion to the triggering mechanisms of the Gwadar mud volcano based solely on the dynamic and stress perturbation induced by co-seismic rupture.

5.2 Finite fault inversion

The earthquake occurs in a remote area of Pakistan where no near-fault seismic observations are publicly available. Our study relies solely on distant observations, which are freely available at IRIS DMC (http://www.iris.edu). We selected broadband waveforms of 27 P waves and 25 SH wave (Figure 5.2) as well as 100 long-period (3-6mHz) seismic signals recorded in vertical and transverse components. We conducted a multiple double-couple (MDC) analysis using the long-period seismic data. This revealed that the 2013 Balochistan mainshock included at least two subevents with different focal mechanisms. The result is shown in Figure S5.1 and Figure S5.2. Details of MDC analysis are given in the appendix.

Figure 5.2: Station distribution

We subsequently use three 63 km (along strike) by 28 km (down-dip) fault segments to approximate the curved causative fault of the 2013 Balochistan earthquake (Figure 5.1).

Hereafter, we refer them as NNE, MD, and SW fault segments from north-northeast (NNE) to southwest (SW). Their strikes are 204^{o}, 230^{o} and 244^{o}, respectively, based on the solution of our MDC analysis (Figure S5.2 and Appendix) as well as the surface deformation observed from optical images ([*Avouac et al.*, 2014; *Jolivet et al.*, 2014]). The preferred fault dips of these three fault segments are 80°, 65°, and 50°, respectively, gradually decreasing from NNE to SW. These dip angles are determined based on our preliminary joint inversions of broadband body waves and long-period seismic waves. Multiple trial finite fault inversions were conducted to look for the optimal position of the intersection of the NNE and MD fault segments. The surface projection of this complicated fault geometry is shown in Figure 5.1. This fault geometry is consistent with that of *Jolivet et al.* [2014] who inferred it based on modeling of satellite optical images. We let the rupture initiate on the NNE fault segment at a depth of 10 km beneath the USGS PDE epicenter (27.00°N, 65.51°E).

Three fault segments (in total) are discretized into 189 subfaults, 7 km x 4 km. The rake angle, slip amplitude, rupture initiation time and the source time function of each subfault are simultaneously inverted by matching the waveforms in the wavelet domain with a simulated annealing method [*Ji et al.*, 2002a; *Ji et al.*, 2003a]. We allow the rake angle to vary from -15° to 45°, slip amplitude from 0 m to 15 m, and rise time from 1.2 s to 12 s. A 1D-layered structure (Figure S5.3) modified from the global CRUST2.0 [*Bassin et al.,* 2000] is used to approximate the near-fault velocity structure. The synthetics of body waves are computed using the first motion approximation algorithm [*Langston and Helmberger*, 1975]; surface waves computed using the normal mode superposition algorithm [*Dahlen and Tromp*, 1998].

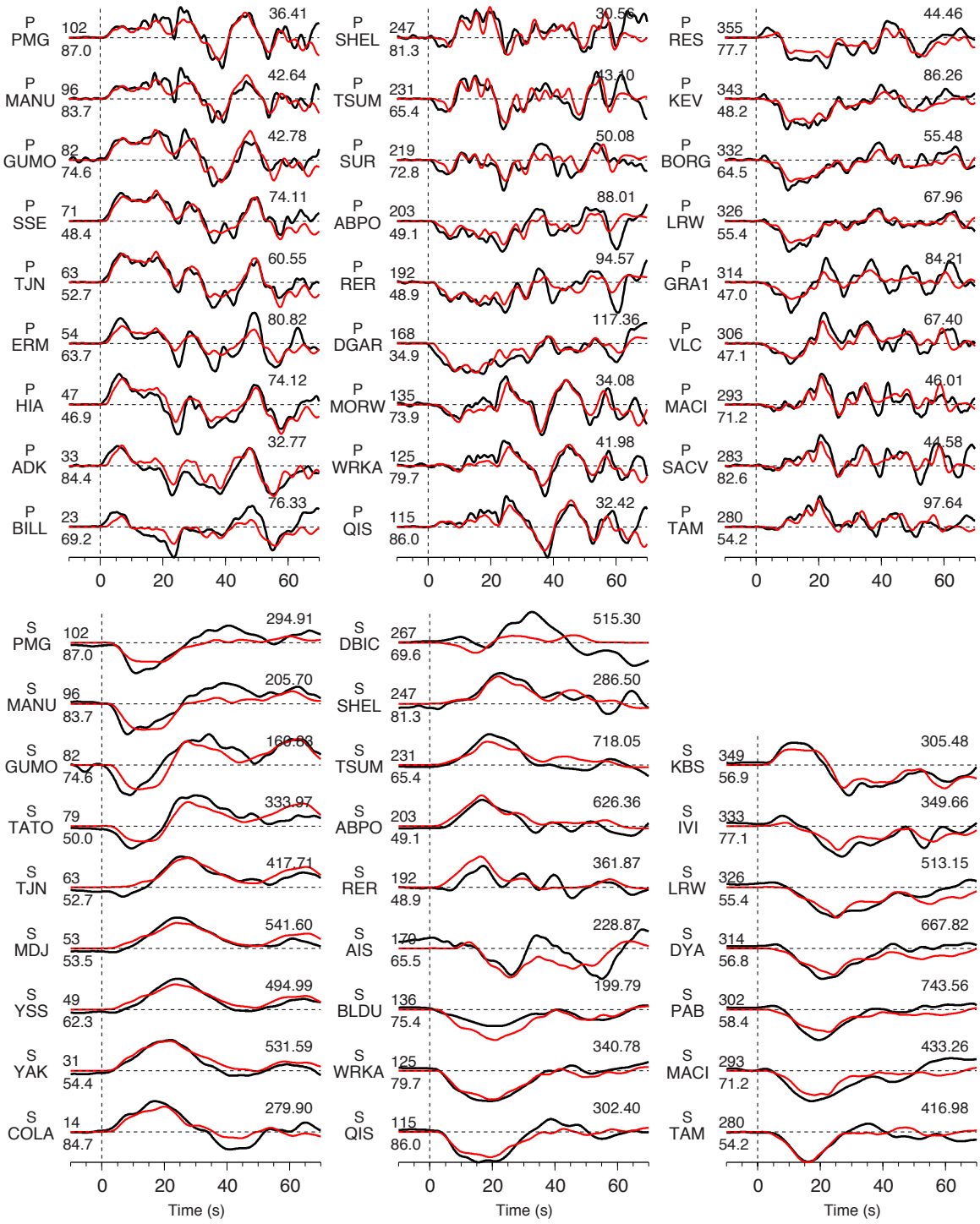

Figure 5.3a: Comparison of teleseismic waveforms for data (black) and synthetics (red). The number at the end of each trace is the peak amplitude in micrometers. The number above the

beginning of each trace is the station azimuth and below it is the epicentral distance in degrees.

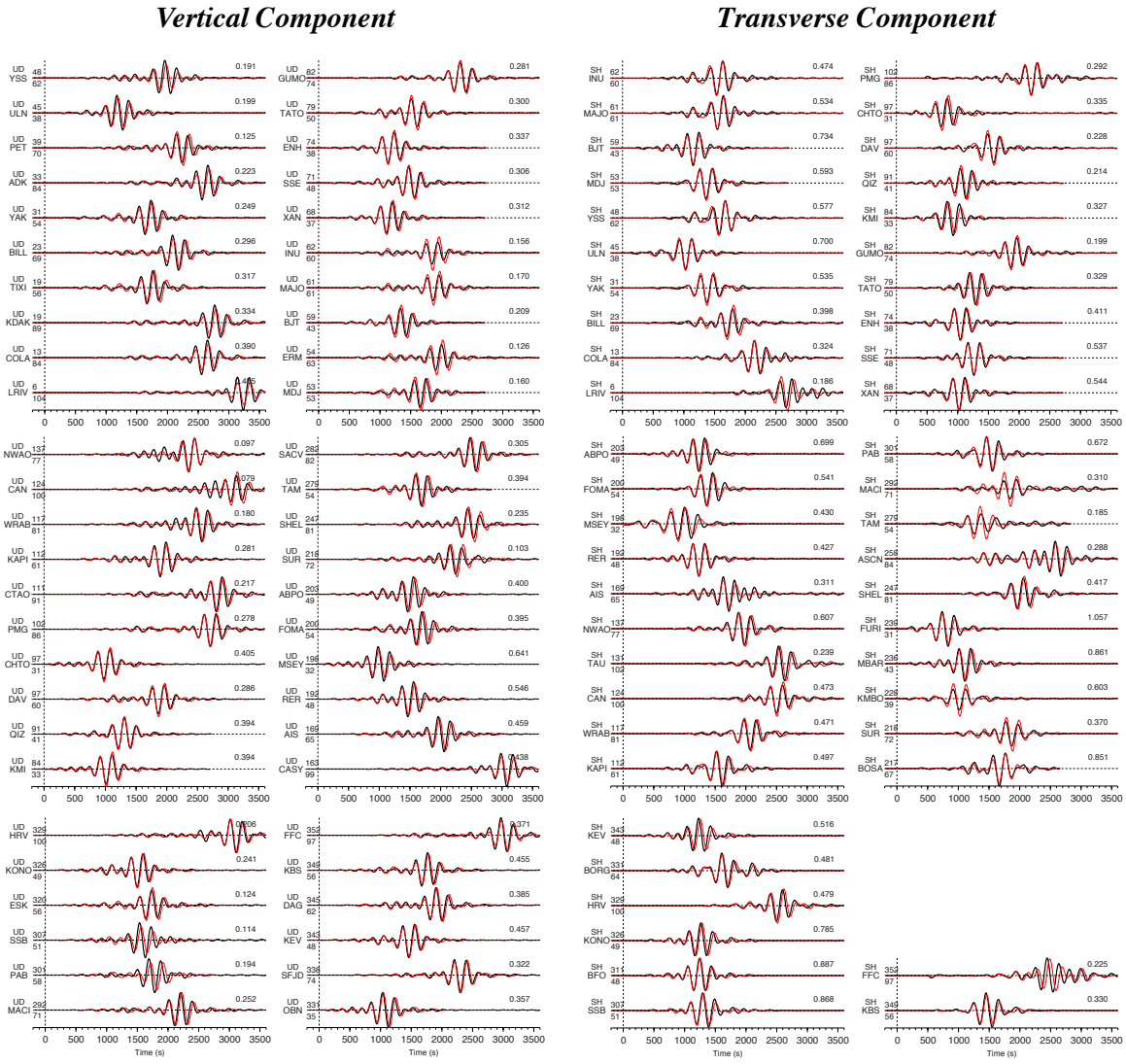

Figure 5.3b: Waveform fit of vertical and transverse components of long-period surface waveforms; black are data, red are synthetics. The number at the end of each trace is the peak amplitude in millimeter. The number above the beginning of each trace is the azimuth of this station and below is the epicentral distance.

As demonstrated by the comparisons of data and synthetics (Figure 5.3), our preferred slip model explains the seismic data well. Figure 5.4(a) shows the inverted fault slip. The 2013 earthquake is dominated by a 60-70 km long fault patch, extending roughly from the hypocenter to 60 km south-southwest. A secondary asperity centered about 90 km southwest is also well resolved. The total seismic moment is 5.73×10^{20} Nm (Mw 7.76), which is slightly larger than the estimate of Global CMT (5.59×10^{20} Nm). The peak slip is 15 m, which occurs on the MD fault segment. Figure 5.4(b) shows the rise time distribution. Note that only when a subfault has significant slip, can the rise time be resolved. We estimate the weighted average rise time as $(\sum_i D_i T_i)/(\sum_i D_i)$, where D_i and T_i denote the slip and rise time of the i-th subfault ([*Ji et al.*, 2002b]), yielding an estimate of 4.8 s. Figure 5.4(c) shows the distribution of average slip rate, which is simply defined as the ratio of fault slip and rise time at each subfault. Because the far field displacement is proportional to the cumulative moment rate of fault rupture, the subfaults with larger slip rate are generally better constrained during the waveform inversion. We are more interested in the average slip rate associated with the subfaults with significant slip. We estimate the weighted average slip rate of the entire fault as $(\sum_i D_i V_i)/(\sum_i D_i)$, where V_i and T_i denote the average slip rate and fault slip of the i-th subfault. The calculation yields an estimate of 2.4 m/s.

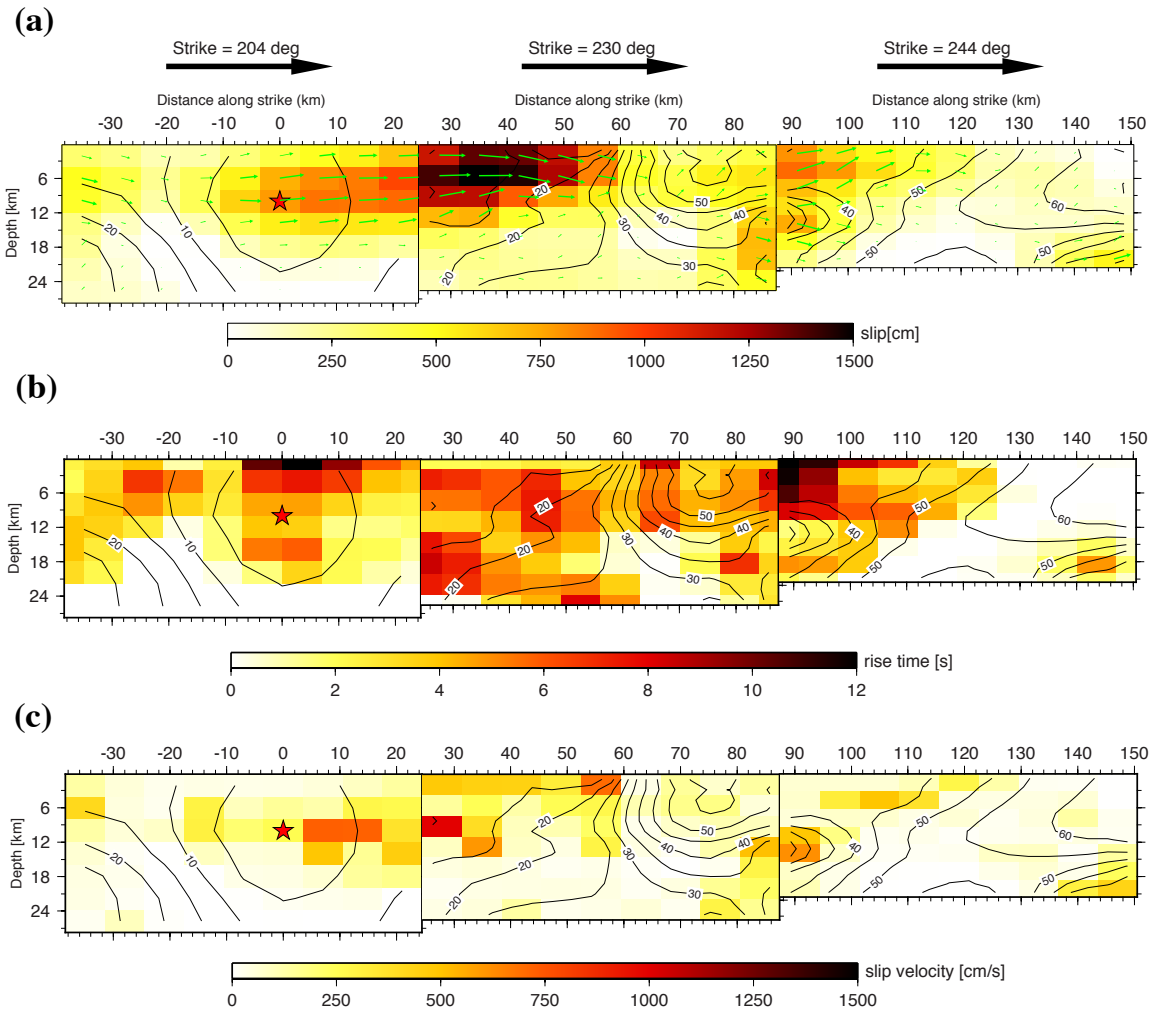

Figure 5.4: (a) Cross section of slip distribution. The strike direction of two fault planes is indicated by the black arrow. The red star marks the hypocenter. The slip amplitude is shown in color with the direction slip of the hanging wall relative to the footwall indicated by green arrows. Contours show the rupture initiation time in seconds. (b) Rise time distribution. (c) Slip velocity distribution.

The rupture of the 2013 Balochistan earthquake initiated energetically in the NNE fault segment and then propagated mostly unilaterally to the southwest direction. The rupture of the MD segments starts at about 10 s, 25 km SSW of the epicenter. The peak slip on the

fault is 14 m. At ~30 s, the rupture nearly stops at 60 km but it restarts at about 90 km. The peak slip of the third asperity is 9 m, though the resolution in this part of the rupture is relatively poor. Figure 5.5 shows the spatial-temporal moment distribution on the fault as a function of along-fault distance. The concentrated moment release primarily occurs during the first 60 km along the fault. The rupture velocity, based on distance from the hypocenter, varies between 2.0 km/s and 3.5 km/s with an average of about 3.0 km/s. However, we observe that centroid moment release at subfaults migrates with a velocity slower than 2.5 km/s. From our model, there is no evidence of super-shear rupture velocity.

Figure 5.6(a) shows the cumulative moment rate functions of three fault segments and their summation. A rupture propagation movie can be found in supplementary material (Movie 5.1).

The total rupture duration is 60 s (Figure 5.6(a)) but two-thirds of the total seismic moment occurs within the first 32 s. The cumulative moment rate (Figure 5.6(a)) during this period is composed of three major pulses at each 10 s time window. Although inversions allow slip to occur in a depth range as deep as 28 km, the majority of moment release and slip occurs within the top 15 km of the fault (Figure 5.6(b)).

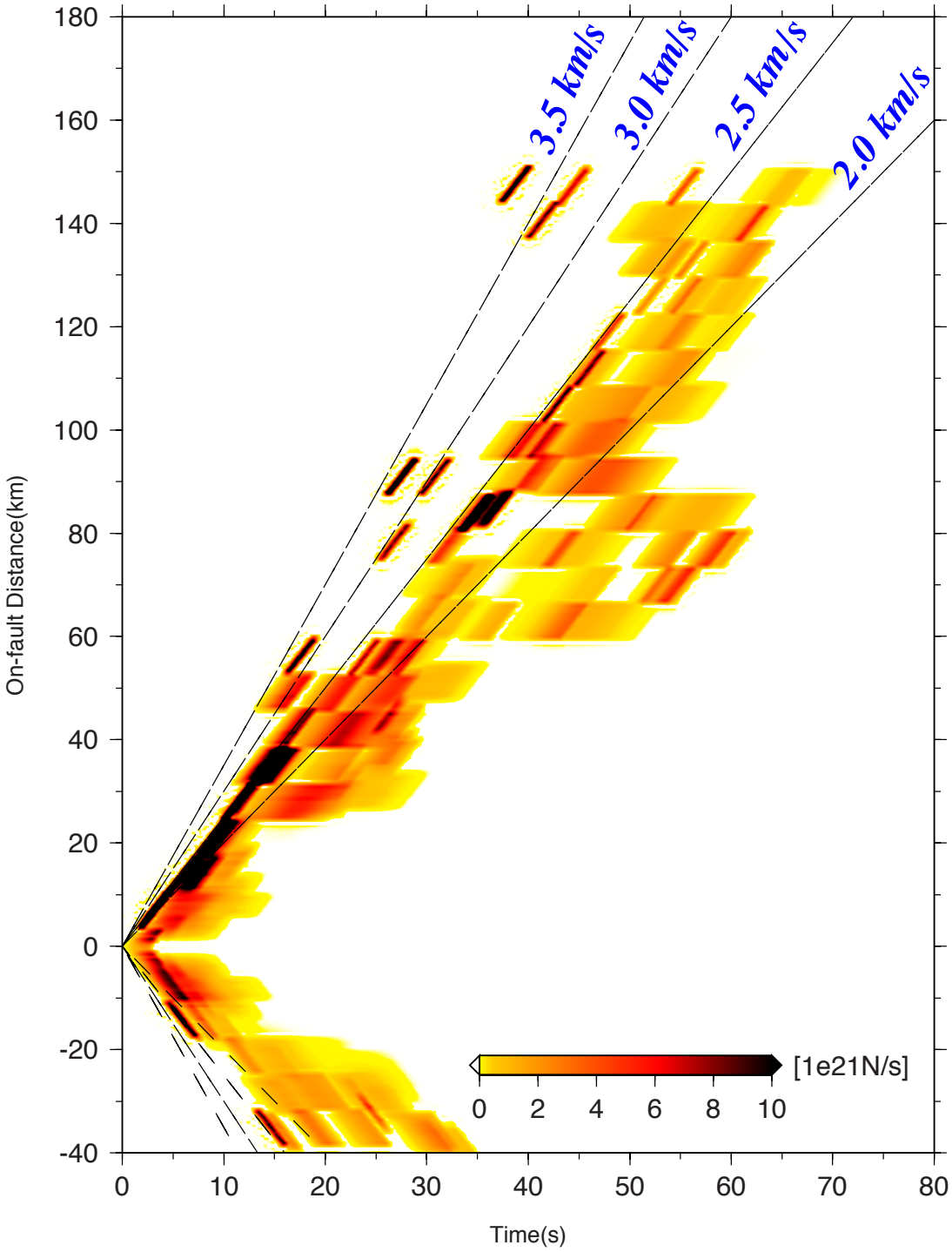

Figure 5.5: Spatial and temporal moment distribution projected along the fault. Zero on the vertical axis marks the mainshock hypocenter. Vertical axis indicates the along-fault distance from the hypocenter with the southwest direction being positive and northeast

direction being negative. The four lines correspond to rupture velocity of 2.0, 2.5, 3.0, 3.5 km/s. The average rupture velocity in both directions is around 2.5 km/s.

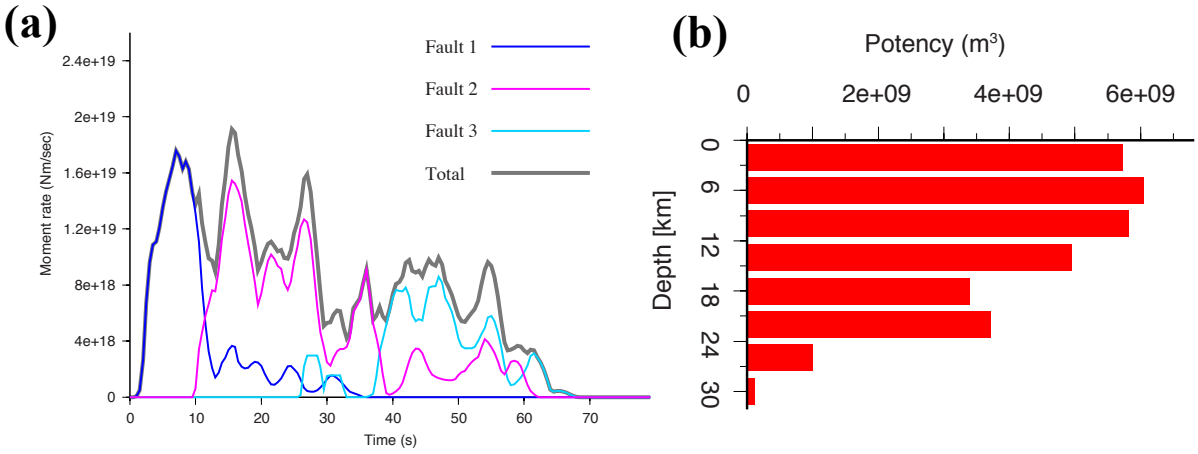

Figure 5.6 (a) Moment rate function, unit is Nm/sec. (b) Distribution of seismic potency (Mo/μ) with respect to depth.

The main features in our source model are robust whether we invert only body waves or jointly invert both body waves and surface waves. The surface waves provide a good constraint on the seismic moment $5.0\text{x}10^{20}$ – $6.0\text{x}10^{20}$ Nm, yielding Mw of 7.73 – 7.78. In contrast to the uniform, continuous, smooth rupture pattern of slip model found by *Avouac et al.*, 2014; *Jolivet et al.*, 2014 who used teleseismic P wave and remote sensing data, our model proposes an inhomogeneous slip distribution with spatial-temporal complexity in terms of slip segmentation and rupture lag. This difference arises mainly from the time reconciliation between body waves and long-period surface waves. The moment tensor of our finalized three-segment fault model has a CLVD component with $\varepsilon = -0.39$. This is

comparable with GCMT solution but much larger than that of MDC, which can be attributed to the dramatic change of dip angle during the rupture process.

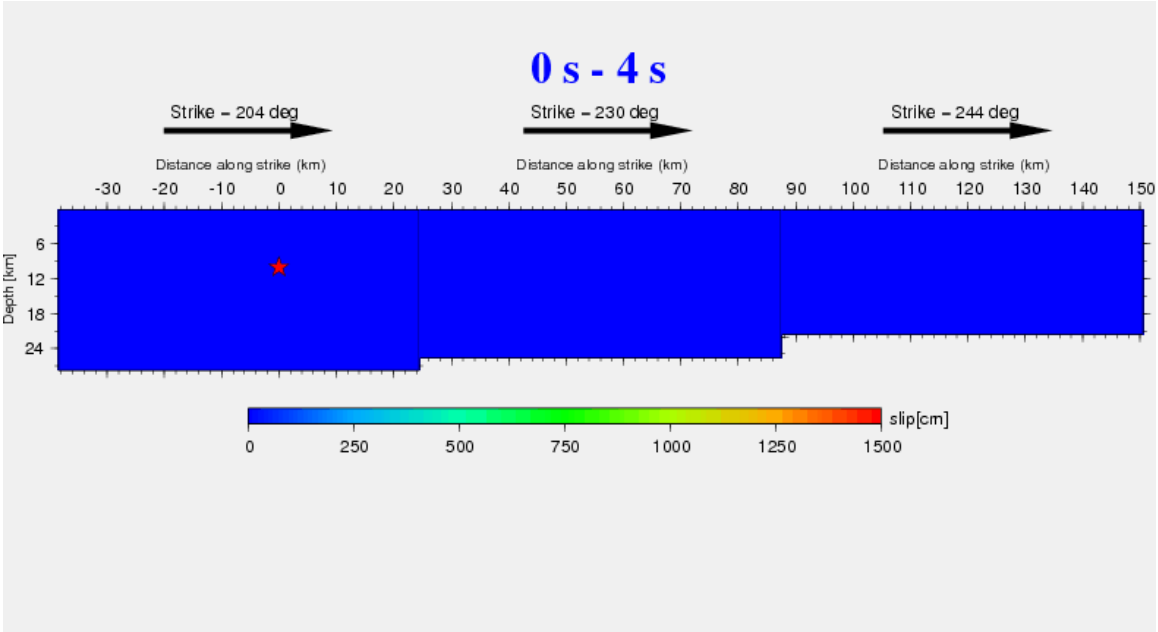

Movie 5.1: Snapshot of kinematic rupture process: Total time is 76s with 4 s intervals.

We forward predicted the synthetic ground motion at Gwadar mud volcano using our preferred slip model and 1D layered Earth model (Figure 5.7). The Earth response is calculated using FK code [*Zhu and Rivera*, 2002] for the 1D velocity model (Figure S5.3). The velocity waveforms are low-pass filtered to less than 0.33 Hz. Although Gwadar is 380 km from the epicenter, the predicted peak amplitudes of horizontal ground shaking are as much as 19 cm/s at the surface (solid lines, Figure 5.7). The peak amplitude of the vertical motion is only 8 cm/s. This is consistent with 2013 Pakistan earthquake being dominated by strike-slip motion. Note that Gwadar is near the P wave nodal plane of the MD and SW fault segments (Figure 5.1). The peak ground motions at Ormara and Hingol are comparable

though their vertical motions are larger. For a comparison, we also predict the particle velocity at a receiver depth of 3 km (red dashed lines, Figure 5.7). As expected, they are similar to the synthetics at surface in shape but are notably smaller. It is a common practice to estimate the dynamic stress using the simple relation $\tau \sim \mu V/c$; μ, V and c denote shear modulus, particle velocity, and wave speed, respectively. A rough estimate of peak dynamic stress at the 3 km depth is of the order of 1.5 MPa (assuming a shear modulus of 3×10^{10} N/m^2 and a near surface velocity of 3.5 km/s for Love wave).

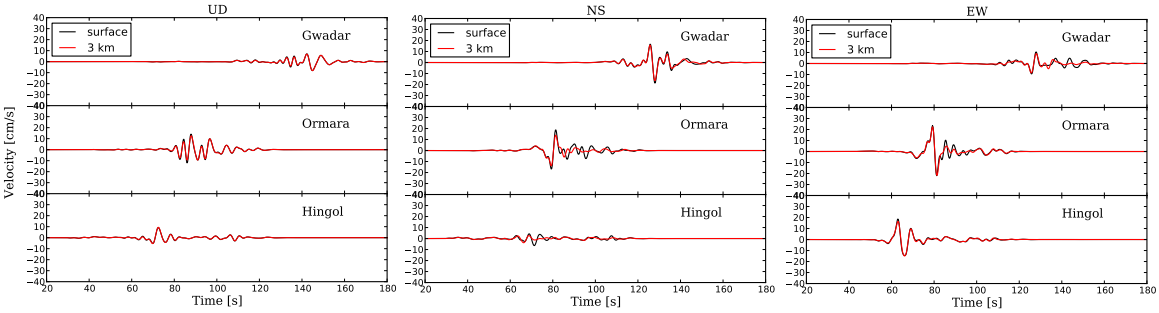

Figure 5.7: Predicted peak velocity seismograms at surface (black) and 3km depth (red) with low-pass filter at 3s at the location of three mud volcanoes. Three components are shown with UD (Vertical), NS (North-South) and EW (East-West). The number at the end of each trace is the peak amplitude in centimeters.

5.3 Static and dynamic stress perturbation at mud volcanoes

We subsequently forward predict the static and dynamic strain perturbation near these coastal cities. This is achieved by linearly differentiating synthetic displacement waveforms in 3D uniform grids. It is straightforward to calculate the corresponding dynamic stress perturbation using the elastic modulus derived from the same 1D velocity structure. The

precision of this calculation depends on the spatial grid space. For the period (> 3 s) we are using, the shortest S-wave wavelength is about 10 km. We adopted a horizontal spatial grid interval of 1.0 km and vertical grid interval of 0.5 km, which are less than one tenth of the shortest wavelength. According to our numerical tests, the precision of this calculation is sufficient.

Figure 5.8 shows the strain and stress calculations at the location of the Gwadar mud volcano at a receiver depth of 3 km. The mud source of Gwadar mud volcano is not known. Typical mud source locates at depth of 1~3 km though a deeper source is possible [*Kopf*, 2002]. The occurrence of earthquakes can influence eruptions of nearby mud volcanoes by compressing the mud source. Figure 8a shows a snapshot of the dynamic volumetric strain perturbation ($\varepsilon_{kk} = \varepsilon_{11} + \varepsilon_{22} + \varepsilon_{33}$) at 144 s after the mainshock rupture initiation. At this moment, the amplitude of dynamic volumetric strain perturbation reaches its maximum $7x10^{-6}$ (for the period range > 3 s) at the Gwadar mud volcano.

Figure 5.8(b) shows the waveforms of all six independent stress components, σ_{11}, σ_{12}, σ_{13}, σ_{22}, σ_{23} and σ_{33}, and the volumetric stress σ_{kk} at the depth of 3 km. In our definition, the indices 1, 2, and 3 are for north, east, and depth directions, respectively. Dilation is positive and compression is negative. Components σ_{11}, σ_{12} and σ_{22} are dominant terms with peak amplitudes of 1.2 MPa, 0.6 MPa and 1.0 MPa, respectively. In contrast, the peak amplitudes of σ_{13}, σ_{23} and σ_{33} are less than 0.3 MPa. Such a difference is expected. Because of the free surface boundary condition, the latter three stress components would be zero on the free surface. We point out that for this circumstance, the stress components σ_{11} and σ_{22} are anti-correlated and have similar peak amplitudes.

In Figure 5.8(a), P_n and S_n denote the first arrivals of P and S waves, respectively. The stress perturbations carried by these body wave phases are not significant. The stress component σ_{11}, σ_{12} and σ_{22} reach the maximum at about 130 s, associated with the arrival of Love waves excited by the rupture of the MD and SW fault segments. The σ_{33} and σ_{kk} reach the maximum amplitude 14 s later, associated with the Rayleigh waves that are radiated mainly from the NNE fault segment. The peak volumetric stress is 0.24 MPa. In contrast, the predicted static volumetric stress is -1.0×10^{-3} MPa. While a static compressional (negative) volumetric stress promotes the mud volcano eruption, its amplitude is two orders of magnitude smaller than the dynamic volumetric stress.

Figure 5.8(c) shows the amplitude spectrum of the stress components. At Gwadar all have a dominant spectral peak at 1/8 Hz and two secondary peaks at 1/20 Hz and 1/4 Hz. This is presumably a combination of source radiation spectrum and propagation effects. As shown in Figure 8d, at 3.0 km depth the peak amplitude of the stress component σ_{11} changes by a factor of seven from 1.4 MPa to 0.2 MPa, when we lowpass filter the synthetic waveform to less than 0.08 Hz. The corresponding volumetric stress becomes less than 0.06 MPa.

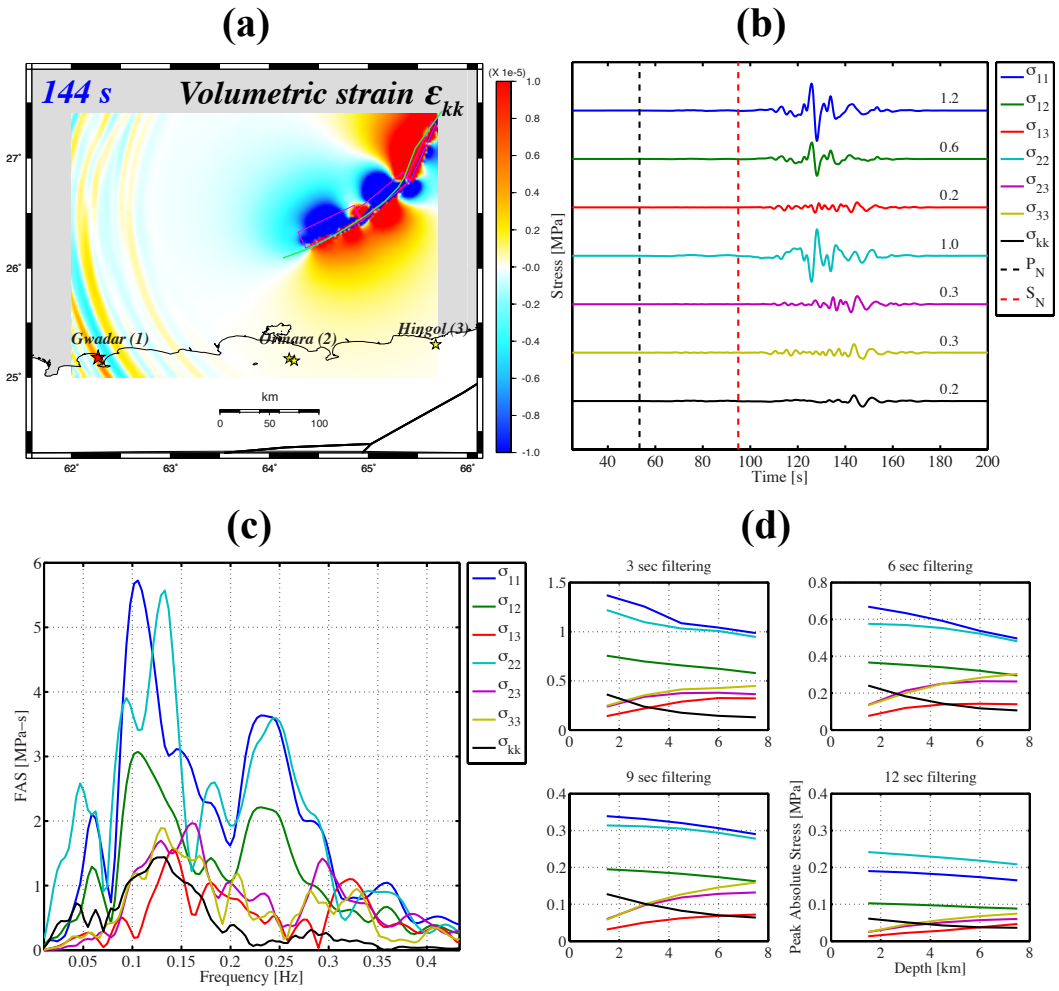

Figure 5.8: Dynamic stress perturbation at mud volcano offshore Gwadar (1) region (Red star: 62.27°E, 25.18°N). (a) Dynamic stress field of σ_{11} (NS) at 124s corresponding to the approximate arrival of the peak amplitude of the Love wave. All seismograms are low-pass filtered at 3 s.. The peak amplitude at is about 2.5 MPa. Red rectangle indicates the surface projection of our source model. (b) Predicted synthetic waveforms of six stress components low-pass filtered at 3s. σ_{kk} represents the volumetric component $(\sigma_{11}+\sigma_{22}+\sigma_{33})/3$. The number at the end of each trace is the absolute peak amplitude in MPa. Black and red dotted line indicate the predicted arrival time of the P and S wave, respectively. (c) Corresponding

Fourier amplitude spectra of six stress components and σ_{kk}. (d) The absolute peak amplitude of six stress components with respect to the depth for low-pass filters at 3s, 6s, 9s, and 12s to investigate any dependency on frequency.

Because the peak stress perturbations are carried by the surface waves, their values are depth dependent. As shown in Figure 5.8(d), when the depth of receivers increases from 1.5 km to 7.5 km, the peak amplitudes of stress components σ_{11}, σ_{22}, and σ_{12} gradually decrease by about one third, whereas stress components σ_{13}, σ_{23}, and σ_{33} steadily increase with depth by roughly a factor of two. The peak volumetric stress σ_{kk} decreases with depth by roughly a factor of two. The amplitude decay is sensitive to the frequency content and is generally smaller for long-period seismic waves (Figure 5.8(d)).

In Figure 5.9 we explore the decay of volumetric stress with distance along a line from the mainshock epicenter to the Gwadar. This line roughly follows the direction of rupture southwestward propagation. If we project the fault to this line, the southwest end of SW fault segment is at 150 km and Gwadar is at 380 km. As shown in Figure 5.5, most of seismic energy is radiated from the asperity near the epicenter. The peak volumetric stress decays with the distance roughly as 1/r, r is the epicentral distance (Figure 5.9). This observation is consistent with the result of *Antonioli et al.,* [2004] who found that the peak dynamic Coulomb stress decays as 1/r. However, if we low-pass filter the data to be less than 0.1 Hz, the decay rate becomes more like $1/\sqrt{r}$, when the site is 50 km away from the southwest end of fault (Figure 5.9).

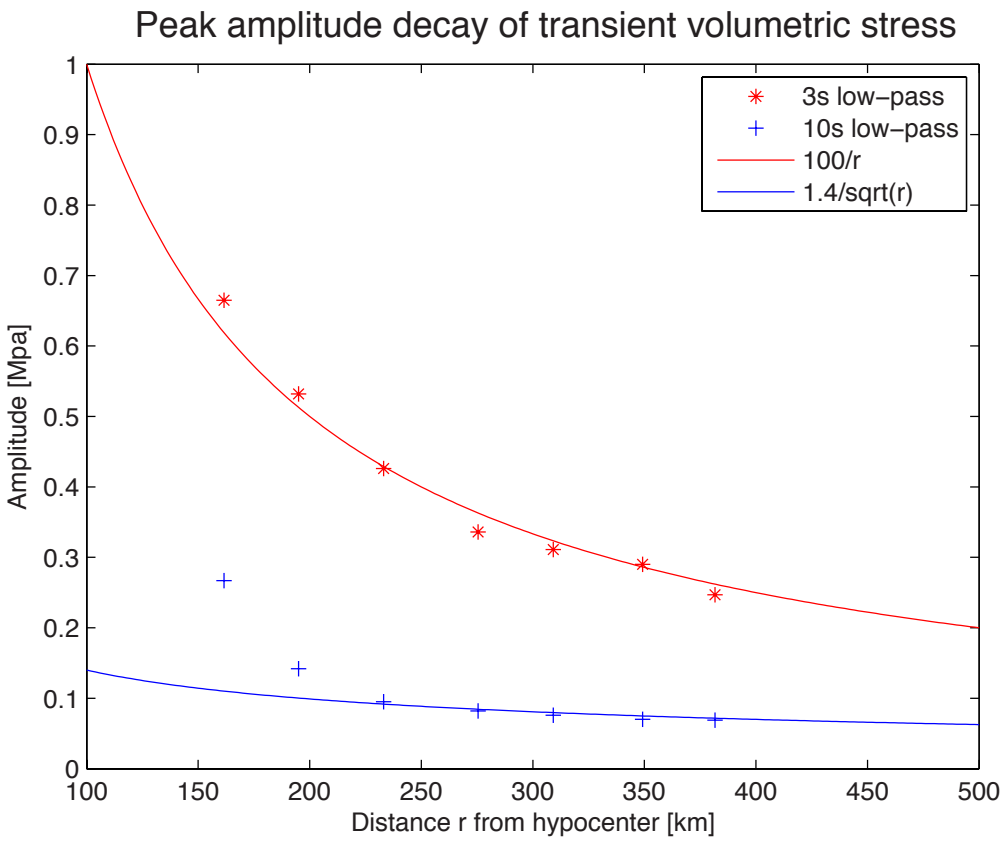

Figure 5.9: Frequency-dependent attenuation of dynamic volumetric stress plotted as a function of distance. Note that frequency bands above 3s and above 10s have different decay factors of 1/r and $1/\sqrt{r}$. The distance is calculated from hypocenter and the overall fault rupture length is about 150km. The points are equally sampled between the end of the fault (shortest distance) and mud volcano offshore Gwadar (longest distance).

Two small mud islands offshore the town of Ormara were reported having gas coming out after the 2013 mainshock. We calculated the induced static and dynamic stress change generated by the mainshock in this region. However, with no available time and location information for these two mud volcanoes, we simply assign the location of mud volcano as (25.17°N, 64.20E°), which is the location of the historical mud volcano that erupted after the

1945 Makran megathrust [*Sondhi,* 1947]. The results are shown in Figure 5.10. Moreover, we also calculated the strain and stress waveforms at Malan Island (25.30°N, 65.68°E) near Hingol. Although no mud island was reported at this location after the 2013 mainshock, mud islands emerged at the same spot in November 1945, March 1999 and November 2010 [Kassi et al., 2013]. The strain and stress computed at Hingol are shown in Figure 5.11.

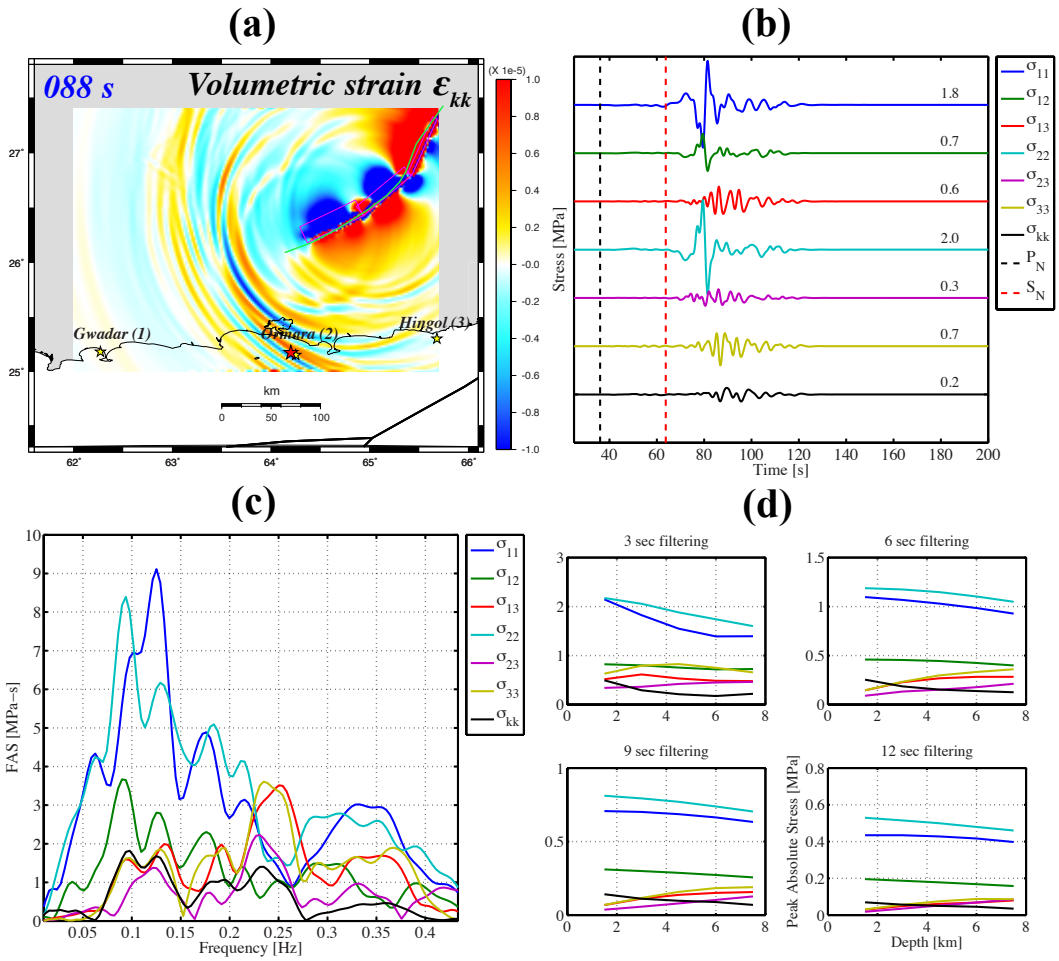

Figure 5.10: Same as Figure 5.8 but for mud volcano offshore Ormara (2) region (red star: 64.20°E, 25.17°N).

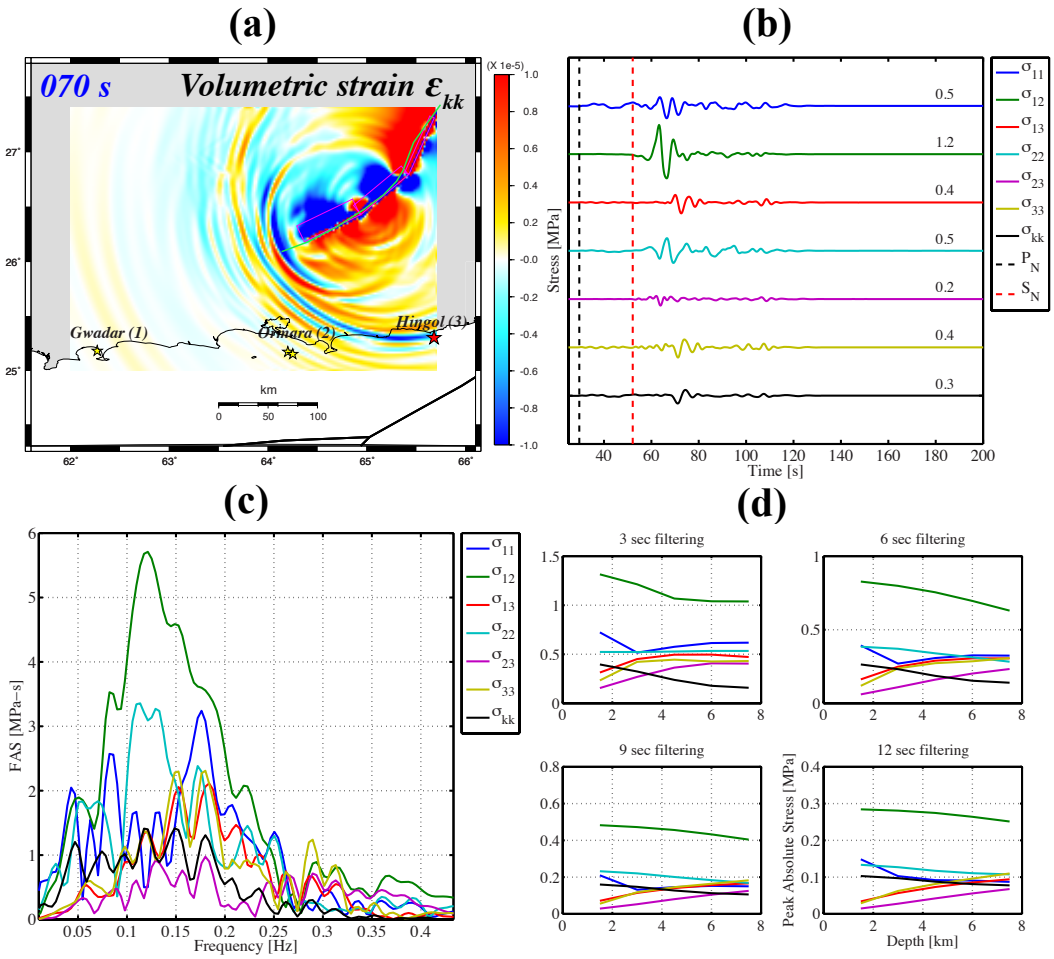

Figure 5.11: Same as Figure 5.8 but for mud volcano offshore Hingol (3) region (red star: 64.20°E, 25.17°N).

The synthetic dynamic stress tensors at sites near two other coastal cities Ormara (Figure 5.10) and Hingol (Figure 5.11) share several consistent features with those of Gwadar volcano. First at Ormara and Hingol the induced static volumetric strain change is ~2.0×10^{-7}, with corresponding volumetric stress change of ~0.01MPa. This amplitude is negligible compared to the peak dynamic volumetric strain of 0.5-0.7x10^{-5} and peak volumetric dynamic stress of 0.2-0.3 MPa. Secondly, horizontal stress tensor components have much

larger amplitudes than their volumetric stress change, presumably due to the dominant strike-slip motion of mainshock. Third, the dominant spectrum peak is at about 1/8 Hz (Figures 5.8(c), 5.10(c) and 5.11(c)). Finally, the peak amplitude variations due to frequency content and depth are pretty similar to those computed for Gwadar.

Mud volcanoes are often associated with weak zones, such as anticlines and vertical faults. The passage of the seismic waves can accelerate the process of shear fractures in these weak zones or slip on a fault producing a free pathway for high-pressure deeper fluids to travel upwards (e.g., [*Mazzini et al.*, 2009]). Assuming that the triggering of weak zone or fault slip follows the static and dynamic Coulomb failure criteria, the stress impact can also be estimated with the information of the target fault.

As shown in Figure 5.1, there is a NW oriented strike-slip fault named "Sonne" across the Makran accretionary wedge. The Gwadar mud volcano locates roughly at the northwest extension of this fault. Geomorphological evidence suggests that this left-lateral fault has been active about 2 ma with a slip rate of 5-7 mm/yr [*Kukowski et al.*, 2000]. *Kukowski et al.* [2000] proposed that the fault cuts through the down-going subducted plate and deforms the Makran accretionary wedge by basal traction. Bonini et al. (2014, unpublished manuscript) found that the new island shows a subtle but clear elongation in an N122^{o}E direction, which may suggest that the mud volcano system was controlled by a similarly oriented local feeder dyke. We assume that the target fault plane has a strike of 315 ° and dip of 80 °, analogous to Sonne fault, for which we calculate the dynamic Coulomb stress perturbation. A typical friction coefficient of 0.4 is used.

Figure 5.12 compares the waveforms of volumetric stress and Coulomb stress. The peak Coulomb stress is associated with the arrival of Love wave at about 130 s, while the volumetric stress is associated with the Rayleigh wave at about 144 s. The computed peak Coulomb stress at 3 km depth is ~1.5 MPa, about 6 times of that of dynamic volumetric stress 0.25 MPa. However, for the signal with periods larger than 10 s, the peak Coulomb stress reduces to 0.29 MPa, which is only four times of that of dynamic volumetric stress 0.07MPa in the same period band.

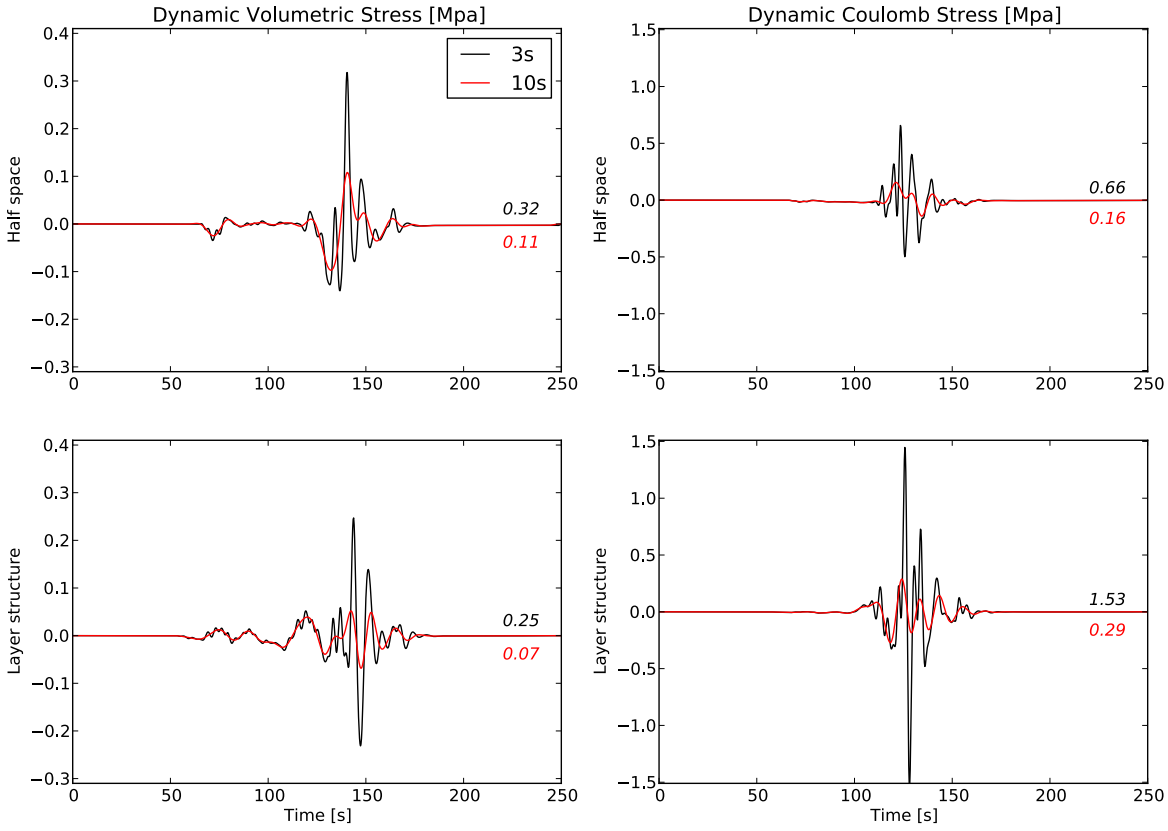

Figure 5.12: Comparison between dynamic volumetric (left) and Coulomb stress (right) using half-space model (up) and 1-D layer model (down). The black line and red line denote stress waveforms that are low-passed filtered at 3s and 10s, respectively. The peak amplitudes are shown on the right side of the plot.

5.4 Discussion

The synthetic dynamic stress estimates shown in the previous section are affected by the uncertainties in source model and velocity structure. *Antonioli et al.,* [2004] showed that the rise time and the rupture directivity are more important for characterizing the simulated stress time histories than the details of the rupture history. According to our best experience, the average rise time and directivity are two of the robust features of finite fault models. However, one has to be aware that modeling of high frequency stress variations still relies on more detailed slip pattern. To illustrate the impact of an inaccurate velocity structure, we adopt a half-space Earth model to estimate the Coulomb and volumetric stress at the Gwadar mud volcano. The results due to a half-space and a 1D velocity structure compared in Figure 5.12. The effects of velocity structure are significant in terms of waveform shape and peak amplitude, but the effects are case dependent, without a simple relationship. For instance, for periods longer than 3 s, the peak Coulomb stress calculated using layered model is 2.3 times of the half-space solution. This discrepancy becomes smaller for long-period (> 10 s) waveforms: the peak amplitude ratio is 1.8 (Figure 5.12). In contrast, the estimate of the peak volumetric stress using the half-space model is larger than that using the layered model. In fact, the discrepancy becomes more pronounced for the relatively long period signals — 0.11 MPa for half-space estimation vs. 0.07 MPa for the layered model. Our results highlight the importance of using a realistic crust model.

The stress calculation at sites of Gwadar and Ormara mud volcanoes might help us to distinguish whether static stress or dynamic stress perturbation is the dominant effect. The evolution of dynamic Coulomb stress and volumetric stress are displayed in the Movie 5.2 and 5.3.

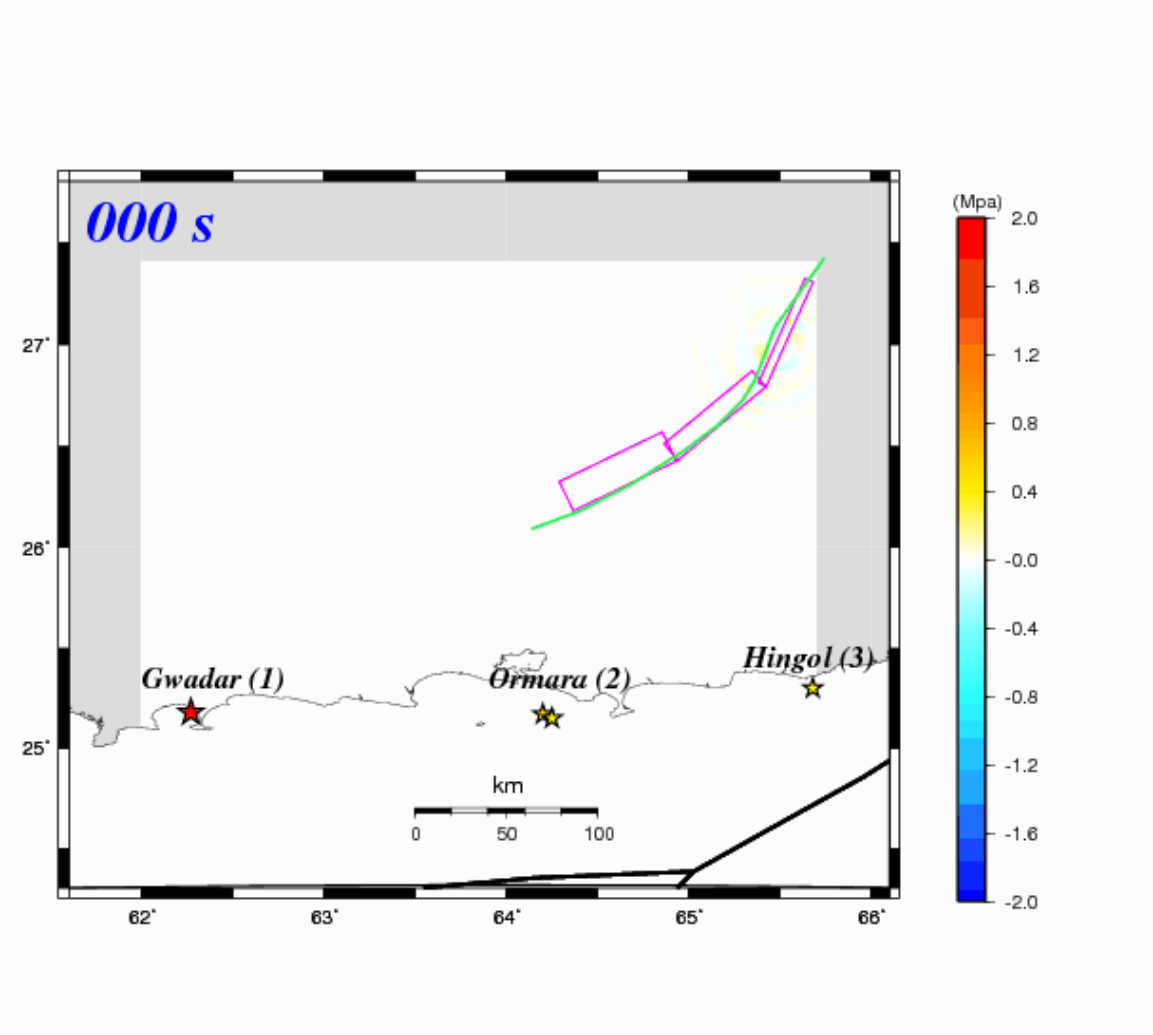

Movie 5.2: Spatial temporal evolution of dynamic volumetric stress, with a unit of MPa. Window length is 250 s and interval is 2s.

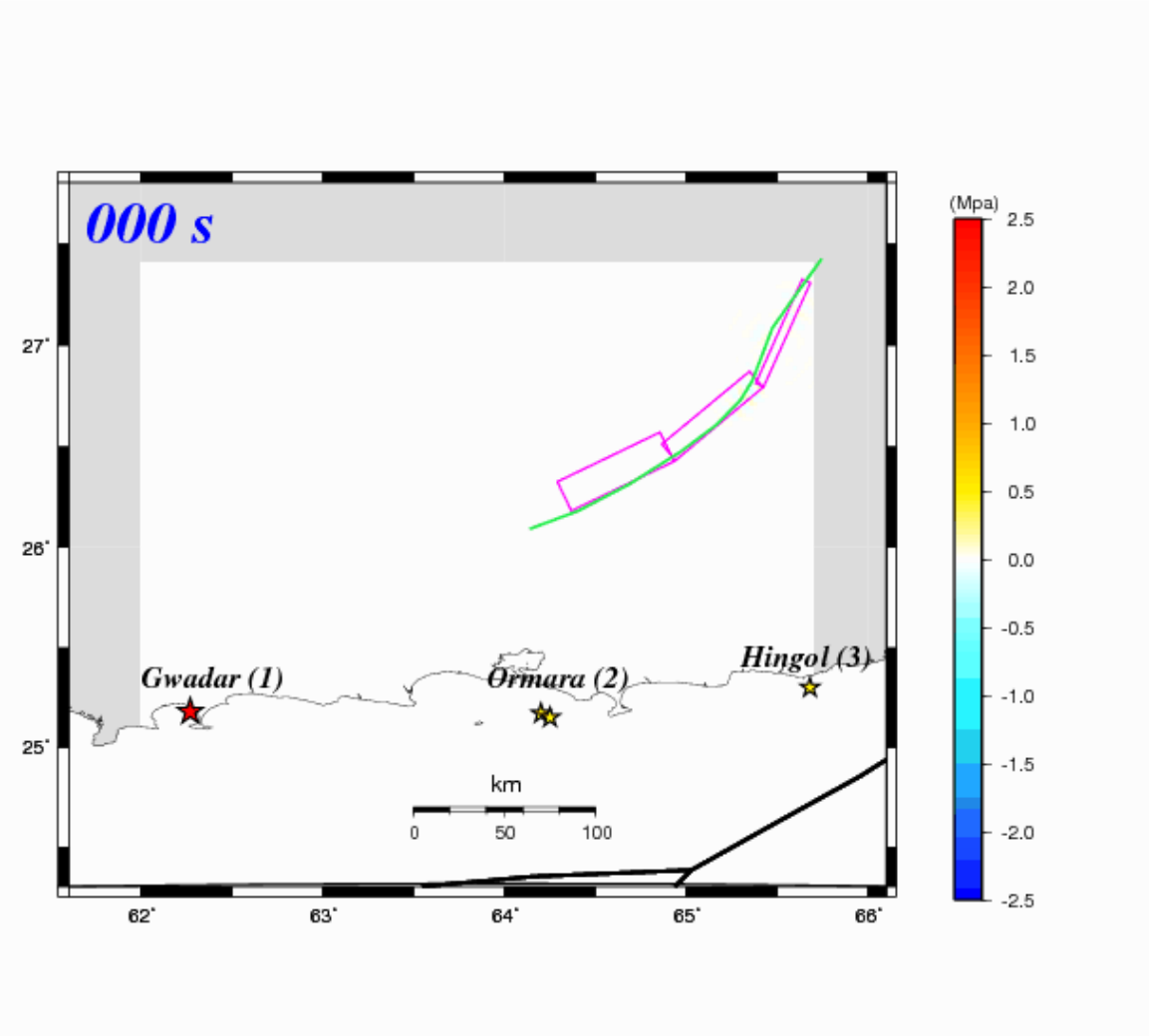

Movie 5.3: Spatial-temporal evolution of dynamic Coulomb stress. Window length is 250 s and interval is 2s.

The peak static and peak dynamic volumetric stress levels along the Pakistan coast, roughly from city Gwadar to city Hingol are contoured in Figures 5.13 a and c. We use a representative receiver depth of 3 km; the synthetic stress waveforms are low-pass filtered to less than 0.33 Hz. Ormara and Hingol are located south of this left-lateral strike-slip earthquake. For both sites the static volumetric stress is positive (or dilation) and the

amplitude is less than 0.01 MPa (Figure 5.13a). As mentioned earlier, a dilational stress perturbation would inhibit an eruption. The Gwadar region is located near the P wave nodal plane of this earthquake. The sign of volumetric stress change depends on the velocity model and the slip model, but the absolute amplitude is very small ~0.001 MPa (Figure 5.13 a). Furthermore, the negative static Coulomb stress perturbation cannot enhance strike-slip failure along the Sonna Fault.

In contrast, the peak dynamic volumetric stress is 0.2-0.3 MPa and peak dynamic Coulomb stress is greater than 1.0 MPa over entire region. The result is depth dependent. As suggested in Figures 5.8, 5.10 and 5.11, the peak amplitude would be about 50% larger if the receiver depth were 1.5 km instead of 3.0 km and 50% smaller if the receiver depth were 4.5 km. These estimates depend on the frequency band of the signal. If we low-pass filter the data to less than 0.1 Hz, the estimates are about 4-5 times smaller.

Although the dynamic stress perturbation is more favorable for triggering mud volcanoes along the Pakistan coast, we cannot distinguish which stress component produces the dominant effect. In the literature, it has been proposed that the dynamic volumetric stress carried by the passing seismic waves can change permeability, nucleate or mobilize bubbles [*Cannata et al.*, 2010] and mobilize magma [*Hill et al.*, 2002; *Sumita and Manga*, 2008]. Alternatively, mud volcanoes are often associated with weak zones, such as anticlines and vertical faults. The passage of the seismic waves can accelerate the process of shear failure in these weak zones or on a fault, producing a pathway for high-pressure deeper fluids to travel upwards (e.g., [*Mazzini et al.*, 2009]). Note that the stress perturbation at the mud volcano site near Hingol is comparable with that at Gwadar and Ormara, but there was no eruption after the 2013 earthquake even though the mud island appeared at the same spot in

March 1999 and November 2010. We suspect that the mud source or gas content in this region has not recovered from the previous eruption and thus is insufficient for an extrusion of a new mud island.

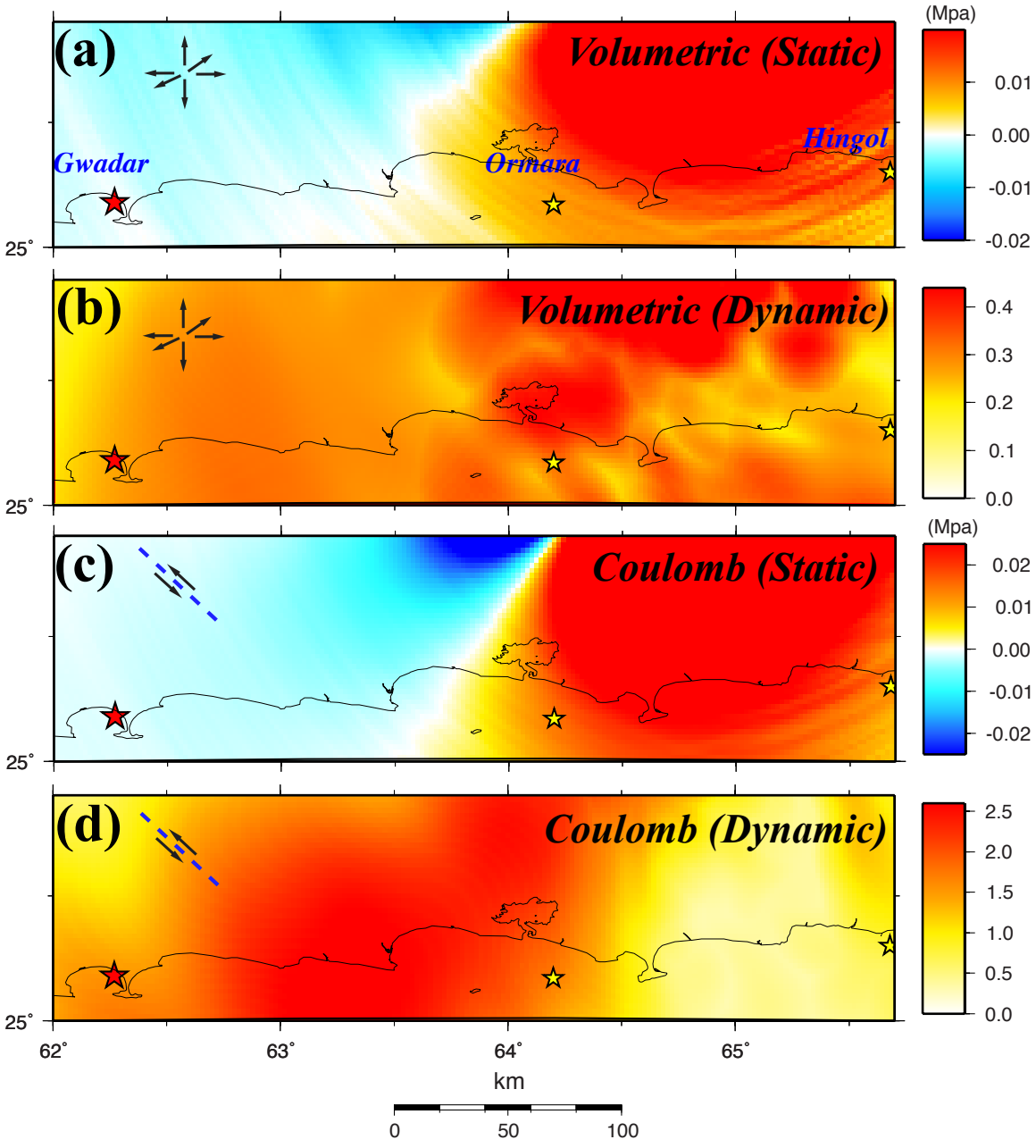

Figure 5.13: Background stress levels around Gwadar, Ormara and Hingol regions. (a) Static volumetric stress. (b) Peak amplitude of the dynamic volumetric stress. (c) Static Coulomb stress using a receiver fault plane with a strike of 315° and dip of 80°— same as the Sonne Fault. (d) Peak amplitude of the dynamic Coulomb stress. The typical range of the induced static stress around the three mud islands is between -0.02 MPa and 0.02 MPa. In contrast, the peak dynamic volumetric and Coulomb stress have significantly higher levels at ~0.5 MPa and ~2.0 MPa, respectively.

5.5 Conclusion

This study attempts to disclose the dynamic interaction between the seismic process of 2013 Pakistan earthquake and mud volcano eruptions. We implemented a multiple double-couple (MDC) approach to derive the variation of the focal mechanism corresponding to the curved fault rupture of 2013 Balochistan earthquake. We find that the dip angle cannot be well resolved by long-period waveforms. A joint inversion of teleseismic body waves and long-period surface waves help us constrain a finite source model where the rupture commenced on a sub-vertical fault and unilaterally spread 150km southwest along Hoshab Fault to the Makran Accretionary Wedge. The rupture duration is about 60s with most significant slip occurring at depths shallower than 15 km. Based on our model of the Balochistan earthquake we find significant dynamic stress perturbations induced near the sites of the mud volcanoes.

Appendix

The moment tensor solutions from different agencies include some abnormal features for the 2013 Balochistan earthquake. Global CMT solution includes an abnormally large compensated-linear-vector-dipole (CLVD) component with a ε of -0.34 ($|\varepsilon| \leq 0.5$, is defined as $-\lambda_2/\max(|\lambda_1|, |\lambda_3|)$, $\lambda_1, \lambda_2, \lambda_3$ are eigenvalues of the moment tensor, ordered such that $\lambda_1 > \lambda_2 > \lambda_3$, Nettles and Ekstrom [1998]). We found (Chapter 2) that the inverted point source moment tensor solution with significant CLVD component is often an indicator that the causative fault geometry is too complex to be approximated with a single double-couple source. Moreover, the inverted dip angle is 47°. While this value is consistent with the result of USGS W-phase analysis, estimated dip 46°, it is uncommon to have a large strike-slip earthquake with a low-angle fault plane. *Jolivet et al.* [2014] obtain a three point-source model by inverting for W-phase waveforms with the location of each point source equally distributed along the surface rupture at a depth of 7.5 km. They argue that the rupture initiated from a sub-vertical north-dipping fault on the northern portion and extended to a 50° north-dipping fault in the southern portion. This geometry is consistent with the asymmetric deformation pattern across the fault observed from optical images. Here, we conduct a multiple double-couple (MDC) analysis using long-period (3-6 mHz) seismic waveforms recorded at 53 selected teleseismic stations to investigate the possible source complexity.

We adopt a normal mode superposition algorithm [*Dahlen and Tromp,* 1998] to calculate the long-period synthetic seismograms of 1D anisotropic PREM Earth [*Dziewonski and Anderson*, 1981] and use the waveforms of September 28 Mw 6.8 aftershock to calibrate the

3D path effects. We approximate the rupture process as multiple double-couples and simultaneously invert for their centroid location, centroid time, strike, dip, rake and scalar moment Mo using a nonlinear simulated annealing algorithm [*Sen and Stoffa*, 1991a]. During the analysis we gradually increase the number of point sources until the variance reduction of the waveform fits no longer justifies adding another point source. The single double-couple inversion yields a seismic moment of 7.3×10^{20} Nm on a nodal plane with a strike of 48° and a dip of 88°. The overall variance reduction is 78.6%. However, the long-period observations within certain azimuthal ranges, display remarkable misfit against synthetics (Figure S5.1). When we use two double-couples to approximate the source, the variance reduction increases to 83% with an excellent waveform fit in long period (Figure S5.2). Increasing the number of point sources beyond two produces insignificant improvement in waveform fit. The inverted two double-couple solution can be interpreted as left-lateral strike-slip rupture on a curved fault extending roughly NNE-SSW. The centroid of the first subevent (27.0°N, 65.4°E, Figure S5.2) is close to the USGS epicenter (26.951°N 65.501°E). Its rupture features shallower slip (centroid depth = 4 km) on a fault plane orienting 212°N and dipping 76° NNW. The rake angle is 21°. The centroid time is 13 s. The second subevent features deeper slip (14 km) on a vertical fault orienting 244°. The rake angle is -30°. The centroid location is (26.4°N, 64.6°E, Figure S5.2), 103 km southwest of the epicenter. It has a centroid time of 23 s after origin time. Compared to the aforementioned moment tensor solution of about 45°, our two double-couple source model has larger dip angle consistent with the general observations for dip angles of large continental strike-slip earthquakes. However, sensitivity analysis performed later reveals that a range of dip angle from 50° to 90° can reach a similar variance reduction 82%~83%.

As such the dip angle is poorly constrained by the long-period waveform for this earthquake. We note that the moment tensor from our best two double-couple model produces a CLVD component with $\varepsilon = -0.17$, just partly explaining the abnormal large CLVD component in the original GCMT solution. However, our value agrees well with newly updated GCMT result with a CLVD of -0.18.

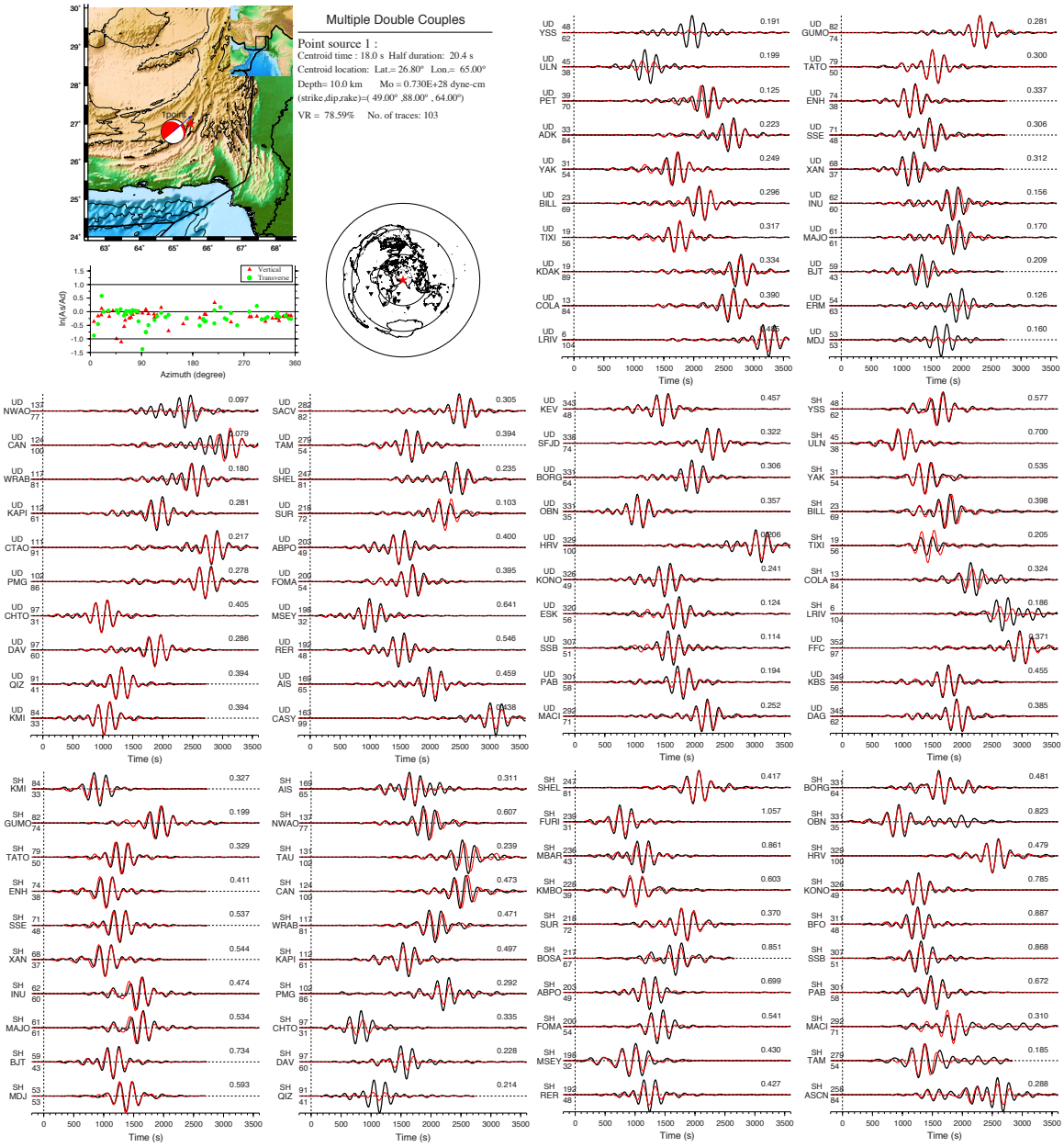

Figure S5.1: Multiple double-couple analysis (MDC) using one point source. The red beach balls represent the preferred MDC solution. Blue arrow denotes the strike direction of the inferred fault plane. The azimuthal variation of amplitude ratio in logarithmic format (ln (As/Ad)) and station distribution are given below. Red triangles and green dots represent the vertical and transverse components, respectively. Long-period waveform fits for all 100 stations are shown. The data are shown in black and the synthetics are in red. The number at

the end of each trace is the peak amplitude in millimeter. The number above the beginning of each trace is the source azimuth ad below is the epicentral distance in degrees.

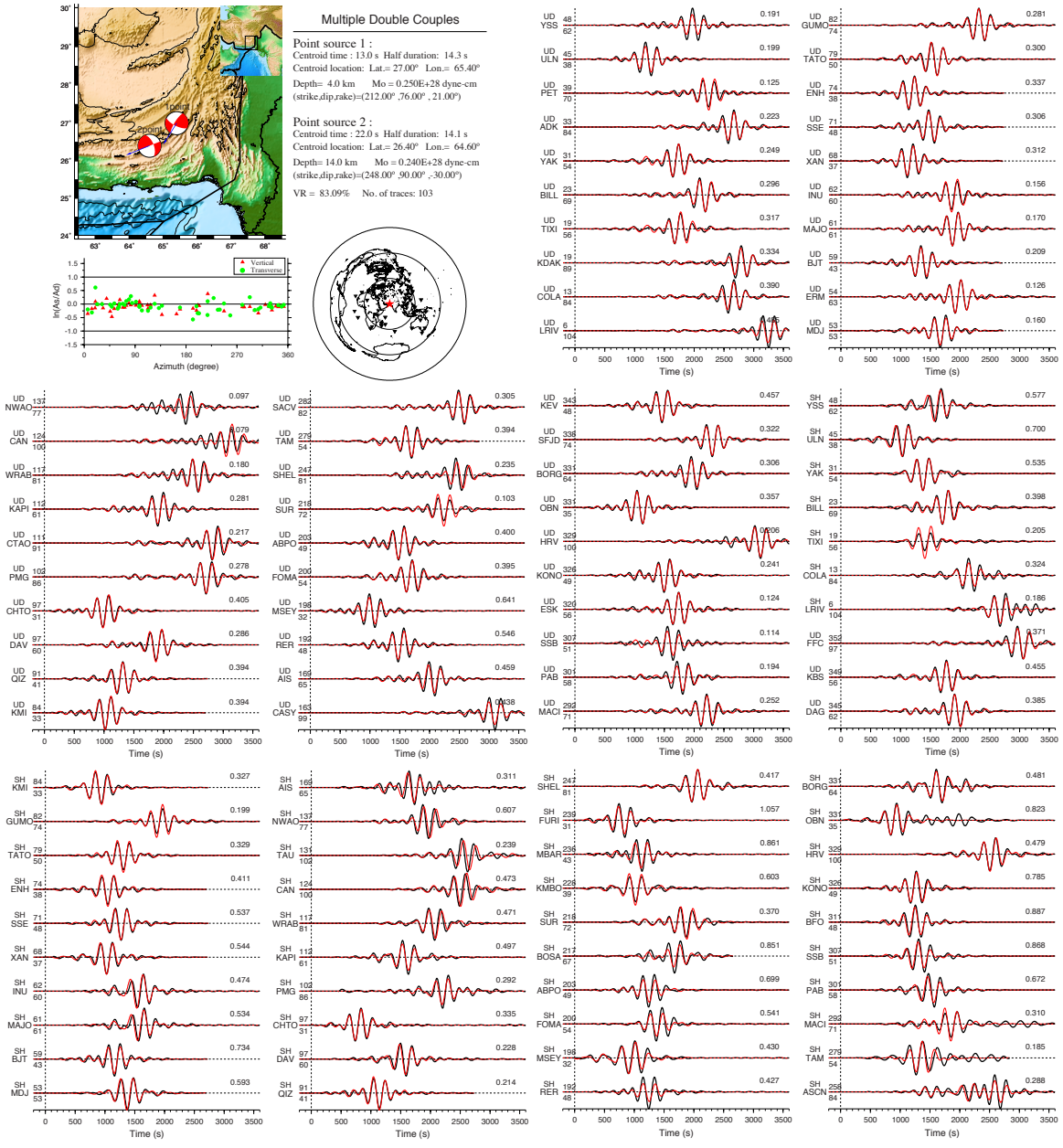

Figure S5.2: Multiple double-couple analysis (MDC) using 2 point sources, with profiles similar to Figure S5.1.

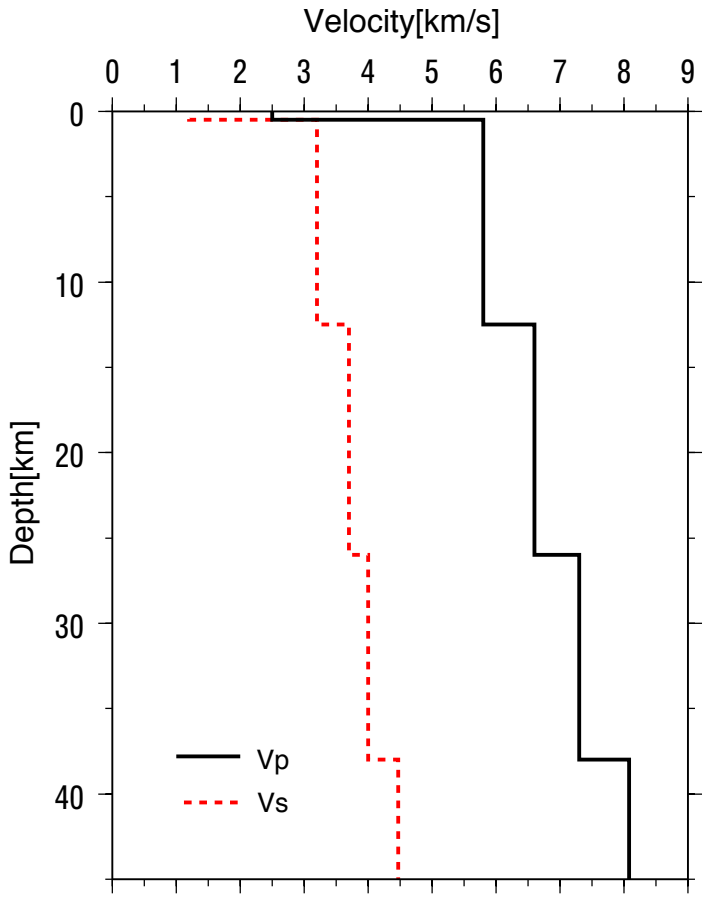

Figure S5.3: 1-D velocity model used in our inversion.

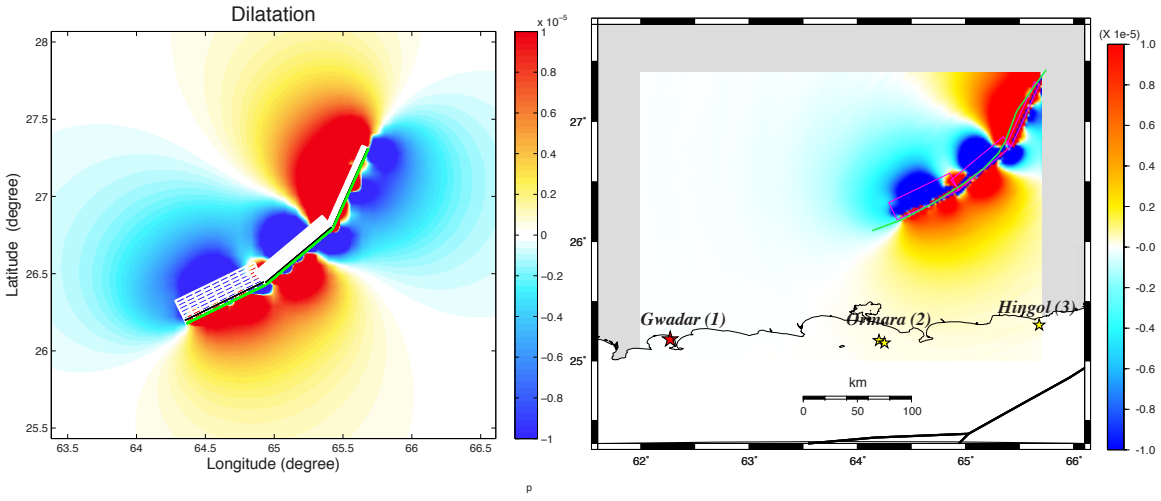

Figure S5.4: Static volumetric strain calculated with Coulomb 3.3 software (Toda et al., 2011) assuming a friction coefficient of 0.25 based on half-space model (left) and with FK method based on our 1-D layered model (right). Note that the pattern and amplitude of two results are highly consistent.

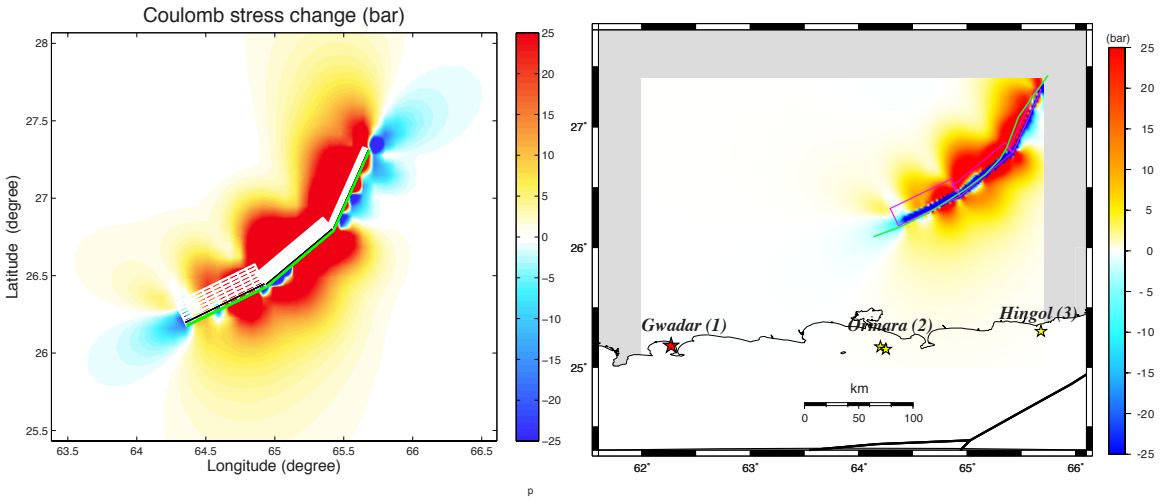

Figure S5.5: Static Coulomb stress calculated by Coulomb 3.3 (left) and F-K method (right). A receiver fault plane with a strike of 315° and dip of 80°, the same as Sonne fault, is used.

REFERENCE

1. Allmann, B. P., and P. M. Shearer (2009), Global variations of stress drop for moderate to large earthquakes, *J Geophys Res-Sol Ea*, *114*.
2. Ammon, C. J., et al. (2005), Rupture process of the 2004 Sumatra-Andaman earthquake, *Science*, *308*(5725), 1133-1139.

3. Antonioli, A., M. E. Belardinelli, and M. Cocco (2004), Modelling dynamic stress changes caused by an extended rupture in an elastic stratified half-space, *Geophys J Int*, *157*(1), 229-244.
4. Antonioli, A., M. Cocco, S. Das, and C. Henry (2002), Dynamic stress triggering during the great 25 March 1998 Antarctic Plate earthquake, *B Seismol Soc Am*, *92*(3), 896-903.
5. Argus, D. F., R. G. Gordon, M. B. Heflin, C. Ma, R. J. Eanes, P. Willis, W. R. Peltier, and S. E. Owen (2010), The angular velocities of the plates and the velocity of Earth's centre from space geodesy, *Geophys J Int*, *180*(3), 913-960.
6. Avouac, J. P., F. Ayoub, S. J. Wei, J. P. Ampuero, L. S. Meng, S. Leprince, R. Jolivet, Z. Duputel, and D. Helmberger (2014), The 2013, Mw 7.7 Balochistan earthquake, energetic strike-slip reactivation of a thrust fault, *Earth Planet Sc Lett*, *391*, 128-134.
7. Bird, P. (2003), An updated digital model of plate boundaries, *Geochem Geophy Geosy*, *4*.
8. Briggs, R. W., et al. (2006), Deformation and slip along the Sunda Megathrust in the great 2005 Nias-Simeulue earthquake, *Science*, *311*(5769), 1897-1901.
9. Brune, J. N. (1970), Tectonic Stress and Spectra of Seismic Shear Waves from Earthquakes, *J Geophys Res*, *75*(26), 4997-&.
10. Cannata, A., G. Di Grazia, P. Montalto, F. Ferrari, G. Nunnari, D. Patane, and E. Privitera (2010), New insights into banded tremor from the 2008-2009 Mount Etna eruption, *J Geophys Res-Sol Ea*, *115*.
11. Chapple, W. M., and D. W. Forsyth (1979), Earthquakes and Bending of Plates at Trenches, *J Geophys Res*, *84*(Nb12), 6729-6749.
12. Christensen, D. H., and L. J. Ruff (1983), Outer-Rise Earthquakes and Seismic Coupling, *Geophys Res Lett*, *10*(8), 697-700.
13. Christensen, D. H., and L. J. Ruff (1988), Seismic Coupling and Outer Rise Earthquakes, *J Geophys Res-Solid*, *93*(B11), 13421-13444.
14. Dahlen, F. A., and J. Tromp (1998), *Theoretical global seismology*, xiv, 1025 p. pp., Princeton University Press, Princeton, N.J.
15. Davies, R. J., and S. A. Stewart (2005), Emplacement of giant mud volcanoes in the South Caspian Basin: 30 seismic reflection imaging of their root zones, *J Geol Soc London*, *162*, 1-4.

16. Delouis, B., J. M. Nocquet, and M. Vallee (2010), Slip distribution of the February 27, 2010 Mw=8.8 Maule Earthquake, central Chile, from static and high-rate GPS, InSAR, and broadband teleseismic data, *Geophys Res Lett*, *37*.
17. Dziewonski, A. M., and D. L. Anderson (1981), Preliminary Reference Earth Model, *Phys Earth Planet In*, *25*(4), 297-356.
18. Ekstrom, G., A. M. Dziewonski, N. N. Maternovskaya, and M. Nettles (2005a), Global seismicity of 2003: centroid-moment-tensor solutions for 1087 earthquakes, *Phys Earth Planet In*, *148*(2-4), 327-351.
19. Ekstrom, G., A. M. Dziewonski, N. N. Maternovskaya, and M. Nettles (2005b), Global seismicity of 2002: centroid-moment-tensor solutions for 1034 earthquakes, *Phys Earth Planet In*, *148*(2-4), 303-326.
20. Engdahl, E. R., R. van der Hilst, and R. Buland (1998), Global teleseismic earthquake relocation with improved travel times and procedures for depth determination, *B Seismol Soc Am*, *88*(3), 722-743.
21. Finlayson, D. M., W. A. Wiebenga, J. P. Webb, A. S. Furumoto, and J. P. Cull (1972), New Britain New Ireland Crustal Seismic Refraction Investigations 1967 and 1969, *Geophys J Roy Astr S*, *29*(3), 245-&.
22. Finlayson, D. M., O. Gudmundsson, I. Itikarai, Y. Nishimura, and H. Shimamura (2003), Rabaul volcano, Papua New Guinea: seismic tomographic imaging of an active caldera, *J Volcanol Geoth Res*, *124*(3-4), 153-171.
23. Frohlich, C. (1994), Earthquakes with Non-Double-Couple Mechanisms, *Science*, *264*(5160), 804-809.
24. Geist, E. L., and T. Parsons (2005), Triggering of tsunamigenic aftershocks from large strike-slip earthquakes: Analysis of the November 2000 New Ireland earthquake sequence, *Geochem Geophy Geosy*, *6*.
25. Gomberg, J., P. Bodin, and P. A. Reasenberg (2003), Observing earthquakes triggered in the near field by dynamic deformations, *B Seismol Soc Am*, *93*(1), 118-138.
26. Hardebeck, J. L., J. J. Nazareth, and E. Hauksson (1998), The static stress change triggering model: Constraints from two southern California aftershock sequences, *J Geophys Res-Sol Ea*, *103*(B10), 24427-24437.

27. Harris, R. A. (1998), Introduction to special section: Stress triggers, stress shadows, and implications for seismic hazard, *J Geophys Res-Sol Ea*, *103*(B10), 24347-24358.
28. Hartzell, S. H., and T. H. Heaton (1983), Inversion of Strong Ground Motion and Teleseismic Waveform Data for the Fault Rupture History of the 1979 Imperial-Valley, California, Earthquake, *B Seismol Soc Am*, *73*(6), 1553-1583.
29. Henry, C., S. Das, and J. H. Woodhouse (2000), The great March 25, 1998, Antarctic Plate earthquake: Moment tensor and rupture history, *J Geophys Res-Sol Ea*, *105*(B7), 16097-16118.
30. Henry, C., J. H. Woodhouse, and S. Das (2002), Stability of earthquake moment tensor inversions: effect of the double-couple constraint, *Tectonophysics*, *356*(1-3), 115-124.
31. Hill, D. P., F. Pollitz, and C. Newhall (2002), Earthquake-volcano interactions, *Phys Today*, *55*(11), 41-47.
32. Hjorleifsdottir, V., H. Kanamori, and J. Tromp (2009), Modeling 3-D wave propagation and finite slip for the 1998 Balleny Islands earthquake, *J Geophys Res-Sol Ea*, *114*.
33. Hreinsdottir, S., J. T. Freymueller, R. Burgmann, and J. Mitchell (2006), Coseismic deformation of the 2002 Denali Fault earthquake: Insights from GPS measurements, *J Geophys Res-Sol Ea*, *111*(B3).
34. Hsu, Y. J., M. Simons, J. P. Avouac, J. Galetzka, K. Sieh, M. Chlieh, D. Natawidjaja, L. Prawirodirdjo, and Y. Bock (2006), Frictional afterslip following the 2005 Nias-Simeulue earthquake, Sumatra, *Science*, *312*(5782), 1921-1926.
35. Ishii, M., P. M. Shearer, H. Houston, and J. E. Vidale (2005), Extent, duration and speed of the 2004 Sumatra-Andaman earthquake imaged by the Hi-Net array, *Nature*, *435*(7044), 933-936.
36. Ji, C., D. J. Wald, and D. V. Helmberger (2002a), Source description of the 1999 Hector Mine, California, earthquake, part II: Complexity of slip history, *B Seismol Soc Am*, *92*(4), 1208-1226.
37. Ji, C., D. J. Wald, and D. V. Helmberger (2002b), Source description of the 1999 Hector Mine, California, earthquake, part I: Wavelet domain inversion theory and resolution analysis, *B Seismol Soc Am*, *92*(4), 1192-1207.
38. Ji, C., D. V. Helmberger, D. J. Wald, and K. F. Ma (2003a), Slip history and dynamic implications of the 1999 Chi-Chi, Taiwan, earthquake, *J Geophys Res-Sol Ea*, *108*(B9).

39. Ji, C., D. V. Helmberger, D. J. Wald, and K. F. Ma (2003b), Slip history and dynamic implications of the 1999 Chi-Chi, Taiwan, earthquake, *Journal Of Geophysical Research-Solid Earth*, *108*(B9), art. no.-2412.
40. Ji, C., K. M. Larson, Y. Tan, K. W. Hudnut, and K. H. Choi (2004), Slip history of the 2003 San Simeon earthquake constrained by combining 1-Hz GPS, strong motion, and teleseismic data, *Geophys Res Lett*, *31*(17), L17608.
41. Jolivet, R., et al. (2014), The 2013 M-w 7.7 Balochistan Earthquake: Seismic Potential of an Accretionary Wedge, *B Seismol Soc Am*, *104*(2), 1020-1030.
42. Kanamori, H., and D. L. Anderson (1975), Theoretical Basis of Some Empirical Relations in Seismology, *B Seismol Soc Am*, *65*(5), 1073-1095.
43. Kanamori, H., and J. W. Given (1981), Use of Long-Period Surface-Waves for Rapid-Determination of Earthquake-Source Parameters, *Phys Earth Planet In*, *27*(1), 8-31.
44. Kennett, B. L. N., and E. R. Engdahl (1991), Traveltimes for Global Earthquake Location and Phase Identification, *Geophys J Int*, *105*(2), 429-465.
45. Kilb, D. (2003), A strong correlation between induced peak dynamic Coulomb stress change from the 1992 M7.3 Landers, California, earthquake and the hypocenter of the 1999 M7.1 Hector Mine, California, earthquake, *J Geophys Res-Sol Ea*, *108*(B1).
46. King, G. C. P., and S. G. Wesnousky (2007), Scaling of fault parameters for continental strike-slip earthquakes, *B Seismol Soc Am*, *97*(6), 1833-1840.
47. Knopoff, L. (1958), Energy Release in Earthquakes, *Geophys J Roy Astr S*, *1*(1), 44-52.
48. Konca, A. O., V. Hjorleifsdottir, T. R. A. Song, J. P. Avouac, D. V. Helmberger, C. Ji, K. Sieh, R. Briggs, and A. Meltzner (2007), Rupture kinematics of the 2005 M-w 8.6 Nias-Simeulue earthquake from the joint inversion of seismic and geodetic data, *B Seismol Soc Am*, *97*(1), S307-S322.
49. Kopf, A. J. (2002), Significance of mud volcanism, *Rev Geophys*, *40*(2).
50. Kuge, K., and H. Kawakatsu (1990), Analysis of a Deep Nondouble Couple Earthquake Using Very Broad-Band Data, *Geophys Res Lett*, *17*(3), 227-230.
51. Kukowski, N., T. Schillhorn, E. R. Flueh, and K. Huhn (2000), Newly identified strike-slip plate boundary in the northeastern Arabian Sea, *Geology*, *28*(4), 355-358.
52. Langston, C. A. (1981), Source Inversion of Seismic Waveforms - the Koyna, India, Earthquakes of 13 September 1967, *B Seismol Soc Am*, *71*(1), 1-24.

53. Langston, C. A., and D. V. Helmberger (1975), Procedure for Modeling Shallow Dislocation Sources, *Geophys J Roy Astr S*, *42*(1), 117-130.
54. Lasserre, C., G. Peltzer, F. Crampe, Y. Klinger, J. Van der Woerd, and P. Tapponnier (2005), Coseismic deformation of the 2001 M-w=7.8 Kokoxili earthquake in Tibet, measured by synthetic aperture radar interferometry, *J Geophys Res-Sol Ea*, *110*(B12).
55. Lay, T., Z. Duputel, L. L. Ye, and H. Kanamori (2013), The December 7, 2012 Japan Trench intraplate doublet (M-w 7.2, 7.1) and interactions between near-trench intraplate thrust and normal faulting, *Phys Earth Planet In*, *220*, 73-78.
56. Lay, T., H. Kanamori, C. J. Ammon, A. R. Hutko, K. Furlong, and L. Rivera (2009), The 2006-2007 Kuril Islands great earthquake sequence, *J Geophys Res-Sol Ea*, *114*.
57. Lay, T., C. J. Ammon, H. Kanamori, K. D. Koper, O. Sufri, and A. R. Hutko (2010a), Teleseismic inversion for rupture process of the 27 February 2010 Chile (M-w 8.8) earthquake, *Geophys Res Lett*, *37*.
58. Lay, T., C. J. Ammon, H. Kanamori, L. Rivera, K. D. Koper, and A. R. Hutko (2010b), The 2009 Samoa-Tonga great earthquake triggered doublet, *Nature*, *466*(7309), 964-U985.
59. Lin, J., and R. S. Stein (2004), Stress triggering in thrust and subduction earthquakes and stress interaction between the southern San Andreas and nearby thrust and strike-slip faults, *J Geophys Res-Sol Ea*, *109*(B2).
60. Lindley, D. (2006), Extensional and vertical tectoics in the new Guinea islands: Implications for island arc evolution, *Annals of Geophysics (supplement to vol. 49, N. 1., 2006)*.
61. Lorito, S., F. Romano, S. Atzori, X. Tong, A. Avallone, J. McCloskey, M. Cocco, E. Boschi, and A. Piatanesi (2011), Limited overlap between the seismic gap and coseismic slip of the great 2010 Chile earthquake, *Nat Geosci*, *4*(3), 173-177.
62. Manga, M., and M. Bonini (2012), Large historical eruptions at subaerial mud volcanoes, Italy, *Nat Hazard Earth Sys*, *12*(11), 3377-3386.
63. Manga, M., M. Brumm, and M. L. Rudolph (2009), Earthquake triggering of mud volcanoes, *Mar Petrol Geol*, *26*(9), 1785-1798.
64. Mazzini, A., A. Nermoen, M. Krotkiewski, Y. Podladchikov, S. Planke, and H. Svensen (2009), Strike-slip faulting as a trigger mechanism for overpressure release through

piercement structures. Implications for the Lusi mud volcano, Indonesia, *Mar Petrol Geol*, *26*(9), 1751-1765.

65. Mazzini, A., H. Svensen, G. G. Akhmanov, G. Aloisi, S. Planke, A. Malthe-Sorenssen, and B. Istadi (2007), Triggering and dynamic evolution of the LUSI mud volcano, Indonesia, *Earth Planet Sc Lett*, *261*(3-4), 375-388.
66. Miura, S., N. Takahashi, A. Nakanishi, T. Tsuru, S. Kodaira, and Y. Kaneda (2005), Structural characteristics off Miyagi forearc region, the Japan Trench seismogenic zone, deduced from a wide-angle reflection and refraction study, *Tectonophysics*, *407*(3-4), 165-188.
67. Moreno, M., M. Rosenau, and O. Oncken (2010), 2010 Maule earthquake slip correlates with pre-seismic locking of Andean subduction zone, *Nature*, *467*(7312), 198-U184.
68. Nettles, M., and G. Ekstrom (1998), Faulting mechanism of anomalous earthquakes near Bardarbunga Volcano, Iceland, *J Geophys Res-Sol Ea*, *103*(B8), 17973-17983.
69. Nettles, M., T. C. Wallace, and S. L. Beck (1999), The March 25, 1998 Antarctic plate earthquake, *Geophys Res Lett*, *26*(14), 2097-2100.
70. Olson, A. H., and R. J. Apsel (1982), Finite Faults and Inverse-Theory with Applications to the 1979 Imperial-Valley Earthquake, *B Seismol Soc Am*, *72*(6), 1969-2001.
71. Park, J., et al. (2005), Earth's free oscillations excited by the 26 December 2004 Sumatra-Andaman earthquake, *Science*, *308*(5725), 1139-1144.
72. Park, S. C., and J. Mori (2007), Triggering of earthquakes during the 2000 Papua New Guinea earthquake sequence, *J Geophys Res-Sol Ea*, *112*(B3).
73. Parsons, T., and A. A. Velasco (2009), On near-source earthquake triggering, *J Geophys Res-Sol Ea*, *114*.
74. Rubinstein, J. L., J. E. Vidale, J. Gomberg, P. Bodin, K. C. Creager, and S. D. Malone (2007), Non-volcanic tremor driven by large transient shear stresses, *Nature*, *448*(7153), 579-582.
75. Ruegg, J. C., et al. (1996), The M(W)=8.1 Antofagasta (North Chile) earthquake of July 30, 1995: First results from teleseismic and geodetic data, *Geophys Res Lett*, *23*(9), 917-920.
76. Scholz, C. H. (2002), *The mechanics of earthquakes and faulting* Cambridge University Press.

77. Sen, M. K., and P. L. Stoffa (1991a), Nonlinear One-Dimensional Seismic Wave-Form Inversion Using Simulated Annealing, *Geophysics*, *56*(10), 1624-1638.
78. Sen, M. K., and P. L. Stoffa (1991b), Nonlinear one-dimensional seismic waveform inversion using simulated annealing *Geophysics*, *56*(10), 1624-1638.
79. Shao, G. F., X. Y. Li, C. Ji, and T. Maeda (2011), Focal mechanism and slip history of the 2011 M-w 9.1 off the Pacific coast of Tohoku Earthquake, constrained with teleseismic body and surface waves, *Earth Planets Space*, *63*(7), 559-564.
80. Subarya, C., M. Chlieh, L. Prawirodirdjo, J. P. Avouac, Y. Bock, K. Sieh, A. J. Meltzner, D. H. Natawidjaja, and R. McCaffrey (2006), Plate-boundary deformation associated with the great Sumatra-Andaman earthquake, *Nature*, *440*(7080), 46-51.
81. Sumita, I., and M. Manga (2008), Suspension rheology under oscillatory shear and its geophysical implications, *Earth Planet Sc Lett*, *269*(3-4), 467-476.
82. Toda, S., R. S. Stein, K. Richards-Dinger, and S. B. Bozkurt (2005), Forecasting the evolution of seismicity in southern California: Animations built on earthquake stress transfer, *J Geophys Res-Sol Ea*, *110*(B5).
83. Tregoning, P., M. Sambridge, H. McQueen, S. Toulmin, and T. Nicholson (2005), Tectonic interpretation of aftershock relocations in eastern Papua New Guinea using teleseismic data and the arrival pattern method, *Geophys J Int*, *160*(3), 1103-1111.
84. Tregoning, P., R. J. Jackson, H. McQueen, K. Lambeck, C. Stevens, R. P. Little, R. Curley, and R. Rosa (1999), Motion of the South Bismarck Plate, Papua New Guinea, *Geophys. Res. Lett.*, *26*(23), 3517-3520.
85. Tsai, V. C., M. Nettles, G. Ekstrom, and A. M. Dziewonski (2005), Multiple CMT source analysis of the 2004 Sumatra earthquake, *Geophys Res Lett*, *32*(17).
86. Zhu, L. P., and L. A. Rivera (2002), A note on the dynamic and static displacements from a point source in multilayered media, *Geophys J Int*, *148*(3), 619-627.